

Galaxy Properties from a Diameter-Limited Catalog

A THESIS

SUBMITTED TO THE FACULTY OF THE GRADUATE SCHOOL
OF THE UNIVERSITY OF MINNESOTA

BY

Juan Enrique Cabanela Larrinaga

IN PARTIAL FULFILLMENT OF THE REQUIREMENTS
FOR THE DEGREE OF
DOCTOR OF PHILOSOPHY

Professor Roberta Humphreys, Adviser

August, 1999

© **Juan Enrique Cabanela Larrinaga 1999**

Galaxy Properties from a Diameter-Limited Catalog

by **Juan Enrique Cabanela Larrinaga**

Under the supervision of **Professor Roberta
Humphreys**

ABSTRACT

I am using the Minnesota Automated Plate Scanner (APS) to construct two galaxy catalogs. The Minnesota Automated Plate Scanner Pisces-Perseus Survey (MAPS-PP) is used to search for modern-day remnant signatures of large-scale structure formation processes, specifically, galaxy alignments relative to surrounding large-scale structure. Weak evidence for such alignments is found, although the type of alignments seen don't strongly support any one large-scale structure formation model. Comparison of the MAPS-PP to pre-existing galaxy catalogs has led to the discovery that the Uppsala General Catalog and Third Reference Catalog of Galaxies exhibit a very strong measurement bias: their diameters are measured to different isophotes at different galaxy inclinations. Therefore previous determinations of the diameter function and the internal extinction properties of other galaxies (most of which have relied on one of these two galaxy catalogs) have suffered from a biased diameter measurement. I avoid this bias by using the APS data (which is obtained using automated computer-based criteria for measuring the structural properties of images digitized from photographic plates) to construct a catalog of over 200,000 galaxies within 30° of the North Galactic Pole (the MAPS-NGP). The MAPS-NGP is the deepest galaxy catalog constructed over such a large area of the sky and

used to re-evaluate previous investigations of the internal extinction in galaxies.

Acknowledgements

Wow, it's finally time for me to graduate! I realize in writing this that I have spent over a quarter of my life in graduate school! While I am enthusiastic to finally bring this part of my life to a close, I have to say it has allowed me to get to know some outstanding individuals. First and foremost, I wish to thank my advisor, Roberta Humphreys. You have been a great mentor and a great friend. I could not have found someone better for getting me through the graduate experience and letting me have the freedom to explore some of the "less reputable" parts of astrophysics. I am proud to have been able to work with you. I wish to thank John Dickey for convincing me to apply for time at Arecibo. That one experience may have delayed this thesis, but it provided me with an experience I will never forget. I also want to thank Kris Davidson and Larry Rudnick for being wonderful sounding boards for some of my crazier ideas about extragalactic astronomy and statistics. Thanks to all of them for the many enlightening discussions. Jeff "Game Bastard" Larsen...what can one say about someone who tries to creatively disintegrate you month after month. Jeff is one of the nicest guys I have known, supporting me in many ways that only someone going through graduate school can. If you are reading this and wondering why I would call Jeff a "Game Bastard," all you need to do is talk to Stan Sagan, Marc Pouilly, Chris Taylor, or Hui Yang about our Star Wars gaming sessions. Gerrex and Ah Nold wish to thank all of them for helping improve their life expectancies, and apologize for occasionally reducing theirs. And I wish to thank them for being good friends. While I am at it, I have to thank Krista Johansen for being a good friend during my first few years at the U and for showing me that astronomy was not necessarily the

only career choice I had (even if it is the one I am currently taking). One meets many people in graduate school, but some friendships can actually pre-date it! I want to thank Francisco Puga for his long friendship, over a quarter of a century now. He has been a great amigo, and I can even forgive him for his bad taste in movies and his, ahem, *mild* insults during various sessions of networked Quake. Chris Arendt and Gerald Burt have brought good doses of the real world into my life, things like parties, movies, camping, and a well-timed weekend in a cabin north of Bemidji. Thanks guys. Leah Smith has also contributed to my sense of the real world, and I know that she is a friend. I know this because she can put up with my constant ripping on her beloved Packers and the fact that I am not a republican. Finally, I also want to thank Rodney and Irma, who have been great friends the last few years...and just think¹ Rodney, I wrote this all on a Macintosh! And beyond friends, there is family. My parents, Miguel Cabanela and Rosa Larrinaga Cabanela, and my brother, Daniel, have been there all along. They supported me even though I was following a rather odd career path. They provided excellent role models (yes, even Daniel) for my educational and personal endeavors. I also need to thank the family I have inherited through marriage, the many members of Club Owen, who have also been very supportive of my career choice (I think I will carry the image of Jeannine wildly jumping up and down in excitement at my landing a job at SCSU for quite some time to come). And finally, I wish to thank my wife, Catherine Lucille Owen Cabanela. When I first came to graduate school here in Minnesota, I was a rather bitter person, having gone through a rather messy relationship. Catherine was the individual who saw past that and started drawing me out. She made it easy for me to fall in love again. Catherine is the prime example that if you are going to choose a spouse, you should make sure they are also your best friend. Te amo con todo mi corazon.

¹or think different...

Dedication

I dedicate this thesis to my parents. They, more than anyone else, have been the best role models I could have hoped for. Any accomplishments of mine are due in no small part to their support. Gracias, Ama y Aita.

Table of Contents

Abstract	ii
Acknowledgements	iv
Dedication	vi
List of Tables	viii
List of Figures	ix
1 Introduction	1
1.1 The Early History of Astronomical Catalogs: Gathering the Nebulae . . .	1
1.2 Early Galaxy Catalogs: Removing “Local” Clutter From The NGC/IC . .	4
1.2.1 POSS-based Galaxy Catalogs	5
1.2.2 The Reference Catalogs of Bright Galaxies	6
1.2.3 Online Galaxy Databases	7
1.3 Building Better Galaxy Catalogs	8
1.3.1 The Automated Plate Scanner Catalog	9
1.4 Goals of this Thesis	9
1.4.1 Galaxy Alignments: Probing Large-Scale Structure Formation . .	10
1.4.2 Probing Internal Galactic Structure	11
2 Galaxy Alignments in the Pisces-Perseus Supercluster	13

2.1	Introduction	14
2.1.1	Expectations from Theory and Models	15
2.1.2	Previous Observational Efforts	18
2.2	Observational Data	22
2.2.1	Modeling the Galaxy Images	27
2.2.2	Data Quality Control	29
2.3	Dataset Cross-Identification, Calibration, and Integrity Tests	37
2.3.1	Photometric Calibration	37
2.3.2	Ellipticity Distribution of the MAPS-PP	38
2.3.3	The PPS Luminosity Function and the Level of Non-Supercluster Galaxy Contamination	39
2.4	Data Analysis Methods	44
2.4.1	Identification of Large-Scale Structures within the MAPS-PP	44
2.4.2	The Sinusoidal Model	47
2.4.3	Position Angle Distributions Tested	47
2.5	Results and Discussion	51
2.5.1	The Identification of Possible Galaxy Alignments	51
2.5.2	Comparison to Previous Work	60
2.6	Conclusions	65
2.7	Future Directions	67
2.8	Acknowledgments	68
2.9	Appendix: Understanding the Ellipticity Distribution	68

3 Determination of Galaxy Spin Vectors in the Pisces-Perseus Supercluster with the Arecibo Telescope **72**

3.1	Introduction	73
3.2	Data	75
3.2.1	Selection Criteria	75

3.2.2	HI Observations	79
3.2.3	Determination of Galaxy Spin Vector Directions and Uncertainty	80
3.3	Data Analysis Methods	87
3.3.1	The Kuiper Statistic	87
3.4	Results and Analysis	89
3.4.1	Probing for Global Spin Vector Alignments	89
3.4.2	Probing for Spin Vector Domains	92
3.4.3	Establishing Limits on Galaxy Alignments	93
3.5	Conclusions	96
3.6	Acknowledgements	99
4	Recent APS Data Reduction Pipeline Improvements	100
4.1	Improved Image Classification	101
4.2	Improved Astrometry	102
4.3	Improved Galaxy Photometry	103
4.4	<i>StarBase2</i> : Database Content Changes	108
5	Creation of a Large Extragalactic Catalog: The MAPS-NGP Catalog	109
5.1	Initial Selection Criteria for <i>StarBase2</i> Queries	112
5.2	Elimination of Duplicate Objects from Plate Overlap Regions	117
5.3	Elimination of False Galaxies from Bright Star Halos	118
5.4	Elimination of False Galaxies due to Ghost Images	125
5.5	Elimination of False Galaxies due to Galactic Globular Clusters	129
5.6	Elimination of Artifacts around some UGC galaxies	130
5.7	Computation of the Surface Density of Galaxies in the MAPS-NGP	131
5.8	Addition of non- <i>StarBase2</i> image parameters to the MAPS-NGP	132
5.9	Galactic Extinction Estimates for MAPS-NGP Galaxies	134
5.10	Summary of the MAPS-NGP Catalog	137

6	Previous Investigations of Internal Extinction in Galaxies	144
6.1	Galactic Extinction: A Local Example of Internal Extinction	146
6.2	Internal Extinction in Other Galaxies - Early Studies	148
6.3	Internal Extinction in Other Galaxies - The Last Decade	151
6.4	Getting Around Selection Effects	158
6.4.1	The Danger of Selection Effects	158
6.4.2	Getting Around Selection Effects with Distance	165
6.4.3	Statistical Descriptions of Inclination Effects: Choloniewski's Estimators	166
6.5	Problems with Recent Studies	170
6.5.1	Huizinga's Diameter-Inclination Effect	171
6.6	Requirements For Determining The Proper Inclination Trajectory	176
7	The MAPS-NGPZT: A Dataset for Inclination Effect Studies	177
7.1	The MAPS-NGPZT Subset of the MAPS-NGP	177
7.1.1	The MAPS-NGPZ: Cross-identification of MAPS-NGP with ZCAT	178
7.1.2	Adjusting Redshifts for Virgo Infall	183
7.1.3	Taking into Account Galactic Extinction	186
7.1.4	Computing Fractional Light Radii and Intensities	187
7.1.5	Taking into Account Cosmological Effects	188
7.1.6	Obtaining Isophotal Diameter and Magnitude Corrections	192
7.2	Summary of the MAPS-NGPZT Subset of the MAPS-NGP	201
8	The Effect of Inclination on a Galaxy's Appearance	204
8.1	Initial Examination of Data: Considering Selection Effects	204
8.2	Application of Choloniewski's Estimators	208
8.2.1	Determining Inclination Trajectories	217
8.2.2	Testing Effects of Morphological Classification Method	221

8.2.3	Inclination Trajectories versus Galaxy Color	226
8.3	Analysis	229
8.4	Future Directions and Considerations	230
References		233

List of Tables

2.1	The Ten POSS I Fields Examined in this Study.	23
2.2	The MAPS-PP catalog of galaxies: APS parameters (Only first 40 entries).	25
2.3	The MAPS-PP catalog of galaxies: Cross-identifications and additional galaxy parameters (Only first 40 entries).	26
2.4	Galaxy Concentrations identified in the MAPS-PP.	45
2.5	Descriptions of the MAPS-PP subsamples.	50
2.6	$\Delta\theta_{con}$ statistics for the “red” subsamples.	53
2.7	$\Delta\theta_{ridge}$ statistics for the “blue” subsamples.	55
2.8	Spearman Rank Correlations for the median $\Delta\theta_{ridge}$ vs. angular distance from the PPS ridgeline for $0.0^\circ < \Delta\theta_{ridge} < 2.0^\circ$	56
3.1	The Arecibo Sample (A subset of 96 MAPS-PP galaxies)	77
3.2	The Arecibo Observations	83
3.3	Arecibo \vec{L} Anisotropy Probabilities, $P(V)$	91
5.1	The 98 POSS I fields in the MAPS-NGP Catalog	113
5.2	The Ghost Images Removed from the MAPS-NGP Catalog	127
6.1	Previous Studies into Internal Extinction Effects	157
7.1	Distance Information for Virgo Cluster Clouds from Gavazzi <i>et al.</i> [1999]	185
7.2	K-Corrections Used (based on Frei & Gunn [1994])	190
7.3	Sources of Galaxy Surface Brightness Profiles	193

7.4	Morphological and Ellipticity Distribution of Galaxy Profiles	194
7.5	Best Fit Parameters for Equations ?? and ?? for the Surface Brightness Profiles of Galaxies	198
7.6	50% and 75% Light Radii Best Fit Parameters for Equation ?? for the Surface Brightness Profiles of Galaxies	199
8.1	Morphological Binning Used With MAPS-NGP And Chołowiecki's Estimators	208

List of Figures

2.1	The MAPS-PP Distribution on the Sky.	24
2.2	Original Galaxy Images versus Model Fits	31
2.3	Disk Component Position Angle Uncertainty versus Disk Component El- lipticity	34
2.4	Bulge versus Disk Ellipticities	35
2.5	Disk Ellipticity versus Position Angle Difference of Bulge and Disk Com- ponents	36
2.6	Disk Ellipticity Distributions	42
2.7	The Pisces-Perseus Supercluster Galaxy Luminosity Function from the MAPS-PP	43
2.8	θ_{ridge} Diagram	48
2.9	θ_{radial} Diagram	49
2.10	θ_{con} Diagram	50
2.11	θ_{con} Distribution in Reddest Quartile	57
2.12	θ_{ridge} Distribution in “Blue” Subsamples	58
2.13	Median θ_{ridge} versus Ridgeline Distance	59
2.14	Ellipticity Directibution in GTT-like MAPS-PP subsamples	64
2.15	MAPS-PP Ellipticity Distribution compared to the UGC and RC3	71
3.1	μ_{offset} , and μ_{wide} Descriptive Diagram	81
3.2	The Distribution of μ , μ_{offset} , and μ_{wide} for the Arecibo Subset	82

3.3	The Arecibo Subset Galaxies Spectra	85
3.4	Illustration of the Kuiper V Statistic	88
3.5	The Arecibo Subset Galaxies Spin Vectors	92
3.6	The MAPS-PP Galaxies Major-Axis Position Angles	94
3.7	The Kuiper Probability for Samples of Known Anisotropy	95
4.1	Diagram of Characteristic Curve of Photographic Response	104
5.1	Map of the MAPS-NGP POSS I Fields	112
5.2	MAPS-NGP Plates Seeing and Surface Brightness Limits	115
5.3	Images of SAO Stars, Their Halos, and Ghost Images	119
5.4	Galaxy Counts around SAO Stars versus Angular Separation	121
5.5	Galaxy Counts in the Region of SAO Stars	123
5.6	Radius of “False” Galaxy Counts about SAO Stars	124
5.7	The Optical Path of Light Forming Ghost Images	126
5.8	A Galactic Globular Cluster that Appeared to be a Cluster of Galaxies	129
5.9	Two UGC galaxies with Extensive False Galaxy Halos	131
5.10	Reddening Estimates for the MAPS-NGP Field	136
5.11	MAPS-NGP Plates $E(B - V)_S$ Distribution	137
5.12	MAPS-NGP Galaxy Catalog	138
5.13	MAPS-NGP Diameter and Magnitude Distributions	139
5.14	MAPS-NGP Catalog Completeness Plots	143
6.1	Lines of Sight Through an Inclined Galaxy Plane	149
6.2	MAPS-NGP Diameters vs. Magnitudes	159
6.3	MAPS-NGP Residuals vs. Ellipticity	161
6.4	MAPS-NGP Magnitude-Limited Subsample	163
6.5	MAPS-NGP Diameter-Limited Subsample	164
6.6	Catalog Diameter Ratios versus APS Ellipticity	173
6.7	Diameter-Inclination Effect versus T Type	175

7.1	Map of the MAPS-NGPZ	178
7.2	MAPS-NGPZ Positional Differences	179
7.3	MAPS-NGPZ Trends with Galaxy Morphology	182
7.4	Assumed 3D Structure of the Virgo Cluster	186
7.5	Cardelli, Clayton, & Mathis Extinction Law	188
7.6	K_O and K_E Correction Models	191
7.7	Sample of Surface Brightness Profiles	196
7.8	Plots of Diameter and Magnitude Corrections	197
7.9	Best-Fit Parameter Trends (O Plate)	200
7.10	Best-Fit Parameter Trends (E Plate)	200
7.11	MAPS-NGPZR Completeness Tests	202
7.12	MAPS-NGPZ Magnitude versus Redshift	203
7.13	MAPS-NGPZ Ellipticity versus Redshift	203
8.1	MAPS-NGP Ellipticity Distribution (O Plate)	206
8.2	MAPS-NGPZT Diameter versus Redshift	207
8.3	MAPS-NGPZT $\alpha(p)$ Functions	211
8.4	MAPS-NGPZT $\beta(p)$ Functions	212
8.5	MAPS-NGPZT $\gamma(p)$ Function	213
8.6	MAPS-NGPZT $\alpha(p)$ Functions (with no μ_{limit} corrections)	214
8.7	MAPS-NGPZT $\beta(p)$ Functions (with no μ_{limit} corrections)	215
8.8	MAPS-NGPZT $\gamma(p)$ Functions (with no μ_{limit} corrections)	216
8.9	MAPS-NGPZT Inclination Trajectories	219
8.10	MAPS-NGPZT Inclination Trajectories (with no μ_{limit} corrections)	220
8.11	ZCAT vs, RC3 Morphological Classifications	222
8.12	MAPS-NGPZT Morphological Distributions	223
8.13	MAPS-NGPZT (with RC3 Reclassifications) Inclination Trajectories	224

8.14 MAPS-NGPZT (with RC3 Reclassifications) Inclination Trajectories (but no μ_{limit} corrections)	225
8.15 MAPS-NGPZ Inclination Trajectories Versus Color	228

Chapter 1

Introduction

If the Lord Almighty had consulted me before embarking on creation,
I should have recommended something simpler.

King Alfonso X (the Wise) of Castile, 1221-1284.

1.1 The Early History of Astronomical Catalogs: Gathering the Nebulae

In this, the last decade of the 20th century, our telescopes scan the heavens nightly, some even from the heavens. These telescopes are capable of observing literally millions of galaxies like our own. And these observations are starting to be used to not only understand the galaxies themselves, but to actually determine the cosmological parameters that describe this universe. In this time when we believe we are finally answering some of the deep questions that astronomers have pondered since before the time of Socrates, it is hard to concieve of a time when our view of the universe was restricted to “just” the Galaxy ... the Galaxy which we reside in but whose true nature as a system of several billion stars we did not understand until relatively recently. With the exception of three nearby galaxies (the Large and Small Magellanic Clouds and the Andromeda Galaxy), galaxies are distant enough that they are not visible to the naked eye despite the fact that they consist of billions of stars. Even our own “Milky Way” derives its name from

the fact that the majority of stars composing it lie too far away to be resolved by the human eye and their combined light is seen as a bright band encircling the dark night sky. It was Galileo who used his most famous invention, the astronomical telescope, to resolve the Milky Way into “a mass of luminous stars gathered together” in the early 17th century. However, these early telescopes were not powerful enough to resolve other galaxies into stars, and in fact, this feat would not be accomplished until the early part of this century. When viewed through the relatively small telescopes of the 17th through 19th centuries, galaxies typically looked like fuzzy clouds of light. Their appearance led to them being considered a simple variant of the other “fluffy” nebulae seen in the sky. The first attempts at understanding their true natures would not occur until over a century after Galileo’s writings on the stellar nature of the Milky Way. In mid-18th century a religiously motivated Englishman named Thomas Wright took up astronomy to better understand the beauty of God’s creation. In one of several (contradictory) theories of the nature of the universe, he postulated that the universe consisted of a spherical shell of stars and that the Milky Way was simply our view (lying within the shell) of a nearby portion of the shell. He speculated that the patchy nebulae seen in the sky were other such star systems. This theory, titled *An Original Theory of New Hypothesis of the Universe*, was published in 1750. In that year, Immanuel Kant, read an article about Wright’s theory which ironically emphasized the most speculative part of the theory, the appearance of the Milky Way as due to our lying within a (locally) flattened distribution of stars, and ignored the spherical model of the universe. Kant took this model of the Sun lying within a flattened distribution of stars and ran with it. Five years later, Kant anonymously published *Allgemeine Naturgeschichte und Theorie des Himmels* (Universal Natural History and Theory of the Heavens) in which he outlined his model of the Milky Way as just one of many systems of stars, “islands” in the universe. This “island universe” model survived basically intact until the early 20th Century, but in another irony of history, the publisher of his book went bankrupt shortly after its publication and most copies of the book were seized to satisfy debts, and thus

Kant's "island universe" model was not well known. It was in fact another German, Johann Heinrich Lambert, whose publication of a theory in which the Milky Way lay on the edge of disk shaped stellar system, one of "innumerable" such systems, got the most attention. During this same time period, the first attempts at developing catalogs of all the known nebulae began. Toward the end of the 16th Century, a French astronomer interested in hunting comets, Charles Messier, developed a catalog of 109 bright nebulae in order to avoid misidentification of these nebulae as comets. In 1781, William Hershel recieved a copy of Messier's catalog and observed them with his telescope (the world's largest at the time). He found that the majority of these nebulae contained stars and concluded (prematurely) that all nebulae, when observed with a sufficently powerful telescope, would be resolved into stars. And thus building on the Messier catalog, Hershel, his sister Caroline, and son John, would eventually catalog over 2500 nebulae in the skies over England. His son eventually transported the Hershel's telescopes to South Africa and scoured the southern skies. In 1864 John Hershel published a "General Catalog" of 4630 objects, all but 450 had been discovered by him, his father, or his aunt. In 1850, the Third Earl of Rosse, an astronomer whose wealth allowed him to build and staff a 72 inch telescope, noted the existance of a special sub-class of nebulae, the "spiral nebulae." It is these spiral nebulae which modern day astronomers call spiral galaxies. It was one of Lord Rosse's observers, a Dane named John Louis Emil Dreyer, who, at the behest of the Royal Astronomical Society, started work on what would become the one of the largest catalogs of nebulae in the night sky. This project started as a series of addenda to Hershel's General Catalog, keeping track of the more recently discovered nebulae. But in time, the Royal Astronomical Society realized that these addenda were not enough. And in 1888, the "New General Catalogue of Nebulae and Clusters of Stars," known to astronomers since as the NGC, a catalog containing 7840 objects was published in the Memiors of the Royal Astronomical Society. The NGC and its two followup Index Catalogs are often collectively refered to as the NGC/IC. And despite the many problems

with positions of objects in the NGC/IC,¹ for the first half of this century the NGC/IC was the standard catalog of not only galaxies, but also nebulae and star clusters. The NGC/IC designations are still used today for most of the objects Dreyer cataloged.

1.2 Early Galaxy Catalogs: Removing “Local” Clutter From The NGC/IC

By the beginning of this century, the unresolved nebulae were known to fall into two categories: the nebulae which were clouds of gas and dust and mostly confined to the band of the Milky Way, and the “spiral nebulae,” found everywhere in the sky except in the Milky Way. The question of the true nature of these spiral nebulae, and whether they lay nearby or at great distances was a topic of great debate. And in fact, it was the topic of what has come to be known as the Curtis-Shapley debate. On April 26, 1920, at the National Academy of Sciences in Washington, DC, Harlow Shapley and Heber Curtis, debated the evidence supporting (Shapley) and refuting (Curtis) the idea that the spiral nebulae were systems external to our own galaxy. And while the Curtis-Shapley debate didn’t make a great splash at the time, it has been used prominently since in many astronomy lectures to introduce the topic of external galaxies. The debate resolved very little as there were mistakes made on both sides (including apparently erroneous observations of supposed angular rotation in the arms of M33 introduced by Shapley as evidence of the local nature of spiral nebulae). An excellent and very readable history of the debate was recently written by Trimble [1995], covering the background and content of the debate. It was the advent of photography and more importantly, its use in astronomy, that drove the resolution of the debate. In 1912, the first redshift was measured for a spiral nebula. These redshifts removed the nebulae from the gravitational

¹This is not a criticism of Dreyer, who performed near heroic work attempting to sort through observations submitted by amateur and professional astronomers alike. In such a large campaign, it is to be expected that some of the contributors would prove less accurate at providing positions for their catalog submissions than others.

control of the Galaxy. And in 1924, Edwin Hubble resolved the Shapely-Curtis debate by finding Cepheids in M31 (the Andromeda Nebula), which allowed determination of the distance M31. Hubble later provided more proof that the spiral nebulae were galaxies like our own by resolving stars in deep photographic images of M31 and M33. Once the distinct nature of spiral nebulae (and galaxies in general) was known, it was inevitable that astronomers would start developing catalogs containing only galaxies. The first such large catalog was produced by Harlow Shapley and Adelaide Ames in 1932. Published as “A Survey of the External Galaxies Brighter than the Thirteenth Magnitude,” this catalog has come to be known as the Shapley-Ames (or occasionally Harvard) catalog (Shapley and Ames [1932]). With 1249 objects, all but 13 of which were in the NGC/IC, this catalog was mostly an identification of all the bright external galaxies in the NGC/IC. The Shapley-Ames catalog remained the prominent galaxy catalog until well after World War II had ended.

1.2.1 POSS-based Galaxy Catalogs

These early catalogs were all based on the compilation of individual observations of objects by many observers. The National Geographic Society - Palomar Observatory Sky Survey was the first attempt to obtain a deep photographic survey of the majority of the sky. This project involved the photographing of the entire sky visible from the Palomar 48-inch Schmidt telescope in two colors.² Between 1949 and 1958, a total of 936 $6^\circ \times 6^\circ$ fields were photographed covering the sky from declination -33° to 90° . The POSS I, as it has come to be called, was the deepest such survey ever created, recording the sky to a depth of over one million times fainter than the limits of the naked eye.³ These photographic plates are one of the densest forms of information storage

²The properties of the Palomar 48-inch telescope is described in Harrington [1952]. The survey itself and its methodology are described in Minkowski and Abell [1963] and in Lund and Dixon [1973].

³There is now a second-epoch palomar Sky Survey in progress, using three colors and a finer grain emulsion. This second survey, called POSS II, has required a nomenclature change in reference to the original POSS, which is now called POSS I

for astronomical observations, recording more objects on one plate than had ever been cataloged before!⁴ It was not long after the POSS I was finished that galaxy catalogs based on visual inspection of the POSS I plates became available. These catalogs would claim to be complete to a given magnitude or diameter limit because for the first time there existed a complete and very deep survey of a large portion of the sky. The first such effort was led by Fritz Zwicky, and involved the visual inspection of 560 POSS I fields looking for all galaxies with photographic magnitude greater than 15.5. The “Catalog of Galaxies and Clusters of Galaxies” (Zwicky *et al.* [1961–68]), which has come to be known as the CGCG, contained positions and apparent magnitudes for 29363 galaxies. In 1974, Peter Nilson completed a much more detailed survey of galaxies on the POSS I, containing all galaxies with diameters greater than 1' or brighter than photographic magnitude of 14.5 with declination greater than -2.5° . The Uppsala General Catalog (Nilson [1973]), known as the UGC, contains detailed image parameters (such as major and minor axis diameters, major axis position angles, red and blue magnitudes, and morphological classifications) for 12940 galaxies. The UGC has since its creation been used extensively by the astronomical community.

1.2.2 The Reference Catalogs of Bright Galaxies

In addition to the UGC, there is a series of three galaxy catalogs produced by Gerard de Vaucouleurs and collaborators which have been highly regarded as a fundamental source of information on galaxies. These catalogs, the *Reference Catalogues of Bright Galaxies*, were compiled in the traditional fashion of collecting observations from a variety sources and were meant as a followup to the Shapley-Ames catalog. The first Reference Catalog (the RC1, de Vaucouleurs and de Vaucoouleurs [1964]), was prepared between 1949 and 1963 and contained 2593 galaxies. It attempted to place diameters,

⁴It can in fact be argued that such plates are still faster than the CCD-based imaging used today, given the large field of views at high resolution possible with photographs versus small fields of view of CCDs. The point is moot however, as photographic plates of observational quality are no longer produced in great quantity.

magnitudes, colors, and redshifts from a variety of sources onto a relatively homogeneous system. The second Reference Catalogue (the RC2, de Vaucouleurs, de Vaucouleurs, and Corwin [1976]) contained 4362 galaxies and introduced a new diameter system, three color magnitudes, and also recorded radio flux information. Both the First and Second Reference Catalogues were limited to galaxies with literature references and were incomplete fainter than magnitude of 13 (the Shapley-Ames limit). The final Third Reference Catalogue of Bright Galaxies (the RC3, de Vaucouleurs *et al.* [1991]) was designed to be complete to a diameter limit of 1' and total B magnitude limit of 15.5 with a redshift less than 15000 km s⁻¹. It also includes all objects in the previous editions of the catalog and any objects of special interest (notably some compact galaxies). It contains detailed information on a total of 23022 galaxies, including cross-identifications with the other galaxy catalogs, morphological classifications, magnitudes in a variety of bandpasses, colors, radio fluxes and linewidths. The RC3 has been used quite extensively as a source of information for a large sample of galaxies.

1.2.3 Online Galaxy Databases

With the advent of the World Wide Web in recent years, a new form of galaxy catalog has appeared, the online database. These online galaxy databases attempt to collect information about any galaxy in the published literature. The most commonly used online database today is most likely the NASA/IPAC Extragalactic Database (NED) located at <http://nedwww.ipac.caltech.edu/>. NED tracks such non-traditional items as galaxy images from the POSS I, bibliographic references to a galaxy (including abstracts), and photometry at all wavelengths. NED can store information that is otherwise difficult to organize and even more importantly, it can be kept more up-to-date than any printed medium. And currently (July 1999) contains information on over 120000 galaxies. In addition to NED, there is the Lyon/Meudon Extragalactic Database (LEDA), located at <http://www-obs.univ-lyon1.fr/leda/>. LEDA was originally created in 1983 as a catalog of cross-identifications with a large catalog of HI observations. They collect information

from the literature, including cross-identifications, bibliographic references and basic characteristics of the measurements. These online catalogs provide an opportunity to expand galaxy catalogs beyond the size manageable in a printed medium. They can also include supplemental material on individual objects organized in a non-linear matter. The major issue with these online databases is that they are not complete, but rather their growth is dictated by what is published. And although they do make excellent resources for the astronomical community to look up previously published information, their heterogeneous nature makes them ill suited for use as extragalactic catalogs.

1.3 Building Better Galaxy Catalogs

One of the major problems with previous surveys has been their non-homogenous selection criteria. The online databases and the reference catalogs are not homogenous in their sky coverage. They include many “objects of special interest” and may include measurements performed in a variety of ways. These catalogs are usually not used as the primary sources of research data, but are more often than not used as reference materials by the astronomical community. A problem with galaxy catalogs that attempt to be complete is reliance on image parameters which have been manually measured. This means that the construction of the catalog is subject to any personal biases of the person or persons making the measurements. It also means that it is difficult to precisely reproduce the previous measurements because they have not been documented. It is only in the last decade that the computational power has become available that allows replacement of manual measuring and analysis techniques with their mechanical and computational equivalents. The Minnesota Automated Plate Scanner (hereafter APS) project is cataloging digitized scans of the POSS I, using machine-based calculation of all image parameters.

1.3.1 The Automated Plate Scanner Catalog

The Automated Plate Scanner is a high-speed, high-precision automated measuring machine located at the University of Minnesota. It was originally built at the Control Data Corporation in cooperation with Professor Willem Luyten. In 1979, Roberta Humphreys relocated the APS and started a project to add more modern computing and data control to the APS. The APS uses a flying spot laser and detection electronics to digitize a pair of POSS I plates in six hours or less. The raw digitized data from a threshold densitometry scan of a pair of POSS I plates typically occupies 500 to 1500 MB of disk space.⁵ This raw data is then processed through a data reduction pipeline in which astrometric and photometric calibrations are performed as well as automated star/galaxy discrimination. The reduced data is then stored in a custom, high speed database (called *StarBase*) and made available to the astronomical community via the World Wide Web.⁶ The APS Catalog of the POSS I includes all POSS I fields with Galactic latitude, $|b| > 20^\circ$ of the Galactic plate. A much more thorough description of the machine and subsequent reduction is provided in Pennington *et al.* [1993] and Odewahn *et al.* [1992]. The first fields of the APS catalog were originally placed online in 1993. It contains all objects detected on both the O and E plates. In 1997, the software used for reducing the raw digitized data and placing it online was extensively refined and optimized. Since 1997, all APS scan data has has been reduced using the new data reduction software.

1.4 Goals of this Thesis

The goal of this thesis has been to use two galaxy catalogs constructed using the APS to improve on previous extragalactic studies. Using the APS Catalog, it is now possible to have a very complete survey containing machine measured image parameters for millions

⁵Supporting the idea that photographic plates record much more information than current CCDs.

⁶The APS web site is located at URL <http://aps.umn.edu/>.

of objects in the sky. The image parameters are measured in a very homogenous manner and a catalog constructed using the APS data is not subject to the physiological biases which may have affected previous galaxy catalogs. Therefore, the APS provides an excellent resource for quickly building very complete galaxy catalogs and reinvestigating the more debatable results obtained using previous galaxy catalogs. For this thesis, two galaxy catalogs have been produced. The two catalogs were used to investigate two separate fields in extragalactic astronomy, the investigation of possible modern day relics of large-scale structure formation and the investigation of the effects of internal extinction in galaxies on their appearance.

1.4.1 Galaxy Alignments: Probing Large-Scale Structure Formation

REBECCA: I never told you about that letter Jane Crofut got from her minister when she was sick. He wrote Jane a letter and on the envelope the address was like this: It said: Jane Crofut; The Crofut Farm; Grover's Corners; Sutton County; New Hampshire; United States of America.

GEORGE: What's funny about that?

REBECCA: But listen, it's not finished: the United States of America; Continent of North America; Western Hemisphere; the Earth; the Solar System; the Universe; the Mind of God – that's what it said on the envelope.

GEORGE: What do you know!

REBECCA: And the postman brought it just the same.

From *Our Town* by Thornton Wilder

The first catalog produced for this thesis is the Minnesota Automated Plate Scanner catalog of the Pisces-Perseus Supercluster (a.k.a. the MAPS-PP). This catalog is a diameter-limited catalog of the region in the sky covering the Pisces-Perseus Supercluster and was built from the original APS catalog (pre-1997). The MAPS-PP was used to investigate the possibility of galaxy alignments due to both large-scale structure formation and more recent interactions. The construction of the MAPS-PP and theoretical motivation for a galaxy alignments study are detailed in Chapter 2. That chapter of the thesis also covers the determination of the Pisces-Perseus galaxy luminosity function

and the techniques used to probe for large and small scale galaxy alignments. Chapter 3 discusses how the MAPS-PP in conjunction with radio observations made at the recently refurbished Arecibo telescope in Puerto Rico are used to construct a catalog of galaxy spin vectors for the Pisces-Perseus Supercluster. This catalog, constructed using edge-on galaxies in the MAPS-PP, contained very accurately determined spin vectors. This spin vector catalog allowed one of the first studies of alignments in actual spin vectors in galaxies rather than using their projection on the sky.

1.4.2 Probing Internal Galactic Structure

As will be emphasized in both Chapters 2 and 3, one of the major problems in extragalactic astronomy is understanding the effects of internal extinction in galaxies. Internal extinction can dramatically affect the appearance of similar galaxies viewed at differing inclinations. It was in part our uncertainty in the effects of internal extinction on galaxy appearance that limited the studies in Chapter 3 (see discussion in Section 3.5). Partly motivated by this problem, I constructed the Minnesota Automated Plate Scanner North Galactic Pole survey (or MAPS-NGP). With over 210000 galaxies, this galaxy catalog is the largest diameter-limited galaxy catalog currently available. The MAPS-NGP was constructed using the revised APS object database and as this is the first thesis based (in part) on the new APS data reduction pipeline, an outline of this new pipeline and its refinements is presented in Chapter 4. In Chapter 5 I discuss the techniques used to build the MAPS-NGP, including the extensive effort made to remove all false galaxy detections from the catalog; and the previous efforts at tackling the problem of inclination effects in galaxies are summarized in Chapter 6. This discussion includes an outline of the problematic nature of studies based on the UGC or RC3, which suffer from a physiological bias called the Huizinga Diameter-Inclination effect, which can dramatically affect visual diameters. Using the APS, I prove the existence of this bias in the UGC and RC3 and provide supporting evidence for Huizinga's interpretation of its source. Chapter 7 discusses the cross-identification of the MAPS-NGP with the

CfA redshift catalog, an inhomogeneous catalog of galaxy redshifts. The redshifts are then corrected for the Virgo infall. The information from the redshift catalog is used to correct magnitude, diameter, and other image parameters for the effects of cosmology and plate-to-plate variations. Using the work of Schlegel, Finkbeiner, and Davis [1998], corrections for Galactic extinction are also applied. The merged catalog, called the MAPS-NGPZ, contains redshifts and APS image parameters for over 8000 galaxies and a subset called the MAPS-NGPZT contains morphological classifications for over 2000 galaxies. Finally, in Chapter 8, I investigate the effects of internal extinction on a galaxy’s appearance. This work uses MAPS-NGPZ in combination with a statistical technique I call “Choloniewski’s estimators” (outlined in Section 6.4.3) to quantify the effect of inclination on a galaxy’s diameter, magnitude, and surface brightness.

Chapter 2

Galaxy Alignments in the Pisces-Perseus Supercluster

Originally published in Cabanela, J. E. and Aldering, G. L. 1998, AJ, **116**, 1094.

Abstract: A search for preferential galaxy alignments in the Pisces-Perseus Supercluster (PPS) is made using the Minnesota Automated Plate Scanner Pisces-Perseus Survey (MAPS-PP). The MAPS-PP is a catalog of ~ 1400 galaxies with a (roughly) isophotal diameter $> 30''$ constructed from digitized scans of the blue and red plates of the Palomar Observatory Sky Survey (POSS I) covering the PPS. This is the largest sample of galaxies applied to a search of galaxy alignments in this supercluster and has been used in combination with previously published redshifts to construct the deepest PPS galaxy luminosity function to date. While previous studies have relied extensively on catalogs with visually estimated parameters for both sample selection and determination of galaxy orientation, the MAPS-PP uses selection criteria and measurements that are entirely machine and computer based. Therefore it is not susceptible to some of the biases, such as the diameter-inclination effect, known to exist in some other galaxy catalogs. The presence of anisotropic galaxy distributions is determined by use of the Kuiper statistic, a robust alternative to the χ^2 statistic more traditionally used in these studies. Three statistically significant anisotropic distributions are observed. The reddest galaxies are observed to be oriented preferentially perpendicular to the local large-scale structure. The bluest galaxies near the supercluster plane are observed to have an anisotropic position angle distribution. And finally, a weak trend for the median position angle of color-selected galaxy subsamples to 'twist' with increasing distance from the Pisces-Perseus Supercluster plane is observed. These position angle distribution anisotropies are weak and are

not consistent with any single primordial or modern-era galaxy alignment mechanism, although a mixture of such mechanisms is not ruled out.

2.1 Introduction

Any successful structure formation theory must explain the observed structure of the Universe over a wide range of scales. Most current cosmogonic theories propose that primordial mass density fluctuations lead to structure through gravitational instability. The size scale of these early density fluctuations is a critical unresolved question. In hot dark matter (HDM) theories, density fluctuations on supercluster scales are dominant, leading to cluster or supercluster-sized structures which only later fragment into galaxies; a so-called “top-down” scenario [Zel’dovich 1970, Doroshkevich & Shandarin 1978, White 1984]. Conversely, cold dark matter (CDM) scenarios have their largest density fluctuations on galactic scales, causing galaxies to form first, a “bottom-up” scenario [Peebles 1969]. The top-down and bottom-up scenarios represent the extremes for possible primordial density fluctuations. Given the presence of significant structure on galactic to supercluster size scales, cosmogonic models may require elements of both scenarios in order to acceptably model reality. Relic signatures from the epoch of formation of the large-scale structures in place today comprise some of the strongest pieces of evidence for testing cosmogonic theories. The cosmic microwave background and galaxy-galaxy power spectra serve as the principal criteria for gauging the success of formation theories. However, other signatures may exist. Any relic galactic property acquired during its formation and not due to subsequent evolution would be especially valuable as a diagnostic of cosmogonic theories. For example, if such a galactic property were observed to be dependent on the large-scale environment, it would be *prima facie* evidence in favor of a “top-down” scenario of large-scale structure development. A possible relic galaxy property is its spatial orientation, as defined by its dynamical axes: the angular momentum axes in spiral galaxies and the principal axes of the velocity dispersion tensor in ellipticals. Dynamical axis orientations are particularly relevant from an

observational standpoint since in many cases they can be constrained through relatively simple measurements of position angles and ellipticities.

2.1.1 Expectations from Theory and Models

Predictions for preferential dynamical axis orientations originate in theories addressing the origin of angular momentum in galaxies. The degree to which galaxies are aligned should be correlated with the relative amount of angular momentum transferred to galaxies from larger scales. In top-down scenarios, the angular momentum in galaxies comes from either the collision of protogalactic gas clouds infalling perpendicular to the supercluster plane, or from the vorticity field in the protogalactic gas produced by shock waves parallel to the cluster plane [Doroshkevich & Shandarin 1978]. In either case, the galaxy dynamical axes would lie preferentially perpendicular to the supercluster plane. For bottom-up scenarios, the angular momentum in galaxies arises from galaxy-galaxy interactions and should not lead to any preferred alignment of the axes of rotation unless there is a preferred direction for galaxy-galaxy interactions [Barnes & Efstathiou 1987, West 1994]. The difficulty in observing primordial galaxy alignments is that subsequent galaxy-galaxy interactions will result in an exchange of angular momentum, altering the orientations of the interacting galaxies. Peebles [1969] estimated that the torque experienced by an elliptical galaxy (modeled as a “homogeneous ellipsoid of revolution”) due to an interaction with a harassing galaxy is:

$$\tau = \frac{dL}{dt} = \frac{3}{4} \frac{GMQ}{r^3} \sin 2\theta, \quad (2.1)$$

where θ is the angle between the galaxy rotation axis and the harassing galaxy (of mass M) exerting the torque, and Q is the quadrupole moment of the galaxy. Equation (2.1) can be used to derive an estimate of the time for a galaxy (presumably initially aligned) to be rotated by its nearest neighbor through 45° :

$$t_{torque} \approx \sqrt{\frac{\pi}{16G\rho} \cdot \frac{1}{\epsilon} \cdot \frac{2-\epsilon}{1-\epsilon}}, \quad (2.2)$$

where ρ is the mass density of the environment and ϵ is the ellipticity of the galaxy being rotated. Thus, assuming the galaxy maintains a constant shape and has a lasting encounter with a single neighbor galaxy, the time for initial alignments to be lost is proportional to the inverse square root of the environmental density. For an elliptical with $\epsilon \sim 0.3$ in an environment with $\rho \sim 10^9 M_\odot \text{Mpc}^{-3}$ (approximately one galaxy comparable to the Milky Way per 100 Mpc^3), $t_{\text{torque}} \approx 28$ Gyrs. Typical rich cluster densities are roughly 100 times higher, decreasing t_{torque} to roughly 3 Gyrs, so that any initial alignments will be undone in much less than a Hubble time. A more detailed angular momentum exchange model developed by Coutts [1996] employs a variant of Equation (2.1) in which galaxies are assumed to be flat (instead of ellipsoidal) and the universe is taken to be in free expansion ($\Omega = 0$). Based on those assumptions, Coutts derived the cumulative affect of multiple encounters over the history of a galaxy. In so doing, Coutts found that a galaxy near the edge of a cluster can expect several hundred galaxy-galaxy interactions in its lifetime, each encounter capable of torquing the galaxy through an angle of 0.1° to 1.0° . Taken cumulatively, the population of galaxies would be dispersed through several tens of degrees from their initial orientations, depending on the number of galaxy-galaxy interactions and thus the density of the environment. Coutts' model supports the assertion that one expects primordial dynamical axes alignments to survive only in lower-density regions, such as the outskirts of superclusters, where galaxy-galaxy interactions have been less common and less disruptive. Verner & Chernin [1987] modeled the exchange of angular momentum in galaxy-galaxy interactions for not only ellipticals, but for spiral galaxies as well. Their results for spirals match the expectation that applying a torque to a spiral results in precession of the rotation axis and not a complete re-orientation of the galaxy. This precession occurs as long as the angular momentum introduced to the spiral is not enough to disrupt the spiral entirely. It should be noted that galaxy-galaxy interactions are not the only way in which galaxy orientations could be changed over time. Quinn and Binney [1992] investigated the possibility that secondary infall could affect the angular momentum distribution in

galaxies. They found that angular momentum from accreted material leads galaxy spin axes to typically lie anti-parallel to their orientation at $z \simeq 0.3$. Therefore, if secondary infall is important current galaxy orientations may reveal little about their original distribution. Galaxy alignments, even if they were to survive, would not be an entirely unambiguous discriminant of cosmogonic models as there are several alternative models which generate galaxy alignments irrespective of the surrounding large-scale structure. Nearest-neighbor alignments are predicted to exist by Sofue [1992] from the exchange of angular momentum between interacting galaxies. However, other N-body simulations of the origin of angular momentum from tidal torques in a CDM universe [Barnes & Efstathiou 1987] predict that nearest-neighbor alignments would not exist. Ciotti and Dutta [1994] suggest that the tidal field in a cluster can result in radial alignments of ellipticals relative to the cluster center. More recently, Ciotti and Giampieri [1998] analytically show that ellipticals can achieve stable orientation both perpendicular and parallel to the gradient of the cluster tidal field. Some such alignments have been observationally confirmed, such as the Binggeli effect, in which cD galaxies are shown to preferentially align themselves with the cluster major axis [Binggeli 1982] and with the local large-scale structure [Lambas, Groth, & Peebles 1988b]. West [1994] proposed a model in which the Binggeli effect is explained as the result of an anisotropic merger history. In this model, the mergers of the protogalactic objects which eventually make up a cD galaxy preferentially occur along the direction of the local large-scale structure, leading to the alignment of cDs with their parent clusters. This model assumes the existence of cluster-scale density fluctuations preceding the formation of cDs, and thus favors a “top-down” cosmogony or a late formation time for cDs. It is clear that whatever the galaxy alignment mechanism, local density will be an important parameter distinguishing between primordial and modern galaxy alignments. Primordial alignments should remain only in low density regions since the galaxy-galaxy interactions in high density regions would have heavily dispersed any primordial signature. Conversely, any modern alignments

should be more pronounced in regions of high density since they require multiple galaxy-galaxy interactions or a strong tidal field. Investigation of galaxy alignments should examine a large enough range of densities so that the mechanism of such an alignment can be better determined.

2.1.2 Previous Observational Efforts

Several studies have not only made predictions for the expected forms of alignments but have also searched for these alignments in observations (an excellent review of the earlier efforts in this field is given by Djorgovski [1987]). But as is often the case in astronomy, direct observation of the the physical parameters of interest, the dynamical axes of a galaxy for example, is not possible. Most studies have instead examined the projection of those axes onto the sky. The search for dynamical axes alignments therefore becomes a search for alignments of the photometric axes of the galaxy images. While most searches for galaxy alignments have concentrated on the Local Supercluster, some have examined the possibility of galaxy alignments in the Pisces-Perseus Supercluster (hereafter PPS, see Figure 1 in Giovanelli & Haynes [1993]). The PPS has several rich clusters within it, meaning that a wide range of density environments can be probed by examining its members. Strom and Strom [1978] investigated a sample of 72 ellipticals in the Perseus cluster and found a preference for the major axes of ellipticals to align with the PPS ridge, at a peak position angle between 60° and 90° . A similar result was obtained by Lambas, Groth, & Peebles [1988a] when comparing the position angles of ellipticals in the Uppsala General Catalog of Galaxies [Nilson, hereafter UGC] to the nearby large-scale structure as indicated by the Lick map [Shane & Wirtanen 1967]. Lambas, Groth, & Peebles [1988a] found alignments between elliptical galaxies and large-scale structure on scales of 0.25° to 0.5° . Looking at a more diffuse sample of 73 galaxies in the “Perseus supercluster” with ellipticity greater than 0.3, Gregory, Thompson, & Tift [1981, hereafter GTT], found a bimodal position angle distribution. This indicated preferred orientations both parallel and perpendicular to the PPS ridge.

Their χ^2 analysis indicated less than a 3% chance that such a distribution is drawn from a random sample. Flin [1988] re-analyzed the work of GTT, using their complete sample of 118 PPS galaxies. Using the position angle and ellipticity information from GTT to compute the the spatial distribution of galaxy angular momentum axes relative to the PPS plane, Flin found a weak anisotropy, with the major axes having a tendency to be perpendicular to the PPS plane. Dekel [1985] searched for alignments between galaxy position angles and their parent clusters using the UGC and ESO-Uppsala [Lauberts 1982] catalogs. Several of Dekel’s subsamples were designed to explicitly investigate alignments in the PPS reported by GTT. Dekel’s method involved examination of the mean position angle difference for a given galaxy and all the galaxies within a ring of radii S and $S + \Delta S$, where ΔS was typically 5° . The expected distribution of position angle differences for a random sample is uniform from 0° to 90° , with a mean of 45° . Dekel notes that if there were a mix of alignments and anti-alignments, the mean might not change, but the dispersion should be larger than that of a sample with no alignments. Dekel found no evidence of significant alignments or anti-alignments in any of his subsamples, including the PPS subsamples. Laubscher [1994, hereafter L94] performed a CCD survey of 208 PPS galaxies selected from the CGCG [Zwicky *et al.* 1961–68] and the CfA Redshift Catalogue (hereafter referred to as ZCAT, Huchra *et al.* [1992]) to a magnitude limit of 15.1. Using a χ^2 test on a variety of subsamples, Laubscher found no evidence for global position angle alignments with greater than 95% significance. Other than Flin [1988], all previous searches for galaxy dynamical axes alignments in the PPS have simply looked at the position angle distribution. Recent searches for alignments in the Local Supercluster have shifted focus from looking for position angle alignments to using both position angle and ellipticity information to determine the 3-D distribution of dynamical axes orientations. Jaaniste and Saar [1978] were among the first to search for alignments in Local Supercluster galaxies and found a weak preference for spin axes to lie parallel to the supercluster plane. This work was strongly criticized by Flin and Godłowski [1986], although their re-analysis of the data, using position angle

and ellipticity information from the UGC combined with redshift information (to isolate galaxies within the Local Supercluster), found essentially the same result. Kashikawa & Okamura [1992, hereafter KO92] examined galaxy alignments in the Local Supercluster using the Photometric Atlas of Northern Bright Galaxies [Kodaira, Okamura, & Ichikawa, hereafter PANBG], which consists of a subset of the Revised Shapley-Ames Catalog [Sandage & Tammann 1981]. The PANBG employs an isophotal ellipse-fitting routine on digital galaxy images from modern plate material to eliminate visual biases. KO92 specifically cite the difficulty of accurately (and consistently) visually determining the ellipticity and position angle of face-on objects as a reason to be wary of the UGC for orientation studies. Using a χ^2 analysis, KO92 found that galaxies near the Local Supercluster plane tend to have their angular momentum axes lying parallel to that plane while those high above the local supercluster plane tended to have spins perpendicular to that plane at 97% confidence level. KO92 also reported a tendency for spiral galaxies near the Virgo cluster to point toward the cluster center at the 99% confidence level. Similar results were independently obtained using a redshift-limited sample of the UGC and ESO galaxies in the Local Supercluster by Godłowski [1994]. Godłowski [1994] claims that observed alignments relative to the supercluster plane are more pronounced in non-spirals than spirals. Due to the mixed results in previous studies, the issue of the reality of alignments for non-cD galaxies remains unresolved. Earlier work has typically used datasets with image parameters determined either by visual inspection or by simplistic models of the light distribution in a galaxy. They have relied on pre-existing catalogs with membership criteria based on parameters determined by visual inspection. Since such visually determined parameters can be subject to bias (c.f. Holmberg 1975), the use of such catalogs for detecting galaxy alignment signals can be perilous. Also, Coutts [1996] notes that most previous studies have looked for alignments on size scales which may be larger than typical alignment scales. Coutts suggests that this may be one reason that some previous studies have not found alignments. It is also notable that all previous studies have used variations of a χ^2 analysis to identify potentially interesting

alignments, when it is known that the χ^2 test is not necessarily reliable for the small sample sizes and low counts per bin often encountered [Nousek & Shue 1989]. To glean anything new from a re-investigation of this subject, a more modern approach, using the computational methods available today, is called for. The selection of the dataset members should involve non-visual, mechanical criteria where any potential selection biases can be better quantified. The galaxy image parameters should be determined by non-visual means, to avoid the possible biases noted by KO92. Moreover, use of a powerful and robust statistical test that is able to quantify the probability of a given distribution being anisotropic, even for small subsamples of the data, is needed. Finally, in order to understand the source of any observed alignments, a deeper survey of one or more well-chosen regions, ideally spanning a range of densities over a variety of size scales, seems preferable to an all sky survey of only the brightest galaxies. For this study, we chose to search for several previously reported forms of galaxy alignments in the PPS, as well as investigate several theoretical forms of alignments not yet observed. The PPS field was chosen because it offers a chance to examine a wide range of density environments in a reasonably small part of the sky. It also offers the advantage that many of the brighter galaxies in the PPS field have redshifts available (thanks mostly to the extensive surveys by Giovanelli and Haynes). These surveys reveal a fortuitous placement of voids in front and behind the structure, meaning a large fraction of bright galaxies in this field will be true PPS members. Using the Minnesota Automated Plate Scanner, a catalog of galaxies in the PPS field was constructed to meet very specific, machine reproducible criteria, completely independent of previous galaxy catalogs. This catalog, referred to hereafter as the Minnesota Automated Plate Scanner Pisces-Perseus Survey (MAPS-PP), includes over a thousand galaxy images obtained much faster than possible for a comparable CCD-based observing program. Special care was taken to model the position angle and ellipticity of the galaxy image, rather than modeling the entire light distribution as a simple ellipse. In this paper we discuss the construction and use of the MAPS-PP for investigation of possible galaxy alignments. Section 2.2

outlines the construction of the MAPS-PP and the reproducibility of the image parameters. In Section 2.3 the photometric calibration of the catalog is reviewed. The level of foreground/background contamination of non-PPS objects in this sample is estimated using a PPS luminosity function constructed with the MAPS-PP (Sec. 2.3.3). The large-scale structure as seen in this dataset is discussed in Sec. 2.4 and the application of a new statistic in this field of research, the Kuiper V statistic, is also introduced. In Section 2.5, we present the results of this search for galaxy alignments on several size scales and relative to structures on various scales in the PPS. The results are compared to previous work. We conclude in Section 6 and outline possible directions for future work in this field in Section 7.

2.2 Observational Data

Using the Minnesota Automated Plate Scanner (hereafter referred to as APS; Pennington *et al.* 1993) we digitized the 103a-O and 103-E (red) plates for ten Palomar Observatory Sky Survey (POSS I) fields along the PPS ridge. A list of these fields is given in Table 2.1. The standard APS post-processing software was used to obtain image rasters and initial image parameters for all O and E plate objects with an O major axis diameter $> 30''$ and for all E plate images with E major axis diameter $> 30''$ not meeting the O diameter criteria. Diameter in this case is an equivalent diameter derived from the enclosed area and ellipticity of the detection isodensity, $D > (D_{sky} + 0.19)$, where D_{sky} is the median sky background obtained on the flyback scan. This diameter, although based on a fixed isodensity, does not necessarily correspond to a fixed isophotal diameter across the sample due to plate-to-plate variations in D_{sky} and in the shape and zeropoint of the density-to-intensity transformation. The image of each object was classified as either a galaxy or a star by visual examination of the digital images. Although the standard APS reduction procedure uses an artificial neural network image classifier [Odewahn *et al.* 1992, Odewahn *et al.* 1993] for star-galaxy discrimination, we chose to perform this visual classification in order to avoid the possible introduction

Table 2.1: The Ten POSS I Fields Examined in this Study.

MLN	E/O	α	δ		Sample size				
					Total	Redshift available	$\chi^2_\nu < 2$	Quality = 1	Color Available
243	406	01:01:16	36:30:41	E	67	23	65	53	62
				O	64	23	63	46	64
244	1189	01:29:27	36:29:22	E	87	49	83	62	82
				O	80	48	76	58	80
245	1225	01:57:36	36:27:54	E	169	98	164	135	157
				O	158	94	135	103	157
289	778	22:28:15	36:29:07	E	204	60	197	150	189
				O	190	56	185	139	190
293	1257	00:04:53	30:31:45	E	159	72	150	114	128
				O	130	67	126	90	128
294	1244	00:31:01	30:31:31	E	122	70	42	63	115
				O	113	66	101	73	113
295	601	00:57:11	30:30:46	E	172	101	45	98	154
				O	158	99	139	96	157
346	1184	23:02:32	30:30:40	E	114	61	111	81	112
				O	111	61	99	65	107
347	914	23:28:41	30:31:25	E	113	47	105	81	91
				O	97	47	85	61	96
403	843	23:28:44	24:31:24	E	181	93	168	120	128
				O	129	83	118	85	129
Total				E	1388	674	1130	957	1218
				O	1230	644	1127	816	1221

of ellipticity or position angle biases in the image selection criteria (subsequent investigation showed no such bias in the classifier). Once the galaxy images were identified, they were visually inspected for foreground stars, which were interactively edited from the images using IMEDIT in IRAF.¹ The galaxies identified form the basis of the APS Pisces-Perseus Survey (MAPS-PP) of galaxies, whose members are listed in Table 2.2, along with image parameters as determined using the methods described in the following sections. Figure 2.1 is an Aitoff projection onto the celestial sphere of the positions of the MAPS-PP galaxies.

¹IRAF is distributed by the National Optical Astronomy Observatories, which is operated by the Association of Universities for Research in Astronomy, Inc. under cooperative agreement with the National Science Foundation.

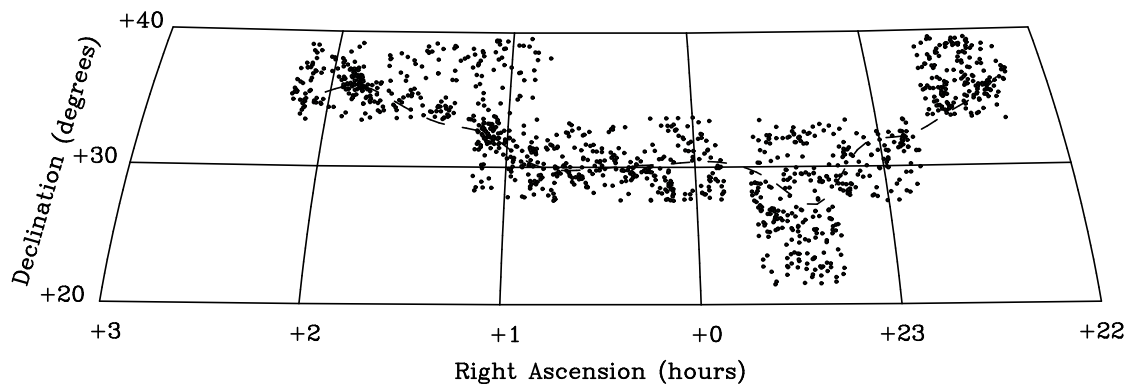


Figure 2.1: A map of the distribution on the sky of O bandpass galaxies in the MAPS-PP. The dashed line is the PPS ridgeline a determined using the method outlined in section 4.1.

Table 2.2: The MAPS-PP catalog of galaxies: APS parameters (Only first 40 entries).

Name ¹	α	δ	ϵ_d^2	θ_d^2	a_O/a_E	m_O/m_E	χ_V^2 (O/E)
O_1257_129824	00:00:16.0	31:12:24.3	0.165	032.9	38.6/37.93	14.70/13.32	0.81/1.11
O_1257_152417	00:00:34.8	30:45:28.8	0.513	131.0	38.0/42.06	15.05/13.53	0.39/0.45
O_1257_163192	00:00:47.6	30:30:16.3	0.525	161.8	36.4/36.02	15.52/13.98	0.41/0.87
O_1257_89934	00:00:54.6	31:52:53.8	0.833	096.4	30.3/29.85	17.24/15.44	0.67/0.73
O_1257_290836	00:01:10.1	28:16:36.9	0.679	138.9	35.6/23.21	16.50/15.43	1.03/0.88
O_1257_35299	00:01:41.3	33:01:39.0	0.747	111.3	38.0/37.15	16.09/14.59	0.63/0.92
O_1257_99930	00:01:41.6	31:46:17.9	0.215	178.2	35.0/35.51	15.63/14.09	1.08/1.27
O_1257_130510	00:01:50.2	31:11:36.3	0.619	072.5	79.7/77.27	14.14/12.86	1.66/1.34
O_1257_323393	00:01:52.3	27:41:19.2	0.508	076.5	36.4/36.72	15.48/13.85	0.58/1.21
O_1257_302541	00:01:59.5	28:01:23.4	0.200	172.2	41.3/48.07	14.97/13.19	0.31/0.43
O_1257_120182	00:02:51.3	31:14:58.0	0.712	179.6	31.3/32.97	16.80/14.57	0.30/0.89
O_1257_80039	00:03:12.5	32:05:34.9	0.801	042.7	43.0/41.40	16.48/14.58	0.33/0.70
O_1257_80361	00:03:27.8	32:11:52.6	0.030	041.6	33.1/9.77	16.51/15.67	0.28/1.02
O_1257_303276	00:03:34.6	28:02:14.3	0.764	016.7	40.6/44.70	16.11/14.51	0.60/1.18
O_1257_324503	00:03:50.9	27:37:58.5	0.723	047.7	34.9/33.22	16.44/15.03	0.62/0.74
O_1257_5619	00:04:40.5	33:38:20.8	0.812	177.7	42.7/44.80	16.57/14.64	0.44/0.64
O_1257_69999	00:04:44.6	32:19:50.9	0.801	039.1	104.9/93.71	13.80/12.45	1.23/1.14
O_1257_110770	00:05:06.4	31:36:32.8	0.747	015.5	31.0/35.09	16.87/14.75	0.34/0.81
O_1257_47047	00:05:26.6	32:47:32.3	0.440	132.4	39.9/41.45	14.77/13.25	0.41/0.54
O_1257_47157	00:05:45.6	32:42:56.7	0.713	163.5	32.1/32.42	16.89/14.93	0.58/0.86
O_1257_47180	00:05:49.0	32:45:02.2	0.786	013.4	43.0/30.33	17.08/15.98	0.40/0.49
O_1257_27320	00:06:12.7	33:09:20.3	0.846	052.6	124.5/124.92	13.97/12.37	0.91/1.35
O_1257_176787	00:06:45.6	30:23:17.2	0.851	053.4	38.2/31.76	16.92/15.85	0.41/0.53
O_1257_37278	00:06:57.6	33:01:50.7	0.171	136.2	60.9/73.97	13.61/11.89	0.46/0.78
O_1257_305411	00:07:11.3	28:03:45.1	0.104	156.8	50.4/56.53	14.08/12.42	0.41/0.55
O_1257_326371	00:07:13.0	27:33:14.7	0.482	146.2	65.0/53.76	14.37/13.00	0.98/0.84
O_1257_282600	00:07:13.7	28:24:42.5	0.340	116.7	32.7/29.12	15.83/14.78	0.83/0.62
O_1257_305466	00:07:18.0	28:00:36.8	0.727	049.5	30.3/36.75	16.39/14.52	0.29/1.40
O_1257_294022	00:07:18.9	28:16:17.8	0.866	045.1	40.6/41.03	16.66/14.84	0.37/1.83
O_1257_315737	00:07:26.7	27:55:55.3	0.285	027.1	46.5/40.67	14.49/13.30	1.81/2.24
O_1257_315746	00:07:28.3	27:52:16.7	0.706	114.6	54.7/43.62	15.48/14.05	0.53/0.81
O_1257_165778	00:07:41.5	30:34:17.2	0.280	052.4	68.7/57.66	14.56/13.35	0.61/0.90
O_1257_259669	00:07:43.6	28:51:35.9	0.797	021.6	30.2/21.07	17.46/16.66	0.29/0.47
O_1257_271214	00:07:51.2	28:42:38.9	0.914	006.3	82.1/69.57	15.81/14.07	0.51/3.79
O_1257_271300	00:07:57.3	28:43:06.9	0.642	115.4	67.6/56.83	14.30/13.16	0.66/0.93
O_1257_247984	00:07:57.4	29:00:15.6	0.760	066.4	36.3/35.77	16.00/14.46	0.61/0.86
O_1257_283077	00:08:00.4	28:24:13.0	0.476	067.7	48.4/49.74	15.03/13.43	0.36/0.72
O_1257_48106	00:08:05.4	32:42:17.6	0.617	045.6	68.3/65.87	14.08/12.73	2.50/1.30
O_1257_326897	00:08:10.1	27:35:25.1	0.486	010.8	30.6/33.85	16.05/14.20	0.26/0.44
O_1257_37773	00:08:11.5	33:04:19.4	0.614	148.2	70.3/69.80	13.29/12.97	2.77/1.92

¹Some rasters of multiple merged galaxies were split when the individual galaxies were large enough to make the diameter cut. These split rasters are indicated by an A, B, or C suffix. Also note that the table published in Cabanela & Aldering [1998] includes measurement uncertainties and $O - E$ colors for each galaxy.

²Ellipticity and position angle listed come from the bandpass indicated by the galaxy name.

Table 2.3: The MAPS-PP catalog of galaxies: Cross-identifications and additional galaxy parameters (Only first 40 entries).

Name ¹	Catalog Name	cz	T	Source ²	A_V	θ_N	R_{ridge}	Σ^3	flag ⁴ (O/E)
O_1257_129824	MCG +05-01-027	4949	—	200	0.17	+0.4	0.87	3.76	1/1
O_1257_152417	CGCG 498-068	4797	—	200	0.19	+0.4	0.44	2.44	1/3
O_1257_163192	—	—	—	—	0.20	+0.3	0.22	2.08	1/1
O_1257_89934	—	—	—	—	0.18	+0.3	1.52	4.07	1/1
O_1257_290836	—	—	—	—	0.13	+0.3	2.10	4.14	3/3
O_1257_35299	—	—	—	—	0.14	+0.2	2.65	3.59	1/1
O_1257_99930	—	—	—	—	0.18	+0.2	1.40	3.56	4/3
O_1257_130510	NGC 7819	4953	3	0	0.17	+0.2	0.82	3.10	4/4
O_1257_323393	00019+2742	—	—	-1	0.15	+0.2	2.69	2.47	3/3
O_1257_302541	UGC 29	—	-5	200	0.15	+0.2	2.35	3.09	1/1
O_1257_120182	—	—	—	—	0.17	+0.1	0.92	2.75	1/1
O_1257_80039	—	—	—	—	0.18	+0.0	1.75	3.91	1/1
O_1257_80361	—	—	—	—	0.17	+0.0	1.87	3.82	3/1
O_1257_303276	—	—	—	—	0.15	+0.0	2.29	4.45	1/3
O_1257_324503	—	—	—	—	0.16	+0.0	2.69	3.82	1/1
O_1257_5619	—	—	—	—	0.15	-0.1	3.32	2.53	1/1
O_1257_69999	UGC 60	5072	3	200	0.14	-0.1	2.01	4.51	2/2
O_1257_110770	—	—	—	—	0.16	-0.2	1.29	2.64	1/1
O_1257_47047	NGC 7836	4886	-5	27	0.13	-0.2	2.48	4.92	1/1
O_1257_47157	—	—	—	—	0.14	-0.3	2.41	4.23	1/1
O_1257_47180	—	—	—	—	0.14	-0.3	2.44	4.23	1/1
O_1257_27320	NGC 13	4808	5	6	0.14	-0.3	2.86	4.51	1/1
O_1257_176787	—	—	—	—	0.17	-0.4	0.22	2.10	1/1
O_1257_37278	UGC 84	5058	-3	200	0.14	-0.4	2.76	4.95	1/1
O_1257_305411	UGC 87	—	-5	200	0.12	-0.5	2.20	10.85	1/1
O_1257_326371	NGC 22	8312	3	6	0.12	-0.5	2.71	5.56	3/3
O_1257_282600	—	—	—	—	0.10	-0.5	1.85	15.06	3/3
O_1257_305466	—	—	—	—	0.12	-0.5	2.25	13.23	1/1
O_1257_294022	—	—	—	—	0.11	-0.5	1.99	15.95	1/1
O_1257_315737	UGC 92	8168	3	200	0.12	-0.5	2.33	14.73	4/4
O_1257_315746	UGC 91	8216	—	200	0.12	-0.5	2.39	11.87	3/1
O_1257_165778	00077+3035	4951	8	6	0.18	-0.5	0.31	2.27	1/1
O_1257_259669	—	—	—	—	0.11	-0.5	1.40	9.07	1/1
O_1257_271214	UGC 95	7851	6	200	0.10	-0.5	1.55	12.72	1/1
O_1257_271300	UGC 96	7033	—	200	0.10	-0.5	1.54	13.30	1/1
O_1257_247984	—	—	—	—	0.12	-0.5	1.26	8.48	1/1
O_1257_283077	UGC 97	—	-2	200	0.11	-0.6	1.86	19.56	1/1
O_1257_48106	UGC 98	4859	3	200	0.16	-0.6	2.45	2.90	4/4
O_1257_326897	—	—	—	—	0.11	-0.6	2.67	5.94	1/1
O_1257_37773	NGC 29	4797	4	38	0.14	-0.6	2.81	3.25	-3/-3

¹Some rasters of multiple merged galaxies were split when the individual galaxies were large enough to make the diameter cut. These split rasters are indicated by an A, B, or C suffix.

²Source numbers are identical to ZCAT source numbers for values < 100, 101 = Giovanelli & Haynes , 102 = Giovanelli & Haynes H_α observations, 103 = Sakai, Giovanelli, & Wegner , and 200 = RC3. There are also a few entries from the Mark II catalogs, they have source numbers 301 = W91CL, 302 = W91PP, 303 = CF.

³Surface density in units of galaxies/ \square° .

⁴The absolute value of the quality flags indicates: 1 = good fit, 2 = prominent dust lane or non-elliptical isodensity affects fit, 3 = irregular appearance affects fit, 4 = prominent spiral pattern affects fit, and 5 = prominent galaxy bar affects fit. If the sign of the flag is negative, the magnitudes include catalog or estimated magnitudes.

2.2.1 Modeling the Galaxy Images

For this study, it was of paramount importance to accurately determine the ellipticities and position angles of the projected galaxy dynamical axes. In the case of spiral galaxies, this is complicated by the bulge/disk overlap, since only the disk is indicative of the dynamical axes orientation. The standard APS image parameters include ellipticity and position angle as determined by a simple ellipse fit to the image, disregarding any image density information. While this is sufficiently accurate for simple images, it can result in a less representative fit in a variety of commonly encountered situations including galaxy images contaminated by foreground stars and inclined galaxies where a large bulge-to-disk ratio rounds out the isodensity contours. Recent work by Byun and Freeman [1995] notes the advantage of fitting galaxies with bulge and disk components using a full two dimensional model, rather than the traditional approach of fitting elliptically averaged one-dimensional profiles. They show that two-dimensional modeling can successfully recover ellipticity and position angles for a wide range of bulge-to-disk ratios at all spiral galaxy inclinations while avoiding several strong systematic errors common in the traditional ellipse fit. Because of these advantages we implemented a two-dimensional model of the expected galaxy density profile to determine the ellipticity (and hence inclination) and position angle of the galaxies in this catalog. This model must not only deal with separating the bulge and disk components, but must also handle the non-linear photometric response inherent in the photographic images. This non-linear response distorts the galaxy surface brightness profiles away from the conventional sum of $e^{1/n}$ components. Since the POSS I plates do not have sensitometer spots on them, there is no straight-forward way of obtaining a density-to-intensity transformation to model the entire density distribution of POSS I galaxy images (although an improved calibration approach has now been developed by the APS group). Therefore, we required a function capable of modeling a galaxy's photographic density profile, including the saturation at high intensities. The galaxy profile is modeled as a variation of a function originally suggested by Monet [1993]. This function has the same general form as the

Fermi-Dirac equation for the energy level populations in a Fermi gas. Our function has two components, which correspond to the bulge and the disk, where the bulge simply has a steeper dependence on radius than the disk. As shown in Figure 2.2, where the fits are compared to the original images, these components provide an adequate representation of pure bulge (ellipticals) and pure disk, as well as composite systems. The functional form of this model for the two dimensional density profile at each point (x, y) relative to the center of the galaxy image (x_0, y_0) is

$$D(x, y) = \frac{D_d}{1 + e^{\alpha_d(r_d - r_{dc})}} + \frac{D_b}{1 + e^{\alpha_b(r_b^2 - r_{bc}^2)}} + D_s. \quad (2.3)$$

The d subscript refers to the disk component, b refers to the bulge component, D_d and D_b are the central component densities, D_s is the background sky density (including plate fog), r_{bc} and r_{dc} are the characteristic radii for the two components, and α_d and α_b are the slopes of the exponential function. The ellipticity (ϵ) and position angle (θ), are contained within the functions for the radii, r_d and r_b , which have the form:

$$r = \sqrt{x'^2 + \left\{ \frac{y'}{1 - \epsilon} \right\}^2}, \text{ where } \begin{cases} x' &= (x - x_0) \cos \theta + (y - y_0) \sin \theta \\ y' &= -(x - x_0) \sin \theta + (y - y_0) \cos \theta \end{cases}. \quad (2.4)$$

When a single component fit performed well, we set $D_b = 0$, fitting the entire galaxy with the disk component as shown in Figure 2.2. Notice that the two components in this function behave in the desired fashion. For $r \ll r_c$, $D(x, y) \approx \text{constant}$, *e.g.*, the profile saturates, as do the galaxy images. For $r \geq 2r_c$, $D(x, y) \approx D \exp(-\alpha r^n)$, *e.g.*, the components take the form of an exponential with $-r^n$ dependence. And finally, for $r \gg r_c$, $D(x, y) \approx D_s$, *e.g.* the background density is approached asymptotically. While this model was designed to represent the density profile of the entire galaxy image, we are principally concerned with the accurate determination of the galaxy position angle and ellipticity. This approach is certainly superior to a simple moments analysis and we found it to be better suited to our purposes than modeling with elliptical annuli. Note that if there exist any fitting errors that are due to inadequacies in compensating for the plate response, the errors will be radially symmetric in most instances and will not affect

the value of the ellipticity and position angle obtained by the best fit. The actual fit of galaxy images to this density model was achieved with a 13-parameter iterative non-linear least squares fit to the entire two-dimensional image, using an improved version of the Levenberg-Marquardt method outlined in Press *et al.* [1992]. Estimates of the uncertainty in the fit parameters are obtained from the diagonal terms of the covariance matrix calculated by this routine.

2.2.2 Data Quality Control

Since non-linear least-squares methods like the Levenberg-Marquardt technique can become trapped in a local minimum, consequently missing the global best-fit, all automated fitting results were checked visually by both JEC and Elizabeth March. The original image, the model image, and a difference image were inspected for large fit residuals. Taking into account limitations of the model, one of six quality flags was assigned: bad fit (need to refit), good fit, best fit possible due to prominent dust lane or non-elliptical isophotes, best fit possible due to irregular appearance of galaxy, best fit possible due to prominent spiral arm pattern, and best fit possible due to prominent spiral bar. Any images which were evaluated as “bad fits” were refit by JEC. This re-fitting consisted of re-running the fitting routine using operator-entered initial estimates for the fit parameters. These initial estimates were used to reduce the chance that the fitting routine would enter a false minimum. This operator-assisted fitting was required for approximately 50% of the images, but should not have introduced any biases, since the fitting-routine was free to find the best-solution, once it was given the operator’s rough guess. No images ultimately classified as bad fits were allowed to remain in the final MAPS-PP sample. These quality flags are used to select a “visually inspected” (VI) subsample of galaxies with the highest quality fits. Position angle uncertainties increase, as expected, with decreasing ellipticity. However, position angle uncertainties generally remained well below 10° until the ellipticity dropped to less than 0.1. These internal uncertainties indicate that the position angles are sufficiently accurate for all but

the most face-on galaxies (See Figure 2.3). In order to convert position angles from the scanner coordinate system to the celestial coordinate system, an accurate plate solution [Aldering 1993] was used to determine the direction of true north, θ_N , relative to machine axes for each image. The extent to which the disk and bulge parameters were successfully decoupled was investigated. As shown in Figure 2.4, the disk and bulge ellipticity values are correlated. The coupling in ellipticity can be understood by considering a plot of disk ellipticity versus position angle residual, as in Figure 2.5. There, the strongest coupling ($\Delta\theta \approx 0$) occurs at high ellipticities as expected, since for bulges with non-zero true ellipticities the major axis is expected to be aligned with the disk major axis when viewed edge-on. This interpretation is supported by the fact that Figure 2.5 shows the more highly elliptical bulges to be more aligned with the disk. In some cases, the bulge component of the model fit a galactic bar rather than a true bulge. This explains the observation that “bulge” ellipticity sometimes exceeds the disk ellipticity. Even in these cases, the disk ellipticity is properly computed and useful for determining the orientation of the galaxy.

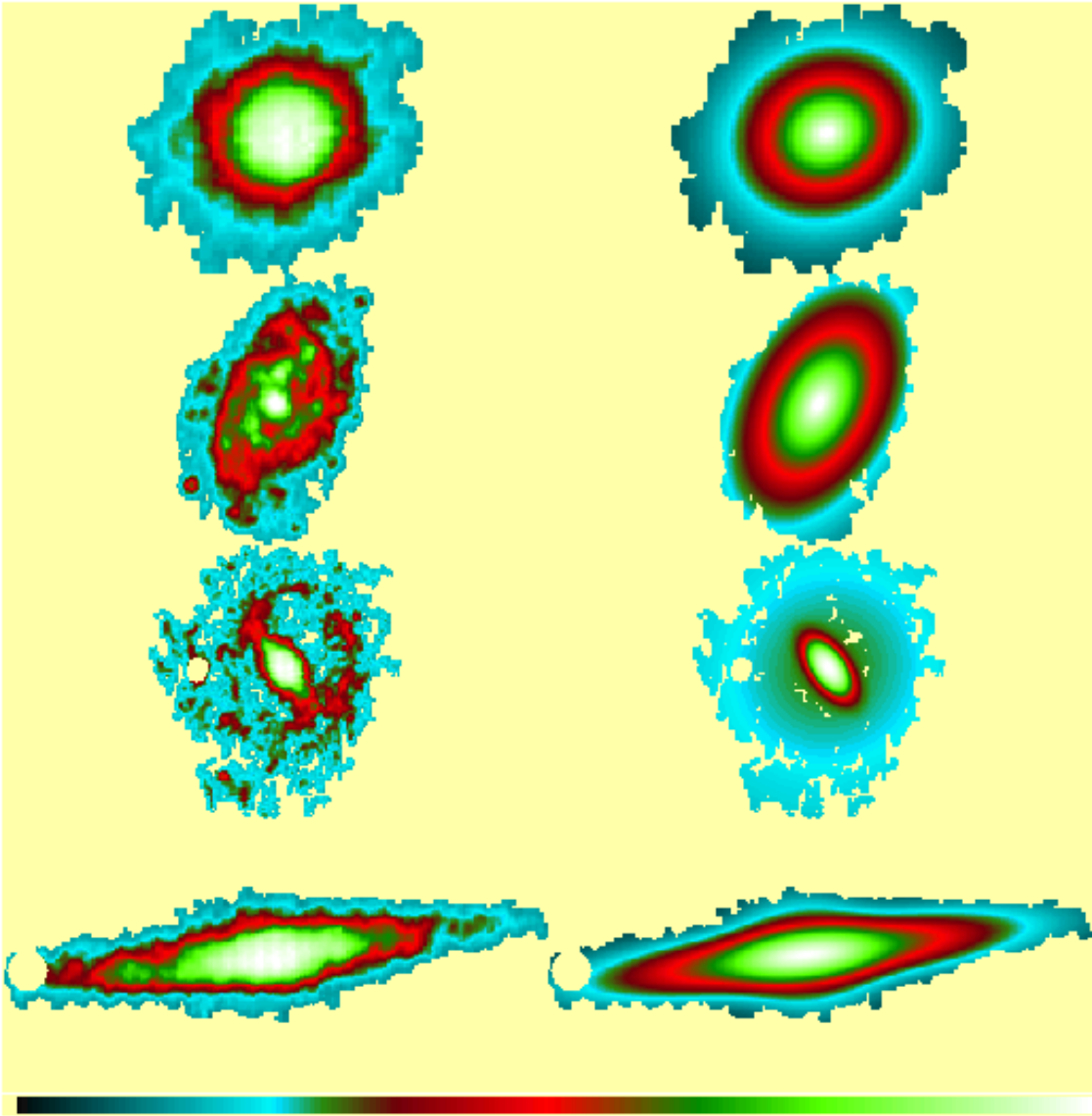


Figure 2.2: A comparison of the original galaxy images (*Left*) versus our fits (*Right*) for 4 galaxies in the sample. The top two pairs show galaxies adequately fit by a single component model, the bottom two pairs show galaxies better modeled by two component models.

Once the entire sample had been fit and quality flags assigned, duplicate galaxy entries due to plate-to-plate overlaps were eliminated; the galaxy image with the best model fit being retained. After removal of these duplicate images, the MAPS-PP contained image parameters for 1388 E plate galaxies and 1230 O plate galaxies. An Aitoff projection of the distribution on the sky of the MAPS-PP sample is shown in Figure 2.1, along with the approximate location of the PPS ridgeline. To ensure the quality and robustness of the galaxy model fits, several tests on the dataset were performed. To investigate the possibility of a scanner-based ‘stretching’ of images as encountered by Djorgovski [1987], the field P293 was rescanned with the plates rotated 90° to the normal scanning orientation. We compared the position angles, ellipticity, and integrated magnitudes as obtained on the rotated plate. In all cases, the scale errors were less than 2% and consistent with zero. The only significant zeropoint shifts occurred in the measurement of integrated magnitudes, for which an external catalog is used to establish consistent photometry as outlined in Sec. 2.3.1. Image parameters for duplicate galaxies located in the plate-to-plate overlap regions were compared. This allowed an assessment of plate to plate variations of the images. It should be noted that the plate overlap regions occur on the edges of the plates, where vignetting is worst and where image quality is poorest. No significant scale differences were found in the ellipticities, position angles, or integrated magnitudes of duplicate images. The diameters did show significant zeropoint shifts, but these are expected due to differing isodensity thresholds on the different plates. Finally, we compared the MAPS-PP O and E bandpass position angles and ellipticities for 86 MAPS-PP galaxies cross-identified with the sample of L94. He provides the best-fit elliptical isophotes at $\mu_B = 20, 21.5, \text{ and } 23 \text{ mag}/\square''$ and $\mu_R = 19, 20.5, \text{ and } 22 \text{ mag}/\square''$ for galaxies observed with a CCD. The outer isophotes of MAPS-PP images reach somewhat fainter, roughly $24 \text{ mag}/\square''$ in O and $23 \text{ mag}/\square''$ in E, than the faintest isophotes fit by Laubscher. However our model fits are density weighted, so we expect to find the best agreement at intermediate isophotal levels. Indeed, our global position angle measurements for the disk component of galaxies in common agree exceptionally

well with those from L94 for $\mu_B = 21.5 \text{ mag}/\square''$ and $\mu_R = 20.5 \text{ mag}/\square''$. Comparison of ellipticities is more complicated as the single isophote nature of the L94 data will tend to produce rounder fits than our method for highly inclined galaxies having strong bulges. We find that our ellipticities become larger than those of L94 for increasing ellipticity, and that this difference is smallest when we compare to the faintest isophotes fit by Laubscher. No trends are present in position angle or ellipticity differences as a function of magnitude or diameter.

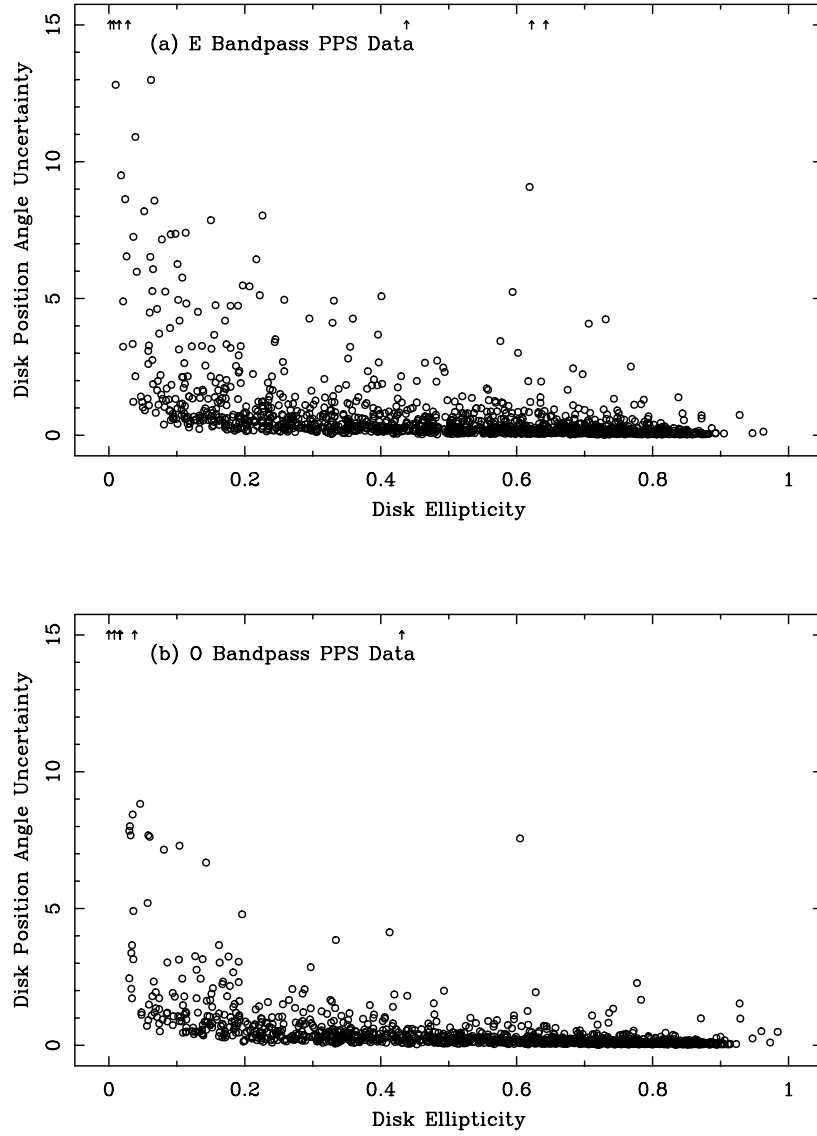


Figure 2.3: Plot of Disk Component Position Angle Uncertainty versus Disk Component Ellipticity for the model fits to galaxies in the MAPS-PP (a) E bandpass and (b) O bandpass. As can be seen, most disk position angles have uncertainties of less than 5° unless the disk ellipticity is less than 0.15 (indicating a face-on galaxy).

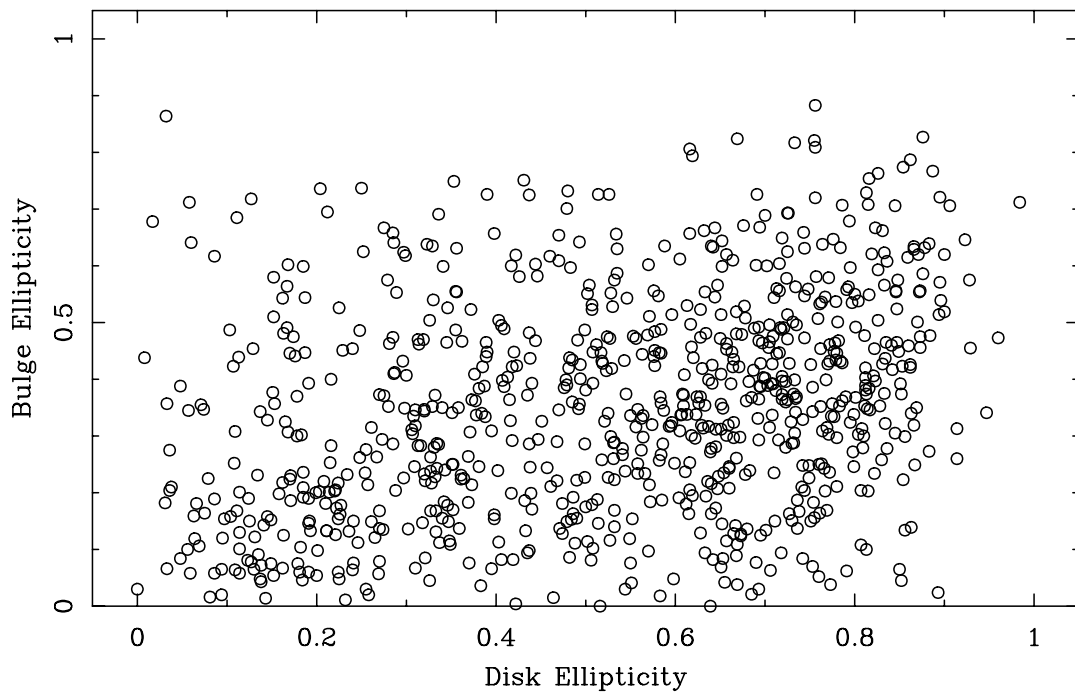


Figure 2.4: Comparison of ellipticities for the bulge and disk model components for the galaxies in the MAPS-PP (O bandpass). Most cases of bulge ellipticities greater than disk ellipticities can be accounted for by a galactic bar being modeled by the bulge component.

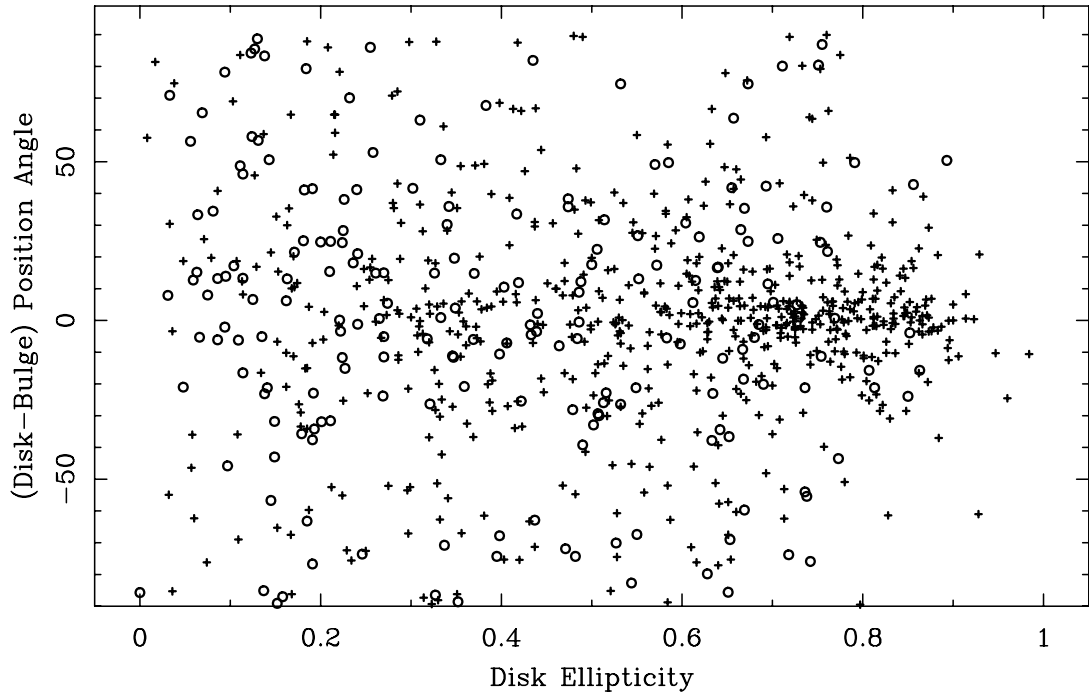


Figure 2.5: Disk ellipticity versus difference of disk and bulge position angle in the O bandpass. This illustrates the amount of coupling between the bulge and disk position angles. Galaxies with bulge ellipticities less than 0.2 are plotted as circles, and as expected, these galaxies show less coupling than systems with higher ellipticity.

2.3 Dataset Cross-Identification, Calibration, and Integrity Tests

The MAPS-PP was positionally matched to existing redshift catalogs, including the ZCAT, the cluster and Pisces-Perseus catalogs of Willick [1990], the Courteau-Faber catalog [Courteau 1996], and recent PPS and A262 redshifts from Giovanelli & Haynes [1993] and Sakai, Giovanelli, & Wegner [1993] respectively. Galaxies were also positionally matched to the Third Reference Catalogue of Bright Galaxies [de Vaucouleurs *et al.* 1991, hereafter referred to as the RC3] to obtain additional morphological information. A separate match was performed to just the UGC, to allow comparison of UGC visual diameter, ellipticity, and position angle estimates to our digital estimates of those parameters. Table 2.3 gives the cross-identification, redshift, and morphological types when available, along with Galactic extinction, as determined below, and fit quality flags as described in Section 2.2.2.

2.3.1 Photometric Calibration

Due to the lack of density-to-intensity calibration and the presence of saturation in the photographic images, independent galaxy magnitudes were difficult to obtain from the APS data. Furthermore, due to plate-to-plate variations in the isophote corresponding to the detection threshold density, the APS integrated magnitudes can exhibit zeropoint shifts of up to 0.7 magnitudes. There is, however, no apparent scale error in the integrated magnitudes, which makes the transformation of these magnitudes to a consistent photometric system a simple matter of determining photometric zeropoints for each plate. The O band magnitudes were calibrated to the CGCG B system separately for each plate, using O-B shifts of +0.68 to -0.63. Similarly, the E band magnitudes were calibrated plate-by-plate to the Mark III uncorrected Gunn r system [Willick *et al.* 1997], using E- r shifts of +0.04 to +0.61. A constant of -0.30 was added to the Gunn r band magnitudes to place them on the Cousins-Kron R system [Schombert, Wallin, &

Struck-Marcell 1990, Barsony 1988]. Thus, in cases where images matched between both bandpasses, an estimate for the $B - R$ color of the galaxy correctly adjusted for plate-to-plate response differences is possible. After the photometric calibration, corrections for Galactic extinction were applied. The relations $A_O = 1.46A_V$ and $A_E = 0.81A_V$ were calculated using the extinction law of Cardelli, Clayton, & Mathis [1989] and the O and E response [Minkowski & Abell 1973]. A_V was estimated using a bilinear interpolation of the Burstein-Heiles extinction maps [Burstien & Heiles 1982] at the location of each galaxy. A_V in the catalog fields ranged from 0.06 to 0.81. Hereafter, O and E magnitudes will refer to these calibrated, extinction corrected magnitudes. It should be noted that due to image size limitations in early versions of the APS software, magnitudes were not calculated for 39 E plate and 41 O plate galaxies. An additional 17 E plate and 7 O plate galaxies which were the result of 'splitting' merged galaxy images have no APS magnitudes. For galaxies without APS magnitudes, cross-identification with the CGCG, Mark III, and RC3 was used to make 34 O and 12 E magnitude estimates. In cases where no catalog match was found, the diameter was used to estimate 7 O and 27 E magnitudes, with the understanding that these magnitudes may only be accurate enough to allow determination of color quartile membership. In all cases where non-APS magnitudes were used, the sign of the quality flag of the galaxy is switched to be negative.

2.3.2 Ellipticity Distribution of the MAPS-PP

Examination of the ellipticity distribution of our catalog, shown in Figure 2.6, shows an increasing number of galaxies with increasing ellipticity. This is unlike the flat ellipticity distribution seen for either the visual-diameter selected UGC or the magnitude selected sample of Sc galaxies of Giovanelli *et al.* [1994]. However, this is the general form of ellipticity distribution expected for an isophotal diameter-limited sample if the Holmberg effect is present. The Holmberg effect, as used here, is the expectation that for (semi-)transparent galaxy disks the surface brightness will increase with increasing

inclination [Holmberg 1975]. This effect leads to larger apparent diameters, and therefore to increasing sample volume with increasing inclination for an isophotal–diameter limited sample. We examined the difference between our ellipticity distribution and that derived from the UGC and offer an explanation of why the difference is observed in the Appendix. This anisotropic ellipticity distribution means that the derived distribution of inclinations, and therefore inferred 3-D orientations, would be biased. Proper analysis of any observed galaxy orientation anisotropies would require either a truly volume–limited sample, a thorough understanding of the true ellipticity distribution for a diameter–limited sample of randomly oriented galaxies, or a comparably sized sample of field galaxies whose ellipticity distribution could be used as a reference. These solutions are outside the scope of this paper; therefore it was decided that position angle anisotropies would be the primary criterion for identifying dynamical axis alignments. This is a weaker test than possible with full ellipticity and position angle modeling of dynamical axes orientations, however, it assures that the expected behavior of the data for purely random galaxy orientations is well understood. In this context, we point out that the influence of the Holmberg effect on inferred galaxy inclination distributions has been ignored in previous studies of galaxy alignments.

2.3.3 The PPS Luminosity Function and the Level of Non-Supercluster Galaxy Contamination

As redshifts are available for only roughly 50% of the MAPS-PP galaxies, it is certain that some galaxies in the MAPS-PP are foreground or background to PPS. Since such (presumably randomly oriented) galaxies would dilute any true alignment signal, it is essential that the amount of such contamination be estimated as it is not possible to isolate all contaminating galaxies. Because the MAPS-PP is a diameter-limited catalog which reaches considerably fainter than the completeness limits of extant redshift catalogs, it is necessary to use a function whose behavior is well characterized to extrapolate the known

bright end of PPS membership to the faint end of the MAPS-PP. The Schechter luminosity function [Schechter 1976] is used, since its behavior is known to adequately represent observed galaxy luminosity functions in a wide range of environments for $M_B < -16$. Therefore, we set about to estimate the bright-end of the PPS luminosity function so that an extrapolation could be performed at the faint end, allowing an estimate of the amount of contamination. This luminosity function for the PPS was estimated using

$$\Phi[m - (m - M)] = \frac{1}{V} N_{PPS}(m) C S(m|D) \quad (2.5)$$

where $N_{PPS}(m)$ is the number of PPS objects in ZCAT per magnitude bin, C is the completeness of ZCAT as it depends on magnitude, and $S(m|D)$ is a selection function representing galaxies lost as a function of magnitude due to the use of a diameter-limit of $30''$. Once the form of the functions in equation (2.5) is determined, the luminosity function for the PPS can be used to establish the expected number of galaxies per magnitude interval; excess numbers over this prediction are assumed to arise from foreground and background galaxies. To estimate $S(m|D)$, a simple linear regression was performed for all galaxies with O apparent magnitude (uncorrected for Galactic extinction) and APS major-axis diameter information to find:

$$\log D = -0.217 m_O + 5.01, \quad (2.6)$$

with $\sigma_{\log D} = 0.15$. A Monte Carlo simulation of 10^5 galaxies per 0.5 magnitude interval over the range $10.5 < m_O < 18.5$ was performed, using equation (2.6) (including Gaussian scatter) to compute diameters, was used to determine how many simulated galaxies survived the $30''$ major-axis cut. The PPS completeness of the ZCAT as a function of absolute magnitude, C , was estimated by comparing the number of ZCAT galaxies in the O bandpass MAPS-PP with redshifts per magnitude interval. Finally, to determine $N_{PPS}(m)$, all known PPS members in our catalog were identified by requiring a PPS member have a redshift of $3500 < cz < 7000 \text{ km s}^{-1}$. Once the distribution in apparent magnitudes was determined, it was converted to a distribution in absolute magnitude at the distance of the PPS, assuming a distance modulus of $\mu_0 = (33.5 - 5 \log(h))$,

where $h = 1$ ($H_0 = 100h \text{ km s}^{-1}\text{Mpc}^{-1}$). Once the functions of all variables on the right hand side of equation (2.5) were calculated, it was possible to determine $\Phi(M)$. A non-linear least squares fit of the Schechter function to $\Phi(M)$ found best fit parameters of $\alpha = -0.88$, $\Phi = 0.011 h^3 \text{ mag}^{-1} \text{ Mpc}^{-3}$, and $M_* = -19.36$ (corresponding to an apparent magnitude 14.14). Figure 2.7a shows this luminosity function compared to the observed number of galaxies. This estimate of the Schechter luminosity function for the PPS, in combination with $S(m|D)$, is used to estimate the number of PPS members in the O bandpass MAPS-PP. When compared to the total O bandpass counts, this provides an estimate of the foreground and background contamination. It should be noted that this PPS luminosity function is deeper than any previously published one by roughly one magnitude. However, our extrapolated Schechter function may underestimate the number of faint PPS galaxies and therefore overestimate the number of contaminating foreground and background galaxies. Higher faint-end PPS counts would be in line with the lower α values reported by Trasarti-Battistoni, Invernizzi, & Bonometto [1997] for the PPS and by Marzke, Huchra, & Geller [1994] for the entire CfA redshift survey. Estimates using our best-fit Schechter function reveal that roughly 35% (413 of 1230) of the galaxies in the MAPS-PP are likely to be foreground or background to the PPS. This is shown graphically in Figure 2.7b. After eliminating known non-PPS members using published redshifts, the MAPS-PP counts were roughly 20% higher than predicted by the PPS luminosity function derived above for all magnitude bins fainter than 14.5. Therefore, any alignment signal will be diluted by roughly 20%, with the exact value depending on the magnitude distribution of the subsample being considered. After eliminating known foreground and background galaxies, 1158 E plate galaxies and 1014 O plate galaxies remain in the MAPS-PP.

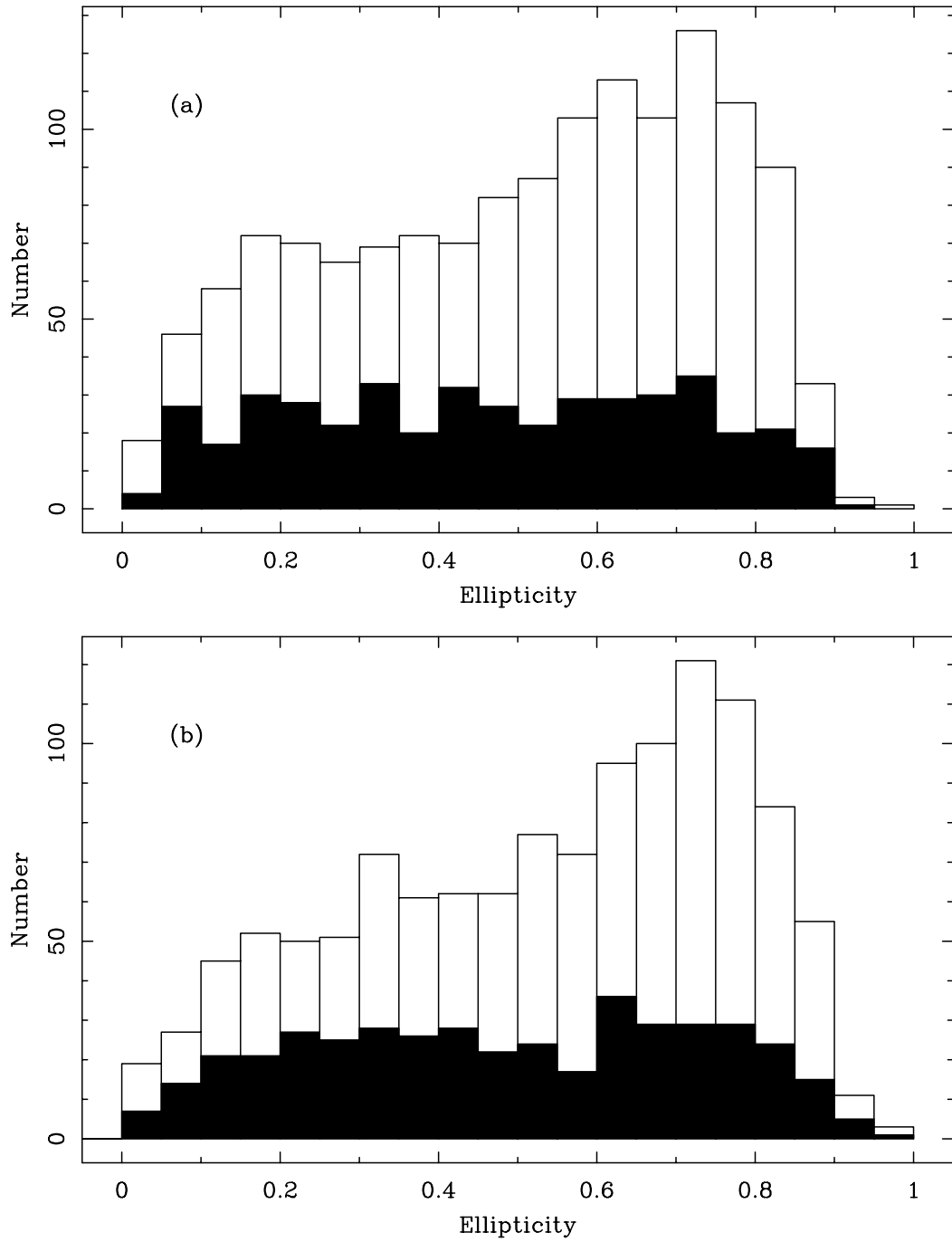


Figure 2.6: Ellipticity histograms for the MAPS-PP galaxies. Figure (a) shows results for the E bandpass and (b) for the O bandpass. In both histograms, the galaxies in the “justPPS” subsample, are indicated by the black histogram. Notice that this later sample, which is roughly volume-limited, and has a much flatter ellipticity distribution than the overall sample.

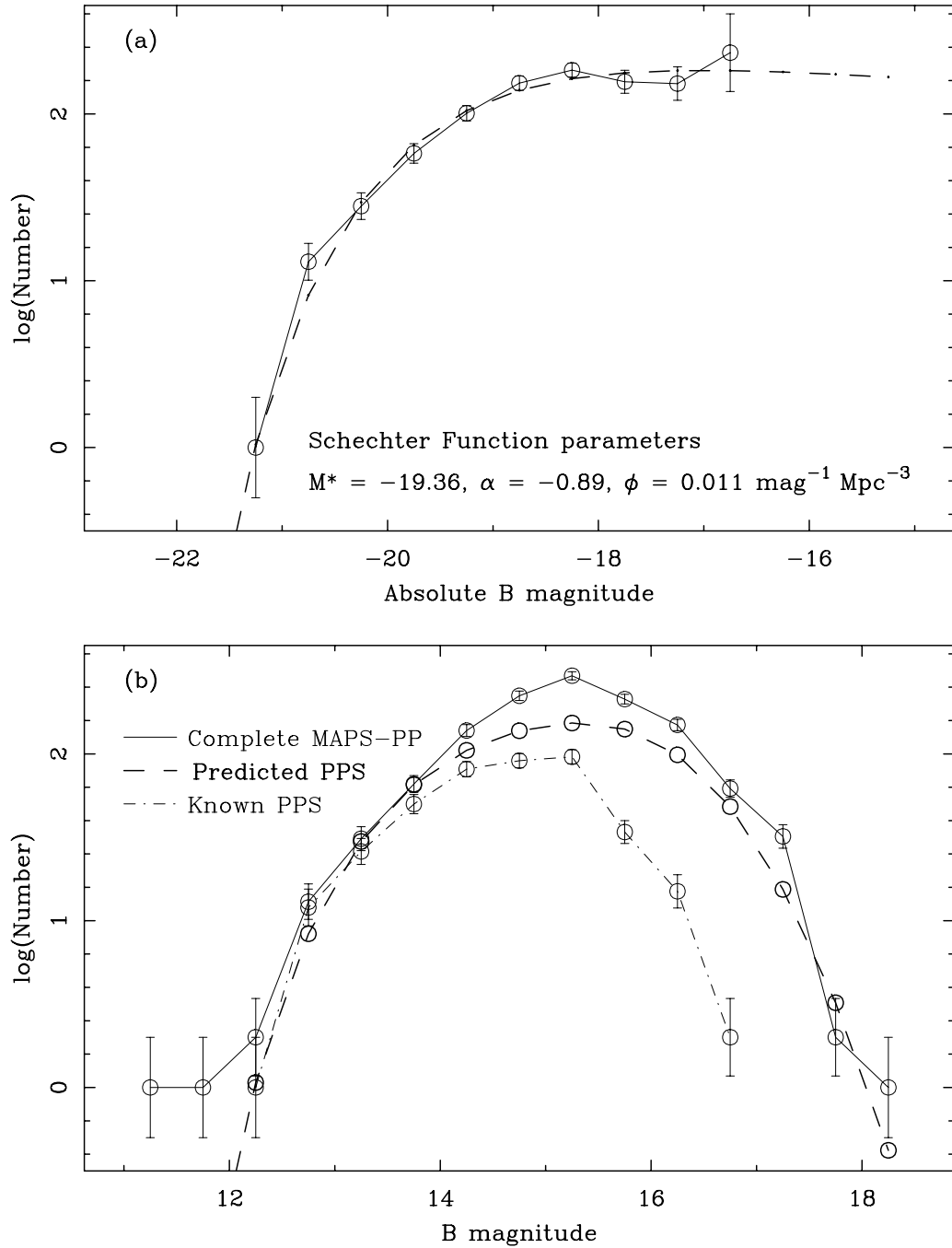


Figure 2.7: Using the O bandpass data and the ZCAT an estimate of the PPS luminosity function and the best fit Schechter function (a) is used to estimate the number of PPS galaxies (b) in the MAPS-PP. These estimated counts have been adjusted for incompleteness due to the diameter limit used. Figures (a) and (b) are vertically aligned so that Absolute magnitude in (a) corresponds to the appropriate apparent magnitude in (b). The method used to determine this luminosity function is outlined in Section 2.3.3.

2.4 Data Analysis Methods

2.4.1 Identification of Large-Scale Structures within the MAPS-PP

Because of the importance of environmental density as a parameter for determining the mechanism responsible for any observed galaxy alignments, the identification of large scale structure in the MAPS-PP is important. Using a two-dimensional version of the adaptive friends-of-friends (FOF) algorithm of Huchra & Geller [1982] (and used by Trasarti-Battistoni, Invernizzi, & Bonometto [1997] in the PPS), possible groups and clusters in the MAPS-PP were identified. Because redshifts are unavailable for almost half of the MAPS-PP, the algorithm was restricted to searching the two-dimensional projection of galaxies onto the sky, essentially identifying overdense regions of the PPS covered by the MAPS-PP. Since groups and clusters found by this search method are observed in projection and may not be real dynamically associated structures, the term “galaxy concentration” (hereafter “GC”) will be used for structures so identified. The GCs were used to determine the orientation of galaxies relative to their local environment. GCs were identified using a percolation algorithm with percolation lengths ranging from $10'$ to $50'$, in increments of $5'$. A minimum GC size of 10 galaxies was required. For each GC, a simple moments analysis provided the GC ellipticity and position angle, using the mean celestial coordinates of the member galaxies as the cluster center. Since the average population and density of the GCs changes with percolation length, it is likely that the GCs correspond to different dynamical structures depending on the percolation length used to generate them. Some GCs built with percolation lengths of $50'$ cover almost the entire PPS, making their identification as clusters troublesome. Cross-matching of the GCs with the Abell [1958] and Zwicky CGCG clusters shows that percolation lengths of 30 – $35'$ give the GCs the most similar diameters to the Abell and Zwicky clusters. Also, GCs which matched to these existing cluster catalogs were typically in the Abell and Zwicky distance groups of 1 or 2, indicating their member galaxies were relatively bright. This is expected since Abell and Zwicky examined galaxies much smaller than

30'' in diameter in order to identify their clusters. Summary properties of the GCs as they depend on percolation length are listed in Table 2.4. The surface density of galaxies

Table 2.4: Galaxy Concentrations identified in the MAPS-PP.

Percolation Length (')		Number of GCs	Number of galaxies			Σ (galaxies/ \square°)			Cross-Matches	
			Min.	Mean	Max.	Min.	Mean	Max.	Abell	Zwicky
10	E	1	14	14	14	58.20	58.20	58.20	1	1
	O	1	13	13	13	48.77	48.77	48.77	1	1
15	E	6	10	12	31	14.32	18.37	34.53	1	2
	O	4	10	13	29	19.48	17.23	26.68	1	2
20	E	15	10	17	78	7.32	14.50	30.04	2	7
	O	11	10	17	60	9.09	15.78	30.07	2	7
25	E	26	10	19	90	4.20	11.12	27.93	5	11
	O	20	10	18	81	4.74	11.01	27.96	3	10
30	E	24	10	26	96	5.16	9.85	22.69	4	8
	O	23	10	21	86	3.92	9.34	21.96	3	8
35	E	23	10	33	106	2.44	8.10	21.55	5	10
	O	23	10	26	96	3.07	8.12	21.57	3	12
40	E	18	10	53	282	2.44	7.69	18.16	2	8
	O	17	11	32	142	2.66	6.66	19.36	1	6
45	E	9	39	115	347	4.42	7.83	13.67	2	7
	O	13	11	46	184	2.66	5.80	13.04	2	6
50	E	7	39	152	408	5.67	8.35	13.39	1	4
	O	11	11	53	188	1.91	5.95	13.04	1	6

was also computed before any parameter cuts, other than a redshift cut, were applied. This allowed for a consistent value of surface density while at the same time allowing the elimination of known non-PPS galaxies which could artificially enhance surface density values and dilute the surface density contrast along the PPS ridge. Using a method outlined by Dressler [1980], the angular separation between each galaxy and its tenth closest neighbor, r_{10} , was determined. Assuming there are 11 galaxies within a circle of radius r_{10} , the number of galaxies per square degree is readily computed. The surface density for galaxies in the MAPS-PP ranged from 0.62 to 98.34 galaxies/ \square° , with a median density of 6.08 E plate galaxies/ \square° and 5.23 O plate galaxies/ \square° . The r_{10} surface densities for MAPS-PP galaxies are given in Table 2.3. For the purposes of this study, the PPS ridgeline was defined using ZCAT galaxies with redshifts in the range $3500 < cz < 7000 \text{ km s}^{-1}$, located within 6.6° of the center declination of the survey

plates. The weighted mean positions for the galaxies were determined in 15 minute wide right ascension bins, weighted by the galaxy surface density (using the method outlined above for computing surface density). Spline interpolation was used to generate the intervening points on the ridgeline with a resolution of $1'$. This PPS ridgeline can be seen plotted on top of the MAPS-PP in Figure 2.1. This ridgeline was the reference used to determine the angular separation of each galaxy from the plane of the supercluster as it is believed that this plane lies roughly perpendicular to the sky [Giovanelli & Haynes 1988]. In the statistical analysis of the MAPS-PP, a variant of the Kolmogorov–Smirnov D statistic was chosen to estimate the probability of a sample having a significantly anisotropic distribution. The usual K–S D statistic is a non-parametric test, utilizing the maximum deviation between the cumulative distribution of the data and that of a reference sample (in our case, a sample designed to have null signal). Press *et al.* [1992] note that the sensitivity of the K–S D statistic to deviations from a cumulative distribution $P(x)$ is not independent of the value of x . This is a serious problem for an analysis of position angles and position angle differences, since they are circular, not linear, quantities. Monte-Carlo simulations using generated position angle distributions of the form

$$N(\theta) = N_0[1 + \Delta \sin 2(\theta - \phi)] \quad (2.7)$$

show that the K–S D statistic can systematically underestimate the significance of the anisotropy of the sample depending on the phase, ϕ , of the anisotropy. Therefore, the Kuiper V statistic, a variant of the K–S D statistic suggested by Press *et al.* [1992], is used instead. This statistic is designed to measure the deviation of the cumulative distribution in a way which circularizes the parameters, allowing for a likelihood estimate with equal sensitivity at all values of x , regardless of ϕ of the distribution. More details on the Kuiper V statistic can be found in Press *et al.* [1992]. For each of the MAPS-PP subsamples (defined in Section 2.5) the criteria for identification of a potential galaxy alignment is a Kuiper V statistic indicating a probability of $P(V) < 5\%$ that a given position angle distribution has been drawn from a null signal sample. Unless stated

otherwise, the null signal samples consist of 2×10^5 datapoints, generated via Monte-Carlo simulations.

2.4.2 The Sinusoidal Model

The disadvantage of using a non-parametric test like the Kuiper statistic is that a model fit can be a more sensitive test for anisotropy. This is true only if the model is a valid description of the data. For example, if a position angle anisotropy manifests itself as increased counts in one direction and decreased counts in the orthogonal direction (as expressed in equation 2.7), fitting this function directly could detect a smaller amplitude (small Δ) position angle anisotropy than the Kuiper statistic would consider significant. This sort of sinusoidal fitting is essentially the technique developed by Hawley & Peebles [1975] to examine position angle histograms. Historical use of this technique and its potential sensitivity to certain position angle anisotropies led to our decision to fit a sinusoid to the position angle histograms of our data. Fitting was accomplished using a least squares fitting routine (GaussFit, described in McArthur, Jeffreys, & McCartney [1994]) to fit equation (2.7) to histograms of the data, always using twelve bins of equal width. A significantly anisotropic fit is defined as one where the probability of finding an amplitude of Δ or larger in a random sample is $P(\Delta) < 0.05$. Sinusoidal models are fit only if the average count per bin is at least 10. In order to reduce the possibility that any anisotropy is not an artifact of our choice of bins, we also perform a second fit, with the bins shifted half a bin width.

2.4.3 Position Angle Distributions Tested

For each subsample of the MAPS-PP an identical battery of tests was performed in an attempt to recover the predicted kinds of galaxy alignments. First, the possibility of nearest neighbor alignments, as suggested by some many-body simulations, was investigated by computing the position angle difference, $\Delta\theta_{gg}$, and angular separation, ΔS_{gg} , for each pair of galaxies. The $\Delta\theta_{gg}$ data were binned by ΔS_{gg} in 0.5° wide bins

and the mean $\Delta\theta_{gg}$ computed in each bin. In the event of random galaxy orientations, the mean $\Delta\theta_{gg}$ in each ΔS_{gg} bin is expected to be 45° . However, this may also be true in the presence of both nearest neighbor alignments and anti-alignments. As suggested by Dekel [1985], the standard deviation of the $\Delta\theta_{gg}$ distribution in each ΔS_{gg} bin was also computed, since this statistic would likely be larger if both alignments and anti-alignments are present than in the case of random galaxy orientations. Galaxy

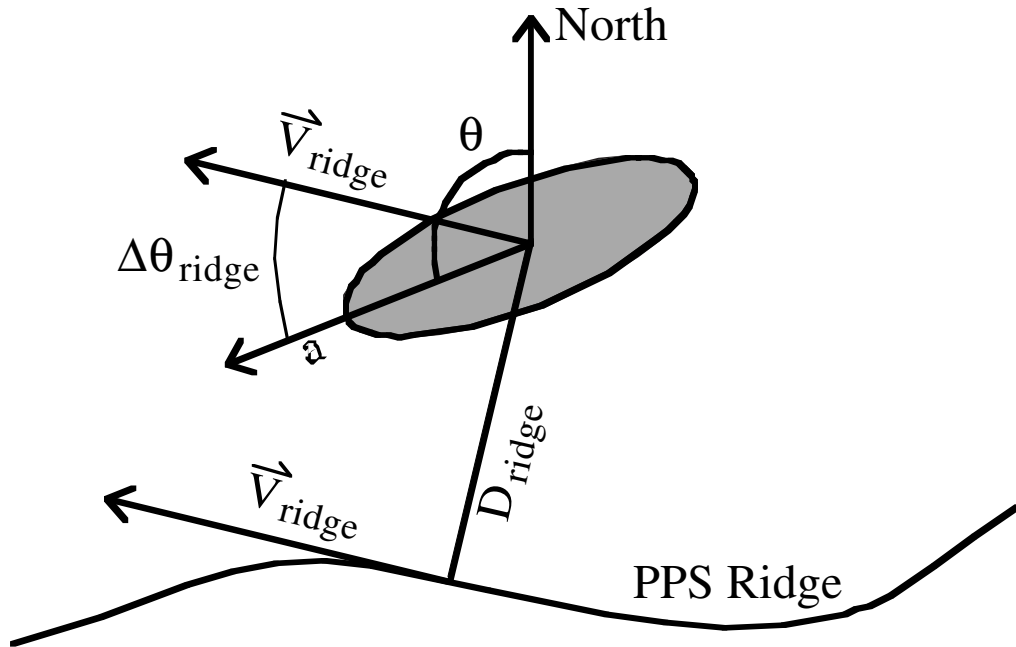


Figure 2.8: Diagram illustrating the definition of the θ_{ridge} value for a galaxy. θ_{ridge} is used to determine the orientation of a galaxy relative to the PPS plane, since this plane is believed to be roughly perpendicular to plane of the sky.

alignments with respect to the PPS supercluster plane were investigated by computing $\Delta\theta_{ridge}$, the difference between the galaxy position angle and the position angle of the closest ridgeline point as defined by the line tangent to ridgeline at that point (see Figure 2.8 for an illustration). The possibility of a variety of alignments relative to local density enhancements was investigated by examining the alignments relative to the GCs. Because any single GC will typically have a relatively small number of galaxies, the GCs were stacked using two techniques. This stacking improved the chances of recovering a

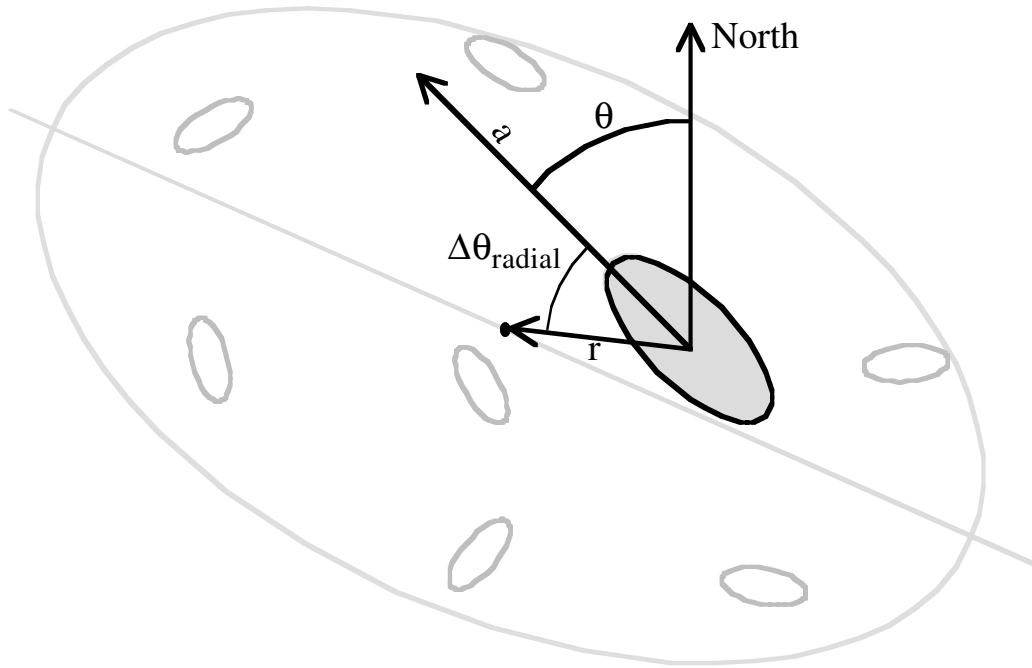


Figure 2.9: Diagram illustrating the definition of the θ_{radial} value for a galaxy. Examining θ_{radial} distribution provides a measure of degree of radial alignments relative to centers of high density “galaxy concentrations.”

weak galaxy alignment signal. The first stacking technique was based on the distribution of galaxy position angles relative to the radial line from the GC center, $\Delta\theta_{radial}$, as shown in Figure 2.9. Finally, the distribution of galaxy position angles relative to their parent GC position angle, $\Delta\theta_{con}$, was examined. Figure 2.10 pictorially describes $\Delta\theta_{con}$.

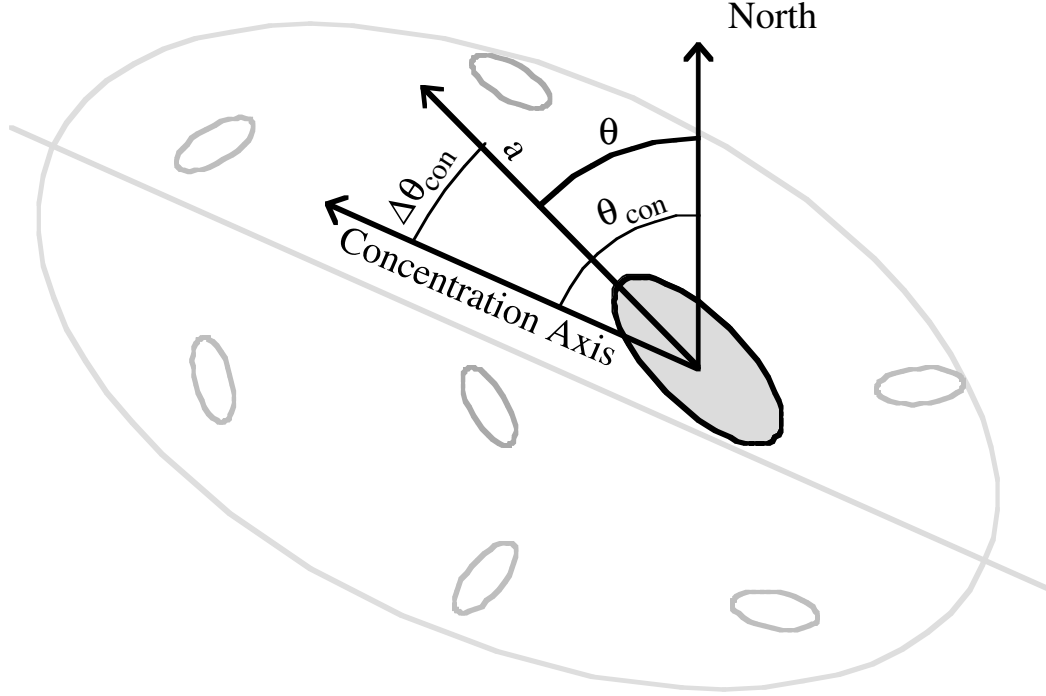


Figure 2.10: Diagram illustrating the definition of the θ_{con} value for a galaxy. The distribution of θ_{con} measures the degree of alignments relative to the local high density environment.

Table 2.5: Descriptions of the MAPS-PP subsamples.

Name	Sample Size (E / O bandpass)			Definition
	Complete	$\chi^2_\nu < 2.0$	Visual	
All	1388 / 1230	1130 / 1128	957 / 816	Complete dataset (duplicates eliminated)
justPPS	444 / 428	314 / 362	255 / 237	Galaxies with measured redshift in the range $3500 < cz < 7000 \text{ km s}^{-1}$
PPS	1158 / 1014	932 / 931	816 / 680	Complete dataset EXCEPT for those galaxies with measured redshift outside the range $3500 < cz < 7000 \text{ km s}^{-1}$
hidens	290 / 254	217 / 233	216 / 180	PPS with surface density in 4th quartile density
middens	580 / 508	466 / 468	398 / 333	PPS with interquartile surface density range
lodens	290 / 254	251 / 232	203 / 168	PPS with surface density in 1st quartile
bright	287 / 253	207 / 203	181 / 133	PPS with magnitude in 1st quartile
midmag	575 / 508	448 / 476	396 / 348	PPS with interquartile magnitude range
faint	288 / 254	268 / 253	232 / 200	PPS with magnitude in 4th quartile
blue	249 / 248	217 / 220	172 / 120	PPS with $O - E$ in 1st quartile
red	252 / 252	208 / 245	196 / 218	PPS with $O - E$ in 4th quartile
spirals	241 / 241	182 / 198	116 / 112	PPS with $0 \leq T \leq 9$
ells	81 / 77	63 / 76	76 / 70	PPS with $-7 \leq T \leq 0$
morph	322 / 318	245 / 274	192 / 182	PPS with $-7 \leq T \leq 9$

2.5 Results and Discussion

Initially three subsets of the complete MAPS-PP were constructed. These were the complete dataset, the $\chi^2_\nu < 2.0$ subset (in which the model fit was required to have a χ^2_ν of less than 2.0), and the “Visually Inspected” (VI) subset (in which the quality flag is required to be one). We want to emphasize that there is a biased T type distribution in the $\chi^2_\nu < 2$ and VI subsets. Most of the excluded objects are $T > 0$, as expected since the model used was simple and didn’t take into account structures typical in spiral galaxies, such as spiral arms. This bias should be kept in mind when comparing the complete dataset to the $\chi^2_\nu < 2$ and VI subsets. For a full breakdown of the numbers of galaxies in each of the subsets see Table 2.1. These three subsamples were further subdivided based on parameter cuts on color, surface density, magnitude, redshift, and morphological class. The redshift and morphological class are only available in those cases where our sample was cross-identified with a pre-existing galaxy catalog listing those parameters. A complete breakdown of all the subdivisions and the number of galaxies in them, is provided in Table 2.5. These subsamples allow investigation of theoretically expected alignments in low density versus high density areas. Investigation of claims by Flin and Godłowski [1986] that spirals show stronger alignments than ellipticals was also possible using both morphological types from existing catalogs and O-E colors.

2.5.1 The Identification of Possible Galaxy Alignments

Because of the large number of MAPS-PP subsamples being investigated (14 subdivisions of 3 subsets, each in 2 bandpasses), there is a non-negligible chance of finding a “significant” result due simply to the fact that there are over 20 different subsamples. Since the E and O bandpass data are expected to show similar results, when the probability of the Kuiper V statistic, $P(V)$, or sinusoidal amplitude, $P(\Delta)$, was small in one bandpass, a correspondingly low probability in the other bandpass is used as a verification of a signal. It was also expected that $P(V)$ and/or $P(\Delta)$ would be correlated for similar tests, e.g., if one test of position angles relative to GCs identified with a $30'$

percolation length shows a low $P(V)$ or $P(\Delta)$, a low probability is also expected for GCs identified with percolation lengths of $25'$ and $35'$. Initially we examined the results as an ensemble. We compared the distributions of $P(V_E)$, $P(V_O)$, $P(V_E)P(V_O)$, $P(\Delta_E)$, and $P(\Delta_O)$, and $P(\Delta_E)P(\Delta_O)$ with those generated from random datasets. The product of probabilities for the E and O subsamples for each statistical measure is a means of testing the extent to which E and O agree in being anisotropic. The random datasets were used to calculate statistical significance, as the random datasets showed a slightly larger incidence of significantly anisotropic distributions than expected from Gaussian statistics. If the Kuiper V statistic probability, $P(V)$, of a sample being drawn from a random galaxy orientation distribution was less than 0.05, it was flagged for further investigation. Likewise for the sinusoidal fits if $P(\Delta)$ was less than 0.05. When the initial statistical reduction was completed, only three statistically significant and reproducible cases of non-random galaxy orientations were found: an anti-alignment of “red” galaxies relative to GCs, an anisotropic distribution of “blue” galaxies within 1° of the PPS ridge relative to the ridge, and a trend of galaxies to change orientation with increasing distance from the PPS ridge. A strong signal for radial alignment of bright galaxies with GCs having a percolation length of $45'$ was seen, however this signal disappeared for all other percolation lengths. The “red” subsamples, consisting of the reddest quartile of MAPS-PP galaxies, were discovered to have non-isotropic $\Delta\theta_{con}$ distributions for GCs identified using percolation lengths of $25'$ to $35'$. This anisotropic signal was observed in the E bandpass “complete” and $\chi^2_\nu < 2$ subsets (and less so in the VI subset). This anisotropy was also detected with a sinusoidal fit amplitude $\Delta \sim 0.4$, having $P(\Delta) < 0.005$. It is not highly significant in the O bandpass for any statistical measure. The signal may be present at smaller percolation lengths, but not at a level which can be confirmed as statistically significant given the small number of galaxies and GCs at shorter percolation lengths. A summary of the $\Delta\theta_{con}$ distribution $P(V)$ values for the “red” subsample for all percolation lengths and subsets is provided in Table 2.6; the most significant results have been highlighted. Figure 2.11 shows a histogram of the $\Delta\theta_{con}$ distributions for the

“red” subsample, which indicates a preference for anti-alignment between the GC and the member galaxies. Note that the “red” subsample is more dominated by ellipti-

Table 2.6: $\Delta\theta_{con}$ statistics for the “red” subsamples.

		Percolation Length (in minutes of arc)								
		10	15	20	25	30	35	40	45	50
# of galaxy concentrations	E	1	6	15	26	24	23	18	9	7
	O	1	4	11	20	23	23	17	13	11
Complete Sample										
N Galaxies	E	7	39	87	132	180	212	227	240	243
	O	7	35	82	115	162	196	214	230	240
$P(V)$	E	0.356	0.679	0.211	0.049	0.016	0.004	0.810	0.459	0.301
	O	0.186	0.661	0.212	0.321	0.064	0.389	0.781	0.870	0.755
$\chi^2_\nu < 2.0$										
N Galaxies	E	7	30	73	109	147	174	187	197	202
	O	7	34	80	110	157	191	209	224	233
$P(V)$	E	0.356	0.549	0.029	0.035	0.047	0.004	0.406	0.786	0.524
	O	0.186	0.519	0.147	0.356	0.076	0.313	0.751	0.852	0.760
Visually Inspected										
N Galaxies	E	7	35	70	108	144	166	178	187	191
	O	7	33	74	99	139	171	184	198	206
$P(V)$	E	0.356	0.890	0.253	0.017	0.135	0.018	0.780	0.647	0.725
	O	0.186	0.795	0.228	0.607	0.099	0.105	0.853	0.468	0.678

cals than the complete sample. However, the “ells” subsample of galaxies previously morphologically typed as ellipticals showed no significant $\Delta\theta_{con}$ anisotropy. This lack of significant anisotropy could be due to the fact that the “ells” subsample is roughly one third the size of the “red” subsample. One might be tempted to interpret this anti-alignment of “red” galaxies relative to GCs as a signature of a global anti-alignment relative to the PPS ridgeline, since the GCs are generally aligned with the PPS ridgeline. However, no anisotropy is indicated in the distribution of $\Delta\theta_{ridge}$ for the “red” galaxies closest to the PPS ridge. Within 1° of the PPS ridgeline, the “blue” subsample shows an anisotropic $\Delta\theta_{ridge}$ distribution. The anisotropy is significant in both the E and O bandpass samples. The signal weakens in the $\chi^2_\nu < 2$ and VI subsets of the MAPS-PP,

but it is still statistically significant in the O bandpass of the $\chi^2_\nu < 2$ and E bandpass of the VI subsets. A summary of statistical results of tests performed on the $\Delta\theta_{ridge}$ distribution is given in Table 2.7. An investigation of the $\Delta\theta_{ridge}$ distribution, as shown in Figure 2.12, indicates that it is neither indicative of alignments or anti-alignments to the PPS ridge. This may also explain why the sinusoidal function fails to find non-zero amplitudes with greater than 1.25σ significance for the distributions in Figure 2.12. However, a statistically significant change in the median $\Delta\theta_{ridge}$ occurs with increasing distance from the PPS ridge. Binning the galaxies by angular separation from the PPS ridge, a Spearman Rank-order Coefficient [Press *et al.* 1992] test of median $\Delta\theta_{ridge}$ versus separation from the ridge shows statistically significant correlation coefficients of $r_S(E) = 0.690$ and $r_S(O) = 0.667$ for galaxies within 2° from the PPS ridge. A simulation of 100 samples of randomly oriented galaxies run through the same parameter space cuts also indicates that these results are significant. This result indicates that the bluest quartile of galaxies tend to become more anti-aligned with increasing distance from the PPS ridge. It should be noted that if data out to 2.5° is included, the trend disappears (see Figure 2.13). This reversal in the median $\Delta\theta_{ridge}$ trend for bins $> 2.0^\circ$ could be an indication that non-PPS galaxies, presumably with a random space orientation, are being sampled, and thus the median $\Delta\theta_{ridge}$ will move back to 45° . This argument is supported by the fact that the mean surface density for galaxies in these distance bins drops for bins $< 2.0^\circ$ but stays relatively flat at $1\text{--}2$ galaxies/ \square° for bins $> 2.0^\circ$ from the PPS ridge. Further investigation of this shift in the median $\Delta\theta_{ridge}$ using the bluest half of the “PPS” subsample shows this effect to be stronger, with $r_S(E) = 0.881$ and $r_S(O) = 0.786$. Exploration of the full “PPS” and the “red” subsamples shows no such significant trends, although the reddest half of the “PPS” subsample shows statistically significant anti-correlation with $r_S(E) = -0.881$ and $r_S(O) = -0.786$, expected since the “PPS” subsample (which is the sum of the reddest and bluest halves) shows no significant correlation of median $\Delta\theta_{ridge}$ with distance from the PPS ridge. Notably, although the “blue” subsample is presumably dominated by spirals, this shifting median

Table 2.7: $\Delta\theta_{ridge}$ statistics for the “blue” subsamples.

		Distance from PPS ridge (degrees)			
		0.0 – 0.5	0.5 – 1.0	1.0 – 1.5	1.5 – 2.0
Complete Sample					
N Galaxies	E	41	52	42	29
	O	41	52	42	29
P(V)	E	0.052	0.029	0.441	0.141
	O	0.068	0.010	0.314	0.395
$\chi^2_\nu < 2.0$					
N Galaxies	E	35	43	36	26
	O	34	44	41	26
P(V)	E	0.125	0.131	0.528	0.113
	O	0.043	0.056	0.425	0.334
Visually Inspected					
N Galaxies	E	27	37	30	22
	O	23	26	19	17
P(V)	E	0.052	0.075	0.104	0.044
	O	0.342	0.178	0.015	0.296

$\Delta\theta_{ridge}$ trend is not observed in the “spiral” subsamples, even though the number of galaxies in these subsamples is comparable. A summary of the results of the Spearman Rank-order Coefficient tests on the various subsamples is listed in Table 2.8; again the most significant results have been highlighted. Some authors (e.g. GTT and Lambas *et al.* 1988a) have employed an ellipticity cut when searching for alignments. Exclusive use of position angles restricts measurement of alignment vectors to the component in the plane of the sky. An ellipticity cut can therefore remove the diluting affects of galaxies whose alignments can’t be measured well using position angles. An ellipticity cut also creates a subsample whose position angles are better determined. Therefore, we constructed samples with $\epsilon > 0.1$ (To assure most $\sigma_\theta < 10^\circ$, as suggested by Figure 2.3) and $\epsilon > 0.3$ (as used by GTT). The anisotropies noted earlier were recovered in the $\epsilon > 0.1$ sample, with somewhat different Kuiper statistic values. In particular the “blue”

Table 2.8: Spearman Rank Correlations for the median $\Delta\theta_{ridge}$ vs. angular distance from the PPS ridgeline for $0.0^\circ < \Delta\theta_{ridge} < 2.0^\circ$.

		“All”	“PPS”	“blue”	blue half	“red”	red half	“Spirals”
Complete Sample								
N Galaxies	E	938	803	164	345	193	362	175
	O	839	715	164	346	193	360	175
R_s	E	0.238	0.524	0.690	0.881	-0.524	-0.881	0.262
	O	0.333	0.183	0.667	0.786	-0.476	-0.786	-0.024
$P(R_s)$	E	0.570	0.333	0.058	0.004	0.183	0.004	0.531
	O	0.420	0.420	0.071	0.021	0.233	0.021	0.955
$\chi^2_\nu < 2.0$								
N Galaxies	E	723	609	140	265	152	265	123
	O	775	658	145	304	186	347	146
R_s	E	0.381	0.595	0.714	0.810	-0.524	-0.333	0.262
	O	0.690	0.643	0.762	0.881	-0.476	-0.690	0.429
$P(R_s)$	E	0.352	0.120	0.047	0.015	0.183	0.420	0.531
	O	0.058	0.086	0.028	0.004	0.233	0.058	0.289
Visually Inspected								
N Galaxies	E	649	561	116	220	150	264	84
	O	570	483	85	189	165	292	83
R_s	E	0.381	0.595	0.786	0.810	-0.333	-0.381	0.476
	O	-0.071	0.262	0.595	0.476	-0.619	-0.357	0.571
$P(R_s)$	E	0.352	0.120	0.021	0.015	0.419	0.352	0.233
	O	0.867	0.531	0.120	0.233	0.102	0.385	0.139

and “red” subsamples show the same anisotropic distributions as the complete sample. The “red” anistropies were recovered in the $\epsilon > 0.1$ subsample with $P(\Delta) < 0.005$ for the sinusoidal fits. The $\epsilon > 0.3$ sample typically had higher Kuiper probabilities of being isotropic, probably due to the 20% decrease in sample size.

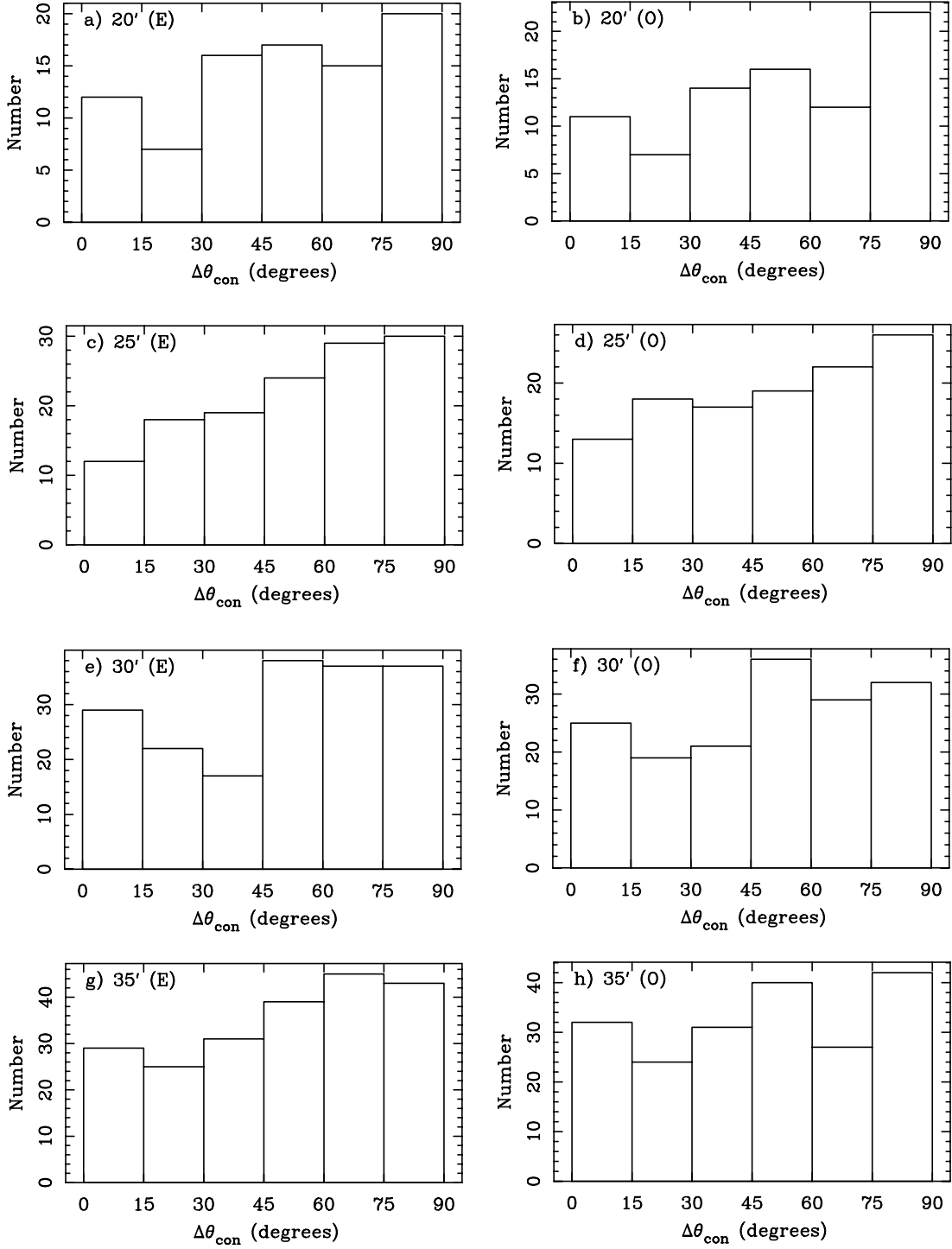


Figure 2.11: The distribution of $\Delta\theta_{con}$ for the reddest quartile E and O bandpass subsamples for percolation lengths of 20'–35'. Notice the anti-alignment of galaxies in GCs.

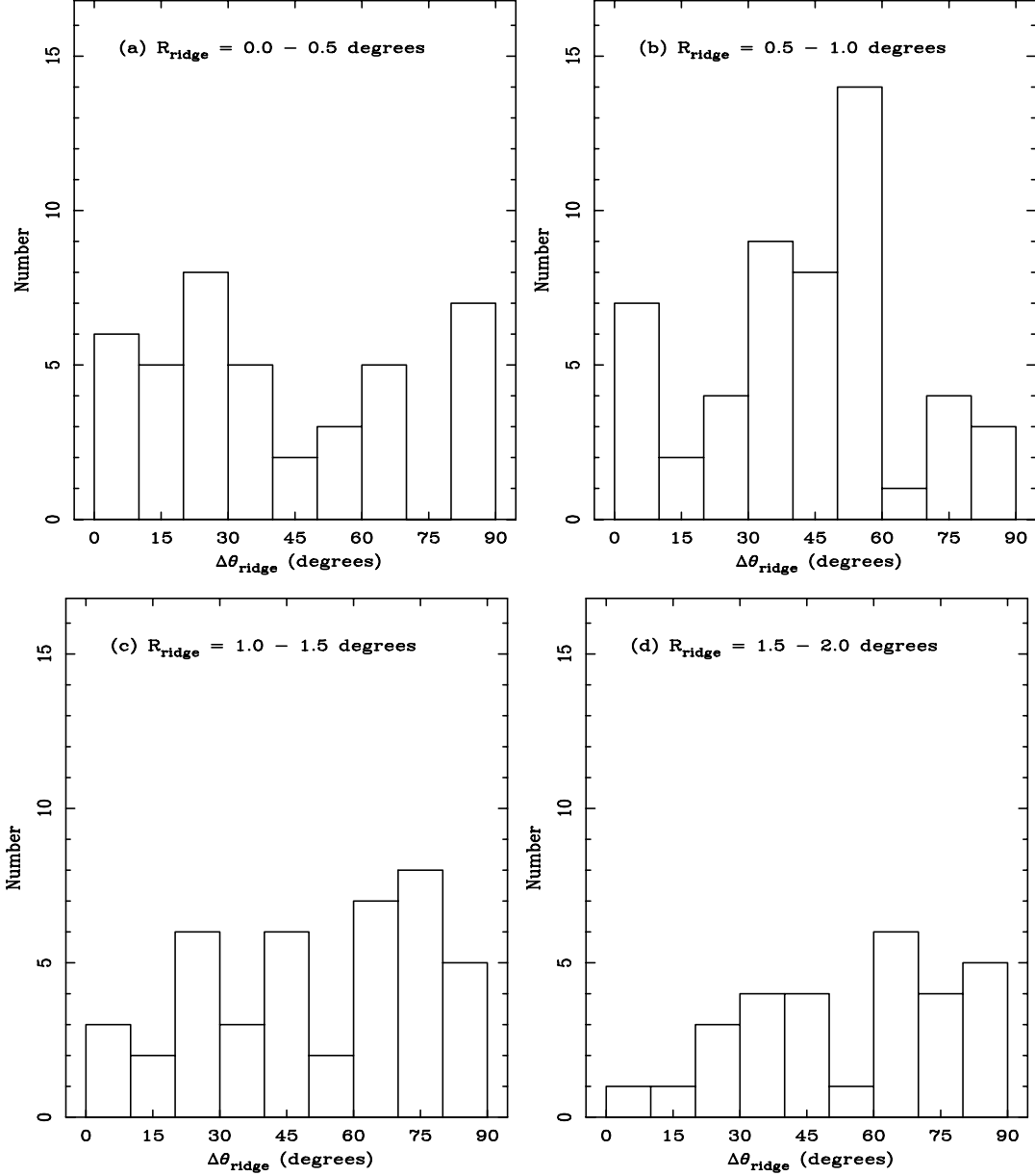


Figure 2.12: The $\Delta\theta_{\text{ridge}}$ distribution for “blue” O bandpass subsample galaxies (a) $0.0^\circ - 0.5^\circ$, (b) $0.5^\circ - 1.0^\circ$, (c) $1.0^\circ - 1.5^\circ$, and (d) $1.5^\circ - 2.0^\circ$ from the PPS ridgeline. The distributions for “blue” galaxies within 1° show a statistically significant anisotropic distribution. These figures indicate the possibility that the median $\Delta\theta_{\text{ridge}}$ changes systematically with distance from the PPS ridgeline.

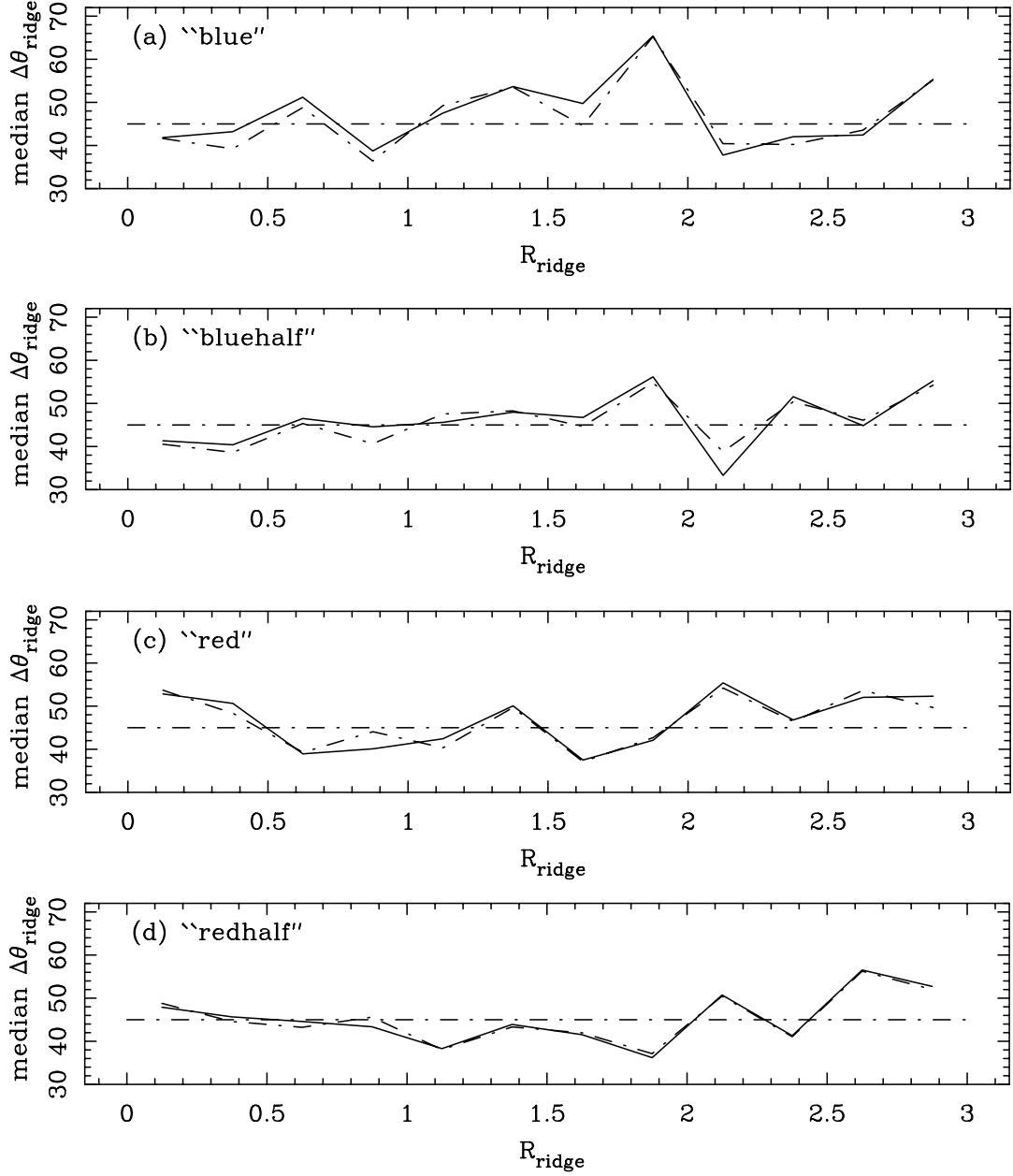


Figure 2.13: The median $\Delta\theta_{ridge}$ versus the distance from the PPS ridge for the (a) “blue” subsample, (b) the bluest half of the “PPS” subsample, (c) “red” subsample, and (d) the reddest half of the “PPS” subsample. Notice that the bluest and reddest halves of the “PPS” subsample show strong trends of $\Delta\theta_{ridge}$ with PPS ridgeline distance for distances of 0.0° to 2.0° . The dashed lines show the expected distribution if the MAPS-PP galaxies are oriented randomly with respect to the PPS ridgeline.

2.5.2 Comparison to Previous Work

Most of the previous studies in the PPS have used fairly small samples of galaxies in comparison to the 1388 E plate and 1230 O plate galaxies in this study. Only the sample of Dekel [1985] is comparable, although it was still less than 50% the size of the MAPS-PP. The MAPS-PP is also deeper than previous samples, assuring a more complete sample of the galaxies in the PPS, not just the brightest galaxies. As outlined in the Appendix, it has been demonstrated that the UGC (which has been used as either the source of the information or a seed catalog for most previous alignment work in the PPS) has a diameter-inclination bias, which leads to an artificially flat ellipticity distribution compared to a truly isophotal–diameter limited sample. The construction of a large sample of galaxies with non visually–determined parameters is one of the significant improvements which is achieved by using a large digital survey like the APS Catalog of the POSS I. Previously, only L94 used a non-visual method of determining galaxy position angles and ellipticities in the PPS. Laubscher used an iterative Fourier solution to the isophotal ellipticity at a series of isophotes, a single component method that will tend to round out the highly edge-on galaxies with high bulge to disk ratios. Use of a robust two–dimensional fit to the galaxy image has allowed the accurate determination of position angles and ellipticities for a wide variety of galaxy image profiles (see Figure 2.2), including face-on galaxies and edge-on galaxies with strong bulges for a very large sample of galaxies. The use of the Kuiper V statistic, instead of the χ^2 statistic, is another refinement in this study. This statistic is very robust, does not depend on binning the data, and is unaffected by a shift in the peak value of a given distribution. Our investigation of the MAPS-PP does not provide any additional support for the conclusions of either Strom & Strom [1978] or GTT that the PPS galaxies show global alignments. Our results do agree with L94 in that no global alignments were found. Furthermore, while it was not possible to directly compare the cluster-based alignments indicated by Strom and Strom (since the MAPS-PP did not include A424), an examination of GCs, both cumulatively, and singly for the GCs co-positional with A262 and the Pisces Cluster,

does not indicate any significant galaxy alignments relative to the supercluster ridge or GC axes. We find no significant galaxy major axis alignments with cluster radial lines in any subsamples, if we assume that GCs correspond to true clusters at percolation lengths of $25'$ to $35'$. This conflicts with the prediction of cluster radial alignments by Ciotti & Dutta [1994]. However, given that our GCs have surface densities indicating they are less dense than the clusters simulated by Ciotti & Dutta [1994], their cluster tidal fields are likely to be weaker, and the radial alignments are expected to not be as strong. A search for a possible bias affecting the GTT sample's position angle distribution has proven interesting. Position angle bias in the source catalog of the GTT, the CGCG, was eliminated as a possibility when an examination of its position angle distribution (using UGC position angles for all CGCG galaxies) showed it to be isotropic. A review of the 53 GTT galaxies (47 with GTT position angles) that overlap with the MAPS-PP shows that position angles in the two catalogs agree relatively well, with the relationship:

$$\theta_{GTT} = 1.01 (\pm 0.03) \theta_E + 0.17 (\pm 3.01) \quad (2.8)$$

$$\theta_{GTT} = 1.00 (\pm 0.02) \theta_O + 3.43 (\pm 2.40) \quad (2.9)$$

and measured dispersions of 8.52° and 7.30° compared respectively to the E and O band-pass data. This indicates that the GTT position angles are consistent with MAPS-PP values. Application of the Kuiper test to the GTT sample galaxies using MAPS-PP position angles and ellipticities for overlap galaxies indicates the sample has $P(V) = 0.031$ of being drawn from a randomly distributed sample. And while only 32 GTT galaxies with ellipticity greater 0.3 (the same ellipticity GTT used) overlap with the MAPS-PP, making a statistically significant determination of the anisotropy in the overlap difficult, the MAPS-PP data shows a flatter position angle distribution than GTT. After comparison of GTT with MAPS-PP, we attempted to construct a subsample of the MAPS-PP with similar properties to the GTT sample. Spatial, ellipticity, and magnitude cuts of $2^h 20^m > \alpha > 1^h 15^m$, $\epsilon < 0.3$, $E \leq 13.5$, and $O \leq 15.1$ were applied to the MAPS-PP to build a ‘‘GTT-like’’ subsample of 68 E and 123 O galaxies. This ‘‘GTT-like’’ sample was run through the standard battery of tests which identified a global position angle

distribution anisotropy in the 13 (14) “GTT-like” ellipticals, with $P(V) = 0.043$ in the E (O) bandpass. Further investigation applying the same morphological T-type, ellipticity, and magnitude (but not right ascension) cuts to “complete” MAPS-PP shows a position angle distribution anisotropy, albeit weaker than in the “GTT-like” subsample, with $P(V) = 0.036$ for 26 E galaxies and $P(V) = 0.028$ for 31 O galaxies. All three parameter cuts appear to be necessary to generate a subsample with this anisotropy. The position angle distribution, shown in Figure 2.14, indicates a preferred E-W orientation, and not the bimodal distribution reported by GTT. Our investigation therefore shows that although the alignment signal reported by GTT can not be dismissed, it can not be taken as clear evidence for global alignments. Our attempt to generate a subsample of the MAPS-PP with similar properties, however, has led to the identification of global alignments for bright, high ellipticity, ellipticals. The alignment is in an east-west direction indicating a general alignment with the supercluster ridge, although this cannot be confirmed statistically in the $\Delta\theta_{ridge}$ distributions, probably due to the small sample size. There also exists the possibility that the alignment of these bright ellipticals could be reflecting the general east-west alignment of their resident clusters, and therefore could represent an extension of the previously observed Binggeli effect in cDs to bright, ellipticals. This also cannot be statistically confirmed due to the low number of galaxies per GC observed. If the PPS is assumed to be observed edge-on, then angular distance from the PPS ridge is indicative of spatial distance from the PPS plane, and thus the observed median $\Delta\theta_{ridge}$ trend indicates that the angular momentum axes of “blue” galaxies tend to be anti-aligned with the PPS plane if near it and aligned with the PPS plane if far from it. An opposite effect is observed in the red half of the galaxies. These sort of position-dependent effects have been observed before by both KO92 and Godłowski [1994] in the local supercluster. KO92 observed the trend for angular momentum axes alignments with the plane for galaxies nearby the plane and anti-alignments for galaxies far from the plane. This same trend is seen in the reddest half of our sample. Godłowski [1994] reported similar results to KO92, but noted the signal was stronger

in the spiral galaxies in their sample. This increasing signal for spirals is the opposite of what is seen in this study. While both KO92 and Godłowski [1994] used redshifts to limit the volume of the sample, they also used galaxy catalogs which may exhibit the diameter-inclination effect we see in the UGC (see Appendix). This effect could result in a biased galaxy orientation distribution and may explain our discrepancy with their results.

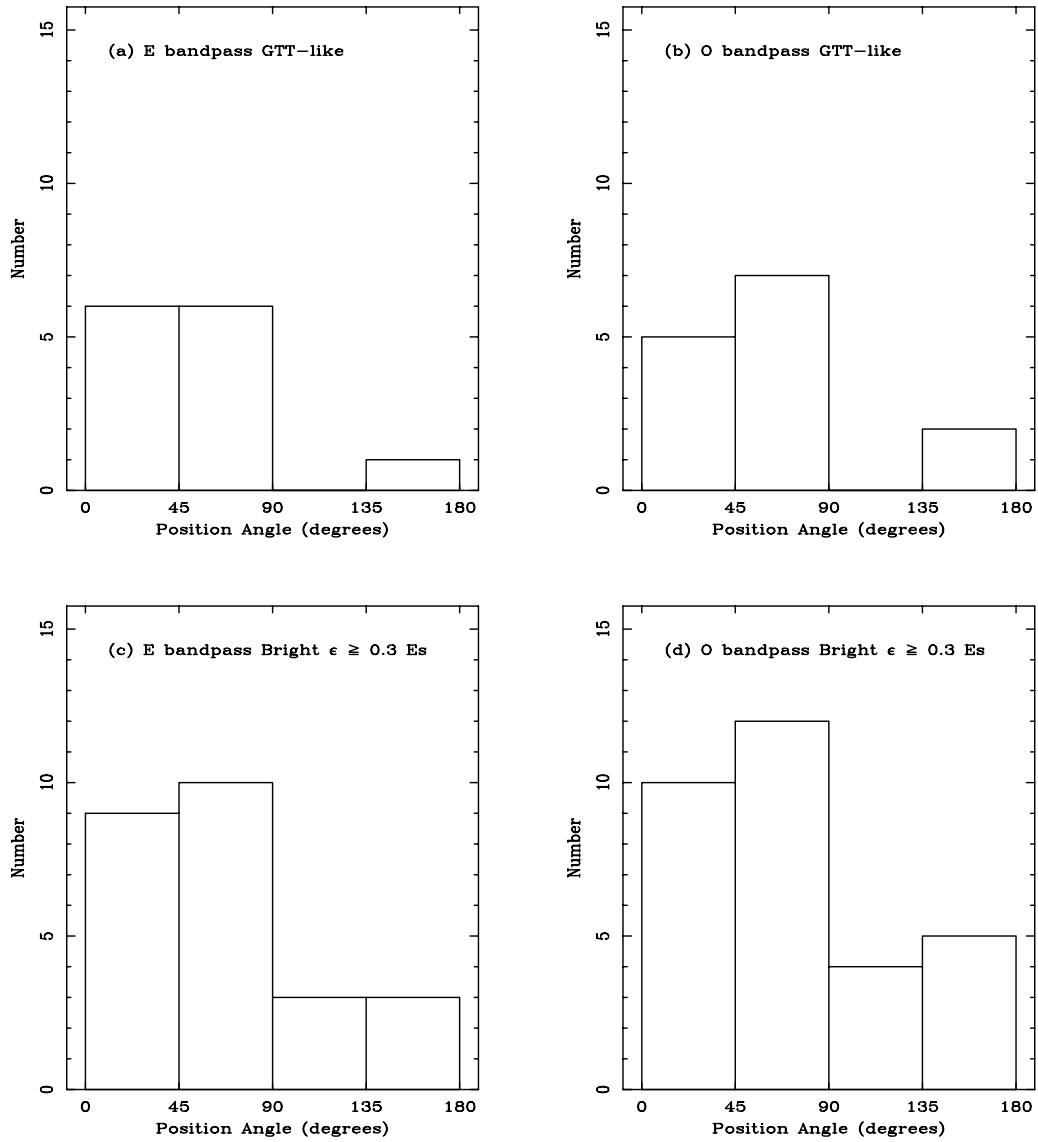


Figure 2.14: The distribution of position angles in the identified Ellipticals in the MAPS-PP designed to reproduce the ellipticity and magnitude cuts in the GTT sample, using the GTT spatial distribution ((a) and (b)) and the complete PPS ((c) and (d)).

2.6 Conclusions

Our search for galaxy alignments related to large-scale structure formation in the PPS is the most extensive to date, probing for a variety of possible forms of galaxy alignments over a large range of size scales in the complete MAPS-PP. Only after the application of color cuts were some possible preferred galaxy orientations observed. Using Monte-Carlo simulations of an anisotropic position angle distribution in the form of equation (2.7), the probability that $P(V) < 0.05$ for a variety of sample sizes and Δ values can be modeled. Modeling of the $P(V)$ distributions includes the assumption that 20% of galaxies are randomly oriented, representing the predicted fraction of non-PPS galaxies in our “PPS” subsamples. These simulations allow estimation of the level of global galaxy alignments that could remain undetected with the Kuiper V statistic. Since the “PPS” subsamples of over 1100 galaxies across the PPS do not show an anisotropic position angle distribution, it can be stated with 95% confidence that the limits on the sinusoidal amplitude, Δ , must be less than 0.23 for any undetected position angle distribution anisotropy in MAPS-PP. The largest previous effort in the PPS, the work of Dekel [1985], has only half as many galaxies, meaning that even using the more robust Kuiper V statistic, an anisotropy as large as $\Delta < 0.33$ could remain undetected at the 95% confidence level. This assumes the same non-PPS contamination as in MAPS-PP. Therefore, this study has established a significantly more sensitive bound on the level of global position angle anisotropy that could be present in the PPS. In principle a sinusoidal fit to the position angle distribution *a la* Hawley & Peebles [1975] is a more sensitive test if alignments of this type are reflected in nature. Our limit on global sinusoidal alignments in the PPS from the full sample using equation 2.7 is $\Delta < 0.10$ at 95% confidence. We note however that fitting equation 2.7 led to no new types of strong anisotropies being recovered which were not found using the Kuiper statistic. The observed anisotropies in the position angle distribution of MAPS-PP galaxies all occur in the higher density regions of the PPS. This indicates the alignments are likely to have been produced relatively recently and are not primordial in nature. The percolation scales at which significant anti-alignments

were observed correspond to physical lengths of 290–436 h^{-1} kpc and mean surface densities of 11.5–15.8 galaxies/ \square° . This suggests that redder (mostly elliptical) galaxies are preferentially anti-aligned to the local environment (possibly clusters). This is not an extension of the Binggeli effect – the observation that cDs tend to be aligned with their parent clusters – to galaxies other than cDs, since the observed alignments are perpendicular to those observed in the Binggeli effect [Binggeli 1982]. If interpreted as anti-alignments of ellipticals to local large-scale structure, these observations directly conflict with the results of Lambas, Groth, & Peebles [1988a]. We can not explain this contradiction, although we note that Lambas, Groth, & Peebles [1988a] compared Lick galaxy counts in various directions relative to individual UGC elliptical position angles, a very different methodology to our own. Our observations could instead be interpreted as a preference for ellipticals to be oriented perpendicular to the supercluster plane since most of the GCs are oriented parallel to the PPS ridge. However, no such signature is observed in the distribution of $\Delta\theta_{ridge}$, which would point to alignments relative to the PPS ridge. The statistical significance of our detection of galaxy alignments is not overwhelming – a situation also faced by previous studies. The conflicting results between this study and previous work may be simply an indication that with enough searching, some subsample with a significant anisotropy is bound to be found. However, we have attempted to address this issue by using non-isolated signals which are reproduced for similar subsets, and which have been compared against random distributions analyzed with the same software. In this manner, we investigate only those signals which have the highest likelihood of being real and not simply the result of a statistical fluke. No simple galaxy alignment mechanism can explain the observed anisotropies in the position angle distributions of these subsamples. One can imagine a mixture of primordial and modern alignment mechanisms working in concert to produce the shift of the median $\Delta\theta_{ridge}$ with increasing distance from the PPS plane, but the fact that the reddest and bluest halves of the MAPS-PP “PPS” sample show opposite trends indicates that morphological type could affect the alignment mechanism present. All in all, no simple

large-scale structure formation scenario can explain all of the observed trends in galaxy position angle distributions in the PPS.

2.7 Future Directions

We would have preferred to use ellipticity to infer galaxy inclinations, however this was not possible. Due to the presence of the Holmberg effect, the expected ellipticity distribution of a randomly oriented sample of galaxies is not well understood. Because of this problem, any diameter-limited or magnitude-limited sample (including the MAPS-PP) is not optimally designed for examination of the problem of galaxy alignments. An ideal sample, which would not risk the introduction of inclination selection effects, would be a true volume-limited sample of galaxies with accurately determined orientations. In the absence of such a volume-limited sample, one needs to either model the ellipticity distribution of an isophotal-diameter limited galaxy sample in the case of random orientations or one needs a comparison field sample. Both of these solutions are outside the scope of this paper, but should be considered in future work. Also, most previous searches for galaxy alignments assume that the galaxy’s orientation on the sky provides enough information about the orientation of its dynamical axes in space, but in fact a given position angle and ellipticity for a galaxy has a four-fold degenerate solution for the galactic angular momentum axis. The only way to completely remove this degeneracy in angular momentum axis direction is to determine which side of the major axis is moving toward the observer (using rotation curves obtained spectroscopically) and whether the north or south side is closer (usually determined by assuming trailing spiral arms, see Sugai & Iye [1995] for example). Recent work with completely determined angular momentum axes for 60 galaxies in the “Ursa Major filament” by Han, Gould & Sackett [1995] found no evidence of alignments, although their small sample size imposes only a weak limit on the strength of any signal. Finally, if one wishes to properly determine the angular momentum distribution of galaxies relative to one another, redshift information is also required so that a full three-dimensional distribution of galaxies (ignoring peculiar

velocities) can be determined. Muriel & Lambas [1992] performed such an analysis using the projected orientations of ESO galaxies on the sky in conjunction with redshift information. They found spiral galaxies tended to be oriented toward their nearest neighbors, an effect they did not observe in projection. They also note that the previously observed alignment (Lambas, Groth, & Peebles 1988a) of the projected orientations of ellipticals with the galaxy distribution around them is confirmed using their sample with redshifts.

2.8 Acknowledgments

We would like to thank Bryan Laubscher, Stéphane Courteau, Martha Haynes, Riccardo Giovanelli, and Shoko Sakai for providing us their redshift and photometric data in electronic form and the referee, G. Djorgovski, for his helpful suggestions. We also thank Roberta Humphreys, Steve Odewahn, Peter Thurmes, and Chris Cournelle for their support and assistance, Elizabeth March for her assistance in examining fits to the images used in this database, and the Mentor Connection of Intermediate District 287 (Plymouth, MN) for giving her the opportunity to work with us. JEC also thanks Jeff Larsen in particular for many fruitful discussions about data reduction and for his comments on early drafts of this paper. This research has made use of the APS Catalog of the POSS I, which is supported by the National Science Foundation, the National Aeronautics and Space Administration, and the University of Minnesota. The APS databases can be accessed at <http://aps.umn.edu/> on the World Wide Web.

2.9 Appendix: Understanding the Ellipticity Distribution

As noted in section 2.3.2, an early examination of the MAPS-PP revealed a complicated ellipticity distribution, marked by an excess of high ellipticity galaxies (c.f. Figure 2.6). This is unlike the ellipticity distribution of the UGC, which is flat for $\epsilon < 0.8$. Further investigation showed that a similar ellipticity distribution was present in the data

from the APM galaxy survey [Maddox *et al.* 1990] using the same major-axis diameter cutoff criteria. This indicates that the ellipticity distribution observed in our sample is unlikely to have been caused by either the hardware or the reduction software. The most likely source for the observed ellipticity distribution is the existence of the Holmberg effect in combination with the use of a roughly isophotal major-axis cut. Huizinga [1994] notes that most current studies of the optical depths of spiral galaxies suggest the outer parts of spirals are optically thin, although the inner parts may be optically thick. Since the isodensity diameter cutoff is at an isophote corresponding to the outer, optically thin parts of a galaxy, this diameter should increase with increasing inclination. This means that MAPS-PP galaxies with larger inclinations can satisfy the diameter cutoff out to greater distances, resulting in their being overrepresented in proportion to their limiting volume. The PPS is by definition a volume-limited structure, so the surplus of high-ellipticity galaxies seen in the MAPS-PP is probably due to the enhanced detection volume for such galaxies which are background to the PPS. The UGC is a field sample and should have an even larger excess of high-ellipticity galaxies, but this is not seen in the UGC. Huizinga noted that in the ESO-Uppsala catalog, the visual diameter cutoff exhibited bias in which face-on galaxies were seen to have larger visual diameters, an effect Huizinga named the “diameter-inclination” effect. This diameter-inclination effect counters the expected effect of a roughly isophotal diameter limit and leads to an almost flat sample of ellipticities in the ESO-Uppsala. Huizinga states that such a bias in visual diameters could explain the flat ellipticity distribution seen in UGC ellipticities. A comparison of the ratio of MAPS-PP major-axis diameters and UGC major-axis diameters to the MAPS-PP ellipticity for matched galaxies shows this ratio is dependent on ellipticity (See Figure 2.15a). A linear fit to this distribution gives

$$D_E/D_{UGCE} = 0.287 (\pm 0.030) \epsilon_E + 0.580 (\pm 0.016) \quad (2.10)$$

$$D_O/D_{UGCO} = 0.265 (\pm 0.029) \epsilon_O + 0.569 (\pm 0.016) \quad (2.11)$$

This diameter ratio dependence on ellipticity indicates that Huizinga’s diameter-inclination bias is probably present in the UGC as well. It indicates that low-ellipticity (face-on)

galaxies in the UGC have their visual diameters systematically overestimated by 40% relative to the visual diameters of the edge-on galaxies with the same isophotal diameter. Courteau noted this same trend in the UGC. Giovanelli *et al.* [1994] also investigated this effect and quantified it. A comparison of the MAPS-PP to their results indicates that the same trends of isophotal to UGC diameter ratio versus axial ratio are seen in both datasets. Giovanelli *et al.* [1994] noted that it was previously assumed that diameter-limited catalogs such as the UGC and ESO-Uppsala did not show any biases due to a lack of the Holmberg effect [Holmberg 1975]. However, they show that it is instead the counterbalancing effect of the diameter-inclination effect that comes into play, creating a catalog with little dependence of photometric properties on inclination. Any future searches for 3-D galaxy alignments must be aware of these effects in the UGC sample before attempting to use its ellipticities to determine galaxy inclination distributions. Furthermore, care must be taken not to use catalogs based (even partly) on the UGC for inclination studies. For example, the RC3, which includes the entire UGC, shows the same trend of APS to RC3 major-diameter ratio versus MAPS-PP ellipticity (See Figure 2.15b). The best fits of this diameter ratio to MAPS-PP ellipticity are

$$D_E/D_{RC3E} = 0.262 (\pm 0.031) \epsilon_E + 0.431 (\pm 0.016) \quad (2.12)$$

$$D_O/D_{RC3O} = 0.262 (\pm 0.030) \epsilon_O + 0.452 (\pm 0.016) \quad (2.13)$$

similar to the case with the UGC. This is probably due in part to the use of UGC diameters in the RC3 in cases when no newer diameters were available. This points to the need for galaxy catalogs built independent of the UGC and other catalogs with visually determined parameters in order to avoid introduction of its selection effects. The MAPS-PP was built using analysis of machine-reproducible digital images and thus its parameters are not susceptible to the same diameter-inclination effect as the UGC.

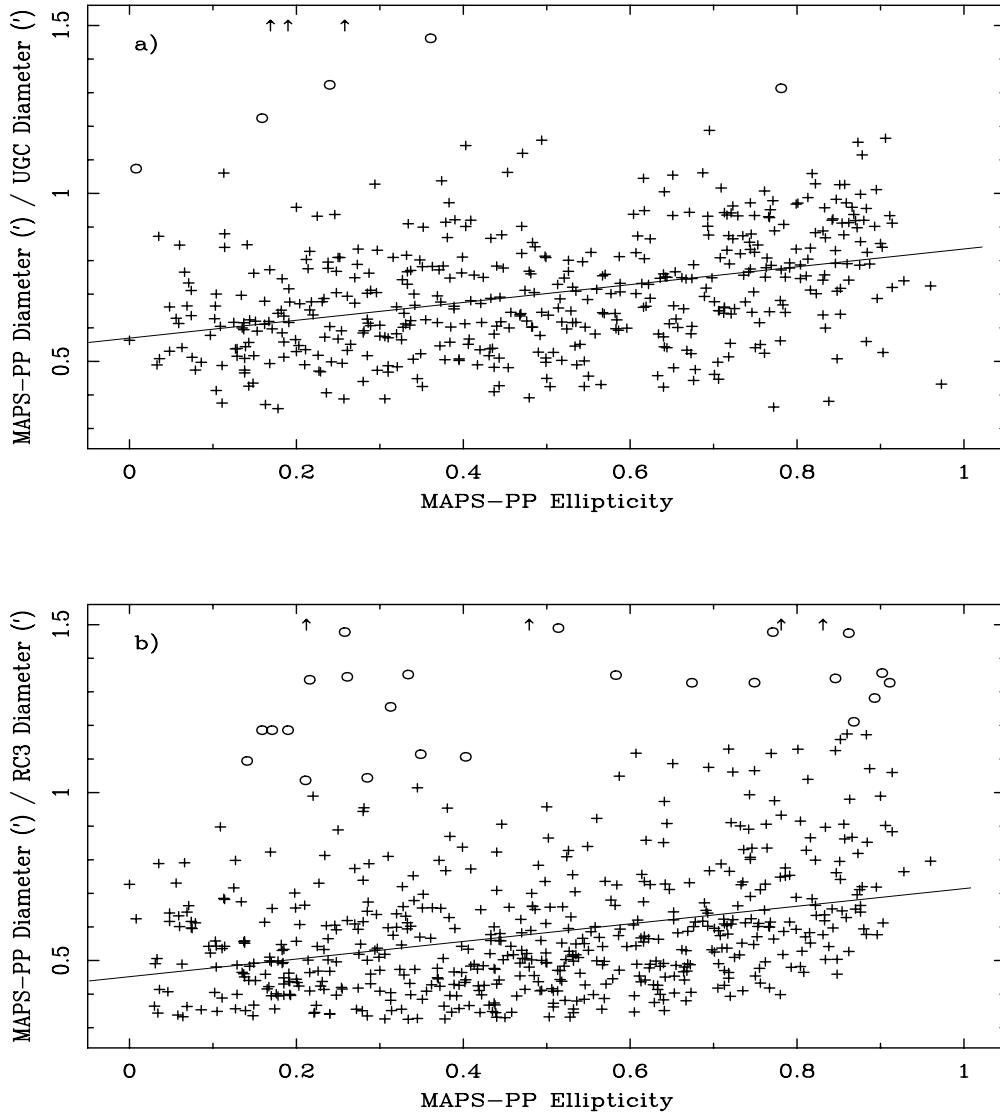


Figure 2.15: MAPS-PP O bandpass data versus (a) the UGC and (b) the RC3. The solid line illustrates a linear fit to this data; some points (marked as circles or arrows) were rejected using an iterative fitting process. Although a linear relation is not an especially good description of the data, the correlation is quite significant and demonstrates that both the UGC and RC3 suffer from a diameter-inclination effect.

Chapter 3

Determination of Galaxy Spin Vectors in the Pisces-Perseus Supercluster with the Arecibo Telescope

Originally published in Cabanela, J.E. and Dickey, J.M. 1999, AJ, 118, 46.

Abstract: We use $H\text{I}$ observations made with the upgraded Arecibo 305M Telescope in August 1998 to obtain accurate spin vector determinations for 54 nearly edge-on galaxies in the Minnesota Automated Plate Scanner Pisces-Perseus Survey (MAPS-PP). We introduce a simple observational technique of determining the sense of rotation for galaxies, even when their $H\text{I}$ disks are not fully resolved. We examined the spin vector distribution of these 54 galaxies for evidence of preferential galaxy alignments. We use the Kuiper statistic, a variant of the Kolmogorov–Smirnov statistic, to determine the significance of any anisotropies in the distribution of galaxy spin vectors. The possibility of “spin vector domains” is also investigated. We find no significant evidence of preferential galaxy alignments in this sample. However, we show that the small sample size places weak limits on the level of galaxy alignments.

3.1 Introduction

The search for galaxy alignments has a long history, beginning with searches for alignments in “Spiral and Elliptical Nebulae” during the late 19th Century. Recent scrutiny of the problem has been motivated by the understanding that establishing the level of galaxy spin vector (\vec{L}) alignments could offer an additional constraint on various theories of galaxy formation and evolution. For example, “top-down” scenarios of Large-Scale Structure formation can lead to ordered distributions of angular momentum on cluster and supercluster scales through a variety of mechanisms [Zel’dovich 1970, Doroshkevich & Shandarin 1978, White 1984, Colberg, White, Jenkins, & Pearce 1998]. In addition to galaxy \vec{L} alignments resulting from various formation mechanisms, galaxy \vec{L} alignments may also be the evolutionary result of anisotropic merger histories [West 1994], galaxy-galaxy interactions [Sofue 1992], or strong gravitational gradients [Ciotti and Dutta 1994, Ciotti and Giampieri 1998]. For a summary of the history of the field, see Djorgovski [1987] and Cabanela & Aldering [1998] (hereafter Paper I). Observational support exists for some forms of galaxy \vec{L} alignments with surrounding large-scale structure. For example, Binggeli [1982] discovered that the major axes of cD galaxies tended to be aligned with the axes of their parent cluster. However, most previous searches for galaxy alignments have had results that one could describe as negative or statistically significant but not strongly so. One complication in earlier efforts has been that most have not truly determined \vec{L} , but rather simply used the position angle (and sometimes ellipticity) of the galaxies in an attempt to determine the possible distribution of \vec{L} . However, for each combination of galaxy position angle and ellipticity, there are four solutions for the true orientation of the galactic angular momentum axis (\vec{L}). This degeneracy in \vec{L} can only be removed by establishing both which side of the major axis is moving toward the observer and whether we are viewing the north or south side of the galaxy, where “north” is in the direction the galaxy angular momentum vector. Therefore previous studies have either restricted themselves to using only position angles of galaxies, or they have often taken all four possible solutions of \vec{L} with equal weight [Flin 1988, Kashikawa and

Okamura 1992]. Several studies have been published regarding searches for alignments using completely determined galaxy angular momentum axes. Helou & Salpeter [1982] used HI and optical observations of 20 galaxies in the Virgo cluster to show that no very strong \vec{L} alignments exist. However, a followup to this study by Helou [1984] found evidence for anti-alignments of spin vectors for binary pairs of galaxies in a sample of 31 such pairs. Hoffman *et al.* [1989] briefly investigated the possibility of galaxy alignments by plotting up the \vec{L} orientations for ~ 85 galaxies with fully determined spin vectors from their Virgo cluster sample and found no obvious alignments. Most recently, Han, Gould & Sackett [1995] used a sample of 60 galaxies from the Third Reference Catalogue of Bright Galaxies (de Vaucouleurs *et al.* [1991], hereafter referred to as the RC3) in the “Ursa Major filament” and found no evidence of galaxy alignments. There are several criticisms one can level against these earlier studies. All the studies attempted to use relatively small samples to map out orientation preferences over the entire sky. Thus only very strong \vec{L} alignment signatures could have been discovered via this method. The samples were selected using source catalogs with “visual” criteria which may have led to a biased sample. For example, as noted in Paper I, the source catalog for the “Ursa Major filament” study, the RC3, suffers from the “diameter-inclination effect,” which leads to a strong bias for preferentially including face-on galaxies over edge-on galaxies of the same diameter [Huizinga 1994]. Finally, no attempt was made to consider the positions of the galaxies within the local large-scale structure before looking for alignments. Considering that the local mass density is critical for determining which alignment mechanism may be dominant, an attempt should be made to look for \vec{L} alignments relative to local large-scale structures. This study is an attempt to avoid some of the issues cited above and obtain a sample of galaxies with well determined \vec{L} in various environments in a supercluster using a mechanically-selected sample of galaxies. For this study, we selected a subsample of the Minnesota Automated Plate Scanner Pisces-Perseus galaxy catalog (hereafter MAPS-PP), which is a true major-axis diameter-limited catalog built using automated, mechanical methods and does not exhibit the “diameter-inclination”

effect (see Paper I). We determined the \vec{L} orientation for the galaxies in this subsample using HI observations. The sample selection criteria are outlined in Section 3.2. The analysis methods are discussed in Section 3.3. Section 3.4 discusses the results of the data analysis. Our interpretation of these results is provided in Section 3.5.

3.2 Data

The galaxy sample for this study was selected from the MAPS-PP. The MAPS-PP catalog was designed to avoid several of the pitfalls of previous attempts to measure galaxy orientations. The MAPS-PP contains ~ 1400 galaxies in the Pisces-Perseus Supercluster field with (roughly) isophotal diameter $>30''$ constructed from digitized scans of the blue and red plates of the Palomar Observatory Sky Survey (POSS I). By using a mechanical measure of the diameter, this catalog avoids the “diameter-inclination” effect seen in both the Uppsala General Catalog [Nilson 1973, hereafter UGC] and the RC3. The MAPS-PP also uses a two-dimensional, two-component fit of the galaxy light profile in order to obtain a more accurate position angle and ellipticity measurement for the component of the galaxy with most of the angular momentum (e.g. - the disk in spirals). Such a full two-dimensional fit has been shown [Byun and Freeman 1995] to be very effective at recovering the image parameters in situations where a simple ellipse fit fails (e.g. - edge-on spirals with a large bulge). More details as to the construction of the MAPS-PP are available in Paper I.

3.2.1 Selection Criteria

For this study, we selected a subsample of the MAPS-PP that could have their \vec{L} determined through HI observations and at the same time could probe the galaxy \vec{L} orientations relative to the large-scale structure of the Pisces-Perseus Supercluster (hereafter PPS). HI observations can determine which side of the major-axis is approaching us, reducing the four-fold degeneracy in the \vec{L} to two solutions. However, because of the great distance to the PPS ($cz \approx 5500 \text{ km s}^{-1}$), the POSS I images don’t generally

have enough detail to make out spiral arm structure, so determining if we were viewing the north or south side of a galaxy would be difficult without re-imaging the galaxies. Instead, we choose to constrain the inclinations of the galaxies in our subsample to be edge-on. This means we effectively reduce the two-fold degeneracy in \vec{L} solution to a single solution and simultaneously we reduce the galaxy alignments analysis problem from a full three-dimensional problem to a much simpler one-dimensional problem. And because the PPS plane itself is viewed very close to edge-on [Giovanelli & Haynes 1988], we are simplifying the problem without losing the ability to probe the angular momentum distribution in relationship to the PPS plane. The primary requirement for including a MAPS-PP galaxy in this study was therefore an ellipticity greater than 0.66. Other criteria for selecting a MAPS-PP galaxy for our HI program were based on observational considerations. To ensure the galaxy could be observed from Arecibo, the Declination was required to be less than 36° . An O (blue) major-axis diameter between $44''$ and $100''$ was needed so that the HI disk of the galaxy was not too small to be targeted on both sides by the Arecibo beam and not too large to be fully sampled. The galaxy was required to be within 2.25° of the PPS midplane (as determined in Paper I) and if the redshift was known, it needed to be between $3500 - 7000 \text{ km s}^{-1}$ in order to increase the chances it was a true PPS member. Finally to reduce the sample size, we selected galaxies with O magnitude brighter than 17. This MAPS-PP subsample consisted of 105 galaxies. The MAPS-PP subsample was cross-identified with the NASA/IPAC Extragalactic Database (NED) in order to obtain previous radio flux measurements and redshifts.¹ We also examined the field around each subsample galaxy and eliminated those in crowded fields, which led to a final MAPS-PP subsample of 96 galaxies (which will hereafter be referred to as the Arecibo sample), listed in Table 3.1.

¹The NASA/IPAC Extragalactic Database (NED) is operated by the Jet Propulsion Laboratory, California Institute of Technology, under contract with the National Aeronautics and Space Administration.

Table 3.1: The Arecibo Sample (A subset of 96 MAPS-PP galaxies)

APS ID	Common Name ¹	α (B1950)	δ (B1950)	m_O ²	$O - E$ ²	a_O ²	R_{ridge} ³ ($^{\circ}$)	Σ ³
O_778_873376	UGC 11993	22:18:25.5	34:58:14.8	15.67	1.49	61.7	0.89	5.60
O_778_731211	22208+3548	22:20:49.5	35:48:04.8	14.66	1.42	52.0	0.25	25.35
O_778_700353	22233+3556	22:23:19.2	35:55:31.0	15.32	1.52	57.4	0.58	10.40
O_778_847676	None	22:24:45.4	35:10:40.3	15.41	1.39	44.0	0.27	11.23
O_778_849054	None	22:25:53.3	35:04:31.8	15.39	1.66	46.7	0.12	9.07
O_778_1040599	NGC 7320B	22:35:10.3	33:39:46.9	15.54	1.47	49.2	0.34	7.17
O_778_923367	None	22:39:36.3	34:39:30.7	14.03	1.39	94.8	1.12	6.39
O_778_755586	None	22:41:32.8	35:38:55.2	15.39	1.52	52.1	2.19	3.20
O_1184_28270	None	22:50:24.2	33:07:53.6	16.26	1.64	44.3	0.86	3.11
O_1184_66567	22508+3230	22:50:47.0	32:29:50.0	14.99	1.44	49.5	0.32	11.28
O_1184_128370	UGC 12231	22:51:11.0	31:21:11.7	14.84	-0.35	62.4	0.84	10.07
O_1184_81567	None	22:55:40.5	32:11:55.6	15.90	1.34	49.2	0.12	6.26
O_1184_196807	UGC 12320	22:59:40.4	30:29:42.0	15.83	1.45	66.8	1.50	6.00
O_1184_121956	UGC 12362	23:03:51.4	31:36:49.0	14.44	1.00	67.4	0.17	2.27
O_1184_275037	MCG +05-54-039	23:07:04.4	29:12:43.0	15.38	1.16	53.0	1.43	2.35
O_1184_313727	UGC 12427	23:10:57.6	28:40:55.9	14.94	0.19	49.4	0.97	5.94
O_1184_347214	None	23:12:38.9	28:00:36.0	15.60	0.46	52.7	0.99	6.24
O_1184_189398	UGC 12458	23:12:43.0	30:40:27.0	16.22	1.51	59.9	0.52	6.82
O_843_144830	None	23:18:38.9	25:22:01.9	15.86	1.50	44.0	2.07	4.80
O_843_65466	None	23:18:59.9	26:12:15.6	15.95	0.96	44.9	1.31	4.95
O_914_404205	UGC 12557	23:20:01.1	28:54:24.1	14.72	1.49	75.0	0.86	5.05
O_914_406137	None	23:23:49.0	28:58:48.0	16.70	1.46	44.8	1.60	5.66
O_914_344933	UGC 12625	23:26:38.5	29:29:58.3	14.73	1.57	84.2	1.72	4.36
O_914_409641	UGC 12644	23:28:58.8	28:54:47.7	14.86	0.56	59.1	0.95	3.69
O_914_371708	None	23:32:07.5	29:26:30.5	16.45	1.45	48.7	0.89	3.28
O_914_413061	None	23:32:17.4	29:02:11.2	16.07	1.47	45.5	0.59	3.05
O_914_511814	None	23:33:55.7	27:39:32.0	16.07	1.24	55.7	0.72	3.32
O_914_416774	UGC 12730	23:38:03.3	28:54:39.3	14.29	1.56	98.6	0.32	2.84
O_914_286281	UGC 12741	23:39:25.1	30:18:15.5	14.54	0.94	57.3	0.74	1.49
O_914_286479	None	23:39:59.4	30:19:12.6	15.63	0.68	44.0	0.72	1.50
O_914_514191	None	23:40:00.1	27:46:03.4	16.26	1.17	52.8	1.53	6.24
O_914_437214	CGCG 498-006	23:42:35.0	28:47:11.1	15.55	1.38	46.1	0.93	4.75
O_1257_181710	MCG +05-01-003	23:52:48.7	30:06:24.8	15.11	1.51	54.2	0.27	3.38
O_1257_106449	UGC 12845	23:53:09.1	31:37:15.8	15.11	1.99	52.4	1.25	2.20
O_1257_149828	UGC 12864	23:54:50.8	30:42:49.4	14.49	1.11	85.0	0.34	3.85
O_1257_140283	NGC 7799	23:56:46.8	31:00:22.1	15.96	1.19	66.9	0.64	2.90
O_1257_307025	UGC 124	00:10:48.1	28:05:27.8	15.45	1.85	55.1	2.12	5.95
O_1257_224112	UGC 147	00:13:07.5	29:23:21.2	15.39	1.83	45.6	0.79	7.56
O_1257_212633	00139+2939	00:13:52.2	29:38:45.5	15.37	0.78	67.6	0.53	18.31
O_1244_265500	UGC 238	00:22:25.5	31:03:58.5	13.70	1.15	99.0	0.99	3.82

¹The common name of the object was determined via cross-identification of APS position with the NASA/IPAC Extragalactic Database (NED).

²The O bandpass magnitude (m_O), $O - E$ color, and O bandpass major-axis diameter (a_O) were all obtained from the APS catalog. The m_O and $O - E$ are zeropointed on a plate-by-plate basis as outlined in Cabanela & Aldering [1998].

³The distance from the Pisces-Perseus ridgeline (R_{ridge}) and local surface density (Σ) are from Cabanela & Aldering [1998]. Σ is in units of galaxies/ \square° .

APS ID	Common Name ¹	α (B1950)	δ (B1950)	m_O^2	$O - E^2$	a_O^2	R_{ridge}^3 ($^\circ$)	Σ^3
O_1244_376417	00254+3029	00:25:21.3	30:29:18.9	15.20	1.34	55.9	0.48	5.08
O_1244_340721	UGC 279	00:25:36.7	30:31:37.5	13.90	1.09	92.3	0.51	4.61
O_1244_270335	00267+3106	00:26:45.2	31:06:17.2	15.57	1.07	83.8	1.12	6.73
O_1244_679996	UGC 310	00:28:39.0	28:42:58.5	14.84	0.62	68.2	1.23	2.29
O_1244_578706	None	00:29:14.4	29:25:41.8	15.88	0.74	45.7	0.54	3.48
O_1244_241809	00313+3110	00:31:15.4	31:10:30.6	15.40	0.00	55.4	1.30	4.67
O_1244_767827	UGC 345	00:32:09.7	28:08:02.5	15.22	0.09	76.1	1.75	1.76
O_1244_185805	00333+3136	00:33:15.9	31:35:41.4	14.23	1.24	68.0	1.75	3.54
O_1244_655424	00347+2853	00:34:41.6	28:52:27.1	14.85	0.84	98.4	0.95	7.96
O_1244_554203	UGC 412	00:36:49.5	29:29:16.8	15.25	1.29	55.9	0.34	10.90
O_1244_595079	UGC 449	00:39:41.7	29:25:26.2	14.96	0.93	63.5	0.40	7.98
O_1244_521380	None	00:40:48.3	29:46:45.6	15.32	0.75	51.2	0.04	12.24
O_1244_442897	None	00:41:53.2	30:04:51.5	16.59	0.50	47.1	0.42	11.42
O_1244_484644	UGC 478	00:43:44.5	29:57:54.9	14.45	1.13	80.4	0.17	13.26
O_601_2598615	UGC 501	00:46:21.1	27:56:44.1	15.47	1.55	91.9	1.95	2.21
O_601_927741	UGC 511	00:47:27.3	31:27:32.8	15.46	0.96	69.8	1.47	5.16
O_601_2448395	CGCG 501-024	00:48:09.5	28:25:40.3	15.69	1.19	44.6	1.50	4.85
O_601_1985337	UGC 525	00:48:52.4	29:26:42.9	15.69	1.42	73.9	0.64	4.96
O_601_1986315	00494+2924	00:49:30.1	29:24:19.4	14.42	1.67	60.4	0.66	6.53
O_601_2601958	None	00:50:49.0	28:00:21.8	16.80	1.60	53.5	2.08	3.56
O_601_1152906	UGC 557	00:52:03.8	31:05:40.0	14.56	0.73	59.5	0.76	20.54
O_601_2454111	UGC 554	00:52:04.6	28:26:44.9	15.22	1.79	50.9	1.71	5.65
O_601_2363374	00521+2835	00:52:06.5	28:35:46.1	14.78	1.79	58.7	1.57	4.48
O_601_1044227	UGC 565	00:52:38.6	31:24:14.1	15.13	0.98	48.1	0.92	13.23
O_601_1267760	CGCG 501-048	00:53:26.0	30:48:15.4	15.38	1.21	55.5	0.47	9.02
O_601_1050939	UGC 598	00:55:06.2	31:12:52.1	14.19	1.44	71.3	0.49	6.20
O_601_1498038	UGC 624	00:57:52.7	30:23:58.1	13.00	0.96	99.9	0.60	6.63
O_601_1063679	UGC 633	00:58:37.0	31:14:23.6	14.16	0.95	90.7	0.01	6.20
O_601_863271	None	01:00:55.7	31:46:46.0	15.29	1.04	60.7	0.15	8.98
O_601_1294945	01011+3056	01:01:04.3	30:55:47.2	15.71	1.11	57.4	0.61	4.65
O_601_978154	UGC 669	01:02:34.0	31:24:52.0	15.19	1.32	72.1	0.39	6.37
O_601_1197694	UGC 673	01:03:24.6	31:08:18.2	15.15	0.81	57.1	0.72	4.65
O_601_657010	UGC 679	01:04:17.9	32:07:21.1	16.17	0.63	51.3	0.10	22.35
O_601_992015	CGCG 501-092	01:05:17.4	31:24:29.8	15.25	1.34	45.1	0.80	9.63
O_601_175820	A82-91	01:05:18.4	33:11:11.4	14.49	1.25	57.8	0.82	17.03
O_601_264028	NGC 407	01:07:49.8	32:51:38.8	14.09	1.44	96.5	0.34	18.31
O_601_359427	None	01:07:57.9	32:45:57.2	16.27	0.63	47.3	0.25	19.90
O_406_436424	01104+3443	01:10:24.4	34:42:01.4	16.52	0.66	49.0	1.94	2.14
O_406_502375	UGC 809	01:13:04.0	33:32:50.3	14.84	0.74	74.2	0.68	2.66
O_1189_285025	None	01:19:39.9	33:46:42.9	15.99	0.83	45.8	0.69	8.12
O_1189_293769	NGC 512	01:21:10.7	33:38:47.5	13.74	1.05	69.5	0.49	6.95
O_1189_251296	01287+3432	01:28:43.2	34:31:32.6	14.81	0.55	56.1	0.76	3.02
O_1189_224928	NGC 634	01:35:25.4	35:06:38.8	13.70	1.13	84.6	0.57	3.98
O_1189_244311	UGC 1166	01:35:42.0	34:44:18.4	14.17	1.23	71.1	0.39	3.38
O_1189_234487	01366+3455	01:36:39.7	34:54:18.6	15.20	0.61	45.6	0.25	3.32
O_1189_216659	NGC 653	01:39:31.7	35:23:12.3	14.17	1.42	83.3	0.36	2.96
O_1189_199608	01446+3547	01:44:34.6	35:47:04.8	14.76	1.08	44.8	0.39	5.38
O_1225_610652	None	01:45:28.6	33:35:47.0	16.99	0.52	48.1	1.81	2.49
O_1225_389102	UGC 1307	01:47:51.9	35:41:06.0	14.32	1.34	76.9	0.26	18.09
O_1225_412197	UGC 1339	01:49:28.8	35:36:36.5	14.39	1.55	48.8	0.29	34.59
O_1225_369028	NGC 714	01:50:33.0	35:58:31.7	14.06	1.62	77.5	0.20	42.61
O_1225_369332	UGC 1363	01:50:58.4	35:59:02.1	14.71	1.49	70.0	0.29	47.93
O_1225_394977	01561+3549	01:56:09.1	35:49:14.2	14.93	1.48	79.2	0.12	9.32
O_1225_484388	UGC 1569	02:01:55.5	34:54:35.3	15.47	1.46	47.3	0.53	2.50
O_1225_531870	02023+3434	02:02:19.7	34:33:02.9	15.01	1.15	51.8	0.76	2.67
O_1225_606718	02087+3349	02:08:40.7	33:48:35.6	14.64	1.13	63.9	1.58	2.54

3.2.2 HI Observations

We obtained 21cm line spectra with the 305m Arecibo telescope of the National Astronomy and Ionosphere Center over 14 nights between August 6 and August 20, 1998.² The new Gregorian feed was used with the narrow L band receiver using a 25 MHz bandpass centered on 1394 MHz (1024 channels). One observation was performed using a 50 MHz bandpass centered at 1400.5 MHz. The beamsize of the 305m Arecibo dish is approximately 3.3' FWHM. For each of our Arecibo sample galaxies, we made two sets of ON-OFF observations, one 90'' to the east of the central position along the major-axis, and a corresponding observation to the west of the galaxy center. Typically, 5 minute integrations were used for each observation, although some galaxies were re-observed to allow better measurement of their weak flux and others known to be bright in HI were observed with shorter integrations. Preliminary data reduction was performed using ANALYZ at the Arecibo facility. For each observation, the two polarizations were averaged together. For each galaxy we then archived both the sum of the east and west ($E + W$) spectra and the difference (in the sense east minus west). It is the difference ($E - W$) spectra that can be used to determine the spin vector, by allowing us to determine which side of the major-axis is moving toward us relative to the galaxy center. Of the 96 galaxies in the original sample, 6 were not observed, 16 were not detected in HI, 3 suffered from strong radio frequency interference (RFI), and one suffered from a distorted baseline. We therefore had a total of 70 galaxies for which there were good detections. Subsequent data reduction was performed on the 70 galaxies for which good $E + W$ detections existed. The spectra were Doppler corrected and the fluxes corrected for gain differences with zenith angle and changes in system temperature. A visual estimate of each galaxy's redshift was made and then radio frequency interference (RFI) within 750 km s⁻¹ of the line was 'removed' from the spectra. RFI 'removal' was performed interactively and the RFI was replaced with a linear interpolation between

²The National Astronomy and Ionosphere Center is operated by Cornell University under a cooperative agreement with the National Science Foundation.

the two endpoints of the spectra. Noise was added to the linear interpolation, using the surrounding spectral channels to determine the noise level. Both the $E + W$ and $E - W$ spectra were baseline corrected using a linear fit to non-HI line channels within 500 km s^{-1} . We determined the HI line properties of the galaxy using the $E + W$ spectra. All velocities follow the optical convention, $v = c\Delta\lambda/\lambda_0$, and are adjusted to be in the heliocentric frame. The flux-weighted mean velocity, v_0 , of the galaxy as well as the line flux is computed. The line width used the mean of the line widths at a threshold of 50% of the boxcar equivalent flux and at a threshold of 20% the maximum flux determined by using an outward searching algorithm [Lavezzi and Dickey 1997]. The reported line width has been corrected for noise and channel width using the method outlined in Lavezzi and Dickey [1997].

3.2.3 Determination of Galaxy Spin Vector Directions and Uncertainty

The direction of the galaxy's spin vector was determined by taking the first moment of the $E - W$ spectra, μ_{E-W} , where

$$\mu_{E-W} = \frac{\int_{v_{min}}^{v_{max}} f_{E+W}(v)f_{E-W}(v)(v - v_0)dv}{\int_{v_{min}}^{v_{max}} [f_{E+W}(v)]^2 dv}, \quad (3.1)$$

where v_{min} and v_{max} are the minimum and maximum velocity of the line respectively, v_0 is the flux-weighted mean velocity of the galaxy, and $f_{E+W}(v)$ and $f_{E-W}(v)$ are the fluxes of the $E + W$ and $E - W$ spectra respectively. Negative μ_{E-W} implies that the eastern side of the galaxy is approaching us relative to the galaxy center, meaning the galaxy's \vec{L} points northward. Positive μ_{E-W} implies \vec{L} points to the south. The uncertainty in μ_{E-W} due to bad baseline and spectral noise was measured using two variants of the normal first moment. To determine the effect of spectral noise on the first moment, we computed μ_{offset} , where we measure the first moment of the flux outside the line by conserving $\Delta v = (v_{max} - v_{min})$, but offset the v_0 , v_{min} , and v_{max} in equation 3.1 to lie outside the line (see Figure 3.1). This gave us a measure of the contribution of spectral noise (presumably similar outside the HI line as inside) to the value of μ . To determine the effect of uncertainty in the baseline fit to the first moment determination, we also

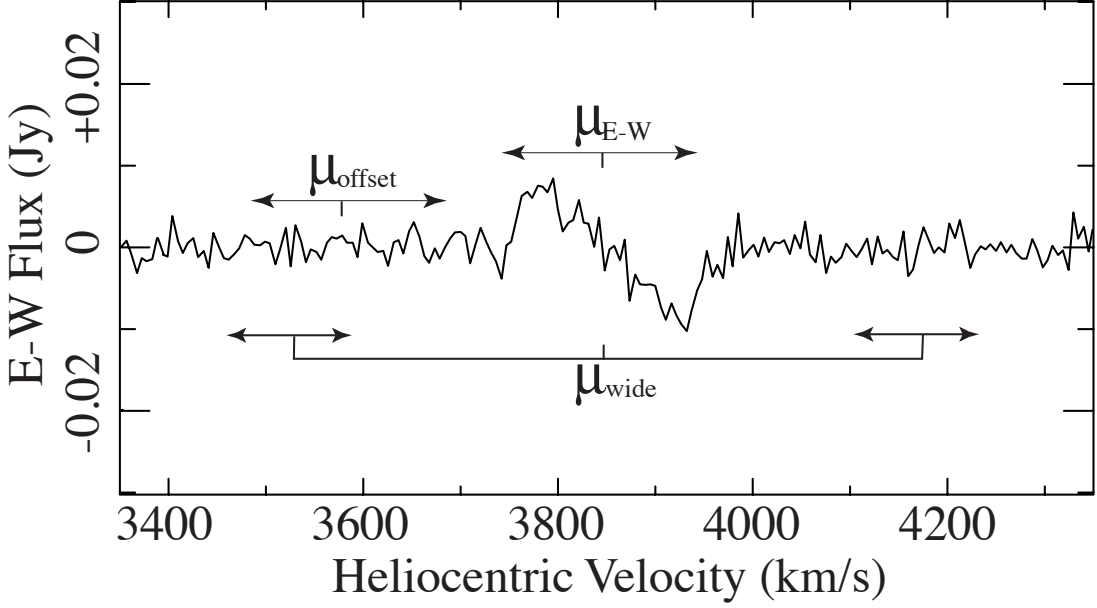


Figure 3.1: This plot shows the ranges of velocity over which μ_{E-W} , μ_{offset} , and μ_{wide} are determined, in this case for the spectrum of UGC 12231.

computed μ_{wide} , where we find the 1st moment about v_0 of the flux outside the line . We then scaled this by $\overline{\Delta v}/\overline{\Delta v_{outside}}$ to determine the amount of μ_{E-W} uncertainty due to uncertainty in the baseline fit. Both μ_{offset} and μ_{wide} are illustrated in Figure 3.1. μ_{offset} and μ_{wide} measurements suggest that galaxies with $|\mu_{E-W}| < 15 \text{ km s}^{-1}$ should be considered to have undetermined spin (see Figure 3.2). To confirm that the $E - W$ spectra are the result of gas being observed on both sides of the major axis, we also computed the cross-correlation, P_{cc} , of the $E + W$ and $E - W$ spectra,

$$P_{cc} = \frac{\int_{v_{min}}^{v_{max}} f_{E+W}(v)f_{E-W}(v)dv}{\int_{v_{min}}^{v_{max}} [f_{E+W}(v)]^2 dv}, \quad (3.2)$$

since we would expect that the $E + W$ and $E - W$ spectra would be orthogonal in those cases where the flux is from both the eastern and western positions. We have empirically found that if $P_{cc} > 0.4$ the $E - W$ flux was likely to be entirely from only one position and thus the spin measurement should be considered undetermined. It should be noted that this process will not eliminate observations of galaxies with an asymmetric HI distribution if there is significant flux in both the eastern and western positions. Such

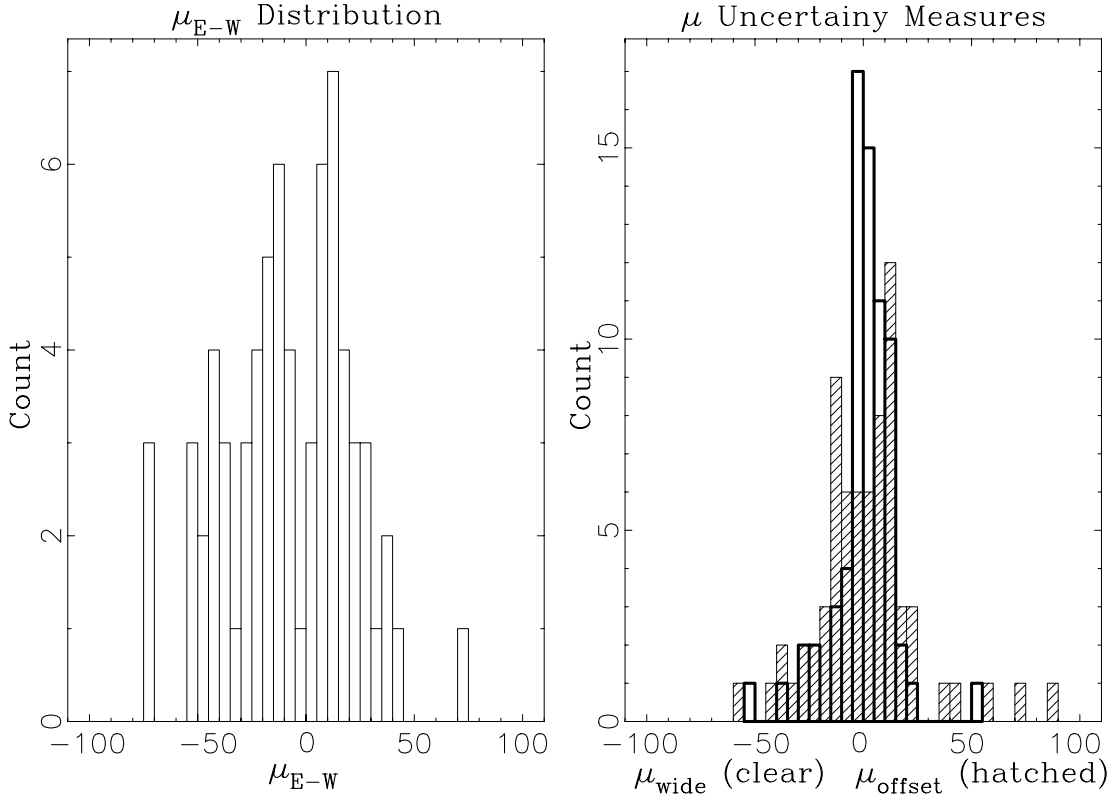


Figure 3.2: The plot on the left shows the distribution of μ_{E-W} values for the 70 Arecibo sample galaxies detected in HI. Negative μ_{E-W} means the galaxy’s \vec{L} points northward. The right plot shows the distribution of μ_{offset} (hatched) and μ_{wide} (clear), both of which have a FWHM of roughly 15 km s^{-1} .

a asymmetric HI distribution would affect the mean velocity, v_0 , and thus may affect the amplitude of μ_{E-W} , but it should not change the sign of μ_{E-W} , which is the observable we use later. The final dataset had 54 galaxies with well determined spin vectors out of the 70 galaxies with good HI detections (see Table 3.2), 16 galaxies having been rejected from the sample due to either large P_{cc} or small μ_{E-W} . For these galaxies, we computed

$$\theta_{\vec{L}} = \theta + 90^\circ(\mu_{E-W}/|\mu_{E-W}|), \quad (3.3)$$

which is the projection of \vec{L} on the plane of the sky. Since the Arecibo sample is chosen to be nearly edge-on, $\theta_{\vec{L}}$ is essentially a complete description of \vec{L} , allowing simple one-dimensional statistical analysis to be used for what is normally a three-dimensional

problem.

Table 3.2: The Arecibo Observations

APS ID	Date ¹	V_{Sun} (km s ⁻¹)	ΔV	F_{obs} (Jy- km s ⁻¹)	Spin ²	μ_{E-W} (km s ⁻¹)	P_{cc}	Comments
O_778_873376	11	5604	334	1.03(0.08)	N	-19.7	-0.203	
O_778_731211	08	—	—	—	U	—	—	Non-detection
O_778_700353	18	—	—	—	U	—	—	Non-detection
O_778_847676	16	—	—	—	U	—	—	Non-detection
O_778_849054	13	—	—	—	U	—	—	Non-detection
O_778_1040599	07	6379	328	1.12(0.08)	U	+14.7	-0.151	
O_778_923367	14	6576	547	2.85(0.16)	U	-11.4	+0.389	
O_778_755586	12	6661	269	1.23(0.10)	U	-8.5	-0.057	
O_1184_28270	12+17	6705	443	1.30(0.10)	S	+38.7	+0.121	
O_1184_66567	13	6791	267	0.85(0.09)	U	-6.1	+0.274	
O_1184_128370	06	3869	200	4.55(0.06)	U	-12.3	-0.023	
O_1184_81567	09	6588	283	1.50(0.07)	S	+21.8	+0.061	
O_1184_196807	06	6597	342	3.10(0.09)	S	+27.6	-0.068	
O_1184_121956	07	6436	358	9.36(0.10)	S	+41.3	-0.163	
O_1184_275037	06	3691	275	5.25(0.09)	N	-28.7	-0.030	
O_1184_313727	06	3674	224	7.24(0.08)	U	+12.4	-0.054	
O_1184_347214	14	5836	235	2.34(0.07)	U	+7.5	-0.061	
O_1184_189398	09	6838	406	1.58(0.10)	S	+25.0	+0.143	
O_843_144830	15	—	—	—	U	—	—	Non-detection
O_843_65466	16	5879	235	3.24(0.09)	U	+8.8	-0.220	
O_914_404205	07	5903	555	5.24(0.10)	N	-74.2	-0.271	
O_914_406137	13+17	5534	187	0.28(0.09)	U	+9.0	+0.300	
O_914_344933	12	5225	435	1.95(0.09)	S	+29.8	-0.210	
O_914_409641	11	5466	213	4.38(0.08)	U	+12.7	+0.001	
O_914_371708	16	—	—	—	U	—	—	Non-detection
O_914_413061	15	—	—	—	U	—	—	Non-detection
O_914_511814	20	8802	372	4.56(0.09)	S	+24.4	+0.068	50MHz bandpass
O_914_416774	14	5191	507	3.87(0.10)	N	-42.9	+0.079	
O_914_286281	14	5208	395	6.34(0.09)	N	-36.9	-0.047	
O_914_286479	17	5057	224	1.82(0.09)	U	-11.6	-0.148	
O_914_514191	15	7134	261	3.10(0.07)	U	-13.3	+0.049	
O_914_437214	15	6895	318	1.43(0.08)	N	-20.7	-0.162	
O_1257_181710	16	5111	272	1.34(0.08)	U	+2.5	+0.214	
O_1257_106449	07	4844	245	11.67(0.06)	S	+36.4	-0.014	
O_1257_149828	12	4647	302	12.82(0.17)	N	-44.9	+0.072	
O_1257_140283	13	4970	245	5.07(0.07)	S	+20.6	+0.029	
O_1257_307025	17	—	—	—	U	—	—	Non-detection
O_1257_224112	18	—	—	—	U	—	—	Non-detection
O_1257_212633	13	4835	245	4.47(0.09)	N	-24.2	-0.001	
O_1244_265500	15	6765	411	8.75(0.12)	N	-44.2	+0.051	

¹Observation date is the day of the month of August 1998. All Dates are UTC.

²There are three possible values for the spin direction, “N” for north, “S” for South, and “U” for Undetermined. The spin direction is determined from the values of μ_{E-W} and P_{cc} .

APS ID	Date ¹	V_{Sun} (km s ⁻¹)	ΔV	F_{obs} (Jy- km s ⁻¹)	Spin ²	μ_{E-W} (km s ⁻¹)	P_{cc}	Comments
O_1244_376417	15	6287	390	3.90(0.09)	U	+14.4	+0.367	
O_1244_340721	11	6269	446	10.75(0.10)	N	-46.2	-0.234	
O_1244_270335	14	6296	275	1.99(0.09)	N	-24.5	-0.058	
O_1244_679996	06	4635	179	3.15(0.14)	U	+8.9	+0.093	
O_1244_578706	17	6966	288	3.08(0.10)	U	-4.3	-0.404	
O_1244_241809	12	4593	138	5.55(0.10)	U	+11.4	+0.164	
O_1244_767827	06	4148	200	4.71(0.09)	S	+18.8	-0.015	
O_1244_185805	18	6292	419	2.05(0.10)	N	-21.7	+0.069	
O_1244_655424	14	5238	342	4.31(0.08)	N	-51.8	+0.149	
O_1244_554203	16	—	—	—	U	—	—	Non-detection
O_1244_595079	13	5249	248	5.04(0.06)	N	-30.4	+0.037	
O_1244_521380	20	4891	283	1.43(0.08)	U	-10.5	+0.181	
O_1244_442897	20	—	—	—	U	—	—	Strong RFI
O_1244_484644	18	4901	459	1.34(0.09)	N	-38.6	+0.220	
O_601_2598615	06	5059	382	4.71(0.19)	N	-52.7	-0.049	
O_601_927741	13	4575	323	3.60(0.08)	N	-28.7	-0.023	
O_601_2448395	17	4972	219	1.69(0.08)	U	-6.2	+0.907	
O_601_1985337	07	4892	227	2.97(0.07)	N	-17.8	-0.346	
O_601_1986315	18	—	—	—	U	—	—	Non-detection
O_601_2601958	None	—	—	—	U	—	—	
O_601_1152906	11	6267	446	10.77(0.10)	N	-46.2	-0.235	
O_601_2454111	None	—	—	—	U	—	—	
O_601_2363374	18	—	—	—	U	—	—	Baseline distorted
O_601_1044227	17	5635	232	1.13(0.09)	U	+18.9	+1.021	
O_601_1267760	18	4623	318	2.08(0.10)	N	-18.7	-0.071	
O_601_1050939	18	5087	146	1.42(0.07)	N	-27.4	+0.100	
O_601_1498038	12	4758	523	9.16(0.12)	N	-73.6	-0.213	
O_601_1063679	14	5535	416	7.15(0.10)	N	-42.8	+0.047	
O_601_863271	None	—	—	—	U	—	—	
O_601_1294945	16	6218	267	2.85(0.08)	N	-15.8	+0.039	
O_601_978154	20	5823	347	1.15(0.13)	U	+9.7	+0.592	
O_601_1197694	16	6213	277	3.72(0.08)	U	+13.2	+0.271	
O_601_657010	16	5069	219	2.51(0.09)	S	+18.6	+0.135	
O_601_992015	None	—	—	—	U	—	—	
O_601_175820	20	—	—	—	U	—	—	Non-detection
O_601_264028	None	—	—	—	U	—	—	
O_601_359427	20	4643	267	1.22(0.09)	U	+3.4	+0.262	
O_406_436424	20	4708	221	1.84(0.08)	S	+17.8	+0.080	
O_406_502375	16	4160	299	3.45(0.10)	U	-54.1	+0.958	
O_1189_285025	17	4851	277	1.00(0.11)	U	+0.5	+0.090	
O_1189_293769	06	4839	534	5.36(0.10)	N	-70.2	-0.008	
O_1189_251296	12	4127	213	3.28(0.07)	U	+8.9	+0.104	
O_1189_224928	13	4884	497	6.83(0.10)	S	+74.1	-0.032	
O_1189_244311	14	—	—	—	U	—	—	Strong RFI
O_1189_234487	15	5126	176	1.71(0.08)	U	-6.4	+0.164	
O_1189_216659	16	—	—	—	U	—	—	Strong RFI
O_1189_199608	17	4786	272	1.11(0.08)	N	-19.7	+0.376	
O_1225_610652	09	5728	221	1.11(0.07)	U	-12.0	-0.104	
O_1225_389102	18	—	—	—	U	—	—	Non-detection
O_1225_412197	18	—	—	—	U	—	—	Non-detection
O_1225_369028	None	—	—	—	U	—	—	
O_1225_369332	20	—	—	—	U	—	—	Non-detection
O_1225_394977	12	5406	366	1.75(0.08)	S	+34.6	+0.099	
O_1225_484388	13	—	—	—	U	—	—	Non-detection
O_1225_531870	10	4334	288	1.14(0.09)	U	+13.2	-0.211	
O_1225_606718	08	6128	435	3.33(0.10)	N	-39.1	+0.326	

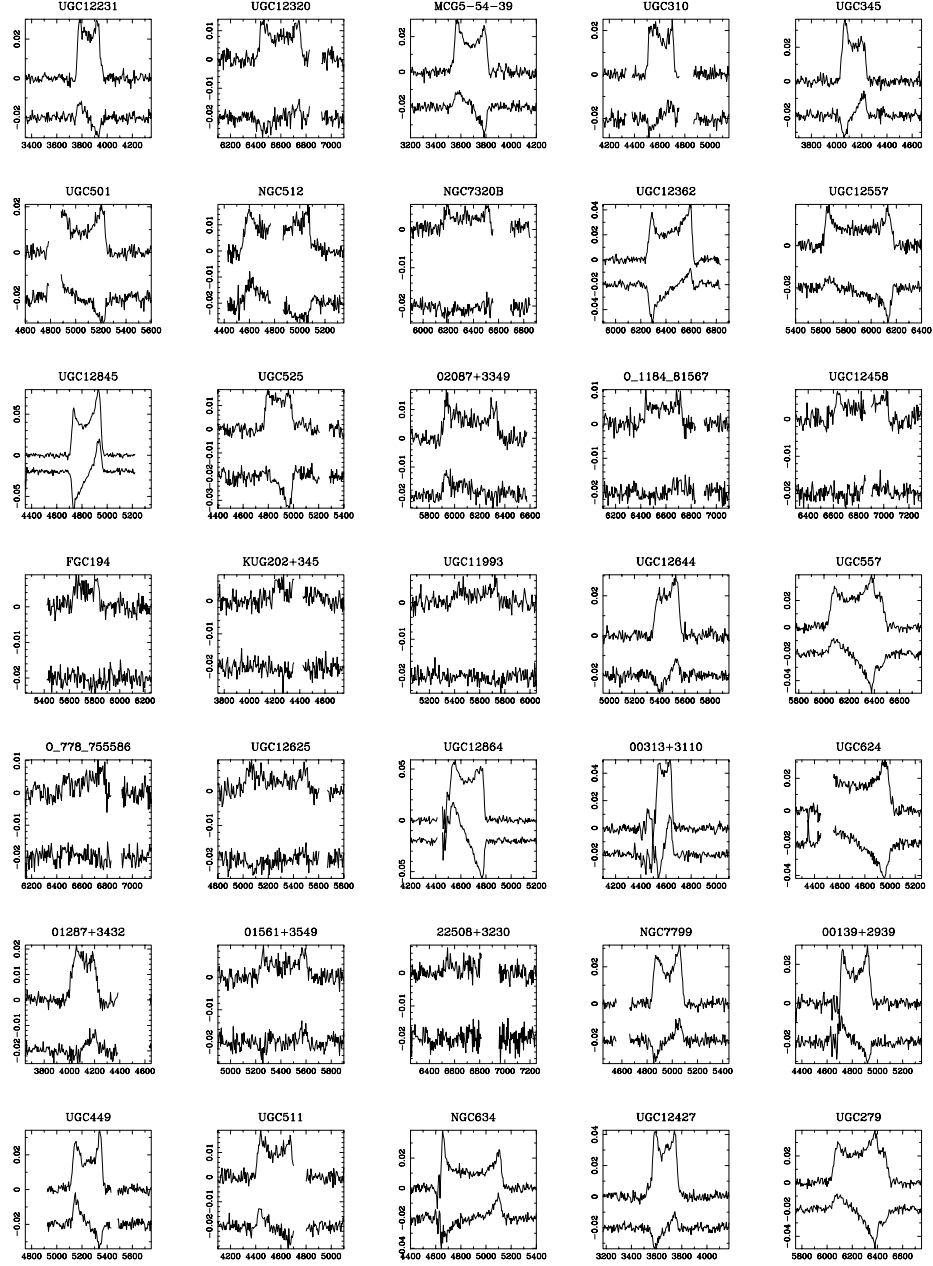
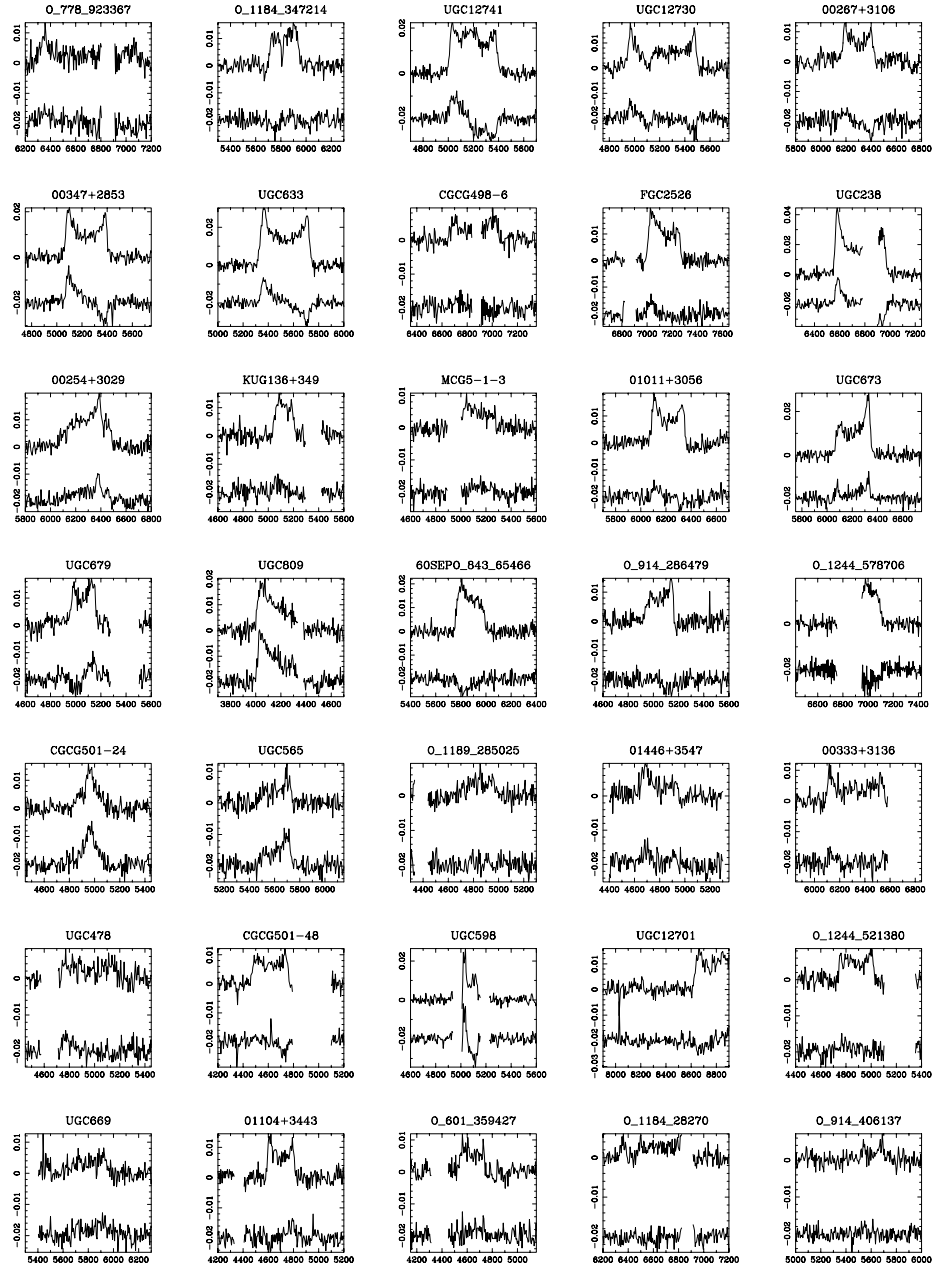


Figure 3.3: The reduced spectra for the Arecibo sample in units of Jy versus km s^{-1} . The top spectrum in each pair is $f_{E+W}(v)$, the bottom spectrum is $f_{E-W}(v)$ shifted by -0.02 Jy. Each spectrum is 1500 km s^{-1} wide and centered on the systemic heliocentric velocity of the galaxy. Spectra are baseline corrected. Gaps indicate where RFI was identified.



3.3 Data Analysis Methods

3.3.1 The Kuiper Statistic

Identification of anisotropies in the observed $\theta_{\bar{L}}$ and θ distributions was initially done by using the Kuiper V statistic, which is a two-sided variant of the Kolmogorov-Smirnov (K-S) D statistic [Press *et al.* 1992]. We use the Kuiper V statistic because the K-S D statistic can systematically underestimate the significance of differences between the observations and the models, especially if the differences are near the ends of the distribution [Press *et al.* 1992]. These tests compare the cumulative distributions of a variable, x (such as $\theta_{\bar{L}}$, $\Delta\theta_{\bar{L}}$, etc.), in the observed sample, $S(x)$, with that for a model of 100000 randomly-oriented galaxies, $S_m(x)$. The Kuiper statistic, V , is then defined as

$$V = D_+ + D_- = \max[S(x) - S_m(x)] + \max[S_m(x) - S(x)], \quad (3.4)$$

the sum of the absolute values of the maximum positive (D_+) and negative (D_-) differences between $S(x)$ and $S_m(x)$.³ V is essentially a measure of the difference between two distributions (see Figure 3.4). If the number of degrees of freedom is known a priori, a simple functional form exists for the probability, $P(V)$, that the two samples whose cumulative distributions differ by V were drawn from the same parent distribution (see Press *et al.* [1992], for example). Therefore, if we are comparing the distribution of x for the observed sample to that of a modeled, randomly-oriented sample, we have a way of estimating the probability that the observed sample is drawn from an isotropic distribution. In this study, we considered a distribution's anisotropy significant if the probability, $P(V)$, that the Arecibo sample could have been drawn from the randomly-oriented sample was less than 5%.

³Note that the normal K-S D statistic is equal to $\max|S(x) - S_m(x)|$. It doesn't distinguish between differences above or below the $S_m(x)$ the curve.

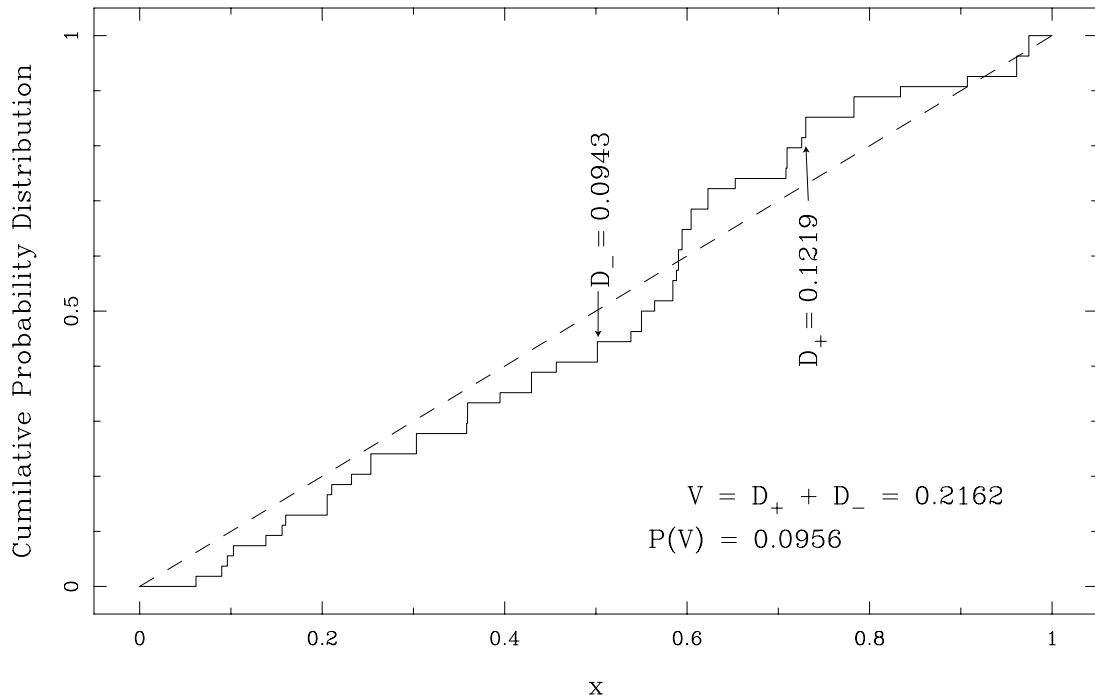


Figure 3.4: This diagram illustrates how the Kuiper V statistic is determined for a given cumulative distribution. The dashed line is the cumulative distribution, $S(x)$, of $\Delta\theta_{\bar{L}}(1)$ for the Arcibo sample. The solid line is the modeled, isotropic distribution, $S_m(x)$. The maximum positive (D_+) and negative (D_-) differences between $S(x)$ and $S_m(x)$ are shown for this sample. The Kuiper V statistic is the sum of D_+ and D_- whereas the K-S D statistic is D_+ (because $|D_+| > |D_-|$ in this case). It has been previously established that V is a more robust measure than D of the difference between two distributions and thus we choose to use V to measure the anisotropy of our data (see Press *et al.* 1992, for example).

In those cases where the number of degrees of freedom is not well determined a priori, we used Monte Carlo comparisons of the observations with 1000 model samples of equal size. This was necessary in order to avoid overestimating the significance of an observed anisotropy. We model a randomly oriented distribution of galaxies by taking the observed sample, randomly reassigning the observed P_{cc} and μ values to various galaxies (μ is determined by randomly reversing the sign of $|\mu|$), and then randomly generating the major-axis position angle, θ . This model kept the spatial distribution of the original sample and the HI observational selection effects while otherwise being a completely randomly oriented model. Comparison of the real distribution of a variable versus its distribution in the 1000 Monte-Carlo samples is used to determine the significance of an anisotropy in some of the more complicated distributions discussed in section 3.4.

3.4 Results and Analysis

3.4.1 Probing for Global Spin Vector Alignments

As a followup to the work done in Paper I, we initially examined some of the distributions similar in nature to the ones investigated in that study. We divided the entire MAPS-PP and Arecibo Samples into 3 subsets each: the high density subset, the low density subset, and the complete sample. The high and low density subsets were created using surface density estimates, Σ , from the MAPS-PP catalog to compute the median surface density. The high and low density subsets include all galaxies with Σ greater than and less than this median value, respectively. For the MAPS-PP subsets we tested the θ -based distributions, whereas for the Arecibo subsets, we tested the $\theta_{\bar{L}}$ -based distributions. Examinations of the $\theta_{\bar{L}}$ and θ distributions show no significant anisotropy in any of the Arecibo or MAPS-PP subsets. Similar results were seen for distributions of $\theta_{\bar{L}}$ and θ relative to other critical angles including the following:

- $\Delta\theta_{\bar{L}}(1)$ and $\Delta\theta(1)$: the difference of $\theta_{\bar{L}}$ and θ , respectively, between nearest neighbor galaxies in that sample. Note that $\Delta\theta(1)$ is used in the Arecibo sample only

to separate the significance of any $\Delta\theta_{\bar{L}}(1)$ alignments from any $\Delta\theta(1)$ alignments.

- $\Delta\theta_{\bar{L}}(Geo)$: the difference of $\theta_{\bar{L}}$ from the geodesic to the nearest neighbor galaxy.
- $\Delta\theta_{\bar{L}}(Ridge)$: the difference of $\theta_{\bar{L}}$ from angle of the Pisces-Perseus Supercluster ridgeline at its nearest point (as determined in Paper I).
- $\Delta\theta_{\bar{L}}(GC - X)$: the difference of $\theta_{\bar{L}}$ from the galaxy concentration position angle built using a percolation length of X arcminutes (galaxy concentrations groupings of galaxies identified using a 2 dimensional friends-of-friends algorithm (redshift is ignored), see Paper I for details).
- $\Delta\theta_{\bar{L}}(GCR - X)$: the difference of $\theta_{\bar{L}}$ from the radial line to the center of the galaxy concentration built using a percolation length of X arcminutes.

These results, shown in Table 3.3, support the observations in Paper I in that no simple θ or $\theta_{\bar{L}}$ alignments appear to be present. Examination of the $\Delta\theta_{\bar{L}}(GC - X)$ distribution does not support the tentative anti-alignments seen in Paper I. We looked for 'twisting' of $\Delta\theta_{\bar{L}}(Ridge)$ versus distance from the PPS ridgeline, and could not corroborate this signal seen in the $\Delta\theta(Ridge)$ distribution of the MAPS-PP in Paper I. We note that the Arecibo sample is considerably smaller than the MAPS-PP, so we cannot rule out the trends seen in Paper I, but we simply cannot support them.

Table 3.3: Arecibo \vec{L} Anisotropy Probabilities, $P(V)$

Distribution	Arecibo Sample			MAPS-PP Catalog		
	all	hi dens	lo dens	all	hi dens	lo dens
N_{gal}	54	23	30	1230	616	615
$\theta_{\vec{L}}$	0.220	0.061	0.064	—	—	—
θ	0.449	0.448	0.807	0.388	0.270	0.341
$\Delta\theta_{\vec{L}}(1)$	0.096	0.462	0.120	—	—	—
$\Delta\theta(1)$	0.121	0.119	0.361	0.667	0.197	0.352
$\Delta\theta(Geo)$	—	—	—	0.606	0.730	0.680
$\Delta\theta_{\vec{L}}(Geo)$	0.384	0.894	0.374	—	—	—
$\Delta\theta(Ridge)$	—	—	—	0.799	0.126	0.900
$\Delta\theta_{\vec{L}}(Ridge)$	0.257	0.142	0.113	—	—	—

“ $\Delta\theta_{\vec{L}}/\Delta\theta$ ” represents $\Delta\theta_{\vec{L}}$ for Arecibo Sample and $\Delta\theta$ for MAPS-PP Catalog,
“(N)” below indicates the number of galaxies in this distribution.

$\Delta\theta_{\vec{L}}/\Delta\theta(GC - 10)$	— (000)	— (000)	— (000)	0.651 (013)	0.651 (013)	— (000)
$\Delta\theta_{\vec{L}}/\Delta\theta(GC - 15)$	0.279 (001)	0.279 (001)	— (000)	0.700 (093)	0.700 (093)	— (000)
$\Delta\theta_{\vec{L}}/\Delta\theta(GC - 20)$	0.699 (009)	0.884 (008)	0.279 (001)	0.823 (224)	0.846 (220)	0.731 (004)
$\Delta\theta_{\vec{L}}/\Delta\theta(GC - 25)$	0.489 (018)	0.954 (014)	0.108 (003)	0.113 (431)	0.062 (389)	0.797 (043)
$\Delta\theta_{\vec{L}}/\Delta\theta(GC - 30)$	0.086 (030)	0.410 (021)	0.252 (008)	0.774 (581)	0.727 (455)	0.596 (127)
$\Delta\theta_{\vec{L}}/\Delta\theta(GC - 35)$	0.046 (042)	0.065 (023)	0.160 (018)	0.590 (722)	0.881 (497)	0.639 (226)
$\Delta\theta_{\vec{L}}/\Delta\theta(GC - 40)$	0.124 (048)	0.244 (023)	0.624 (024)	0.095 (817)	0.113 (508)	0.946 (310)
$\Delta\theta_{\vec{L}}/\Delta\theta(GC - 45)$	0.214 (052)	0.016 (023)	0.815 (028)	0.307 (902)	0.380 (509)	0.692 (394)
$\Delta\theta_{\vec{L}}/\Delta\theta(GC - 50)$	0.494 (052)	0.106 (023)	0.917 (028)	0.616 (948)	0.742 (509)	0.905 (440)
$\Delta\theta_{\vec{L}}/\Delta\theta(GCR - 10)$	— (000)	— (000)	— (000)	0.858 (013)	0.858 (013)	— (000)
$\Delta\theta_{\vec{L}}/\Delta\theta(GCR - 15)$	0.279 (001)	0.279 (001)	— (000)	0.839 (093)	0.839 (093)	— (000)
$\Delta\theta_{\vec{L}}/\Delta\theta(GCR - 20)$	0.931 (009)	0.683 (008)	0.279 (001)	0.741 (224)	0.720 (220)	0.232 (004)
$\Delta\theta_{\vec{L}}/\Delta\theta(GCR - 25)$	0.764 (018)	0.365 (014)	0.850 (003)	0.779 (431)	0.665 (389)	0.862 (043)
$\Delta\theta_{\vec{L}}/\Delta\theta(GCR - 30)$	0.767 (030)	0.523 (021)	0.871 (008)	0.346 (581)	0.605 (455)	0.765 (127)
$\Delta\theta_{\vec{L}}/\Delta\theta(GCR - 35)$	0.359 (042)	0.473 (023)	0.707 (018)	0.040 (722)	0.247 (497)	0.546 (226)
$\Delta\theta_{\vec{L}}/\Delta\theta(GCR - 40)$	0.917 (048)	0.711 (023)	0.475 (024)	0.670 (817)	0.264 (508)	0.271 (310)
$\Delta\theta_{\vec{L}}/\Delta\theta(GCR - 45)$	0.281 (052)	0.253 (023)	0.428 (028)	0.457 (902)	0.849 (509)	0.127 (394)
$\Delta\theta_{\vec{L}}/\Delta\theta(GCR - 50)$	0.148 (052)	0.568 (023)	0.039 (028)	0.274 (948)	0.196 (509)	0.973 (440)

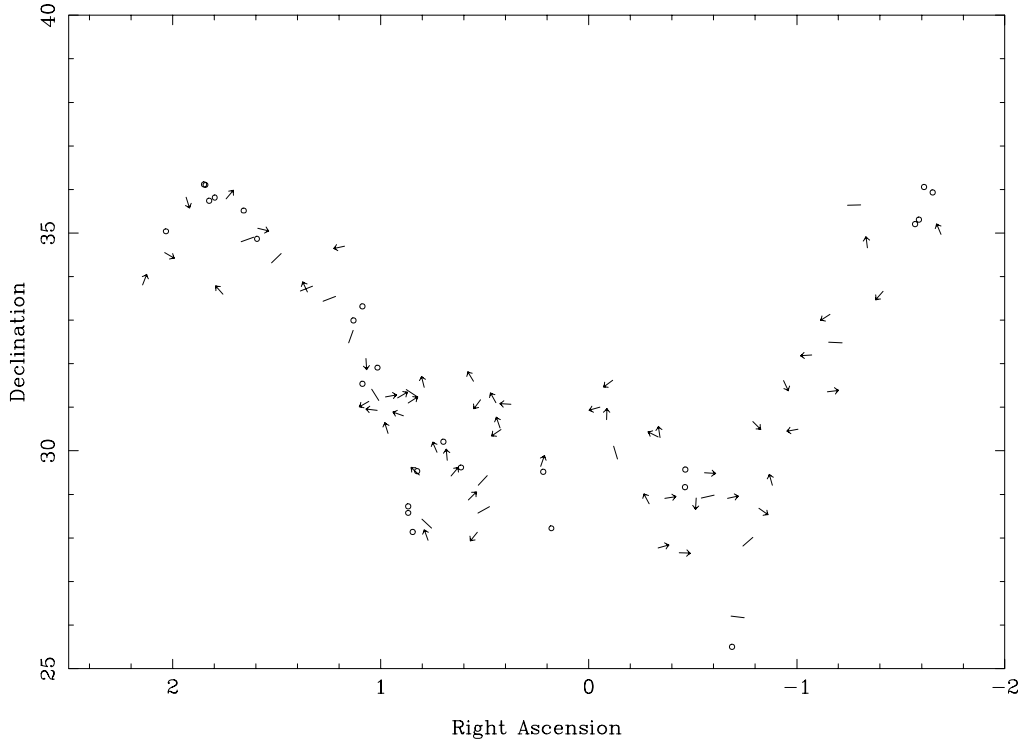


Figure 3.5: This map shows the distribution of the entire Arecibo subsample on the sky, with varying symbols depending on the value of $\theta_{\vec{L}}$. If $\theta_{\vec{L}}$ is well-determined, an arrow shows its direction, if $\theta_{\vec{L}}$ is not-well determined, but the galaxy was detected in HI, a line shows the direction of $\theta_{\vec{L}}$, but not the sign. A circle marks those galaxies that were undetected in HI.

3.4.2 Probing for Spin Vector Domains

An initial visual inspection of the plot of the distribution of $\theta_{\vec{L}}$ on the sky (Figure 3.5) appears to show some $\theta_{\vec{L}}$ alignments. Specifically, in many cases if you pick a galaxy at random and then compare its $\theta_{\vec{L}}$ with that of nearby galaxies, the difference is often less than 90° . It appeared to the authors that there was a visual impression of the PPS being divided up into “spin vector domains,” regions with preferred \vec{L} orientations. Because visual impressions are subjective, we devised tests to look for possible spin vector domains as well as looking for the alignments of the sort reported in Paper I for the galaxy major-axes. We attempted to confirm visual impression of \vec{L} domains seen in Figure 3.5 by examining the orientations of several nearest neighbors, instead of

just the nearest neighbor. To this end, we computed the $\Delta\theta_{\vec{L}}(N)$ distribution, which is the summed distribution of $\Delta\theta_{\vec{L}}$ (respectively) for the N closest galaxies within 3° of each galaxy. If \vec{L} domains exist, the $\Delta\theta_{\vec{L}}(N)$ distribution should be peaked toward the lower values of $\Delta\theta_{\vec{L}}(N)$. Because the $\Delta\theta_{\vec{L}}(N)$ distribution about one galaxy is not independent of the distribution about that galaxy's nearest neighbors, the number of degrees of freedom is uncertain *a priori*. This means that the standard function to determine the probability, $P(V)$, of two distributions being identical doesn't work. Instead, we gauge $P(V)$ by generating 1000 Monte Carlo samples and computing the Kuiper V statistic of their $\Delta\theta_{\vec{L}}(N)$ distributions. By comparing the value of V for the observed sample with the distribution of V in the 1000 Monte Carlo samples, we have an estimate of the likelihood that a greater value of V is obtained, $P(V)$. We therefore use $P(> V)$ in lieu of the $P(V)$ used in cases where we know the number of degrees of freedom. We examined the $\Delta\theta_{\vec{L}}(N)$ distributions for the N closest galaxies of the Arecibo samples, for N ranging from 3 to 10. These samples show no significant anisotropy when compared to Monte Carlo generated datasets, indicating that the visual impression of \vec{L} domains is either incorrect, or that the \vec{L} domains are too weakly aligned to confirm with this test. Because in Paper I only a simple nearest neighbor test was performed, we also examined the $\Delta\theta(N)$ distribution for the MAPS-PP samples, in order to see if \vec{L} domains might be visible in the larger MAPS-PP dataset. We found that for N ranging from 3 to 10, the $\Delta\theta(N)$ distributions showed no evidence of significant anisotropies. This appears to indicate that it is unlikely that \vec{L} domains exist in the Pisces-Perseus Supercluster.

3.4.3 Establishing Limits on Galaxy Alignments

In order to quantify the largest anisotropic signature that could remain "hidden" from our statistical techniques, we performed a simple simulation. We generated samples drawn from random 'sinusoidal' distributions described by the probability distributions

$$P(\Theta)d\Theta = \left[1 + \alpha \cos\left(\Theta\frac{2\pi}{\lambda}\right) \right] d\Theta, \text{ where } \Theta \in [0, \lambda], \quad (3.5)$$

MAPS-PP Catalog (Major-Axis PA)

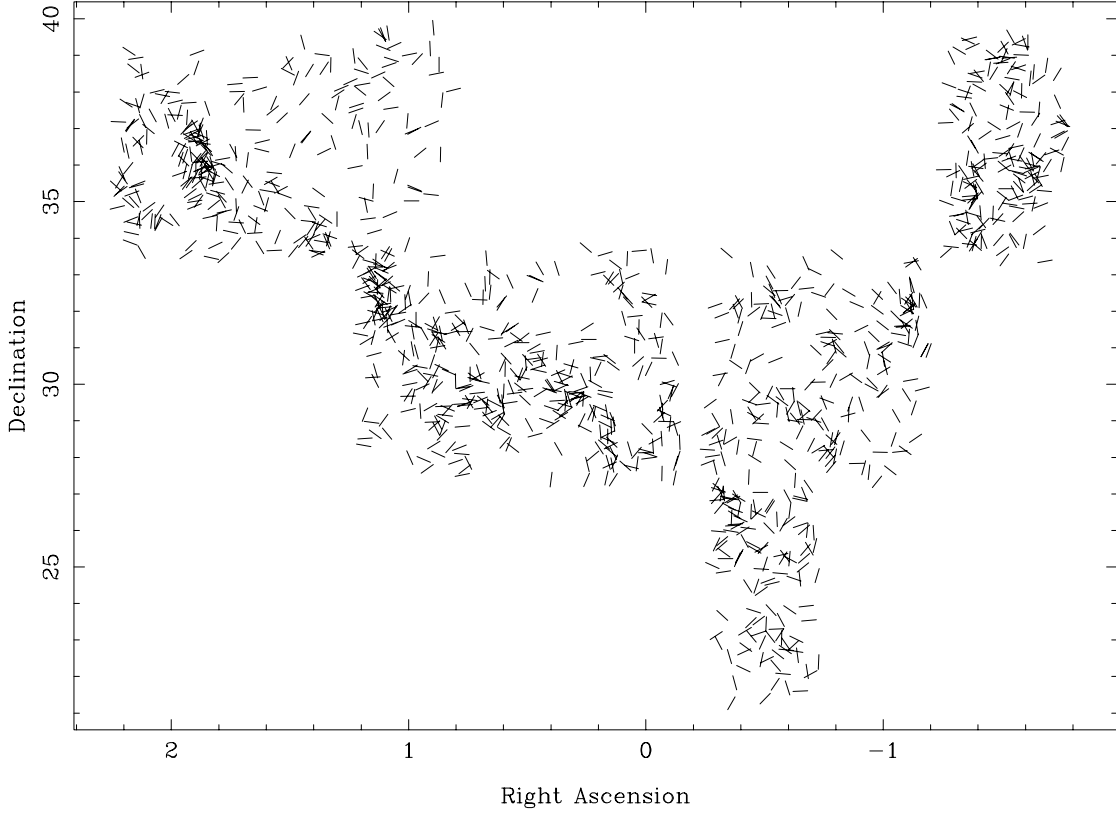


Figure 3.6: This map shows the major-axis position angle distribution of MAPS-PP O sample of 1230 galaxies on the sky. Note that apparent alignments are visible to the eye.

and

$$P(\Theta)d\Theta = \left[1 + \alpha \cos\left(\Theta\frac{2\pi}{\lambda}\right)\right] d\Theta, \text{ where } \Theta \in \left[0, \frac{\lambda}{2}\right], \quad (3.6)$$

where α is the amplitude of the 'sinusoidal' component of the probability in percent. In these two distributions, Θ represents either the expected θ or $\theta_{\bar{L}}$ distributions in the cases of large-scale alignments (equation 3.6), or the $\Delta\theta$ and $\Delta\theta_{\bar{L}}$ distributions in the cases of alignments (equation 3.6), anti-alignments (equation 3.6) or both (equation 3.5) between nearby galaxies. Using these two distributions, we can generate samples with a predetermined amplitude, α , for the alignments present and then compute the value of $P(V)$, the probability of the sample having been drawn from a random sample. By repeatedly doing this, we can determine the distribution of $P(V)$ for a given α and

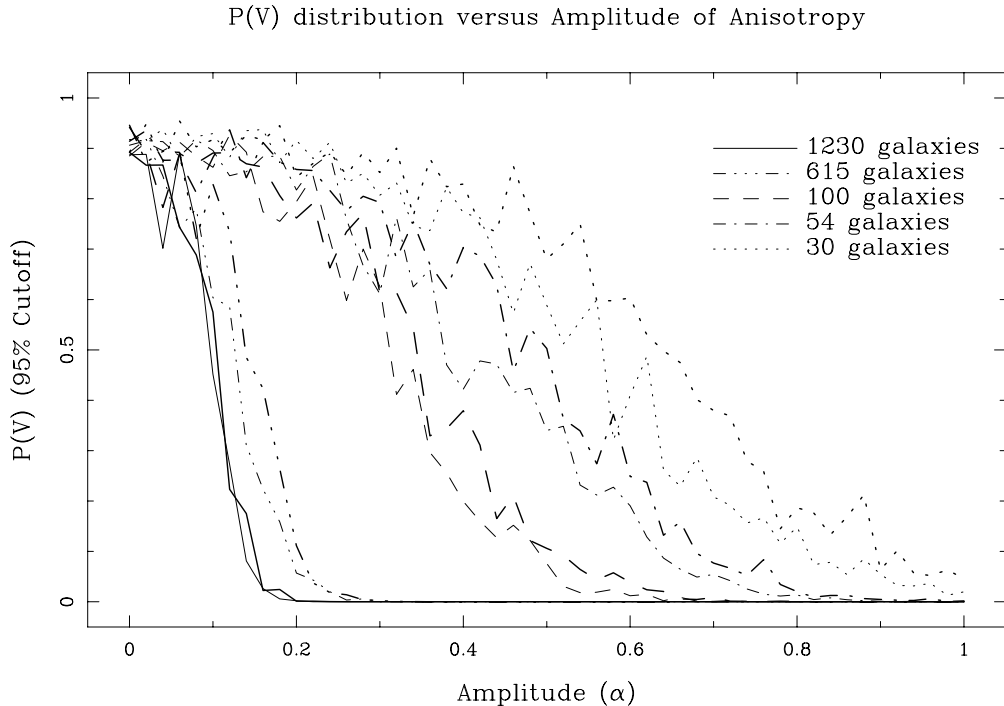


Figure 3.7: This plot shows the 95% cutoff value of $P(V)$, which is the value of $P(V)$ which 95% of all distributions lie below. Samples of 30, 54, 100, 615, and 1230 galaxies were generated via equation 3.5 (thin lines) and 3.6 (thick lines). The value of α for which these lines drop below a value of 0.05 is referred to as α_{95} . α_{95} represents the smallest amplitude of a sinusoidal anisotropy for which 95% of the distributions would be detected via the Kuiper Test. Notice the similar results for distributions generated by both equation 3.5 and equation 3.6.

sample size. For samples of 30, 54, 100, 615, and 1230 galaxies (the sizes of our subsets as noted in Table 3.3), we computed the $P(V)$ distribution for 100 generated Θ samples with amplitudes, α , ranging from 0% to 100% in steps of two percent (see Figure 3.7). We then examined at which point 95% of the $P(V)$ distribution dropped below 0.05, our criterion for calling a distribution significantly anisotropic. This gave us an estimate of the largest amplitude sinusoidal anisotropy that could have been missed, which we call α_{95} . α_{95} is therefore the smallest amplitude of a sinusoidal anisotropy for which there is a 95% chance of detection given the criteria of $P(V) < 0.05$. For our Arecibo sample, we find that with 54 galaxies $\alpha_{95} \approx 0.75$, therefore we can only eliminate global spin

vector alignments with sinusoidal amplitudes greater than 75%. This sample does not place very strong limits on level of any spin vector alignments present. With the 1230 galaxies in the MAPS-PP catalog, we find $\alpha_{95} \approx 0.15$. Therefore we can eliminate the possibility of galaxy major-axis alignments at amplitudes greater than 15%. Major-axis alignments place very weak limits on the level of spin vector alignments due to the fact that the orientation of the major-axis of the galaxy, with no additional information, only restricts the spin vector to a plane. However, if there is a spin vector alignment, it must be reflected in the major-axis distribution of the edge-on galaxies. We find that in a subsample of 729 MAPS-PP galaxies restricted to $\epsilon > 0.50$, there is no significant major-axis anisotropy of any sort. For a sample of 729 galaxies, we find $\alpha_{95} \approx 0.20$, therefore, we can confidently state that there are no spin vector alignments with sinusoidal amplitude greater than 20% (within the uncertainty due to the two-fold degeneracy in mapping major-axis position angle to spin vector). We would like to have computed α_{95} for the spin vector domain tests in order to gauge their sensitivity but it was computationally too expensive.

3.5 Conclusions

We have constructed the only catalog of well determined spin vectors for galaxies in the Pisces-Perseus Supercluster. Our study is the first radio study that explicitly looks at the spin vector distribution of galaxies in a supercluster and was optimized toward that end. We developed a simple technique for obtaining spin vector determinations and accessing the level of uncertainty in the spin vector determinations due to both spectral noise and uncertainty in fitting the continuum. We were intentionally rather conservative in our data selection criteria, possibly rejecting several well measured spin vectors. There are several problems currently hampering the determination of the angular momentum distribution of galaxies relative to each other and to the surrounding large-scale structure. One major problem is that we do not have a very clear understanding of the internal extinction in galaxies and its effect on the appearance of the galaxy with

changing inclination. Therefore, it is very difficult to accurately determine the inclination of a galaxy based solely on its ellipticity and position angle. This also makes it more difficult to construct a proper volume-limited sample for a large-scale angular momentum study. One could obtain redshifts for all the galaxies in a diameter-limited or magnitude-limited galaxy catalog and select a volume-limited subsample, but without a clear understanding of internal extinction, we cannot correct magnitudes and diameters for inclination. We compensated for these uncertainties of the effects of internal galaxy extinction by restricting our sample to highly edge-on galaxies. This had the added benefit of making the HI spectra of the galaxies as broad as possible, and thus making it easier to determine the \vec{L} orientation. We note that this restriction to edge-ons could make reduction of alignments relative to large-scale structure difficult, since we would be restricting analysis to galaxies with \vec{L} in the plane of the sky. However, in this study, the edge-on orientation of the Pisces-Perseus Supercluster means our sample galaxies' \vec{L} lie in the plane perpendicular to the supercluster plane, which is advantageous for reducing the complexity of the analysis. This does reduce our sensitivity to any \vec{L} alignments that lie outside the plane of the sky. For example, if galaxies' \vec{L} are preferentially oriented in a given direction within the plane of the Pisces-Perseus Supercluster (e.g. toward a cluster in the supercluster plane) rather than simply being restricted to that plane, we may not detect such an alignment in our sample, since we restrict \vec{L} of sample galaxies to the plane perpendicular to the supercluster plane. It would be interesting to perform similar observations of a “face-on” version of Pisces-Perseus, where we would then be restricting \vec{L} to the supercluster plane and possibly investigating a new class of \vec{L} alignments. The technique we outline for obtaining spin vector measurements could be applied to quickly obtain \vec{L} measurements for many galaxies in superclusters other than Pisces-Perseus. It is also notable that this technique could be transferred to multi-fiber spectroscopy. By assigning two fibers to each galaxy, one could simultaneously determine the \vec{L} directions of many galaxies much more quickly than a comparable line slit spectrograph observations. No rotation curve information would be available, but it would allow quick collection of

a large sample of well determined galaxy \vec{L} . Our examination of the \vec{L} distribution of galaxies in Pisces-Perseus provides no support for any form of anisotropic \vec{L} distribution. We do not provide confirmation of the possible \vec{L} alignments noted in Paper I for the major-axis distributions of Pisces-Perseus galaxies. Given the relatively small size of the Arecibo sample, rather large anisotropies in the spin vector distribution of the Arecibo sample (see Section 3.4.3) could remain undetected with our technique. We do note that by using a sample of 729 nearly edge-on galaxies from the original MAPS-PP catalog, we feel we can restrict the sinusoidal amplitude of any spin vector anisotropy present to be less than approximately 20% the background ‘random’ distribution, at least in the plane perpendicular to the Pisces-Perseus supercluster ridge. It is unclear at what level galaxy \vec{L} alignments might be expected as no recent simulations have been designed with the goal of estimating galaxy alignments. We expect that if galaxy alignments are produced by large-scale structure formation, the alignments would be strongest in areas of low density, where the relative scarcity of subsequent galaxy-galaxy interactions suggests the initial \vec{L} distribution would be better preserved. However, as noted in the introduction, galaxy alignments can arise from a variety of evolutionary processes, in both high and low density environments. It would be interesting if in modern computer simulations of galaxy evolution, the angular momentum of the resulting galaxies was investigated for \vec{L} alignments and predictions as to the amplitude (and type) of any anisotropies in the \vec{L} distribution were made. As we showed in Section 3.4.3, sample sizes need to be large (on the order of at least 500 galaxies) in order to unambiguously detect weak alignments. There are two paths toward increasing the sample size. We could examine a denser cluster with a greater number of targets satisfying our edge-on criteria such as the Coma cluster. It would be interesting to investigate the possibility of tidally induced galaxy alignments in denser environments as predicted by Ciotti and Dutta [1994] and Ciotti and Giampieri [1998]. The only previous study looking for galaxy alignments in Coma was plagued by stretched imaging [Djorgovski 1987], so alignment results for this cluster are still unclear. Our other option for increasing sample size is to develop a better

understanding of the internal extinction in galaxies so that we could use galaxies of all inclinations. The first author is currently investigating using image parameters of a large number of galaxies obtained using the APS database in order to better determine the internal extinction properties of galaxies.

3.6 Acknowledgements

We would like to thank telescope operators Miguel Boggiano, Willie Portalatin, Pedro Torres, and Norberto Despiau for their good humor and help with observing (And especially Norberto for his “lucky coffee”). JEC would like to thank Chris Salter, Tapasi Ghosh, Jo Ann Etter, and Phil Perillat for helping make his first radio observing experience excellent, both professionally and personally. Travel was sponsored by the National Astronomy and Ionosphere Center (NAIC) and the University of Minnesota Graduate School. This research has made use of the APS Catalog of the POSS I, which is supported by the National Aeronautics and Space Administration and the University of Minnesota. The APS databases can be accessed at <http://aps.umn.edu/> on the World Wide Web. Some data reduction was performed at the Laboratory for Computational Science and Engineering (LCSE) at the University of Minnesota. Information about the LCSE can be found online at <http://www.lcse.umn.edu/>.

Chapter 4

Recent APS Data Reduction Pipeline Improvements

Because the inclination studies in the remaining portion of this thesis are the first major project to take advantage of the improved APS data reduction pipeline and database (called *StarBase2*), I will briefly outline the major changes to the data relative to the original *StarBase*. The improved data reduction pipeline, implemented and debugged in summer of 1997, was initially developed by Greg Aldering. Since then, all online APS fields have been reduced with this improved pipeline, including the 97 fields used in the construction of the Minnesota Automated Plate Scanner North Galactic Pole Catalog (MAPS-NGP). The motivation for the new pipeline was twofold; computational efficiency and an improved catalog. It was realized that some of the routines in the original data reduction pipeline were computationally inefficient. By combining optimization of the original data reduction routines, reducing the level of required human interaction, and moving the data reduction process from our Sun SparcStation 10 to an SGI Indigo (which is a considerably faster computer), the time for data reduction and database creation for a pair of POSS I plates shrank from about 20 hours to on the order of 2 hours! Another motivation for designing a new data reduction pipeline (hereafter the “new pipeline.”) was improved image classification, astrometry, and galaxy photometry.

These changes to the data reduction pipeline, of special importance to this thesis, are outlined below.

4.1 Improved Image Classification

The automatic classification of objects on the plates into either stars or galaxies is achieved in the APS Catalog via an artificial neural network star-galaxy classifier initially developed by Steven Odewahn [Odewahn *et al.* 1992]. The computational problem of image classification comes down to getting a computer to do something a human can do relatively easily; differentiate the pointlike images of stars from the non-pointlike images of galaxies. There are several image parameters obtained from the APS data reduction process which are useful to varying extents, but determining which combination of image parameters best separates stellar from non-stellar images is a complex problem. This problem has been solved by using an artificial neural network (ANN) to determine which combination of image parameters provides accurate image classification. An artificial neural network (ANN) is essentially a computer program which simulates the human ability to take nonlinear combinations of inputs to arrive at the correct answer to some problem. Our image classification ANN works by assigning a table of weights to a set of input image parameters and combinations of image parameters and using this to determine the values of the two output nodes. The output in these two nodes can be (roughly) interpreted as the ANN's estimate of the probability that the object is a star or a galaxy. The advantages of the ANN is that it is robust and can deal well with noisy input data. The ANN determines the best set of weights to use for image classification via a supervised learning technique with the appropriate training set of images that have been classified by a human classifier. We used a technique called "back propagation" to automatically train the ANN to best replicate the results of a human classifier. In the original data reduction pipeline, the training set used to "train" the image classifier was limited by the limits of the human classifiers with POSS I images. Since star/galaxy separation by a trained human classifier for images on the POSS I is

only typically possible down to stellar O magnitudes of about 19.5, there was no way to train the ANN for image classification of objects fainter than $O \sim 19.5$. For images fainter than this human limit, the set of weights used for image classification was simply extrapolated. This meant that while $> 99\%$ of stars with O magnitudes of 12 to 19.5 and $> 95\%$ of galaxies down to $O \sim 19.5$ are correctly classified, the classification accuracy quickly drops as we go fainter, with most objects being classified as stars instead of galaxies (which are known to dominate at fainter magnitudes). The artificial neural network has been retrained all the way to the plate limit by using objects identified as galaxies from the Infante catalog of Faint Objects at the North Galactic Pole [Infante and Pritchett 1995]. The Infante catalog was built using deeper plate material, allowing human classification of much fainter galaxies. Cross-identification of Infante’s deeper galaxy catalog with the APS catalog allowed development of a training set that extended (accurately) all the way down to the plate limit. The only remaining classification problems are classification of the brightest objects (which while improved in the new catalog by use of the diffraction “spike” parameter, still suffers from the lack of a large training set of images) and the classification of blended star-star and star-galaxy images.¹

4.2 Improved Astrometry

The technique used to map scanned plate-based positions for objects into positions on the sky is called astrometry. The astrometric routine used by the APS catalog was initially written by Bill Zumach, but now includes very extensive revisions by Greg Aldering. The APS astrometric solution in the original APS data reduction pipeline was derived by mapping the SASORT reported image centers of Lick Proper Motion (Lick NPM1) catalog stars to positions reported in that catalog.² Typical residuals between

¹The problem of blended images is currently being investigated as part of APS research into automated morphological classification of galaxy images.

²The SASORT reported image centers roughly correspond to the center of the best-fit ellipse, determined via a moments analysis of the image.

APS plate positions to the Right Ascensions and Declinations of the NPM1 are approximately $0.3''$, for stars. Unfortunately for galaxies, their positions were considerably less accurate, in part because of their extended nature. The major improvement made to the astrometric reduction process in the new pipeline is that the solution is now based on the median centroid from the background subtracted pixel data for both stars and galaxies. While not dramatically affecting the computed central positions of stellar images, this median centroid provides much more accurate and consistent astrometry for large galaxy images than was possible using the SASORT positions.

4.3 Improved Galaxy Photometry

Obtaining accurate photometry from POSS I plates is a nontrivial problem. The emulsion on photographic plates is a collection of silver halide grains which react to incoming photons during exposure of the plate to starlight while in the telescope. The developing process “fixes” the state of the grains, making those that have reacted with incoming photons opaque and washing away the undeveloped grains. The density of the silver halide grains, D , is determined by measuring the transmittance of a laser, T , through the plate material such that,

$$D = -\log T. \quad (4.1)$$

The density of these silver halide grains depends on the number of photons that have interacted with the grains on the plate before developing. The characteristic curve describing density versus intensity of incoming light (shown in Figure 4.1) can typically be divided into several regions; the “fog”, the “toe”, the linear region, and “saturation.” All photographic emulsions have a minimum density called the “fog.” This minimum density is due to the simple fact that the undeveloped grains are not completely transparent. Once we start increasing the intensity of incoming photons, the density of the grains will start to change. There is a minimum finite intensity necessary to start grain reactions in the emulsion. Upon exceeding this minimum intensity, the grains start to react. This

point in the density-to-intensity curve is called the “toe.” The density of the emulsion rises slowly with increasing intensity. Eventually, we reach the linear part of the curve, where density rises linearly with respect to the logarithm of the intensity. The slope of this curve, called its “contrast,” reaches its maximum in the linear region. Finally, if we keep increasing the intensity, we reach an upper limit to the density, D_{max} , which occurs when all the grains in a region have interacted with photons. This part of the curve is typically referred to as “saturation,” and indicates that we can no longer detect any increase in intensity of photons with this photographic material, since all the grains have already reacted. For photometry of images classified as stellar, the APS data

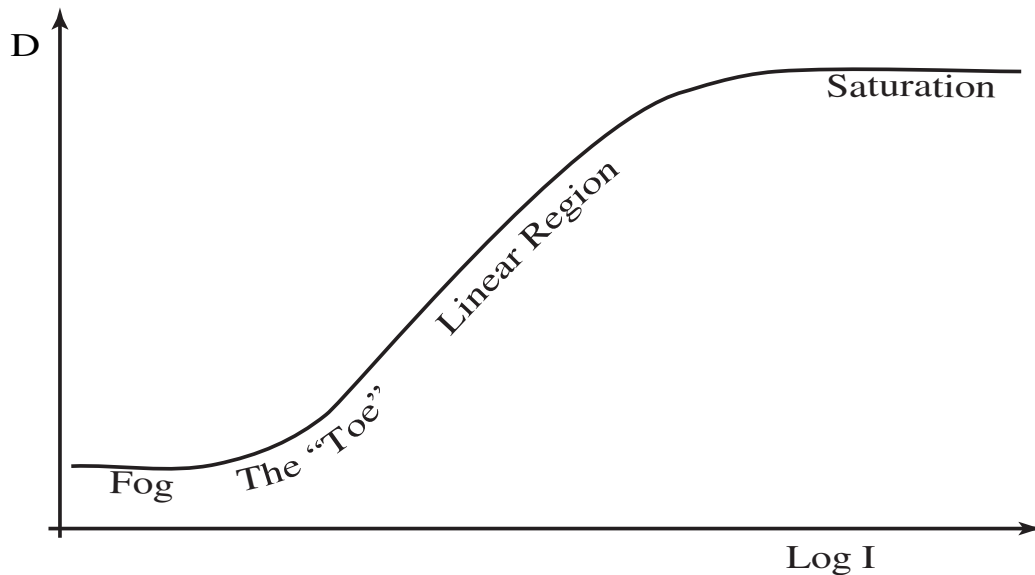


Figure 4.1: This diagram illustrates the response of a photographic emulsion to light. The density of the silver halide grains that react to light is initially constant as there is a minimum number of impinging photons necessary before the density rises above its minimum “fog” value. The rate of increase of density with intensity is initially non-linear, called the “toe” of the characteristic curve. As the intensity of light increases, the emulsion enters a linear region where intensity and grain density have a linear relationship. If we increase the intensity of light beyond the limits of the linear region of the characteristic curve, most of the silver halide grains will have reacted and “saturation” occurs. Any additional increase in the number of impinging photons will not increase the density beyond the maximum density, D_{max} .

reduction software avoids the problem of fitting a density-to-intensity relationship by

using a simple relationship between the isophotal diameter of a stellar image compared to an independently measured magnitude. A diameter-magnitude relationship is expected for stars because they are essentially uniform in profile and the shape of the point spread function (PSF) is constant across the plates, only scaling with respect to the brightness of the star. Since APS diameters are determined at one surface brightness level, by sampling many stars of differing brightness, we can essentially map out the shape of the PSF. As Larsen [1996] pointed out, any function that fits the PSF should also fit the diameter-magnitude relationship. The function that was assumed (by Aldering) for the diameter-magnitude relation has the form:

$$Magnitude = SB_0 + 2.5 \log \left(\left(\frac{Diameter}{r_0} \right)^\beta + \left(1 + \left(\frac{Diameter}{r_m} \right)^2 \right)^\gamma \right). \quad (4.2)$$

in which we have a Moffat profile of core radius r_0 and exponent β and wings represented with a power law of core radius r_m and exponent γ . On each plate, a set of photometric standard stars is used and their diameters compared to their known magnitudes, allowing plate-by-plate calibration of the relationship between the diameters and magnitudes via the Marquardt-Levenberg non-linear least-squares fitting method [Press *et al.* 1992]. Once the diameter-magnitude relationship is fit on each plate, that function is used to determine the magnitudes of all images classified as stars. This method was developed by Jeffrey Larsen and is described in more detail in his Ph.D. Thesis [Larsen 1996]. Photometry of galaxies is a bit more complicated. Galaxies appear as extended images on the POSS I plates, and therefore in order to determine their total brightness, we must integrate the flux over the entire image. There does not exist a simple magnitude-diameter relationship for these images because their appearance is *not consistent*. Therefore, we must have a good understanding of the density-to-intensity (D-to-I) relationship for a given plate in order to convert the known grain densities in the extended image into corresponding intensities of incoming light, which can be then integrated to determine a total brightness for the galaxy. In the original data reduction pipeline, the method for determining a plate's D-to-I relationship was developed by Steven Odewahn. It operated by comparing the image density data to available stellar photometry or galaxy surface

photometry. The more fundamental technique was to compare the APS galaxy surface brightness profiles with those from high quality CCD imaging to determine a simple D-to-I relationship. However, for many fields, detailed galaxy surface photometry was (and remains) unavailable, so in those cases Odewahn implemented a technique introduced by Bunclark & Irwin [1983] in which the D-to-I relationship is determined by comparing stellar PSF profiles over a wide range of magnitudes. This was done by minimizing the scatter among flux normalized stellar brightness profiles and fitting the function

$$\log I = \alpha + \beta D. \tag{4.3}$$

by solving for the best-fit β value fit, then dealing with the zero-point, α (see Odewahn & Aldering 1995 for more complete description). Difficulties exist with this technique for determining a plate's D-to-I relationship. The pixel data used for this fitting was not background subtracted and thus would always suffer from a zeropointing error. The method relied on obtaining a large number of stellar profiles for bright stars, where the image classifier is less than 99% accurate, which meant that the procedure needed to be interactive in order to allow user removal of contaminating galaxies before solving for β and α . Furthermore, the scatter minimization often resulted in a degenerate solution of $\beta = 0$. Hence, the solution of the best-fit parameters to equation 4.3 was not very robust. Even in those cases where a good solution to equation 4.3 is obtained, we know that this equation is a simplistic model for the behavior of the photographic emulsion. A better model for the response of the photographic emulsion could lead to a better fit to the density to intensity relationship. An additional property of plates not considered in equation 4.3 is that as an exposure progresses and grains have reacted with incoming photons, the number of grains available to react with subsequent photons is diminished. Thus the sensitivity of an emulsion as a function of exposure time must drop exponentially in the transition between the linear region of the D-to-I curve and saturation. These two properties are combined into a relationship between the intensity

of incoming photons, I , and the density of the reacted grains of

$$D = D_{max} \left(1 - e^{-\alpha I} \right). \quad (4.4)$$

However, it turns out that photographic emulsions suffer from reciprocity failure and a number of other effects which can break the relationship between the incoming intensity of photons and the density of developed grains. This can be accounted for by allowing a slightly non-linear relationship of I of the form:

$$D = D_{max} \left(1 - e^{-\alpha I^{\beta\gamma}} \right). \quad (4.5)$$

where the exponent βI^γ reflects the fact that I is non-linear and that the non-linearities themselves are associated with the intensity. An improved D-to-I calibration has been developed by Greg Aldering and Jeff Larsen. The new D-to-I calibration technique uses the background subtracted magnitude pixel data for both stars and galaxies, unlike the previous D-to-I calibration. The background values for the density, D_{sky} , are obtained from the flat-fielded, gain-corrected MBACK, which is a low-resolution background scan done prior to the high-resolution scan. Finally, the improved D-to-I calibration actually uses the more accurate photographic emulsion model of equation 4.5. The solution for α , β , and γ in equation 4.5 is obtained using the density profiles of large images classified as stars. Rejection of misclassified galaxies is done by comparing the density profiles of all images relative to their mean density profile. Outliers, presumably galaxies which have very non-stellar density profiles, are rejected and the mean density profile is refined. It should be noted that since we are working with images of bright objects the vast majority of objects are stars, so automated rejection of outliers is a very safe procedure for eliminating galaxies from the sample. Solving for α , β , and γ given the mean density profile is done using the Marquardt-Levenberg non-linear least-squares fitting method [Press *et al.* 1992]. The zero point, α , is set by the photometric standards. It should be noted that $I = I_{object} + I_{sky}$, where in this model the intensity of the sky, I_{sky} , is a free parameter which is determined by finding the appropriate value of I_{sky} given the background density D_{sky} , which is known from the MBACK scan. This method also

provides an estimate for the seeing on that plate. Once the D-to-I relationship for a plate has been determined in this manner, the density data is used to derive an integrated magnitude, *magi*, for each object on the plates.

4.4 *StarBase2*: Database Content Changes

With the improved data reduction pipeline, we also took the opportunity to implement an improved online database, *StarBase2*. The data in *StarBase2* come from the new pipeline, so they include all the improvements to astrometry, photometry and image classification outlined earlier. In addition to improvements in the data, there were also two major changes in *StarBase2* versus *StarBase* (the original APS online database) in terms of its behavior as a database. Given that *StarBase2* was the source database for the MAPS-NGP, I will briefly outline the changes made to the database itself. *StarBase2*, like the original *StarBase*, automatically selects the appropriate magnitude from between the two photometry techniques used based on the image's classification. If the image is classified as a star, the magnitude determined via the magnitude-diameter relation, called *magd*, is used. For images identified as galaxies, then the new D-to-I calibration-based magnitude, called *magi*, is used instead. However, with *StarBase2*, the user can also request the other magnitude in the query. Therefore, if an object is later found to have been misclassified, the appropriate magnitude estimate is still available. One final improvement is that *StarBase2* provides the unique ID number of the matching object on the other color plate. This makes cross-identification of objects between plates covering the same field much easier, and avoids the issue of reproducing the work already done to produce the APS catalog, since every object in the APS catalog must (by construction) have been identified on both the O and E plates. As of Summer of 1999, *StarBase2* has supplanted *StarBase* as the database provided by the APS online. Its improvements have been thoroughly used in the latter half of this thesis, especially the improvements in galaxy photometry and astrometry.

Chapter 5

Creation of a Large Extragalactic Catalog: The MAPS-NGP Catalog

Astronomy is perhaps the science whose discoveries owe least to chance, in which human understanding appears in its whole magnitude, and through which man can best learn how small he is.

G. C. Lichtenberg (1742-99), German physicist and philosopher

I have constructed a large major-axis diameter-limited catalog using the Minnesota Automated Plate Scanner (APS) catalog for a statistical study of the properties of galaxies. As noted previously (section 2.9) and as discussed more thoroughly in Section 6.5.1), the APS catalog, which uses threshold densitometry scans of the Palomar Observatory Sky Survey (POSS I) plates, does not suffer from measurement biases due to human physiology. This is a great advantage for the APS Catalog versus most previous galaxy catalogs, such as the Uppsala General Catalog (UGC) and Third Reference Catalog of Bright Galaxies (RC3). This machine-measured catalog presents an opportunity to build a large, isophotal diameter-limited galaxy catalog, something that can not be reliably done using galaxy catalogs based on visual diameter estimates. For this study, I intentionally restricted myself to working with galaxies in fields within 30° of the North

Galactic Pole (NGP). There are two main motivations for this restriction. First, it is known that Galactic extinction is rather small over most of this region and therefore its effects on the appearance of galaxies would be minimal (see section 5.9 for estimates of Galactic Extinction in the MAPS-NGP). We also know that blended stellar images will often be misclassified as galaxies. However, the number of blended stellar images reaches a minimum as you examine POSS I plates at higher galactic latitude, so while this contamination can not be easily eliminated, our restriction of working near the NGP minimizes the problem. Because of these restrictions on the catalog, this catalog came to be called the Minnesota Automated Plate Scanner North Galactic Pole (MAPS-NGP) catalog. There are several caveats in building a major-axis diameter-limited catalog with the APS catalog. Because of its immense size (the final APS catalog is expected to contain image parameter descriptions of over 10^8 objects), the APS catalog is not stored as a sequential data file, but rather as a hashed series of several thousand database record files. Thus in order to build a large catalog, one must make repeated queries of the APS database software, *StarBase2*. And while the restriction to high Galactic latitude minimizes the presense of blended images in the final catalog, I have also identified certain features on the POSS I plates, such as scratches, the diffraction halos around bright SAO stars, ghost images due to internal reflection of SAO stars, blended images of stars in globular clusters, and the regions around certain low surface brightness features of some bright galaxies, which can cause ‘false’ galaxies to be found on the plates. These identifiable false galaxies had to be removed from the final catalog before science could be done. Finally, the photographic plates comprising the POSS are not uniform. The limiting surface brightness ($\mu_{threshold}$) on the plates can vary by a couple of magnitudes from plate to plate (e.g. See Table 5.1). This means that the limiting isophote for the major-axis diameters we measure will vary from plate to plate. Therefore, this catalog will not be a truly diameter-limited catalog but will rather be an *approximately* isophotal diameter-limited catalog. Attempts to correct image parameters for these variations in limiting surface brightness can be made, but this is dealt with after the initial

MAPS-NGP catalog is created. Below I outline the procedure for creation of the initial MAPS-NGP catalog. Note that most of the later work exploring internal extinction in galaxies relies on distance estimates to galaxies, and so a subset of the MAPS-NGP (cross-identified with existing redshift catalogs) is used. This chapter instead focuses only on the techniques used to construct a large diameter-limited catalog from the APS database.

5.1 Initial Selection Criteria for *StarBase2* Queries

I initially identified the 98 POSS I fields which lie (at least in part) at Galactic latitude $b > 60^\circ$. These fields and their basic plate properties are listed in Table 5.1. Of these 98 fields, one field (P616) was unavailable for data reduction, leaving 97 fields online in *StarBase2* which met the initial $b > 60^\circ$ requirement (See Figure 5.1). As seen in Figure 5.2, there are considerable plate to plate variations in the seeing and limiting surface brightness ($\mu_{threshold}$) of the APS scanned images. The variations in seeing can strongly affect the mapping of image axial ratios to galaxy inclinations for small images (e.g. those of size on the order of a few seeing disks). Variations in $\mu_{threshold}$ mean that the isophote to which the diameter of each MAPS-NGP object is measured varies on a plate to plate basis. These plate-to-plate variations are one of the issues that will have to be considered in any analysis of the isophotal diameter distribution of the MAPS-NGP.

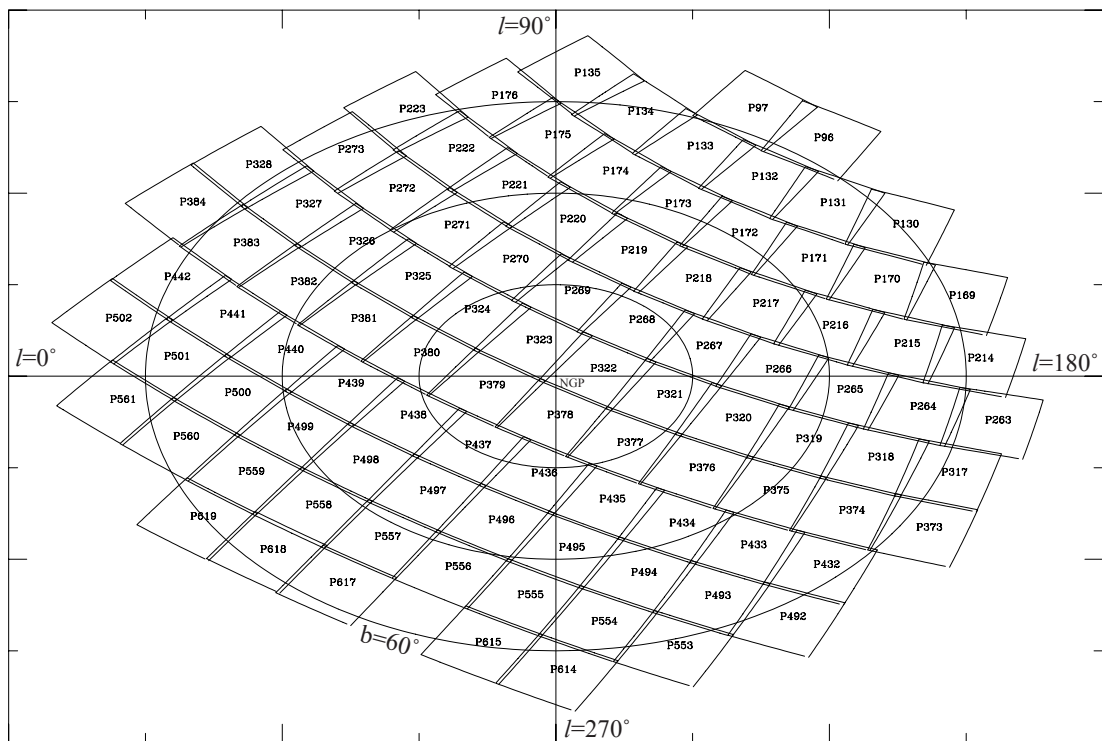


Figure 5.1: This map shows the placement of the 97 MAPS-NGP POSS I fields on the sky in Galactic coordinates.

Table 5.1: The 98 POSS I fields in the MAPS-NGP Catalog

APS Project	POSS ID	l ($^{\circ}$)	b ($^{\circ}$)	N_{Stars}	$N_{Galaxies}$	Seeing ($''$)		μ_{sky}		μ_{thresh}	
						O	E	O	E	O	E
322	64	169.94	86.92	59702	57065	2.99	3.14	22.68	22.13	23.22	22.82
323	1393	65.36	85.99	55069	46925	2.99	2.60	23.27	22.31	24.06	22.93
378	1435	271.82	85.44	39318	27584	2.45	2.74	23.37	22.38	24.01	22.48
379	1581	345.89	84.74	42147	34359	2.60	2.84	23.52	22.34	23.40	22.40
321	1398	196.28	81.78	41367	33437	2.84	2.45	23.18	21.56	23.79	22.82
268	105	134.95	81.73	37590	29497	2.60	2.94	22.49	22.94	23.06	22.67
377	135	236.70	80.94	50811	46113	2.40	2.74	23.11	22.83	23.09	22.87
269	110	97.11	80.91	52683	44021	2.70	2.94	22.95	22.24	23.64	22.41
324	131	48.48	80.66	52169	40718	2.84	2.99	23.74	23.71	23.64	22.87
437	1572	308.13	80.05	38166	26014	3.04	3.09	23.19	24.12	23.14	22.98
380	125	12.75	79.86	47680	36702	2.70	2.99	23.25	22.83	22.49	22.61
436	1576	276.78	79.03	32553	20032	2.60	2.70	23.37	22.24	23.32	22.22
267	1599	164.46	78.84	34119	24311	2.30	2.30	23.52	21.68	24.60	23.03
438	80	337.22	78.22	57190	41208	2.84	2.74	23.37	21.86	23.67	22.85
270	116	74.81	77.08	53125	47952	2.60	2.55	22.20	22.43	23.04	23.09
320	1379	200.70	76.21	36774	27172	2.70	2.40	23.61	21.47	24.44	22.67
435	89	254.98	75.78	43240	34705	2.70	2.50	22.03	22.28	22.32	22.89
218	115	133.93	75.62	36916	29017	2.65	2.79	23.41	22.63	23.06	22.54
219	133	111.39	75.56	47295	39315	2.94	2.74	23.00	22.77	23.30	22.62
376	103	225.21	75.46	58374	59580	2.74	3.82	23.70	21.95	24.20	22.69
325	86	45.19	75.07	61453	52212	2.50	2.74	23.77	22.67	24.11	22.93
439	1019	355.98	74.54	52463	40872	2.65	2.70	23.09	22.48	23.44	22.88
381	68	22.47	74.33	47765	34454	2.84	2.50	22.47	22.02	22.76	22.78
266	109	178.40	74.17	52615	50315	2.50	2.70	23.05	21.86	23.28	22.78
497	41	306.36	74.06	51978	38516	2.84	2.65	24.08	24.86	23.68	23.11
496	1563	285.44	73.39	35929	20568	2.55	2.40	21.99	21.43	22.51	22.85
217	1367	152.90	73.27	35612	25995	2.50	2.74	22.75	23.63	22.42	22.59
220	154	92.69	73.13	41221	30124	2.30	2.65	23.55	22.19	23.25	22.40
498	1420	326.59	72.82	55812	43193	3.14	2.99	22.32	21.33	23.49	22.84
271	106	64.70	72.09	44415	31726	2.70	2.55	22.11	21.71	22.82	22.91
434	1406	241.75	71.43	36387	25615	2.74	2.50	22.29	22.22	22.28	22.67
495	1385	267.82	70.98	48482	34617	2.79	2.74	23.72	22.68	24.57	23.07
319	99	201.65	70.59	50780	46827	2.74	3.23	23.64	21.85	24.54	22.71
499	1079	342.97	70.00	51511	34041	3.14	2.50	23.21	21.21	22.96	22.11
440	81	7.45	70.00	59716	45107	2.79	2.70	23.74	22.48	24.28	22.80
375	1353	219.26	69.78	47256	41125	2.65	2.84	22.99	22.43	23.86	23.15
172	1408	131.02	69.67	36603	25589	2.35	2.60	24.00	22.57	23.52	22.81
173	1350	114.62	69.63	42138	30618	2.65	2.70	22.45	23.61	23.12	22.61
326	70	44.59	69.46	63207	47662	2.74	2.55	23.80	22.55	23.77	23.38
216	719	165.31	69.34	43634	31380	2.70	2.65	22.87	22.06	23.49	23.03
221	1386	80.49	69.15	44806	31638	2.70	2.35	23.91	21.51	24.60	22.84
265	695	184.81	68.88	43469	33400	2.99	2.25	22.32	22.57	22.86	23.70
382	61	27.91	68.63	69710	54483	2.60	2.84	22.23	22.66	23.52	23.09
557	104	305.54	68.07	51923	35903	2.84	3.23	24.04	21.09	24.02	21.76
171	1338	145.70	67.66	34459	26032	2.60	2.84	22.03	22.88	21.70	22.21
556	1560	289.76	67.56	48887	35595	2.55	2.89	22.45	24.29	23.03	22.55
174	1593	100.07	67.56	30113	17383	2.70	2.79	21.93	24.18	21.91	22.43
494	468	254.59	67.44	46124	37652	4.07	3.04	22.00	21.56	22.41	22.12
558	1561	321.05	67.12	47598	31723	2.65	1.91	23.05	22.65	23.10	22.25
272	127	59.93	66.67	60422	49221	2.60	2.79	22.80	24.63	23.09	23.01
433	51	233.23	66.60	46157	36302	2.70	2.74	22.87	22.80	23.16	23.50
500	1051	354.91	66.20	52166	32578	2.99	2.99	22.24	21.73	22.76	22.54
555	1611	275.44	65.69	42936	32141	2.79	2.70	22.83	21.24	23.65	22.57
441	1417	15.04	65.08	56337	37297	2.30	2.79	22.86	21.81	23.40	22.49
318	1357	201.43	64.96	42651	34676	2.70	2.84	23.08	22.25	24.08	22.81
559	90	334.70	64.89	70613	50276	2.89	2.45	24.50	22.49	24.31	23.23

APS Project	POSS ID	l ($^{\circ}$)	b ($^{\circ}$)	N_{Stars}	$N_{Galaxies}$	Seeing ($''$)		μ_{sky}		μ_{thresh}	
						O	E	O	E	O	E
215	1349	172.66	64.56	44995	36585	2.84	2.94	22.90	21.90	22.99	22.37
222	145	73.35	64.34	58781	44519	2.74	2.70	22.65	22.56	22.91	23.29
170	700	156.58	64.10	38424	27864	2.89	2.84	23.60	25.41	23.40	23.66
374	1366	215.24	64.06	45973	37054	2.79	2.70	24.14	23.21	23.71	22.65
175	120	89.32	63.95	56334	47768	2.84	2.84	23.24	22.38	23.53	22.91
132	729	124.58	63.91	51976	48959	2.60	2.79	23.12	22.34	24.18	23.07
327	1390	44.94	63.82	55960	36077	2.65	2.79	23.46	22.89	23.66	23.13
264	731	187.83	63.35	40650	29731	2.89	2.70	23.64	22.55	24.14	23.60
133	675	112.13	63.20	47171	37178	2.89	2.79	22.12	21.81	23.06	22.72
493	66	244.89	63.17	43545	30146	2.70	2.74	22.08	23.99	22.63	22.91
383	102	31.70	62.89	67002	54955	2.84	2.60	22.07	20.75	22.61	22.65
131	1389	136.79	62.79	42484	30870	2.89	2.65	23.37	22.37	23.86	22.89
554	495	263.48	62.74	41611	32499	2.84	2.70	23.22	21.68	23.65	22.27
617	1578	305.06	62.07	35901	32890	2.55	2.60	24.07	19.98	22.52	19.69
501	65	3.78	61.80	76170	58247	2.60	2.70	23.05	22.57	23.11	22.93
560	96	345.91	61.68	63999	42134	2.74	2.65	22.59	21.76	23.20	23.11
616	1405	292.35	61.66	—	—	—	—	—	—	—	—
432	463	227.22	61.53	43051	31969	3.09	3.43	23.50	21.85	23.91	22.35
618	1595	317.66	61.43	51383	34395	2.84	2.60	22.41	20.96	23.10	22.25
273	1610	57.74	61.08	42715	25516	2.40	2.45	21.63	21.57	22.25	22.28
134	1409	101.36	60.81	44719	30353	2.74	2.79	22.39	22.19	23.06	22.86
615	1401	280.41	60.13	46574	30890	2.65	2.84	21.94	22.71	22.05	22.56
130	59	147.03	60.05	56352	50356	2.70	2.70	22.31	22.26	23.03	23.37
442	54	20.55	59.96	88312	73916	2.84	2.55	23.83	22.46	24.36	23.00
169	709	163.82	59.55	56416	51014	2.70	2.74	22.31	21.30	23.27	22.73
619	465	329.19	59.47	64414	42662	2.74	2.65	22.49	21.79	23.00	22.11
176	1368	82.13	59.36	48794	31727	2.74	3.04	22.77	22.47	23.31	22.56
317	1387	200.66	59.35	42150	29168	2.89	2.50	23.61	21.89	23.99	22.77
214	690	176.88	59.35	48487	41476	2.99	2.94	23.91	22.40	24.05	22.75
223	1371	69.23	59.12	46935	24909	2.74	2.65	22.28	22.16	22.67	22.66
553	1392	253.86	59.01	49613	36226	2.94	2.65	23.18	21.66	24.17	22.97
492	976	237.58	58.51	43156	27661	2.74	2.65	23.61	21.64	24.06	22.92
373	1380	212.10	58.31	41671	29812	2.65	2.89	22.95	24.08	23.62	22.33
328	1092	45.78	58.20	64889	43007	2.60	2.79	23.47	22.19	23.92	22.94
96	1427	126.97	57.80	47078	34653	2.84	2.50	22.73	21.30	23.41	22.65
561	1418	354.89	57.78	73514	48218	3.04	3.43	23.04	21.77	24.26	22.78
263	1032	189.13	57.72	42912	30212	2.65	2.65	24.07	23.18	23.90	22.73
614	471	269.83	57.63	59678	47373	2.55	3.19	21.91	20.48	22.29	21.02
97	704	116.67	57.57	49020	33755	2.70	2.74	21.88	22.69	23.02	23.51
384	87	34.73	57.15	65765	44923	2.89	2.60	22.31	22.50	22.82	22.87
135	715	93.23	57.13	50082	32231	2.55	2.74	22.47	22.94	22.57	22.85
502	1087	10.52	57.03	69476	46157	2.70	3.43	24.36	22.33	23.98	22.76

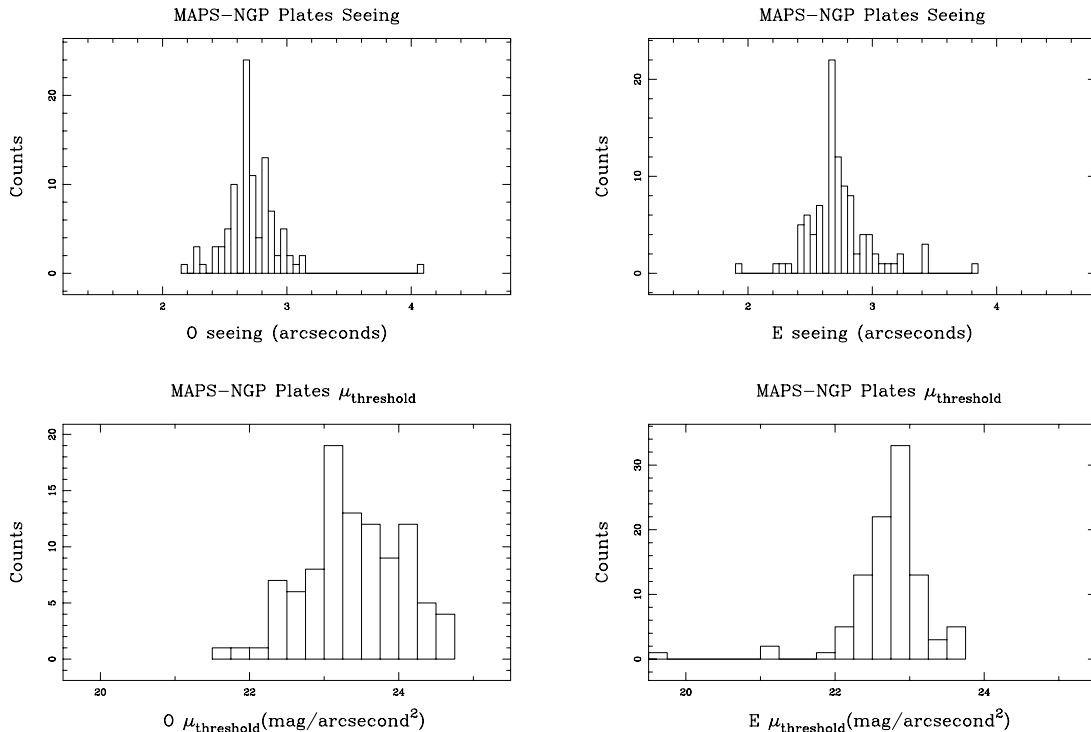


Figure 5.2: These plots show the distribution of seeing and APS scanning threshold surface brightness ($\mu_{\text{threshold}}$) values for the 194 POSS I plates composing the MAPS-NGP. These values are also listed in Table 5.1. These values are only available for POSS I plates in *Starbase2* because they are computed by the new density-to-intensity algorithm described in Section 4.3.

A custom piece of software, *NGPbatch*, was written to automatically handle the querying of the *StarBase2* database, the cross-identification of objects between the two plate colors, and the reorganization of the data into a custom binary datafile format to conserve hard drive space. Initially, *NGPbatch* performed 194 successive *StarBase2* queries, one for each plate in the region of the MAPS-NGP (97 fields, one O and one E plate for each field). The query requested all O plate objects fulfilling all of the following criteria:

- The O plate object must be classified as 'galaxy' (APS image classification is determined from O plate image parameters).
- The O plate object's ellipticity must be less than 0.9. This criteria is designed to prevent the inclusion of scratches on one plate which have been cross-identified

with a real object on the E plate. Any real objects cross-identified with scratches would have image parameters which are suspect. This should not exclude any real galaxies as spiral galaxies have maximum observed ellipticities of approximately 0.8.

- The object’s magnitude must be greater than 0.0. Objects for which photometry failed for some reason or another are assigned magnitudes of -1. These objects have suspect image parameters and so are rejected from the catalog.
- The O plate object’s diameter must be greater than 129 Encoder Resolution Elements (ERE). This value was chosen to ensure that all objects with major-axis diameters greater than 10'' were included in the initial cut. “Diameter” as reported by *StarBase2*, dia_{APS} , is really a measure of the surface area of the object. The dia_{APS} is calculated from the surface area, A , under the assumption that the image is circular, such that

$$dia_{APS} = \sqrt{\frac{4A}{\pi}} \quad (5.1)$$

Therefore, to convert the *StarBase2* diameter, d_{APS} , into major-axis diameter, d , we use the equation for the surface area of an ellipse with semimajor-axis a and semiminor-axis b :

$$\begin{aligned} A &= \pi ab \\ &= \pi a^2(1 - \epsilon) \\ &= \frac{\pi d^2(1 - \epsilon)}{4}, \end{aligned} \quad (5.2)$$

where ϵ is the ellipticity of the ellipse. Combining equations 5.1 and 5.2 we find

$$d = \frac{d_{APS}}{\sqrt{1 - \epsilon}} \quad (5.3)$$

Therefore, with a maximum ellipticity, ϵ , of 0.9, and minimum desired major-axis diameter, d , of 10'' and a scale of 40.8 ERE per arcsecond, we arrive at a minimum *StarBase2* diameter of 129 ERE for our sample.

For the E plate queries, the same query limits were used except that a minimum diameter of zero was required.¹ Once the *StarBase2* queries for a given field were completed, the O plate diameters are converted into major-axis diameters in arcseconds and an O plate major-axis diameter limit of 10'' imposed on objects flagged for inclusion in the final catalog. The flagged O plate objects are cross-identified with the E plate objects and image parameters from both plates are recorded for later study. The final result of *NGPbatch* is a galaxy catalog containing image parameters from both the O and E plates for 249238 objects identified as galaxies on the 97 online O plates within 30° of the NGP with O plate major-axis diameters greater than 10''. In the initial catalog produced by the *NGPbatch*, there has been no effort to eliminate misclassified or duplicate objects outside of plate scratches (which show up as objects of exceptionally high ellipticity). The remaining work necessary to finish the MAPS-NGP catalog's creation involves cleaning out duplicates and objects that are likely to have been misclassified as galaxies due to artifacts of the scanning and/or data reduction process.

5.2 Elimination of Duplicate Objects from Plate Overlap Regions

The first major modification to the initial catalog involved the elimination of duplicate objects in the catalog. The *StarBase2* catalog contains many duplicate objects because there are regions of the sky where two or more POSS I plates overlap. In order to make sure the MAPS-NGP contains only unique objects, a positional search was performed to identify any objects which overlapped within their respective diameters. For such objects, since there was no simple criterion for determining which object had the better measured image parameters, the object closest to its respective plate center was kept and

¹This diameter limit will eliminate some very large galaxies from the sample, since their images were too large to be loaded into SASORT's image array. These images that could not be loaded into SASORT were assigned a diameter of -1. This will be important later when the MAPS-NGP is cross-identified with pre-existing galaxy catalogs.

the other matches were deleted from the MAPS-NGP catalog. Duplicates elimination removed 11011 objects from the MAPS-NGP.

5.3 Elimination of False Galaxies from Bright Star Halos

To reduce the possibility of inclusion of plate defects in the APS catalog, the APS catalog has the requirement that all objects must be present on both the O and E plates. However, there are several situations in which plate defects can occur co-positionally on both plates, leading to misidentification of plate defects as true objects. One such situation occurs with the diffraction halos around bright stars which will appear on both plates (see Figure 5.3) and often end up being classified as a cluster of galaxies. This was a recognized problem in the construction of the APS catalog and there is a stage in which interactive removal of these bright star halos occurs. However, this interactive editing is usually applied only to the brightest stars (those brighter than approximately magnitude 4), so any contamination around fainter stars must still be considered. Therefore, I edited the regions around every *Smithsonian Astrophysical Observatory Star Catalog* [1966, hereafter SAO] star. The SAO lists almost all stars brighter than 9th magnitude and should provide the locations of all significantly bright stars. To make automatic removal of false galaxy counts around SAO stars possible, I needed to determine the relationship between the SAO magnitude, m_{SAO} , and the angular radius, $r_{false}(m_{SAO})$, at which the galaxy counts around SAO stars drop back down to the background sky level. This was done by first performing *StarBase2* queries of large regions around a small sample of SAO stars to make an initial estimate for the $r_{false}(m_{SAO})$ function. Using this estimate, a second batch of *StarBase2* queries covering smaller regions around several thousand SAO stars can be performed in a reasonable amount of time.

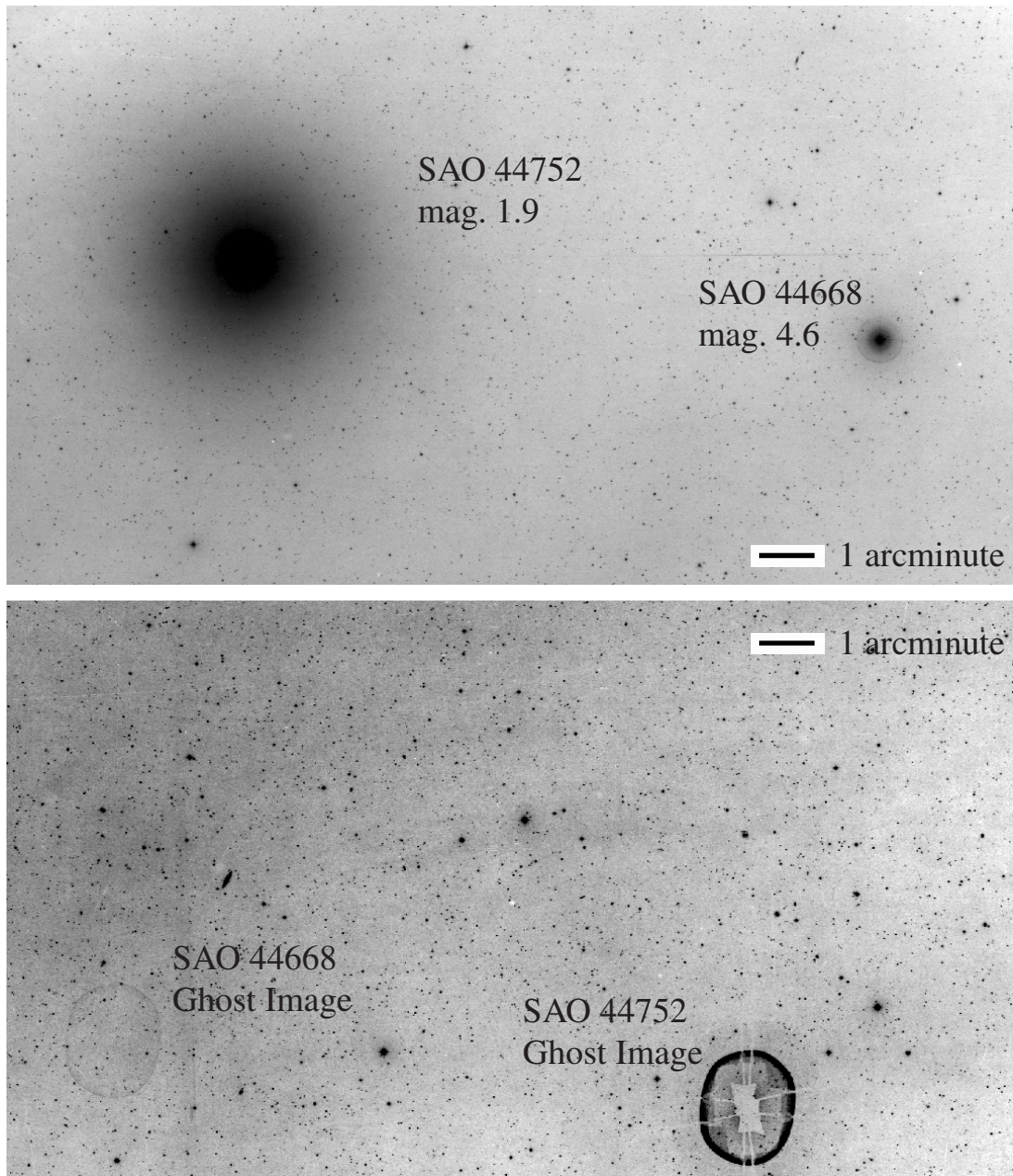


Figure 5.3: The top image in this pair of images from the O plate of P174 shows two relatively bright SAO stars, the 1.9 magnitude SAO 44752 and the 4.6 magnitude SAO 44668. Notice that the halo of the brighter SAO star is much larger. The bottom image shows the ghost images due to internal reflection of the light from these two stars off of the emulsion, then off the corrector plate, and back onto the emulsion on the other side of the plate. Note that while the ghost image of the fainter SAO 44668 is much fainter, it is the same size as the ghost image from the much brighter SAO 44752.

To make the initial estimate for $r_{false}(m_{SAO})$, I queried *StarBase2* and retrieved all the O plate objects identified as galaxies (with no diameter limit) within a $900''$ of a subsample of SAO stars in the MAPS-NGP region. These query results were used to make a plot of the surface density of galaxies versus angular separation from SAO stars for a variety of SAO magnitudes (binned in 0.2 magnitude wide bins). These plots allowed me to make an initial visual estimate of the angular separation, $r_{viscutoff}(m_{SAO})$, at which the surface density of galaxies drops down to the background level of galaxies. This estimate of $r_{viscutoff}(m_{SAO})$ was fit by the 3^{rd} order polynomial:

$$r_{viscutoff}(m_{SAO}) = -3.0285m_{SAO}^3 + 84.943m_{SAO}^2 - 808.67m_{SAO} + 2659.6. \quad (5.4)$$

I then performed a much more extensive second series of *StarBase2* queries, retrieving all galaxies within $r_{test}(m_{SAO})$, of all SAO stars in the MAPS-NGP field where

$$r_{test}(m_{SAO}) = \left\{ \begin{array}{c} 600'' \\ 6r_{viscutoff}(m_{SAO}) \\ 2700'' \end{array} \right\}, \text{ if } \left\{ \begin{array}{l} r_{viscutoff}(m_{SAO}) < 100'' \\ 450'' > r_{viscutoff}(m_{SAO}) > 100'' \\ r_{viscutoff}(m_{SAO}) > 450'' \end{array} \right. \quad (5.5)$$

I multiplied $r_{viscutoff}(m_{SAO})$ by six in order to ensure that I was searching far enough from the SAO star to get to regions unaffected by the SAO halo while at the same time restricting the *Starbase2* queries to a manageable region of the sky. These *StarBase2* query results were used to compute the surface density of galaxies in the APS catalog versus angular separation from the SAO star and SAO star magnitude (See Figure 5.4).

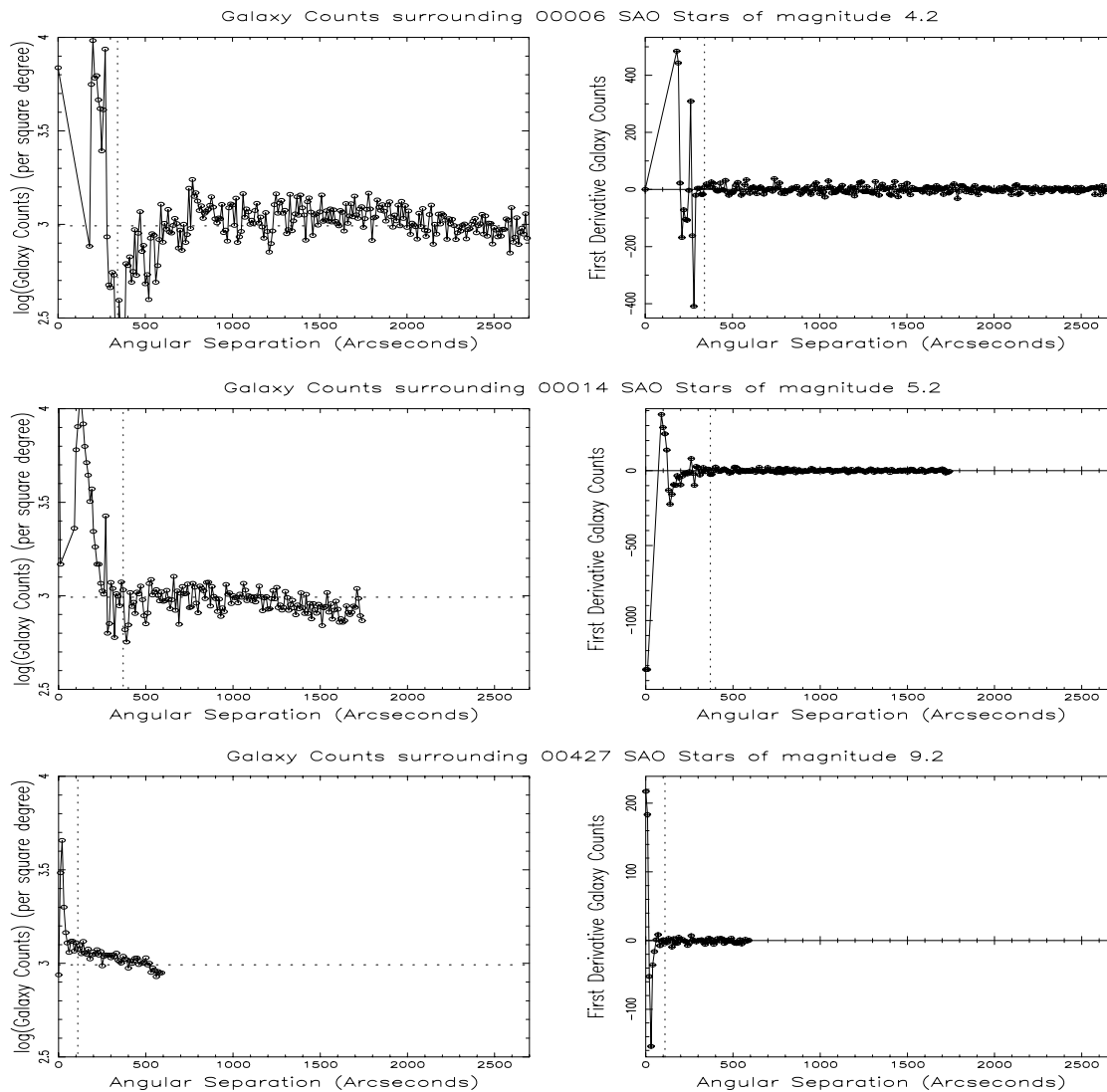


Figure 5.4: A sample of APS galaxy counts and their derivatives (versus angular separation) around SAO stars in three magnitude bins: 4.2–4.4, 5.2–5.4, and 9.2–9.4. Notice that the galaxy counts (in units of galaxies/ \square°) all peak close to the SAO star, showing that the SAO star diffraction halo is causing excessive APS galaxy counts relative to the background level of counts (established by looking at the galaxy counts far from the SAO stars). The dashed horizontal line in each plot shows the estimated background level of galaxy counts. The dashed vertical line in each plot shows the estimate for $r_{false}(m_{SAO})$ for that magnitude bin.

Using the information on the surface density of galaxies versus angular separation from SAO stars, I made an estimate of $r_{false}(m_{SAO})$ by computing the first derivative of the galaxy counts (versus angular separation) and finding when it dropped 1σ below its mean value in the outer $300''$ of each SAO magnitude bin. I then added $60''$ to this estimate of $r_{false}(m_{SAO})$ as a “safety” margin. Estimates for $r_{false}(m_{SAO})$ were made for all magnitude bins where there were 5 SAO stars or more. Using these estimates, I fit a 3^{rd} order polynomial to obtain a functional form for the relationship between SAO magnitude, m_{SAO} , and the radius, $r_{false}(m_{SAO})$, at which false galaxy counts start to occur:

$$r_{false}(m_{SAO}) = -2.4m_{SAO}^3 + 65m_{SAO}^2 - 600m_{SAO} + 2100. \quad (5.6)$$

Using equation 5.6, I removed 15673 entries lying within $r_{false}(m_{SAO})$ of an SAO star from the catalog. Note that use of equation 5.6 for SAO stars brighter than 4^{th} magnitude is an extrapolation, but hopefully an acceptable one since most of these bright SAO stars have had their halos interactively deleted from the APS catalog. For SAO stars with no visual magnitude information, I assumed a magnitude of 11.

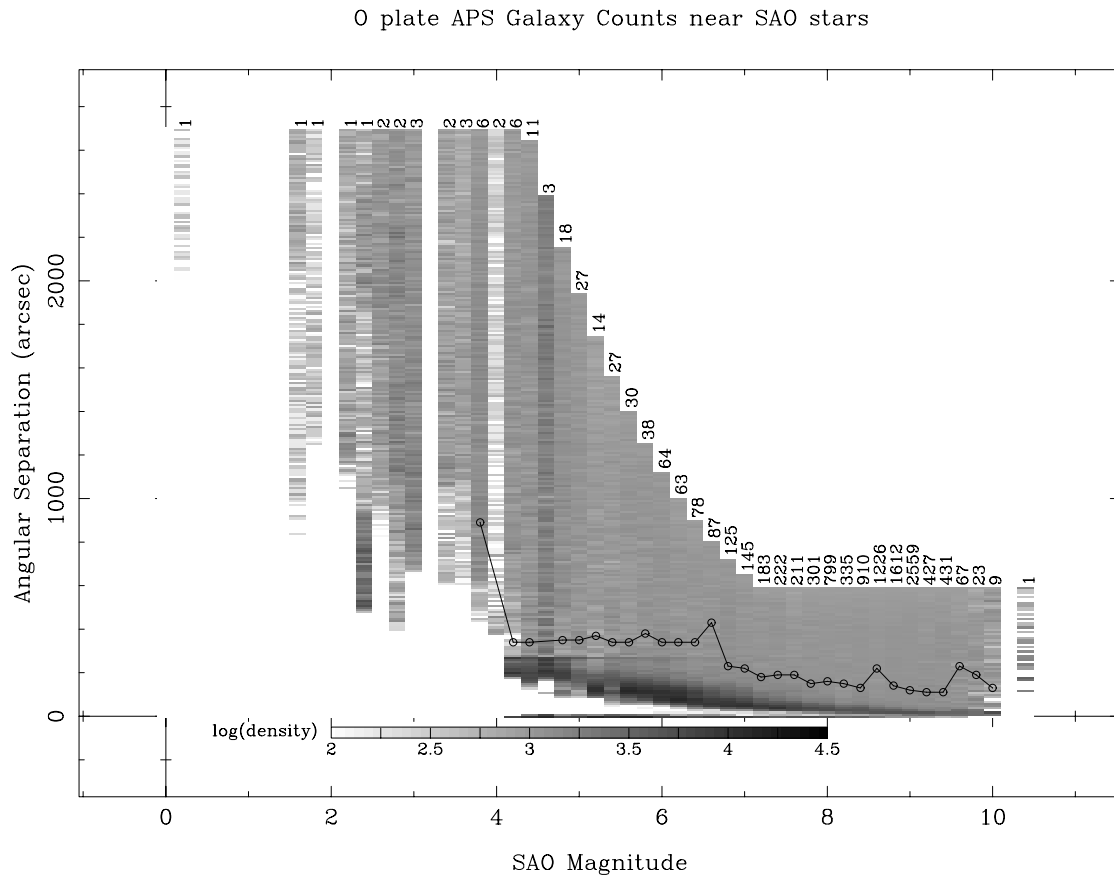


Figure 5.5: This plot shows the APS O plate galaxy counts (in grayscale) versus angular separation from SAO stars of different magnitudes. The number above each magnitude bin is the number of SAO star halos used for computing the galaxy counts in that magnitude bin. The boundary between the mean background level of galaxy counts and higher galaxy counts due to the SAO stars diffraction halo is indicated by the solid line.

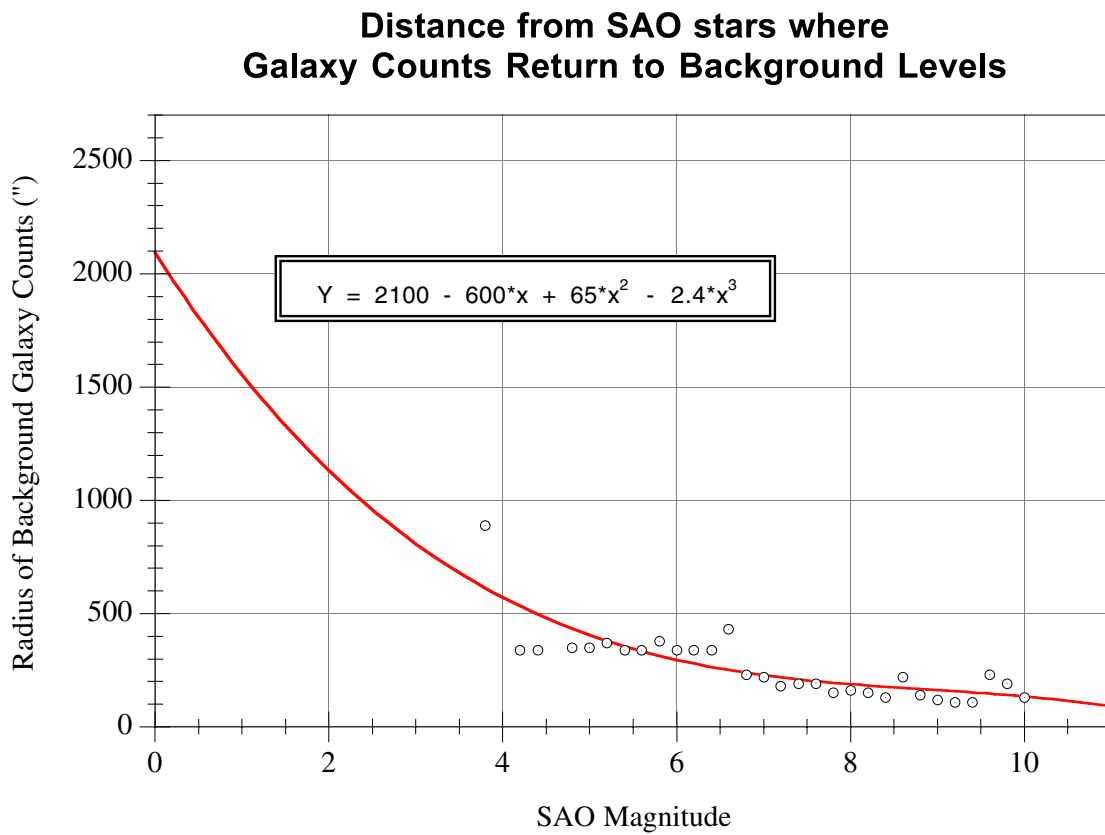


Figure 5.6: Using the datapoints shown in Figure 5.5 separating the SAO halo “enhanced” galaxy counts from the background level, I fit a 3rd order polynomial to obtain a functional estimate for the radius at which the SAO diffraction halo is influencing galaxy counts by creating “false” galaxies.

5.4 Elimination of False Galaxies due to Ghost Images

Ghost images is the name given to the images that appear on POSS I plates in positions symmetrically opposite the plate center from bright stars (as shown in Figure 5.3). The ghost images are formed by the successive reflection of light off the emulsion, then off the corrector plate of the Oschin Schmidt 48-inch telescope, and finally off the mirror. This optical path for the ghost images is illustrated in Figure 5.7. In theory, it should be a very simple matter to perform a gnomonic projection of bright SAO stars to transform the sky position in (α, δ) into the flat plate coordinates (ξ, η) , then reflect those coordinates across the plate center $(\xi_{center}, \eta_{center})$ to get $(\xi_{ghost}, \eta_{ghost})$, and then perform a reverse gnomonic projection to get the position of the ghost image in sky coordinates, $(\alpha_{ghost}, \delta_{ghost})$. However, this process assumes that the plate center position $(\xi_{center}, \eta_{center})$ is perfectly aligned with the optical axis of the telescope. Given the fact that the plate scale is $67.39''/\text{mm}$, a misalignment of 1 millimeter in the placement of the plate in the holder can result in an error of over $1'$ in the position of the plate center, and a greater error in the position of the ghost image. Therefore, any method of computing the position of ghost images based on the positions of SAO stars on the plates is at best an estimated position. I attempted to use the estimated ghost image positions obtained using the SAO star positions to set up an automated ghost image search algorithm, hoping to refine the ghost image positions we estimated. Techniques such as cross-correlation of nearby galaxy positions with a template ghost image did not work, likely because in many cases the contrast in the ghost image relative to the background was too small to easily detect. It proved faster to simply make a list of the estimated ghost image positions for all 97 fields in the MAPS-NGP region and then hand measure the correct positions of the ghosts directly off of the prints of the POSS I. I found that there were 98 ghost images visible on the plates covering the MAPS-NGP field and their positions determined to an accuracy of $2' - 3'$. These 98 ghost image positions are listed in Table 5.2. The positions estimated via gnomonic projection were found to be typically offset by at least $4'$ and sometimes up to $12'$. There was no trend

in the error of the estimated ghost image position relative to the distance of the image from the plate center. The estimated positions were useful for finding the very faintest ghost images. There were no visible ghost images for SAO stars fainter than magnitude 5.1. Because the ghost images are formed by unfocused light, they are always the same size, $23' \times 20'$, regardless of the brightness of the SAO star causing the ghost image. Therefore, the elimination of any false galaxies in the MAPS-NGP involved deletion of all galaxies within $17.5'$ of the known ghost image positions. 1702 galaxies within ghost images were eliminated from the MAPS-NGP.

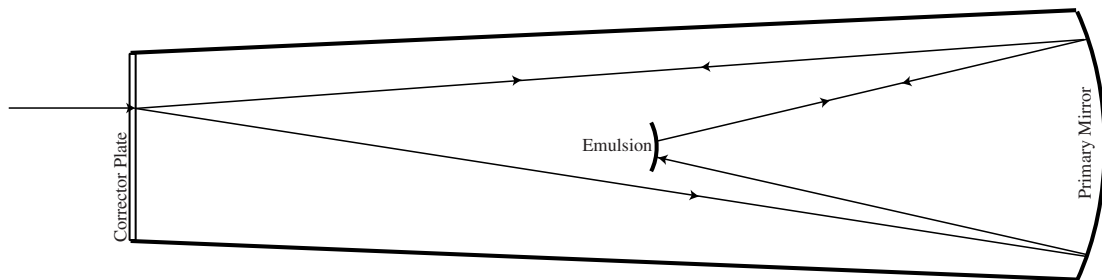


Figure 5.7: This diagram illustrates the optical path of light forming ghost images. The light from a star or galaxy normally passes through the corrector plate hits the primary mirror and then hits the emulsion. However, in the case of very bright stars, enough of the light may bounce back off the emulsion, then subsequently off of the primary mirror, the corrector plate, and the primary mirror, to generate a ghost image on approximately the symmetrically opposite side of the emulsion of the bright star. Ghost images typically do not lie precisely on the symmetrically opposite side of the plate because of misalignment of the emulsion relative to the optical center of the Schmidt telescope.

Table 5.2: The Ghost Images Removed from the MAPS-NGP Catalog

Project	Ghost Position		SAO	SAO Star Position)		SAO magnitude
	α (B1950)	δ (B1950)		α (B1950)	δ (B1950)	
P96	12:09:00.0	+62:34:00.0	28553	12:51:50.1	+56:13:51.1	1.7
P96	12:54:30.0	+61:31:00.0	28315	12:12:57.6	+57:18:36.9	3.4
P130	11:07:40.0	+52:40:00.0	28179	11:51:12.6	+53:58:22.0	2.5
P131	11:50:30.0	+55:05:00.0	28366	12:21:36.1	+51:50:20.6	5.0
P131	12:21:45.0	+52:57:00.0	28179	11:51:12.6	+53:58:22.0	2.5
P132	12:37:30.0	+50:40:00.0	28553	12:51:50.1	+56:13:51.1	1.7
P133	13:06:15.0	+52:00:00.0	28843	13:38:50.6	+54:56:03.0	4.8
P133	13:20:30.0	+51:51:00.0	28751	13:23:13.5	+55:14:53.0	4.0
P133	13:22:00.0	+51:55:00.0	28738	13:21:55.8	+55:10:56.6	4.0
P133	13:22:00.0	+51:55:00.0	28737	13:21:54.9	+55:11:09.5	2.4
P134	13:42:05.0	+55:20:00.0	29071	14:14:23.7	+51:35:49.9	4.9
P134	13:45:00.0	+54:56:00.0	29046	14:11:41.5	+52:01:23.6	4.6
P134	14:17:48.0	+51:57:00.0	28843	13:38:50.6	+54:56:03.0	4.8
P135	14:51:45.0	+55:03:00.0	29137	14:23:29.6	+52:04:52.3	4.1
P169	10:34:30.0	+50:12:00.0	43629	11:06:51.6	+44:46:12.6	3.1
P170	11:07:30.0	+46:51:00.0	43886	11:43:25.0	+48:03:24.2	3.9
P171	12:14:15.0	+46:50:00.0	43886	11:43:25.0	+48:03:24.2	3.9
P174	13:34:23.0	+45:32:00.0	44752	13:45:34.3	+49:33:44.1	1.9
P174	13:46:30.0	+45:48:00.0	44668	13:32:24.8	+49:16:15.9	4.6
P175	14:12:18.0	+48:44:00.0	44965	14:14:29.0	+46:19:01.9	4.3
P176	14:33:25.0	+47:00:00.0	45357	15:02:08.3	+47:50:53.3	4.9
P214	10:21:45.0	+39:33:00.0	43512	10:51:06.5	+43:27:24.0	4.8
P214	10:41:18.0	+42:27:00.0	43379	10:30:19.3	+40:41:00.2	4.8
P214	10:52:00.0	+41:13:00.0	43310	10:19:21.5	+41:45:06.3	3.2
P215	11:12:18.0	+43:26:00.0	62354	10:58:02.6	+39:28:51.8	5.1
P215	11:13:30.0	+42:14:00.0	43557	10:56:40.3	+40:41:51.8	5.1
P215	11:18:00.0	+39:25:00.0	43512	10:51:06.5	+43:27:24.0	4.8
P218	12:38:00.0	+41:16:00.0	44230	12:31:22.3	+41:37:44.1	4.3
P219	12:53:09.0	+42:02:00.0	44549	13:15:18.1	+40:50:07.2	4.7
P219	13:15:42.0	+44:16:00.0	63257	12:53:41.5	+38:35:16.8	2.9
P222	14:37:30.0	+44:37:00.0	64203	14:30:03.8	+38:31:34.1	3.0
P223	15:06:42.0	+42:37:00.0	45337	15:00:03.7	+40:35:12.8	3.6
P263	10:18:00.0	+34:10:00.0	62053	10:24:59.9	+36:57:50.9	4.4
P263	10:20:00.0	+37:04:00.0	62038	10:23:03.2	+34:03:05.1	4.8
P264	10:47:54.0	+36:38:00.0	62297	10:50:31.2	+34:29:05.6	3.9
P265	11:17:36.0	+32:40:00.0	62491	11:16:24.7	+38:27:36.4	4.8
P265	11:18:30.0	+37:42:30.0	62486	11:15:46.9	+33:22:02.6	3.7
P267	12:11:30.0	+37:40:00.0	62928	12:13:59.5	+33:20:26.6	5.1
P268	12:28:00.0	+32:17:30.0	63257	12:53:41.5	+38:35:16.8	2.9
P269	13:13:30.0	+34:52:00.0	63338	13:03:24.3	+36:03:57.5	5.1
P269	13:22:15.0	+32:17:30.0	63257	12:53:41.5	+38:35:16.8	2.9
P271	13:52:00.0	+35:23:00.0	64053	14:15:53.0	+35:44:21.9	4.8
P271	14:18:30.0	+36:24:00.0	63793	13:49:35.2	+34:41:28.4	5.0
P272	14:33:30.0	+32:44:00.0	64203	14:30:03.8	+38:31:34.1	3.0
P273	14:45:30.0	+37:39:00.0	64589	15:13:29.1	+33:30:01.2	3.5
P317	10:22:54.0	+26:52:30.0	62173	10:35:54.7	+32:14:11.5	4.8
P319	11:26:06.0	+27:16:30.0	62484	11:15:31.2	+31:48:38.9	3.9
P321	12:01:06.0	+30:16:00.0	82313	12:24:26.9	+28:32:46.1	4.6
P321	12:01:24.0	+31:16:30.0	82310	12:23:54.2	+27:32:42.1	5.1
P322	12:28:00.0	+31:06:30.0	82537	12:49:15.9	+27:48:44.7	5.1
P323	12:59:00.0	+30:49:00.0	82706	13:09:32.4	+28:07:52.0	4.3

Project	Ghost Position		SAO	SAO Star Position)		SAO magnitude
	α (B1950)	δ (B1950)		α (B1950)	δ (B1950)	
P323	13:04:00.0	+31:03:00.0	82659	13:04:46.8	+27:53:33.3	4.9
P323	13:10:48.0	+27:54:30.0	63288	12:57:53.0	+31:03:15.6	5.1
P326	14:11:42.0	+29:27:00.0	83416	14:32:30.1	+29:57:41.2	4.5
P326	14:14:45.0	+28:51:00.0	64202	14:29:40.4	+30:35:24.1	3.8
P327	14:54:00.0	+32:00:00.0	83500	14:42:48.1	+27:17:02.7	2.7
P327	14:55:48.0	+32:30:00.0	83488	14:41:13.4	+26:44:22.0	4.9
P328	15:01:30.0	+29:54:30.0	83831	15:25:45.9	+29:16:37.3	3.7
P374	10:56:51.0	+22:01:00.0	81583	10:52:54.6	+25:01:00.8	4.5
P375	11:28:42.0	+23:17:00.0	81736	11:12:32.8	+23:22:06.0	4.9
P375	11:30:24.0	+25:51:00.0	81727	11:11:27.1	+20:47:52.7	2.6
P376	11:48:45.0	+26:25:00.0	81998	11:45:24.5	+20:29:48.7	4.5
P377	12:05:30.0	+20:46:00.0	82273	12:19:59.6	+26:07:24.3	4.8
P377	12:11:18.0	+22:40:00.0	82211	12:13:48.8	+24:13:23.6	5.1
P381	13:44:33.0	+21:45:00.0	83203	14:08:07.1	+25:19:39.8	4.8
P383	14:36:30.0	+21:52:30.0	83624	14:59:55.0	+25:12:17.2	4.9
P384	15:22:48.0	+22:14:00.0	83671	15:05:06.2	+25:03:46.3	5.0
P432	10:46:45.0	+14:37:00.0	81637	10:59:39.8	+20:26:54.2	4.4
P433	11:22:30.0	+19:16:00.0	99512	11:11:37.1	+15:42:11.4	3.4
P434	11:34:48.0	+20:07:00.0	99809	11:46:30.6	+14:51:05.8	2.2
P434	11:36:18.0	+14:30:00.0	81998	11:45:24.5	+20:29:48.7	4.5
P436	12:39:12.0	+16:59:30.0	100053	12:18:11.5	+18:04:08.3	4.9
P437	12:48:36.0	+17:21:30.0	100357	12:56:27.1	+17:40:42.4	5.0
P438	13:25:09.0	+17:13:00.0	100443	13:07:33.3	+17:47:36.3	4.5
P439	13:29:18.0	+16:25:00.0	100766	13:52:18.2	+18:38:51.3	2.8
P439	13:34:15.0	+19:03:00.0	100725	13:47:03.9	+16:02:42.7	4.3
P439	13:36:30.0	+17:23:00.0	100706	13:44:53.1	+17:42:18.9	4.5
P440	13:55:42.0	+15:33:00.0	100944	14:13:22.8	+19:26:31.0	0.2
P440	14:16:20.0	+16:20:00.0	100766	13:52:18.2	+18:38:51.3	2.8
P441	14:18:33.0	+18:36:00.0	101138	14:38:22.5	+16:37:54.2	4.9
P442	14:55:42.0	+16:02:00.0	101250	14:49:04.8	+19:18:27.0	4.6
P442	15:01:54.0	+18:08:00.0	101184	14:42:54.4	+17:10:30.2	4.7
P493	11:12:48.0	+12:18:00.0	99587	11:21:19.1	+10:48:17.6	4.0
P495	12:07:30.0	+13:59:00.0	119213	12:02:39.7	+09:00:38.3	4.2
P497	12:45:48.0	+11:49:00.0	100384	12:59:41.2	+11:13:38.9	3.0
P501	14:18:48.0	+09:14:30.0	101145	14:38:45.5	+13:56:30.5	3.9
P501	14:36:45.0	+14:31:30.0	120426	14:20:55.0	+08:40:23.9	5.1
P553	11:15:36.0	+04:36:30.0	118804	11:18:33.5	+06:18:13.1	4.1
P554	11:38:09.0	+04:16:30.0	119035	11:43:17.3	+06:48:34.7	4.2
P555	12:10:53.0	+04:08:00.0	119164	11:58:18.6	+06:53:35.1	4.6
P557	12:52:30.0	+07:20:00.0	119674	12:53:05.0	+03:40:07.6	3.7
P558	13:18:30.0	+05:21:00.0	119855	13:15:04.7	+05:43:58.0	5.0
P559	13:49:39.0	+07:05:00.0	120004	13:31:35.8	+03:54:54.4	4.9
P561	14:35:30.0	+05:13:00.0	120434	14:21:41.9	+06:02:45.5	5.1
P561	14:36:12.0	+02:37:00.0	120426	14:20:55.0	+08:40:23.9	5.1
P614	11:33:30.0	-02:53:00.0	119076	11:48:05.4	+02:02:47.6	3.8
P614	11:47:06.0	+00:30:00.0	138298	11:34:23.3	-00:32:51.2	4.5
P616	12:18:06.0	+00:09:00.0	138917	12:39:07.5	-01:10:31.6	2.9
P616	12:40:00.0	+00:39:00.0	138721	12:17:20.8	-00:23:20.6	4.0
P619	13:49:36.0	+00:39:00.0	139420	13:32:08.6	-00:20:27.5	3.4

5.5 Elimination of False Galaxies due to Galactic Globular Clusters

Some Galactic globular clusters can appear, due to their high stellar density, as small clusters of galaxies. Using the angular diameters listed for globular clusters in the Catalogue of Galactic Globular Clusters by Monella [1985], I eliminated galaxies in the MAPS-NGP which appeared to lie within the bounds of known Galactic globular clusters. MAPS-NGP “galaxies” were found within three globular clusters², resulting in 318 objects being rejected from the MAPS-NGP catalog (See Figure 5.8).

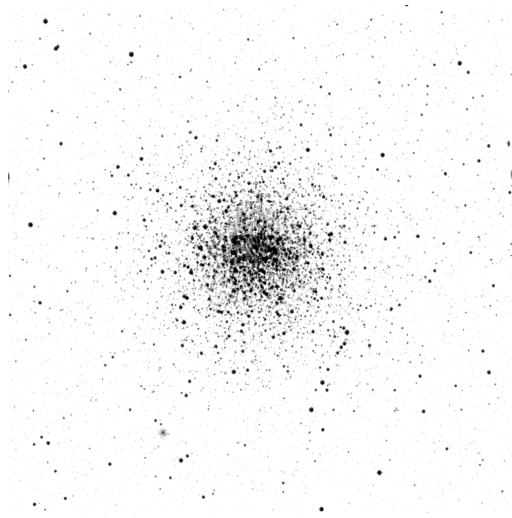


Figure 5.8: This image from the APS image database shows the $20' \times 20'$ field around NGC 5466, a globular cluster with an angular diameter of $9.2'$. Due to the large number of blended stellar images in a globular cluster, many of the stars in this field were classified as galaxies, thus leading to the appearance of a very small cluster of galaxies in the APS catalog. Therefore, the MAPS-NGP galaxies located ‘inside’ the bounds of known Galactic globular clusters were deleted.

²The three Galactic Globular Clusters purged from the MAPS-NGP catalog were NGC 4147 with a diameter of $4.1'$, NGC 5053 with a diameter of $8.9'$, and NGC 5466 with a diameter of $9.2'$

5.6 Elimination of Artifacts around some UGC galaxies

A final known source of false galaxies is the low surface brightness portions of bright UGC galaxies. Because the POSS I plates are scanned in threshold densitometry mode, any low surface brightness structures can be split into multiple APS images which are artifacts of the presence of the low surface brightness edges of bright UGC galaxies. The number of such artifact images around UGC galaxies depends on the granularity of galaxy's appearance and the exact threshold density for the data on a given plate. In order to locate and eliminate these false galaxies, I first cross-identified the UGC with the MAPS-NGP, and located the largest image with $O > 18$ and $0.2 < \frac{APS_{diameter}}{UGC_{diameter}} < 1.1$. This image was recognized as the MAPS-NGP counterpart to the UGC galaxy. I then eliminated any galaxies located within an ellipse of the UGC galaxy except for the already identified UGC counterpart.³ Many UGC galaxies did not make it into the MAPS-NGP sample because they are very large and are cannot be assigned a diameter by SASORT.⁴ In most cases, zero or one galaxies were eliminated as artifacts per UGC galaxy, but in some cases, several tens of MAPS-NGP entries were identified as artifacts.⁵ In these cases, it is usually apparent that the galaxy has extensive low surface brightness portions that are getting identified as small clusters of galaxies (see Figure 5.9). A total of 2073 UGC galaxies were identified in the MAPS-NGP while 1069 additional UGC galaxies which were not matched had entries in their part of the sky removed from the catalog. A total of 2766 objects were deleted from the MAPS-NGP as likely artifacts around UGC galaxies.⁶ At this point, all the known contaminants of the MAPS-NGP catalog have

³In actuality, I used an ellipse with the same ellipticity and orientation as the UGC galaxy, but 150% the radius, in order to be certain I eliminated most artifacts.

⁴This problem occurs because the large images of UGC galaxies can overwhelm the image array limits of SASORT. As noted in Section 5.1, in these cases, SASORT assigns the image a diameter of -1.

⁵The most extreme case was for the field around UGC 7353 (a.k.a. Messier 106), a nearby SBbc spiral with very flocculent arms, which had 87 artifacts eliminated around it.

⁶If I had used a smaller diameter limit in constructing the MAPS-NGP, it is likely that more artifacts would be found around the UGC galaxies. This is important should anyone in the future attempt to use deeper galaxy catalogs in this kind of study.

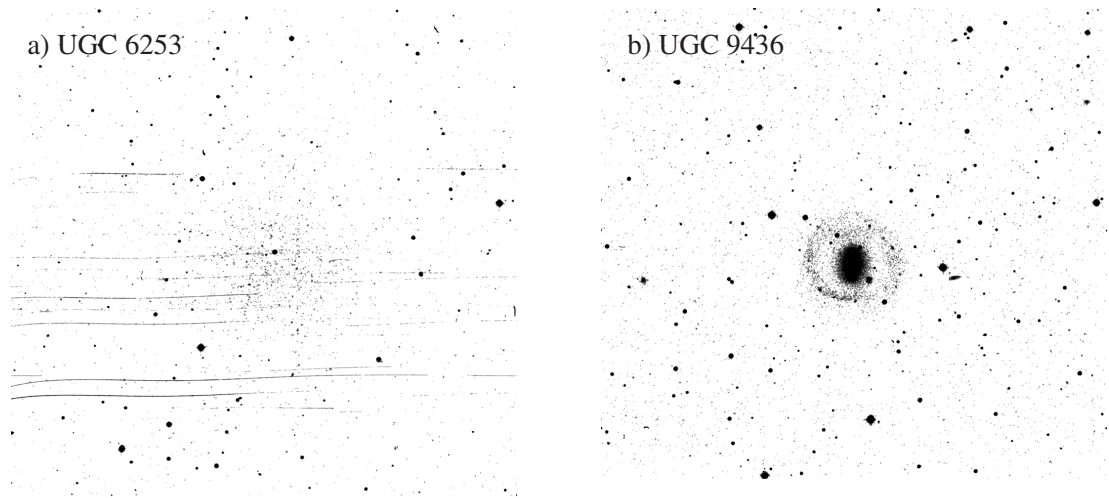


Figure 5.9: These two images from the APS image database show the $20' \times 20'$ fields around (a) UGC 6253 (Note: the lines in this image are scratches on the plate.) and (b) UGC 9436. The contrast in these two images has been increased 80% in order to highlight the low surface brightness portions of the images. 32 and 21 false galaxies were eliminated as artifacts surrounding these two galaxies.

been purged and a total of 217768 galaxies covering approximately $3089 \square^\circ$ on the sky remain in the MAPS-NGP. There is still one additional source of contamination that I am not (currently) able to eliminate: merged star-star and star-galaxy images. While the automated removal of such contaminants is currently part of research by others in the APS project, I know I have minimized the problem by selecting fields at high Galactic latitude. Further discussion of this issue is included in Section 5.10.

5.7 Computation of the Surface Density of Galaxies in the MAPS-NGP

Using a technique introduced by Dressler [1980], an estimate of the local surface density of galaxies was computed for each galaxy in the MAPS-NGP. Dressler's method is to compute the the angular separation between each galaxy and its tenth closest neighbor, r_{10} . Assuming there are 11 galaxies within a circle of radius r_{10} , the estimate

of the local surface density of galaxies is then simply

$$\Sigma = \frac{11}{\pi r_{10}^2}, \quad (5.7)$$

in units of galaxies/ \square° if r_{10} is in degrees. Using this technique and an optimized method for finding the ten nearest galaxies, I obtained estimated nearby surface densities for all galaxies in the MAPS-NGP.

5.8 Addition of non-*StarBase2* image parameters to the MAPS-NGP

While the MAPS-NGP catalog contains all the image parameters present in *StarBase2*, there are several image and image quality parameters useful to this study that are computed during the data reduction process which are **not** included in *StarBase2*. These parameters are however recorded in an intermediate data file called an *imgpars* file. I restored the *imgpars* files for the 194 plates covering the MAPS-NGP. I then retrieved the following additional image and image quality parameters for each object in the MAPS-NGP catalog:

- **Mean Surface Brightness** (μ_{mean}): The mean surface brightness of the galaxy in units of magnitudes per square arcsecond. The mean surface brightness is determined using the D-to-I relationship and the background subtracted pixel data for the galaxy.
- **Effective Radius** (r_{eff}): Also called the half-light radius, the effective radius is the radius enclosing half the light in the galaxy. The APS reported effective radius, $r_{eff_{APS}}$, is converted into a major-axis effective radius, r_{eff} , by using

$$r_{eff} = \frac{r_{eff_{APS}}}{\sqrt{1 - \epsilon}} \quad (5.8)$$

which has a similar derivation as equation 5.3. This assumes that ϵ is constant with radius, which is not absolutely true, but only approximately so.⁷

- **Concentration Indices** (C_{31}, C_{32}, C_{21}): The concentration indices are measures of the ratio of the radii enclosing 100% (r_{100}), 75% (r_{75}), and 50% (r_{50}) of the galaxy's light.⁸ Specifically:

$$C_{31} = r_{100}/r_{50} \tag{5.9}$$

$$C_{32} = r_{100}/r_{75} \tag{5.10}$$

$$\text{and } C_{21} = r_{75}/r_{eff}. \tag{5.11}$$

C_{31} was shown to be correlated with morphological type by Odewahn and Aldering [1995], although there is too much scatter in the relationship to make a one-to-one correspondence between C_{31} and morphological type.

- **Image Quality Flag:** This image quality flag notes images that are possibly problematic. The potential problems that get flagged include bad fuz ($flag = 1$) and jitter ($flag = 2$) values, clipped images where a stripe boundary crosses the image ($flag = 4$), MBACK access errors ($flag = 5$), and computed sky density values which are negative ($flag = 6$). In addition to these problems, galaxies with SASORT ellipticities greater than 0.95 are flagged ($flag = 3$), although the ellipticities in *StarBase2* come from a flux weighted moments analysis which occurs after SASORT.

⁷In spirals, the presence of the bulge tends to round out the inner isophotes relative to the outermost isophotes.

⁸The concentration index definitions shown here are different than those stated in Odewahn and Aldering [1995] and were determined by direct examination of the IMGPARS code. Subsequent private conversations with Aldering have confirmed that Odewahn and Aldering [1995] incorrectly stated the definition of their concentration indices.

5.9 Galactic Extinction Estimates for MAPS-NGP Galaxies

In order to aid in later analysis of the data, it is important to know the level of Galactic extinction affecting objects in the MAPS-NGP catalog. I have therefore included reddening estimates for $E(B-V)$ from two sources. The more traditional catalog of reddening estimates has been the Burstein & Heiles [1982] catalog which used HI maps and galaxy counts, hereafter referred to as $E(B-V)_{BH}$ estimates. More recently, Schlegel, Finkbeiner, and Davis [1998] have used direct observations of Galactic dust from IRAS and DIRBE observations to obtain a new all sky map of $E(B-V)$ estimates (hereafter, $E(B-V)_S$ estimates). As noted by Schlegel, Finkbeiner, and Davis [1998], most extragalactic research in the last 17 years has used the $E(B-V)_{BH}$ estimates. Burstein & Heiles [1982] assumed that the dust to HI ratio can be modeled by the background galaxy counts whereas Schlegel's group assumed that the distribution of dust grain sizes is constant.⁹ Neither assumption is completely true, but the $E(B-V)_S$ estimates can be considered better in part because of their higher resolution (which resolves a lot of the filamentary structure of the dust) and because they are based on direct observations of the dust (See Figure 5.10). For both $E(B-V)_{BH}$ and $E(B-V)_S$ estimates, I have used bilinear interpolation between map points in order to get reddening estimates for each MAPS-NGP galaxy's position. Both reddening estimates are stored in the MAPS-NGP for use later in determining the Galactic extinction in the line of sight without extensive lookup times. The $E(B-V)_S$ estimates indicate that the strongest reddening in the MAPS-NGP field is on the order of $E(B-V)_S \approx 0.11$ which implies a maximum extinction of $A_O \approx 0.48$ and $A_E \approx 0.27$ in the MAPS-NGP field.¹⁰ The $E(B-V)_S$ distribution for the MAPS-NGP has a median value of 0.021 and a mean of 0.0223 with

⁹This constant distribution of grain sizes is important since the relationship between optical extinction and FIR emission depends on grain sizes.

¹⁰This reddening to extinction conversion is based on the UV to NIR extinction law of Cardelli, Clayton, and Mathis [1989] and is detailed in section 7.1.3.

a standard deviation of 0.0095 (see Figure 5.11). The $E(B - V)_{BH}$ estimates have a very similar distribution to the $E(B - V)_S$, although a handful of galaxies have much higher reddening estimates than $E(B - V)_S$.

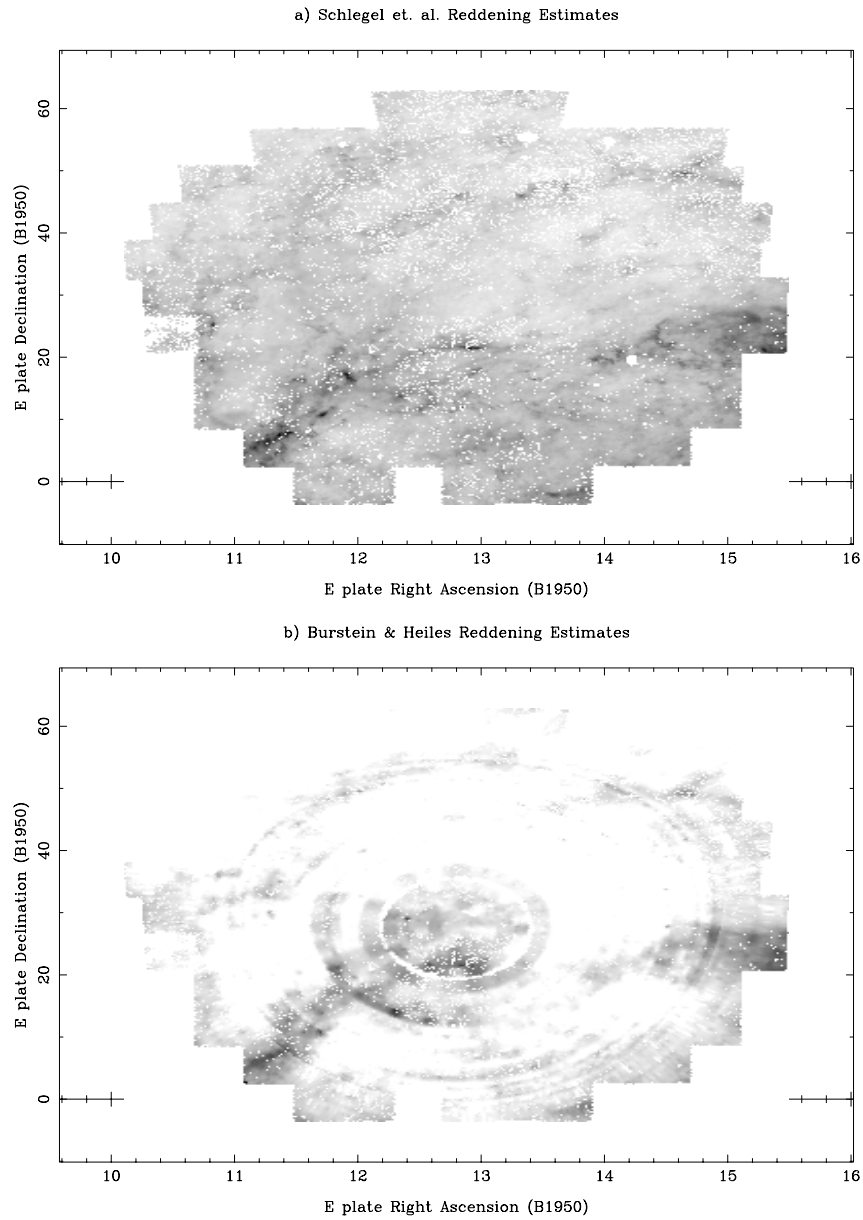


Figure 5.10: These two plots show estimates for the mean $E(B - V)$ in $15' \times 15'$ cells covering the MAPS-NGP according to (a) Schlegel, Finkbeiner, and Davis [1998] and (b) Burstein & Heiles [1982]. Note especially the much higher resolution and spatial coverage of the Schlegel, Finkbeiner, and Davis [1998] reddening maps. The $E(B - V)$ range shown is from 0.00 to 0.09 magnitudes.

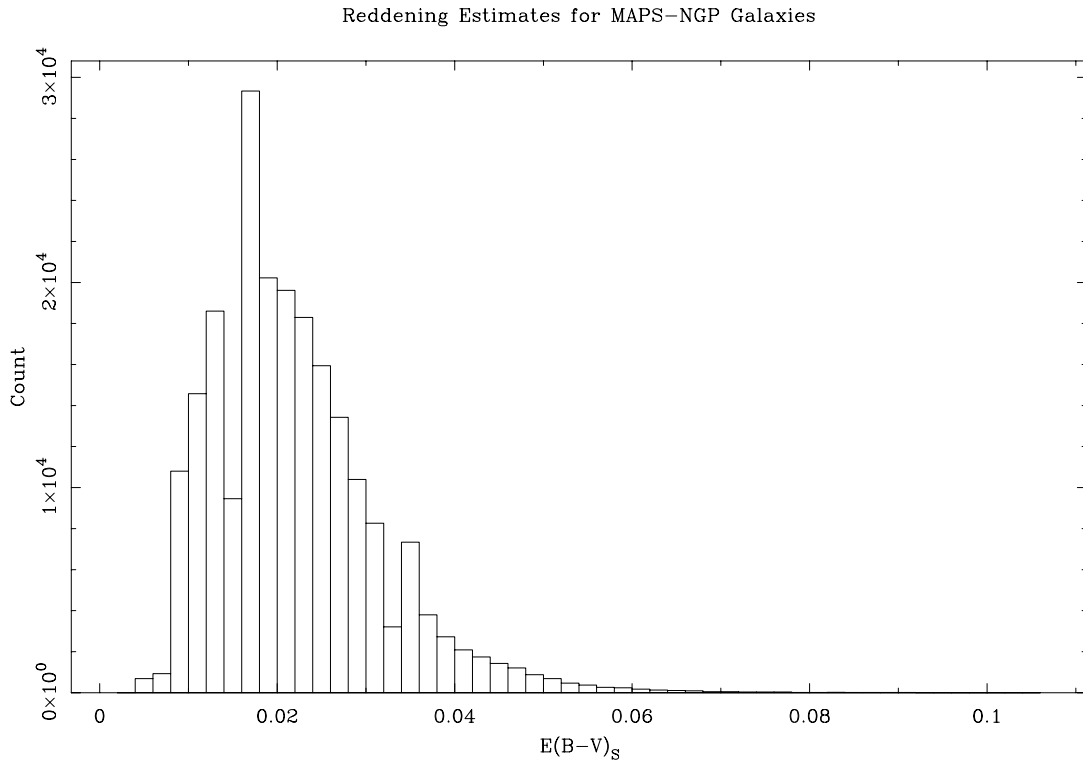


Figure 5.11: The distribution of $E(B - V)_S$ for MAPS-NGP galaxies. Notice that this distribution indicates most galaxies on the MAPS-NGP fields have reddenings of less than 0.025 magnitudes.

5.10 Summary of the MAPS-NGP Catalog

The MAPS-NGP catalog is a major-axis diameter-limited catalog of galaxies in the APS object catalog with diameters greater than $10''$ and located on plates within 30° of the North Galactic Pole (NGP). It contains 217768 galaxies covering approximately 3089° of the sky.¹¹ No duplicate objects exist in this catalog. Furthermore, all known sources of false or uncertain galaxy classification, such as bright star halos, ghost images of bright stars, misclassification of blended stellar images in globular clusters, and artifacts around bright galaxies due to threshold densitometry have been removed. The

¹¹ 3089° equals about 0.9 steradians, or just over one quarter of the area of the upcoming Sloan Digital Sky Survey (SDSS).

distribution of MAPS-NGP galaxies on the sky is illustrated in Figure 5.12 and the distribution of diameters and magnitudes is shown in Figure 5.13.

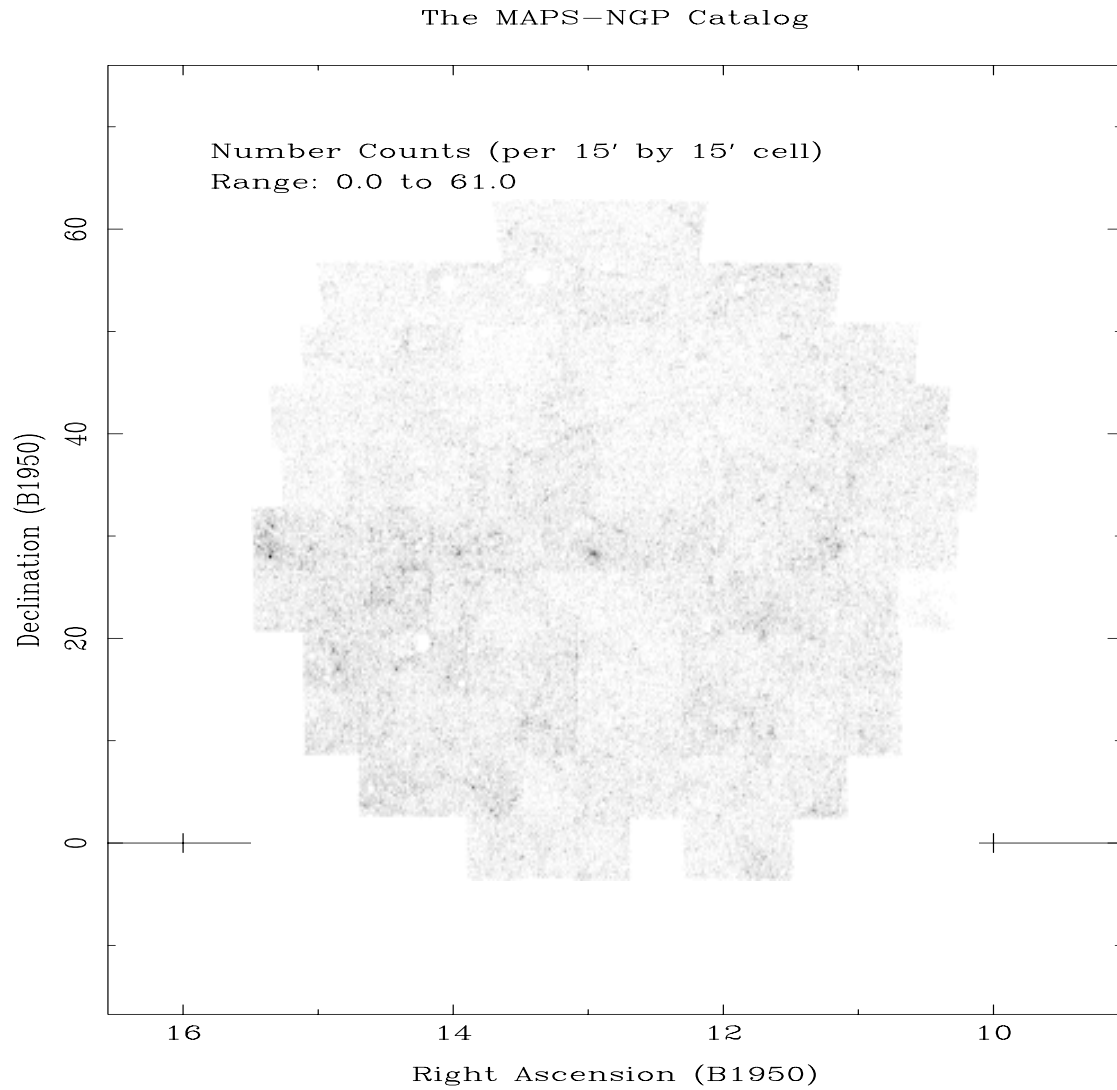


Figure 5.12: This grayscale map shows the distribution of galaxies in the MAPS-NGP. The plot shows the galaxy number counts in $15' \times 15'$ cells covering the MAPS-NGP field, ranging from 1 to 60.4 galaxies.

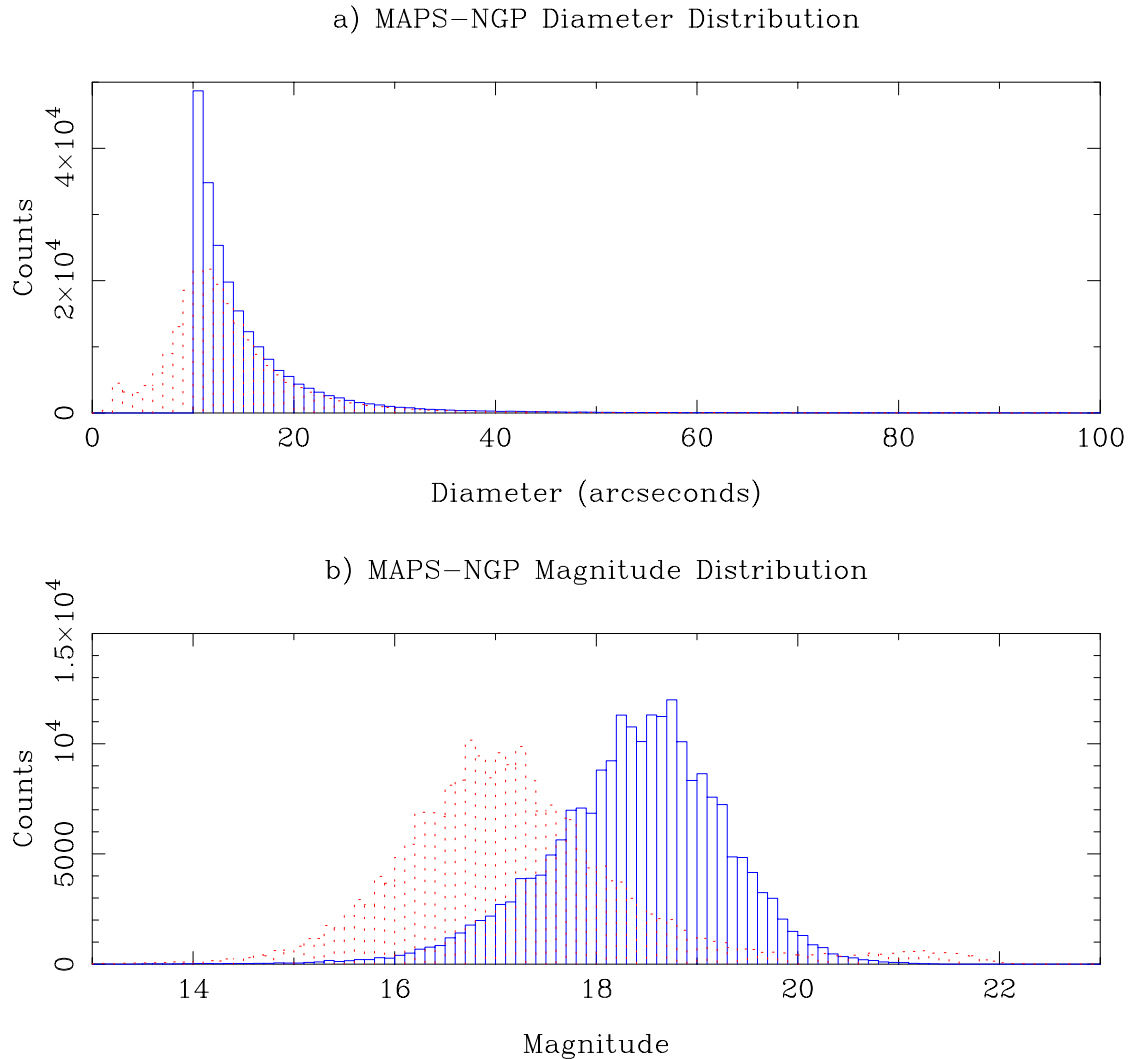


Figure 5.13: The (a) angular diameter and (b) magnitude distributions for the MAPS-NGP for both the O and E plates.

The only remaining major source of false galaxy counts would be merged stellar images in the field. Since I chosen the fields surrounding the NGP, essentially looking directly out of the disk of the galaxy, the number of merged stellar images in these fields should be minimized. This argument is supported by Figure 3.3 of Larsen [1996], which is a plot of the total number of APS galaxy counts versus Galactic latitude. It illustrates that galaxy counts do not generally rise 2σ above the mean galaxy counts at the NGP until you are within 45° of the Galactic Plane ($|b| < 45^\circ$). This suggests that the number of

misclassified galaxies due to blended stellar images is roughly constant, at least over the MAPS-NGP. Visual inspection of images for a random sample of 2700 objects classified as galaxies (down to the plate limit) on P323 found that roughly 5% of these “galaxies” are actually stellar blends.¹² The choice of a galaxy catalog centered on the NGP was in part driven by the desire to have a catalog requiring relatively small Galactic extinction corrections. The median MAPS-NGP reddening of $E(B - V)_S = 0.021$ corresponds to extinctions of $A_O = 0.09$ and $A_E = 0.05$ magnitudes, indicating that we are indeed working with a low extinction dataset. There are a variety of tests one can perform in order to assess how complete our diameter-limited catalog is. The classical completeness tests are the $\log(N) - \log(S)$ and $\log(N) - \log(\theta)$ tests. These tests compare the total number of galaxies down to a certain flux level (S) or diameter (θ). Since flux goes as inverse square of the distance ($S \propto r^{-2}$) and volume goes as the cube of the distance ($V \propto r^3$), then if galaxies are distributed homogeneously in space ($N \propto V$), then we expect $N \propto S^{-\frac{3}{2}}$ and

$$\log(N) \propto -\frac{3}{2} \log(S). \quad (5.12)$$

Figure 5.14a shows the plots of $\log(N)$ versus $\log(S)$ for both the O (solid line) and E (dashed line) data from the MAPS-NGP. The flat plateau at low fluxes indicates that we have reached the flux limit of the catalog at $O \approx 18.6$ and $E \approx 16.8$ magnitudes. If we use the Pisces-Perseus M_* determined in Section 2.3.3, then this completeness limit implies that the MAPS-NGP contains all L_* galaxies within a distance modulus of ~ 38 or approximately 400 Mpc ($cz \approx 0.1$ assuming $h = 0.75$). There is also a cutoff at high fluxes which makes the $\log(N) - \log(S)$ relationship steeper than $-\frac{3}{2}$. This high flux cutoff partly due to a real high luminosity cutoff and partly to a small incompleteness in the MAPS-NGP sample due to a high diameter cutoff imposed by the fact that no one APS object is allowed to extend over a stripe boundary.¹³ Between the high and low

¹²This visual inspection of P323 images was performed several years ago by undergraduates Daniel Thayer and Jennifer Webster.

¹³APS scanning stripes are roughly $13'.4$ high, so we expect relatively few galaxies to be affected by this cutoff.

flux limits, the $\log(N) - \log(S)$ relationship does indeed have a slope of $-\frac{3}{2}$, indicating the sample is complete down to the lower flux limits. Similar to the $\log(N) - \log(S)$ test, the $\log(N) - \log(\theta)$ assumes a homogenous distribution of galaxies and that galaxy diameters (θ) go as the inverse of distance, such that we expect

$$\log(N) \propto -3\log(\theta). \quad (5.13)$$

As shown in Figure 5.14b, the MAPS-NGP does obey this relationship from diameters of $100''$ ($\log \theta = 2$) to diameters of about $10''$ in both O and E. Note that the E curve extends to diameters smaller than our diameter limit of $10''$ because the diameter limit is imposed on the O plate diameter only. The incompleteness at large diameters is due to a combination of objects too large for SASORT diameters to be computed (see footnotes in Section 5.1) and objects whose diameters are underestimated because the object crosses a APS scanning stripe boundary. As noted by Hudson & Lynden-Bell [1991], Schmidt [1968] introduced an interesting homogeneity test, the $\langle V/V_{lim} \rangle$ test. In this test, we compute the ratio of the volume of space with a radius equal to the galaxy's distance (V) versus that volume of space at the catalog limit (V_{lim}). We expect that if a sample is homogeneous in distribution, than the mean value of this ratio, $\langle V/V_{lim} \rangle$, should be approximately 0.5. We use the fact that diameter is inversely proportional to distance, so that we can state $V \propto \theta^{-3}$ and

$$\langle V/V_{lim} \rangle = \langle \theta_{lim}^3 / \theta^3 \rangle. \quad (5.14)$$

I can therefore use the diameter distribution to compute $\langle V/V_{lim} \rangle$ for the MAPS-NGP catalog assuming different limiting diameters, θ_{lim} . Figure 5.14c shows that in fact $\langle V/V_{lim} \rangle$ does not seem to equal 0.5. Rather, for large limiting diameters we find that $\langle V/V_{lim} \rangle$ is significantly greater than 0.5, indicating that most galaxies are in the outer half of the volume enclosed by galaxies down to θ_{lim} . This may be due to local inhomogeneities or due to the fact that the MAPS-NGP is indeed missing some of the very large (in angular diameter) galaxies. In summary, the MAPS-NGP is a large extragalactic catalog which is very complete for angular diameters of $10''$ to $\sim 100''$. In

addition to the internal extinction studies presented later in this thesis, the MAPS-NGP could be used for studies of the large-scale distribution of galaxies. With the inclusion of a diameter function, it could be used to statistically estimate the distances to any galaxy clusters visible in the MAPS-NGP. The actual identification of galaxy clusters itself would be very interesting.¹⁴ Finally, the technique of building this extragalactic catalog and removing the known non-extragalactic contaminants to the APS Catalog of the POSS I has already found use elsewhere in building large-scale galaxy catalogs from the APS catalog.¹⁵

¹⁴Application of binary trees to identifying clusters in the MAPS-NGP is currently being investigated by an undergraduate.

¹⁵A galaxy catalog for another portion of the sky has been built using the techniques outlined in this Chapter for a preliminary study of Galactic extinction by Dr. Jacek Choloniewski.

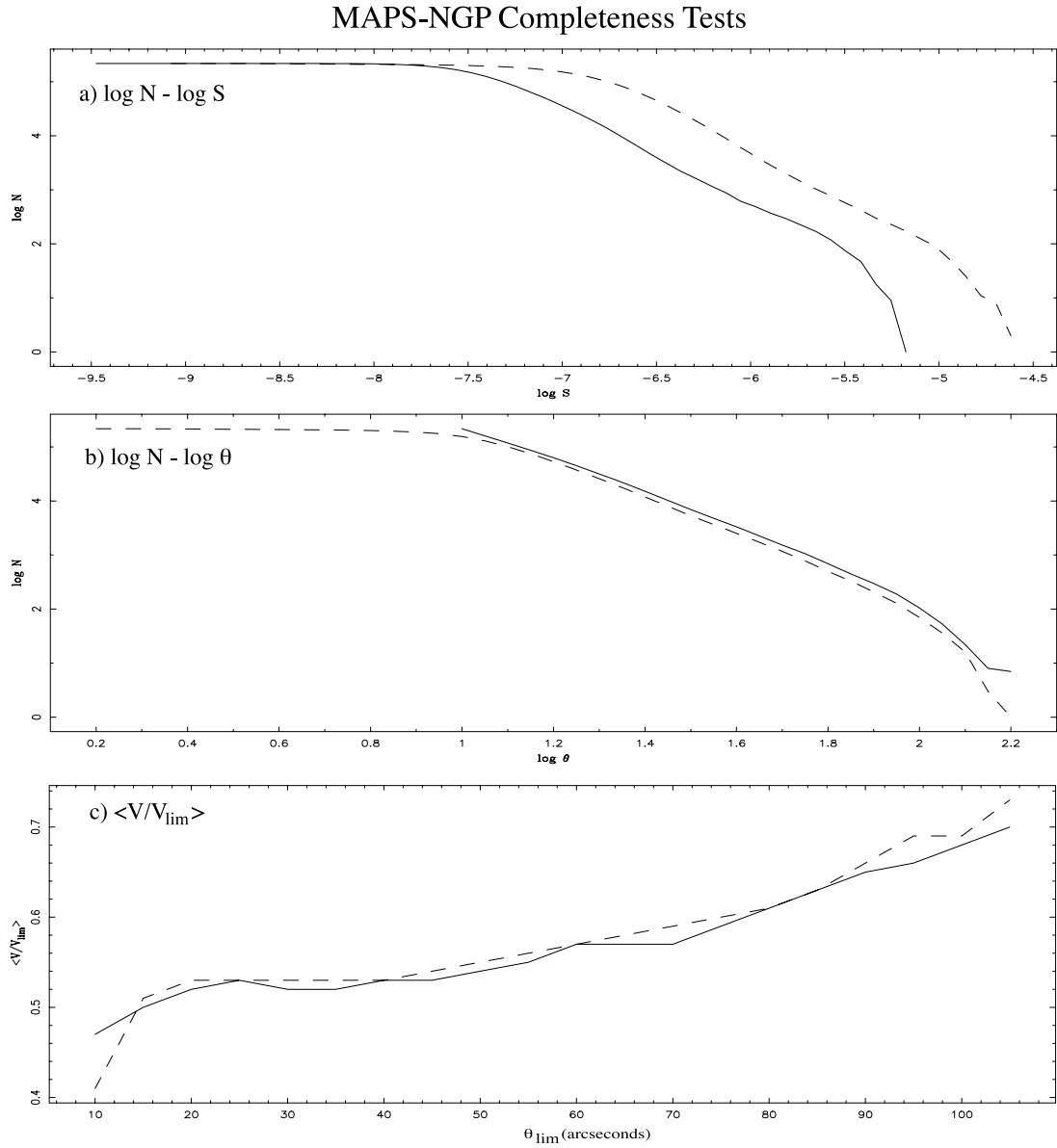


Figure 5.14: These three plots display the results of various completeness tests on the MAPS-NGP catalog for both the O (solid line) and E plate (dashed line) data. a) The $\log(N) - \log(S)$ and b) $\log(N) - \log(\theta)$ tests essentially compare total number counts of galaxies as we go to smaller flux (S) or smaller diameter (θ) limits. c) The $\langle V/V_{lim} \rangle$ test provides a measure of where in our sample volume most of the catalog galaxies are located.

Chapter 6

Previous Investigations of Internal Extinction in Galaxies

Darkness is to space what silence is to sound, i.e., the interval.

Marshall McLuhan (1911-80), Canadian Communications Theorist

Today, astronomers know that while space may be a very empty vacuum, there is more to the darkness of space than an “interval” of emptiness between stars. The darkness is partly aided by the presence of an obscuring medium, called interstellar dust, in the spaces between the stars.¹ And while we are now starting to have a reasonable understanding of the distribution of dust in our own galaxy, as noted in 3.5, the internal distribution of dust in other galaxies and the internal extinction it causes are not very well understood. This unclear understanding of the internal extinction properties of galaxies leads to uncertainty in determining a galaxy’s intrinsic physical properties (e.g. - luminosity, isophotal diameter, and surface brightness) if it is not oriented face-on from our point of view. Empirically, we know from the dust lanes we see in the Milky

¹It should be noted that dust is *not* the solution to Olber’s paradox of why the night sky is dark. Olber noted that in an infinite universe any line of sight should eventually hit the surface of a star, so the night sky should be as bright as the surface of a star. Dust doesn’t resolve this since it would be heated by this amount of starlight and would start glowing thermally. Olber’s paradox is traditionally resolved by noting that the observed expansion of the universe leads to large portions of the universe to lie beyond our “horizon.”

Way (and in other galaxies) that extinction is important. However, we do not know enough about the distribution and extent of dust in galaxies to allow easy “correction” of galaxy luminosities, diameters, and surface brightnesses for inclination. Such inclination corrections are very important to any studies that hope to obtain the intrinsic properties. Examples of situations for which a good understanding of the effects of inclination on a galaxy’s appearance are important include:

- Studies attempting to derive the luminosity distribution functions of galaxies must consider the effects of inclination on the observed isophotal diameter.
- Similarly, the less common studies of galaxy diameter distribution functions need to consider inclination effects.
- Attempts at deriving galaxy distances using the Tully-Fisher relationship between HI (or CO) line width and optical (or near-IR) luminosity must correct the observed integrated luminosity for internal extinction.
- Studies of the stellar content of galaxies may have to take into account internal extinction if the optical thickness of galaxies is high enough.
- If galaxies are optically thick, one would have to model the evolution of dust as well as stars in order to interpret observations of galaxies at cosmological distances.

Therefore, accurate measures of the effects of internal extinction in galaxies are quite important for other extragalactic studies. In order to give the reader a feel for the background of the field of internal extinction studies of galaxies, I will now provide a brief history of the field. I will be concentrating on empirical studies, as modeling of inclination effects is, as will be pointed out later, very model dependent.

6.1 Galactic Extinction: A Local Example of Internal Extinction

In the early part of the 20th Century, the development of astronomical photography allowed astronomers for the first time to probe the vast number of stars and galaxies below the threshold of visual observation. Dutch astronomer, Jacobus Cornelius Kapteyn, working at a facility that had no telescopes of its own, used this new technology in conjunction with one of first international astronomical collaborations, to coordinate the deepest star count observations ever made. Using these observations, Kapteyn constructed the first detailed model of the galaxy in 1920, which came to be known as *Kapteyn's Universe*. This model characterized the Galaxy as a flattened spheroid roughly 18 Kpc across with the Sun located only 650 pc from the center of the Galaxy. The almost heliocentric nature of the model disturbed Kapteyn. He knew that the presence of an absorbing medium in interstellar space could drive the observations toward a heliocentric model as it made farther stars dimmer than the r^{-2} dimming due simply to the star's distance. However, there was little observational evidence for Galactic extinction being significant outside of the dark bands in the Milky Way. Kapteyn [1909] had looked for signs of interstellar absorption, such as reddening, but found little extinction in his data. Summarizing the opinion of the day, Harlow Shapley [1918] in his paper on the distribution of globular clusters in the sky noted that in order to explain the lack of globular clusters visible near the plane of the Milky Way, one could consider a variety of theories, including "general absorption of light in space" which he dismissed as seeming "clearly impossible."² Ironically, Shapley notes that "dark obstructing nebulae which are frequently found in or near the Milky Way are undoubtedly capable of obliterating or greatly diminishing the light of any cluster involved in the nebulosity or beyond it." Shapley and others seem to have clearly understood that dark nebulae were

²Shapley [1918] is the same paper which noted that the center of the distribution of globular clusters was roughly 13 Kpc distant, supporting the non-heliocentric model of the galaxy.

due to extinction of background light by intervening interstellar clouds, but didn't consider the possibility of low level extinction in other parts of the sky (specifically close to the Galactic plane) could cause a "Zone of Avoidance" by obscuring background galaxies and globular clusters. It was Shapley's "opponent" in the famous Curtis-Shapley debate, Heber Curtis [1918], who pointed out that if the dark bands in the Milky Way corresponded to the dark bands seen in edge-on spirals, then this should explain the "Zone of Avoidance" as being due to obscuration within our own Galaxy (and that other spiral nebula are external galaxies similar in structure to our own). Robert Trumpler found strong evidence of interstellar extinction in 1930 in comparing the distances to open stellar clusters computed via their angular size and their total luminosity. Trumpler [1930] found that the distances determined by total luminosity were systematically smaller than distances determined by angular size. This indicated extinction on the order of 0.7 magnitudes per Kpc (much lower than the extinction in dark bands in the Milky Way, which can exceed several magnitudes per Kpc). By the 1950s, it was assumed that there was a thin obscuring layer to the Galaxy. In Edwin Hubble's *Realm of the Nebulae*, an early book on extragalactic astronomy aimed at the general public, he notes what while most obscurations is in clouds, that there is believed to be an "absorbing layer" of material with an optical depth of about 0.5 magnitude. There is no radial change in the thickness of this "absorbing layer" noted in Hubble's book. Current thinking is that interstellar extinction is caused by sub-micron sized dust grains which absorb and scatter the light. By noting that gas and dust tend to exist in common, Burstein & Heiles [1982] used HI maps and galaxy counts to make estimates of the level of Galactic extinction across most of the sky. Recently, direct observations of the dust have been used to map Galactic Extinction as well [see Schlegel, Finkbeiner, and Davis 1998]. While the exact distribution of the absorbing layer in the galaxy is not well known, it is assumed to track with the gas, which is considered to be, to first order, a double exponential distribution (consisting of both an exponential radial distribution and exponential vertical [relative to the plane] distribution). A good reference on recent thinking on Galactic extinction

is Whittet [1992].

6.2 Internal Extinction in Other Galaxies - Early Studies

Holmberg’s 1958 study, marks the start of statistical investigation of internal extinction in spirals other than the Galaxy. Conceptually, the approach in this work is easy to understand. Holmberg started by gathering observations of the axial ratios, luminosities, and diameters of 119 spirals. One would expect that if there is no extinction, the total flux of the galaxy (given by its integrated magnitude m_0) would be preserved with inclination. Holmberg computed the average “face-on” surface brightness (essentially an integrated flux) for each galaxy:

$$S_0 = m_0 + 5 \log(a). \quad (6.1)$$

He observed that edge-on galaxies had higher S_0 (lower surface brightness) than face-on galaxies (from 1.03 magnitudes for presumably dust-poor Sc galaxies to 1.33 magnitudes for Sa/Sb galaxies). This suggested that galaxies had considerable internal extinction. While he disregarded the possibility, Holmberg pointed out that this trend could be caused by increasing isophotal diameters with inclination. This isophotal diameter behavior might be expected, since as a galaxy is inclined to our line of sight, the number of stars in any line of sight through the galaxy should increase relative to the face-on value (see Figure 6.1). This would increase the locally observed surface brightness, and thus the isophotal diameters. An increase in isophotal diameter would result in higher S_0 values. And while one might expect such a trend, Holmberg [1958] found no evidence for such a trend and assumed isophotal diameters are independent of inclination. While Holmberg [1958] found no evidence of isophotal diameter changes with inclination, de Vaucouleurs [1959] did. Therefore, de Vaucouleurs [1959] argued that galaxies’ luminosities are constant with inclination and that thus galaxies were effectively “transparent,” with little or no internal extinction. This “transparent” assumption is also made in de Vaucouleurs and de Vaucouleurs’s 1964 *Reference Catalog of Bright Galaxies*, such that

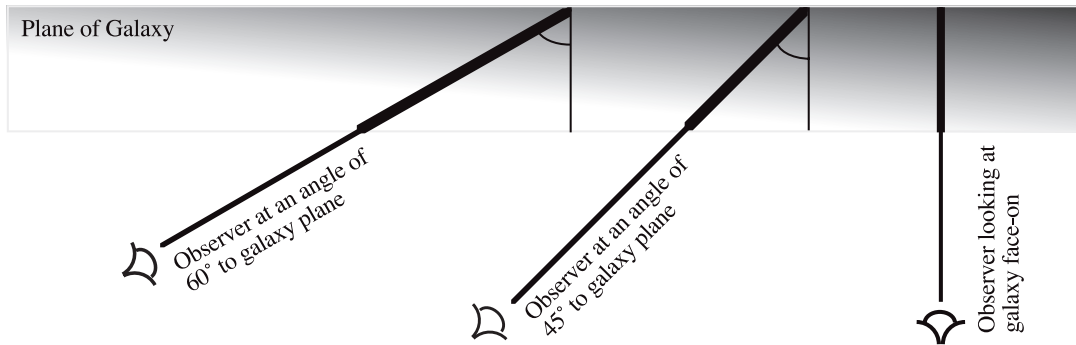


Figure 6.1: As our line of sight into a galaxy is more inclined, the length along our line of sight through the galaxy increases roughly as $1/\cos(i)$. Of course, the actual increase in the number of stars in the line of sight depends on the distribution of both stars and dust in the galaxy.

integrated magnitudes in that catalog are not corrected for inclination.³ In preparation for the *Second Reference Catalog of Bright Galaxies* (1976, RC2), Heidmann, Heidmann, & de Vaucouleurs (1972a,b,c, HHV) published three papers in which they investigated the effect of inclination on a galaxy’s appearance. Their study used HI observations of galaxies as a reference for the intrinsic flux, since they claimed 21 cm radiation is not significantly affected by internal extinction. By comparing the behavior of the ratio of HI flux to total magnitude versus inclination and HI “surface brightness” (computed using optical diameters) versus inclination, they found both optical magnitudes and diameters vary with inclination. HHV claimed that Holmberg [1958] overestimated the inclination dependence of magnitudes because he ignored inclination dependence of diameters. They also assert that de Vaucouleurs [1959] overestimated the inclination dependence of diameters because he used magnitude-limited sample. Later that year Tully [1972] criticized the HHV study. Tully claimed that a reanalysis of the “most homogenous” subset of data from the HHV study failed to show any inclination dependent behavior in the HI data. Tully also found the theoretical calculation of maximum level of HI absorption made by HHV “must be considered extremely uncertain.” In a prelude to

³Huizinga [1994] notes that while the *Reference Catalog of Bright Galaxies* assumes optical thinness, color corrections were made versus inclination.

Burstein, Haynes, and Faber [1991] review of the field, Tully noted that in a magnitude versus diameter plot, one could see the population of galaxies shift with inclination (see Figure 1 of Tully [1972] or for a variant of this plot, Figure 6.2 of this thesis) but the key question was what direction the distribution was shifting. Tully's reanalysis of then recent HI observations found that while magnitude varied with inclination, isophotal diameter did not, that is that inclination moves a galaxy vertically downward in a diameter versus magnitude plot. A decade later, Burstein [1982] in investigating the mass and luminosities of spirals dedicated an appendix to investigating the effects of inclination. By looking at the H (near-IR) bandpass pseudo-surface brightness (which assumed the optical diameter squared represented the surface area of the galaxy) versus HI line width, he found that the H pseudo-surface brightness changes with inclination. However, most of this could be accounted for by the expected change in HI line width versus inclination. Thus, agreeing with Holmberg [1958], he found little change in B diameter versus inclination. A few years later, Burstein and Lebofsky [1986] found that detection rate of UGC Sc spirals by the **Infrared Astronomy Satellite** (IRAS) at $100 \mu\text{m}$ varied with inclination. They note this could be explained by a large change in isophotal diameter versus inclination or by higher than expect internal extinction at $100 \mu\text{m}$ in Sc galaxies. Investigating changes in isophotal diameter versus inclination, they note that if isophotal diameters increase with inclination, then a diameter-limited sample of edge-on galaxies would be deeper (as noted in this thesis in Section 2.3.2), and thus the galaxies farther, reducing their IR flux-limited detection rate. They then introduce the first test of inclination effects using redshifts, which involved plotting the distance (redshift) versus diameter for low and high ellipticity subsets of their sample. If there is a change in isophotal diameter with inclination, one would expect to see the redshift distribution to occupy a broader range of values. They saw no such effect in their plot of UGC diameters versus redshift and concluded that isophotal diameters do not change with inclination, and therefore implied higher than expected internal extinction at $10 \mu\text{m}$. During this time, Tully and Fouqué [1985], motivated by the very disparate results

in attempts to determine the Hubble constant, investigated the necessity for corrections to fundamental observables. Using a sample of 101 galaxies with B and H magnitudes, B diameters, and HI line profile widths, they found deviations from the expected $B - H$ versus HI line width relationship had an inclination dependence, indicating that the B magnitude was dependent on inclination. They also performed Burstein's test, comparing the H pseudo-surface brightness to the HI line width for 202 galaxies and found an inclination dependence in the B diameters. They conclude that the RC2 corrections to B diameters and magnitudes are correct. Stavely-Smith and Davies [1987] reached a similar conclusion using HI observations of 128 galaxies, finding no change in HI flux versus inclination, thus arguing the RC2 inclination corrections for diameter and magnitude were approximately correct. CCD-based investigations in the same year by Cornell *et al.* [1987] also supported the diameter and magnitude corrections used in the RC2, although Cornell *et al.* [1987] did state that RC2 corrections overestimated true isophotal diameters by about 14%. By the late 1980s, the standard view of galaxies was that they were optically thin in their outer regions, with internal extinction increasing toward the inner parts of galaxies. This explained not only the increase in isophotal diameters with inclination, but also the decrease in integrated luminosity with inclination, which required some extinction in galaxies (as do the observed dust lanes in some edge-on spirals). There may have been some debate as to the exact levels of extinction, but all in all, it was assumed galaxies were mostly optically thin in their outer regions.

6.3 Internal Extinction in Other Galaxies - The Last Decade

The first attempt at using a large survey to study internal extinction in galaxies was Valentijn [1990], who studied over 9000 galaxies Sb/Sc galaxies from the *Surface Photometry Catalogue of the ESO-Uppsala Galaxies* (1989, ESO-IV). He found that the B bandpass central surface brightness and the surface brightness at the half-light radius didn't vary with inclination for a sample of 2600 Sb galaxies indicating optical thickness. He then investigated the outer regions of galaxies by examining the behavior of the

ratio of isophotal diameter at 26 mag/□'', D_{26} , and the half-light diameter, D_e , versus inclination. He found D_{26}/D_e did not vary with inclination. Valentijn interpreted these results as indications that galaxies behave optically thick (he used the term “opaque”), even at the 26 mag/□'' isophote! This required dust (or some other absorbing bodies) to have a scale height comparable (or larger!) to stars, something not observed in the Galaxy. This was not the first claim that spirals could be optically thick, even in the outer portions of the disk. In the previous year, Disney, Davies, and Phillips [1989] had noted that a lot of the classical tests for optical extinction, the diameter (or luminosity or color) vs. inclination tests were highly model dependent. Therefore, for example, if galaxies have a very high opacity, very thin layer of dust in their midplane, we would always see just the “upper half” of the galaxies, and therefore we might see optically thin behavior from a galaxy that was really optically thick. They essentially argue that all previous work is inconclusive because the results are very highly model dependent. They then suggested that in fact the optically thick model matched the observed behavior of spirals. Specifically, they argue that:

- Optical thickness would explain the apparent lack of high surface brightness galaxies as due to internal extinction.
- Gas column densities have been related to extinction levels [Burstein & Heiles 1982] in the Galaxy. Using observed gas column densities in other galaxies, the transition to optically thick to optically thin behavior should occur at a B isophote diameter of about 23 – 24 mag./□''. CO distribution in other galaxies also suggests similar isophotal diameter for the transition to optical thickness.
- The fairly constant radio-continuum to FIR ratio observed for a wide variety of spirals can be more easily explained if galaxies are optically thick, such that FIR emission is not starburst driven but rather driven by stellar and dust densities.

One of major points of Disney, Davies, and Phillips [1989] was however to point out the extreme model dependence of the observations supporting the “optically thin” model of

galaxies. The Disney, Davies, and Phillips [1989] and Valentijn [1990] results regarding the possible optically thick nature of galaxies became the impetus for a series of contradicting papers during the last decade. Choloniewski [1991] in developing his method for empirically determining the effect of inclination on isophotal diameter, luminosity, and surface brightness showed that redshift was necessary to properly disentangle the various effects. He also showed that diameter-limited and magnitude-limit surveys would lead to sharply different conclusions due to selection effects. In their review paper on the effect of galaxy inclination on observed galaxy properties, Burstein, Haynes, and Faber [1991] in a less mathematically rigorous method reached a similar results (Their results are discussed below in more detail in Section 6.4). Both of these studies used the UGC diameters and ZCAT catalog redshifts to determine that galaxies appear to behave in an optically thick manner.⁴ De Vaucouleurs and the other authors of the *Third Reference Catalog of Bright Galaxies* (1991, RC3) also concluded galaxies are optically thick and apply no diameter corrections to their catalog entries. Huizinga and van Albada [1992] redid the analysis of Valentijn’s ESO-LV Sc galaxies, using diameter and magnitude-limited subsamples. They found that the local surface brightness in the outer regions of galaxies did increase with inclination. They also saw an increase in half-light radius with inclination. Their results supported the idea of galaxies behave as if they have low internal extinction in their outer regions and higher extinction in their inner regions. They argue that Valentijn’s results are due to Valentijn ignoring secondary effects of inclination, such as the change in the half-light radius with inclination and its effect on the half-light surface brightness. Kodaira, Doi, and Shimasaku [1992] also criticized Valentijn’s results. They used V bandpass Schmidt plate data to confirm that the central and half-light surface brightnesses are independent of inclination. They then use some simple galaxy modelling to argue that the bulge component leads to inclination independent behavior of central and half-light surface brightness, not an extraordinary

⁴It should be noted that Choloniewski [1991] clearly states that his tests show galaxies to *behave* optically thick, it does not necessary translate into true optical thickness as such a determination is highly model dependent *a la* Disney, Davies, and Phillips [1989].

level of internal extinction. Giovanelli *et al.* [1994] performed a very detailed study of CCD I-band images of 1750 northern Sc galaxies. They found that galaxies tend to be optically thin, especially in their outer regions, although they are not as transparent as some people had previously assumed (Giovanelli *et al.* estimate 1.05 magnitudes total extinction going from face-on to edge-on). They also found the center of the galaxy to be optically thick in I band (with $\tau < 5$). A comparable study of CCD I-band images of 1350 southern galaxies by Byun (1992b) found similar results, although his face-on to edge-on magnitude change was only 0.7 magnitudes. Giovanelli *et al.* also noted that the diameters in the UGC were *not* isophotal, a problem that will be discussed in much more detail in Section 6.5.1. Some multibandpass attacks at the problem of internal extinction have also been attempted. Boselli and Gavazzi [1994] use H , V , B , and U band observations of ~ 500 galaxies and found considerable extinction in the V , B , and U bandpasses. They conclude that galaxies are typically optically thick. Peletier *et al.* [1995] used the $B - K$ colors of 37 Sb-Sc galaxies versus inclination to investigate extinction. Since the near-IR K band should be barely affected by dust, $B - K$ is a very good measure of amount of extinction versus inclination. They find the galaxy centers to be optically thick (with central face-on optical depth of $\tau \sim 2$ in B). They also find that the outer regions of galaxies do suffer from some extinction but are optically thin (with a maximum optical depth of $\tau \sim 0.5$ seen three scale lengths out).

Some Recent Alternative Approaches

Note that most of the previously described methods use large collections of optical observations of galaxies at a variety of inclinations in order to empirically attack the problem of internal extinction. However, with the advent of multiwavelength and computational astronomy in recent years, there have been several new approaches to the problem of estimating the level of internal extinction in galaxies. Most of these “alternative” techniques have shown late spiral types to be optically thin. Byun [1992a] measured the level of internal extinction using direct methods which (they claim) are free

of statistical bias or selection effects. One such method was to look at optical rotations curves taken in $H\alpha$ versus HI rotation curves for several edge-on galaxies. If galaxies were optically thick, the $H\alpha$ rotation curve would be due to light coming only from an outer layer of the galaxy, giving it the appearance of solid body rotation, and thus should it look very different from the HI rotation curves. However, Byun [1992a] found the $H\alpha$ and HI profiles to appear comparable, suggesting galaxies are optically thin. Bosma *et al.* [1992] performed a similar $H\alpha$ versus HI rotation curve comparison and found that the outer portions of more luminous early type spirals do become optically thick at about a radius of about one half the 25 mag./ \square'' isophotal radius. Byun (1992a) also looked for an asymmetric light distribution in face-on spirals. The bulge in these galaxies is bisected by the dust layer of the galaxy (presumably restricted to the galactic plane). Thus if we look along the minor axis of the galaxy, one would expect the half of the galaxy closer to us than the bulge would be darkened relative to the other half (for which there are more stars “above” the obscuring dust than “below” it from our line of sight). Byun examined three galaxies and found the spirals to have optically thin disks. Byun, Freeman, and Kylafis [1994] performed numerical simulations of the radiative transfer problem in order to determine which observables might be the best diagnostics for dust in galaxies. They found that there were some serious problems with using the previous diagnostics.⁵ They introduced some new diagnostics that had to deal with the structural appearance of the galaxies (e.g. - how offset the galaxy center appeared, how asymmetric the galaxy appears, etc.). Using their new diagnostics, they had previously found [Byun 1992a and Byun 1992b] that most galaxies appear to be optically thin. Xu and Buat [1995] used numerical simulations of far IR (FIR) emission in galaxies to show that the observed FIR emission in galaxies (typically only about 30% of the bolometric luminosity) is too low for galaxies that are optically thick. By modelling the galaxies

⁵The study by Byun, Freeman, and Kylafis [1994] appears to have been geared toward determining dust content in the galaxy, that is modelling the galaxy’s structure. This thesis is more concerned with developing proper empirical corrections for galaxy inclination, not with modelling the actual dust distribution within galaxies.

as a thin layer of dust embedded in a thicker layer of stars, they find observations are more consistent with disks of face-on optical depth $\tau \sim 0.6$ and thus optically thin. Numerical modelling by Trewella *et al.* [1997] suggests that central face-on optical depths of $\tau \sim 2.5$ and that galaxies become optically thin approximately one scale length from the center. Similarly, Xilouris *et al.* [1997] used comparisons of numerical simulations to the observed appearance of edge-on spiral UGC 2048 and found it was best fit by a galaxy that is optically thin when viewed face on. Jones, Davies, and Trewella [1996] used the distribution of galaxy inclinations for Sc galaxies in the ESO-LV, UGC, and RC3 measured at the 25 B mag/ \square'' isophote. They compared the observed distributions to modelled ones and find galaxies to be optically thin. Similar results have been hinted at by Cabanela and Aldering [1998] in their examination of the distribution of ellipticities of galaxies in the MAPS-NGP catalog, a diameter-limited catalog (see Section 2.9). One final interesting attack on the problem has been to directly measure extinction through galaxies by using a background source (or sources) to directly observe the effects of extinction due to a foreground galaxy. Using overlapping spiral galaxies NGC 540 and UGC 807, Andredakis and van der Kruit [1992] found the foreground galaxy (NGC 540) to be effectively transparent with an upper limit on the internal extinction of 0.3 magnitudes in B . White and Keel [1992] found similar results looking at another overlapping pair, although they did find spiral arms to have higher optical depth than interarm regions. Reaching out to the extreme edges of galaxies, Zaritsky [1994] claimed some extinction of background galaxies due to dust in the halos of two galaxies (NGC 2835 and NGC 3521). Using the average $B - I$ color of background galaxies at 60 kpc and 220 kpc, Zaritsky found a color difference of 0.067 mag (a 2σ effect). A similar search for dust in the halo of NGC 7814 by Lequeux, Dantel-Fort, and Fort [1995] found no such extinction. A summary of most of these previous studies into internal extinction is given in Table 6.1.

Table 6.1: Previous Studies into Internal Extinction Effects

Study	$N_{galaxies}$	Found Galaxies to Behave Optically ...
Holmberg [1958]	119	Thick [assumed constant diameter]
de Vaucouleurs [1959]	37	Thin
HHV [1972]	~ 50	Thin
Tully [1972]	92	Thick
Burstein [1982]	~ 50	Thick
Tully and Fouqué [1985]	600	Thin
Burstein and Lebofsky [1986]	2000	Thick
Stavely-Smith and Davies [1987]	128	Thin
Cornell <i>et al.</i> [1987]	118	Thin
Disney, Davies, and Phillips [1989]	—	Thick
Valentijn [1990]	~ 2600	Thick to 26 mag/ \square''
Choloniewski [1991]	5578	Thick
Burstein, Haynes, and Faber [1991]	4056	Thick
Huizinga and van Albada [1992]	1350	Thin
Kodaira, Doi, and Shimasaku [1992]	505	Thin
Byun [1992a]	5	Thin
Byun [1992b]	1350	Thin
Bosma <i>et al.</i> [1992]	2	Thin outer radii, Thick at about 0.5 25 mag/ \square'' radius
Andredakis and van der Kruit [1992]	1	Thin
White and Keel [1992]	1	Thin
Byun, Freeman, and Kylafis [1994]	—	Thin
Giovanelli <i>et al.</i> [1994]	1750	Thin
Boselli and Gavazzi [1994]	~ 500	Thick
Peletier <i>et al.</i> [1995]	37	Thin outer radii, Thick inner
Xu and Buat [1995]	—	Thin
Jones, Davies, and Trewhella [1996]	7459	Thin
Xilouris <i>et al.</i> [1997]	1	Thin
Cabanela and Aldering [1998]	1300	Thin

6.4 Getting Around Selection Effects

As noted earlier, in 1991 both Chołoniewski [1991] and Burstein, Haynes, and Faber [1991] pointed out the fact that in both diameter-limited and magnitude-limited surveys, attempts to determine the effect of inclination on both diameter and magnitude will be strongly hampered by selection effects. Both papers showed that in a diameter-limited survey, the mean diameter is not a function of inclination, similarly, in a magnitude-limited survey, the mean magnitude is also not a function of inclination. This means that some of the traditional tests, such as plotting the apparent magnitude (or angular diameter) versus inclination or plotting angular diameter versus magnitude for a sample of galaxies will *not* be a good diagnostic for effect of inclination on photometric properties. I will now outline in more detail the problem and how it can be resolved using one additional parameter for the galaxies, their redshifts.

6.4.1 The Danger of Selection Effects

So how did Burstein, Haynes, and Faber [1991] explain the previous variety of results? In part, they showed that, depending on what selection criteria one chooses, you will find the same sample can appear to behave optically thick or thin. Consider a galaxy survey to contain basically galaxies of similar type. For any galaxy of luminosity, L , at distance, r , the observed magnitude is:

$$m = -2.5 \log(L) + 5 \log(r), \quad (6.2)$$

And now given the fact that angular diameter, θ , is inversely proportional to distance, r , then

$$m = -2.5 \log(L) - 5 \log(\theta). \quad (6.3)$$

Thus, without considering any additional effects, we'd expect a plot of the logarithm of the galaxies' angular diameter versus integrated magnitude to have a slope of roughly -5. And in Figure 6.2 a plot of $\log(\theta)$ versus m for large galaxies in the MAPS-NGP

shows a distribution that does indeed have a wide distribution with a slope of -5 .⁶ By

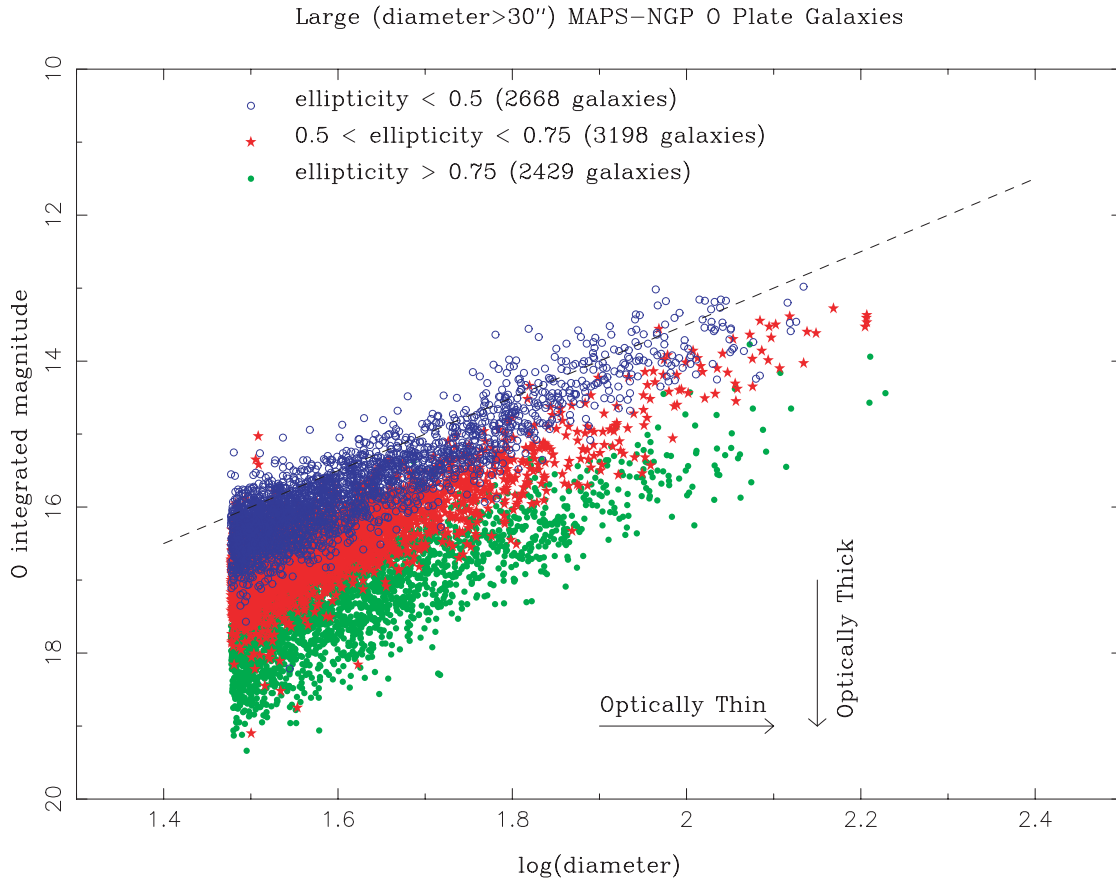


Figure 6.2: This plot of the O plate MAPS-NGP $\log(\theta)$ versus integrated magnitudes, m , shows the expected relationship with a slope of -5 between these variables (the predicted slope is indicated by the dashed line). The arrows indicate the behavior of a purely optically thick galaxy and a purely optically thin galaxy for increasing inclination and are discussed more thoroughly in the text.

using three different symbols to code galaxies with different ellipticities in Figure 6.2, we see that there is a substantial shift in the distribution with changing ellipticity (and presumably, inclination to the line of sight). To investigate, I consider a line (drawn as a dashed line in Figure 6.2) described by

$$m = 23.5 - 5 \log(\theta). \quad (6.4)$$

⁶Large galaxies are used in this figure in order to avoid the effects of seeing on the appearance of a galaxy, something that is critical for proper determination of their ellipticities.

This line is not a best fit, but is simply meant to represent a sort of upper envelope of the distribution. Considering the diameter and magnitude residuals versus this line (shown in Figure 6.3) shows they are likely tied to the ellipticity. However, we can not disentangle the diameter and magnitude dependences on ellipticity and as noted by Burstein, Haynes, and Faber [1991], this is where many previous studies have made their major error. In the extreme case of no internal extinction, the galaxy is completely transparent to radiation, so we should see all the radiation it emits at all inclinations. However, because of the increase in the number of stars in our line of sight as the galaxy is inclined (see Figure 6.1), we expect the local surface brightness along the major axes to increase and thus the isophotal diameters should increase. Therefore a face-on optically thin galaxy would move horizontally to the right in Figure 6.2 with increasing inclination. In the other extreme of a galaxy that is so optically thick that we only see the “outer crust” of stars, we would expect no line of sight induced surface brightness increase, so the isophotal diameter would remain the same with increasing inclination. However, as inclination increases, the galaxy would occupy less angular area on the sky, so its integrated magnitude would decrease, causing it to move vertically downward in Figure 6.2 with increasing inclination. In a case between the two extremes one would expect a galaxy to move toward the lower righthand side of Figure 6.2 with increasing inclination to the line of sight. Notice that the shift in the entire distribution of galaxies with increasing inclination is consistent with either the expected optically thin behavior, the optically thick behavior, or some combination of the two. Using only magnitudes and diameters to deduce the correct “inclination trajectory” will fail because we do not know the correct path followed by a galaxy as it is inclined: vertical, horizontal, or somewhere in between. Furthermore, without a true “inclination trajectory,” it can be shown that selection effects dramatically affect the results.

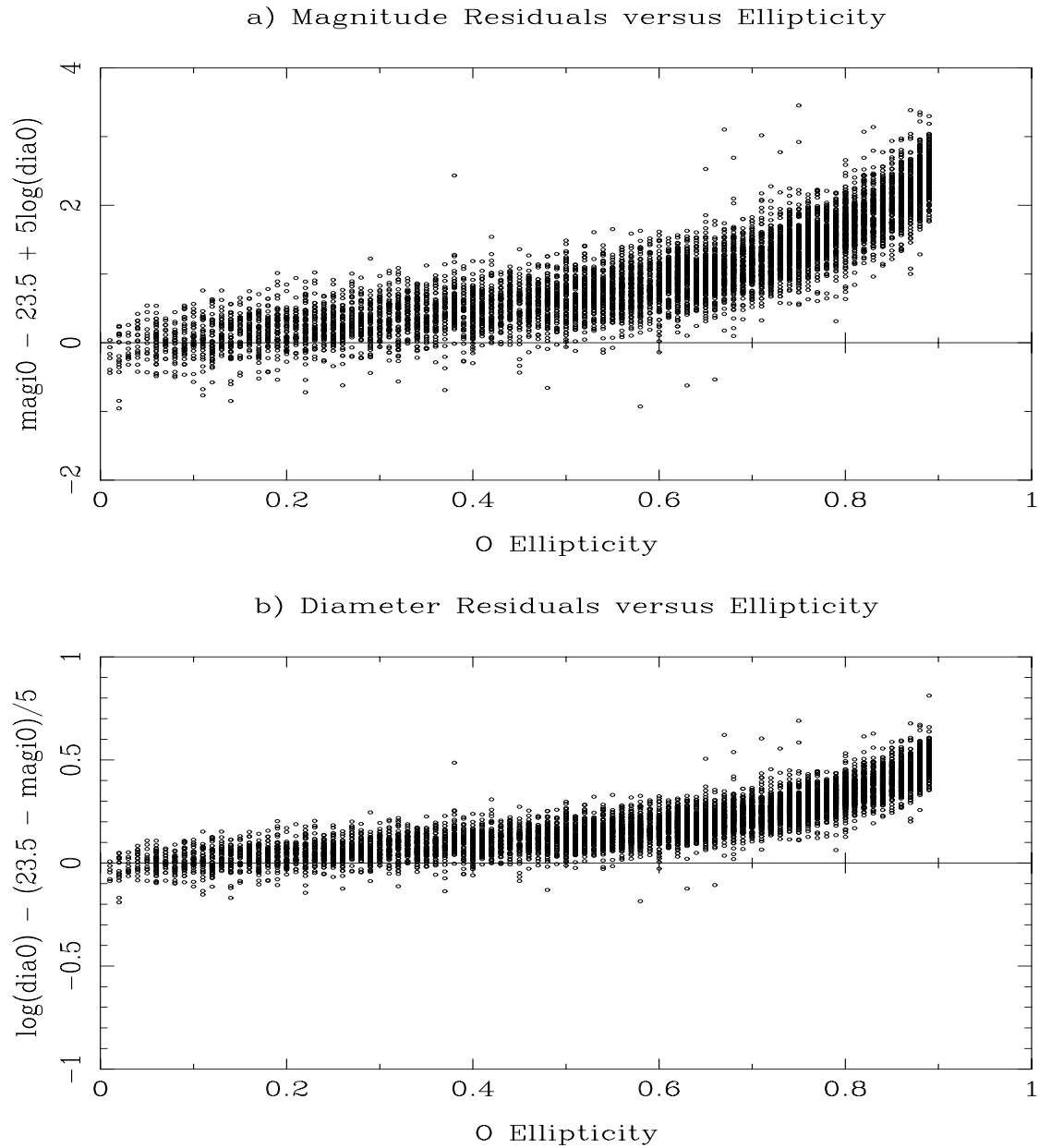


Figure 6.3: Using the dashed line in Figure 6.2 as a predicted slope, I plotted the difference between that dashed line and the actual location of the galaxy in (a) O integrated magnitude and (b) O $\log(\theta)$ versus ellipticity. From these plots, it is clear there is some relationship between ellipticity (and thus inclination) and a change in observed magnitude and diameter.

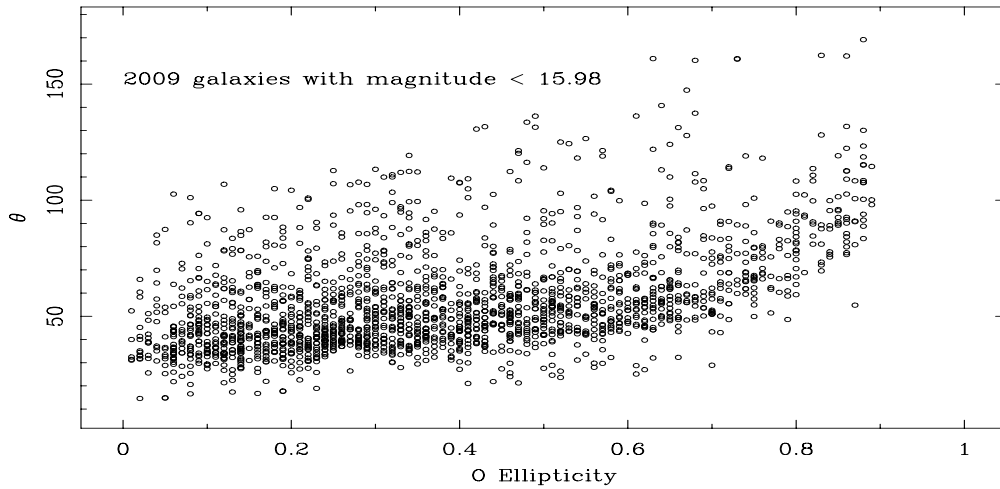
To demonstrate the importance of selection effects, I created two subsamples of the MAPS-NGP similar to subsamples of the ESO-LV generated by Burstein, Haynes, and Faber [1991]:

- a magnitude-limited sample of 2009 galaxies with magnitude ≥ 15.98
- a diameter-limited sample of 2011 galaxies with diameter $\geq 46.2''$.

Both of these subsamples should be complete since the MAPS-NGP has been demonstrably shown to be complete to a diameter-limit of $10''$ (see Section 5.10), considerably deeper than the diameter and magnitude limits above. In Figure 6.5 we see two plots of the diameter-limited subsample, one of diameter versus ellipticity and the other of magnitude versus ellipticity. These plots show diameter invariant with ellipticity and magnitude dimming with increased inclination, thus under the traditional interpretation, this would imply an optically thick appearance. This is because a horizontal (magnitude limited) cut through the sample in Figure 6.2 drives the most inclined objects to have large diameters. The similar plots for a diameter limited subsample (Figure 6.4 show diameter increasing with inclination and magnitude being constant with inclination, which would traditionally be interpreted as an optically thin interpretation. Again, this is a selection effect due to the fact that a vertical (diameter limited) cut in Figure 6.2 drives the most inclined objects to have large magnitudes. Figures 6.4 and 6.5 graphically illustrate what Choloniewski [1991] mathematically proved, the selection-criteria for a sample of data can dramatically affect the distribution seen in magnitude (or diameter) versus ellipticity plots. Notice that the same dataset has produced results traditionally considered to be both optically thick and optically thin. Therefore, when attempting to interpret the effects of inclination from a galaxy survey, one must carefully consider the selection criteria and properly adjust for them. The mathematical reduction method which correctly considers selection effects was introduced by Choloniewski [1991] and is detailed in 6.4.3.



a) magnitude-limited Subsample of MAPS-NGP (diameter distribution)



b) magnitude-limited Subsample of MAPS-NGP (magnitude distribution)

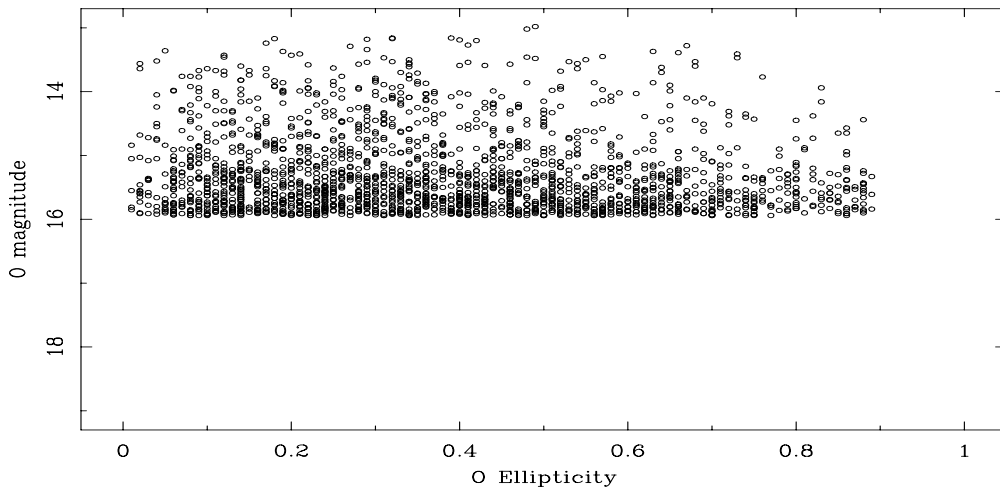


Figure 6.4: This plot of the magnitude-limited subsample of 2009 galaxies in the MAPS-NGP shows that (a) a plot of diameter versus ellipticity in this subsample shows no trend whereas (b) a plot of magnitude versus ellipticity shows a strong trend toward dimmer magnitudes at higher ellipticities. Therefore, traditional tests would show this sample to be optically thick.

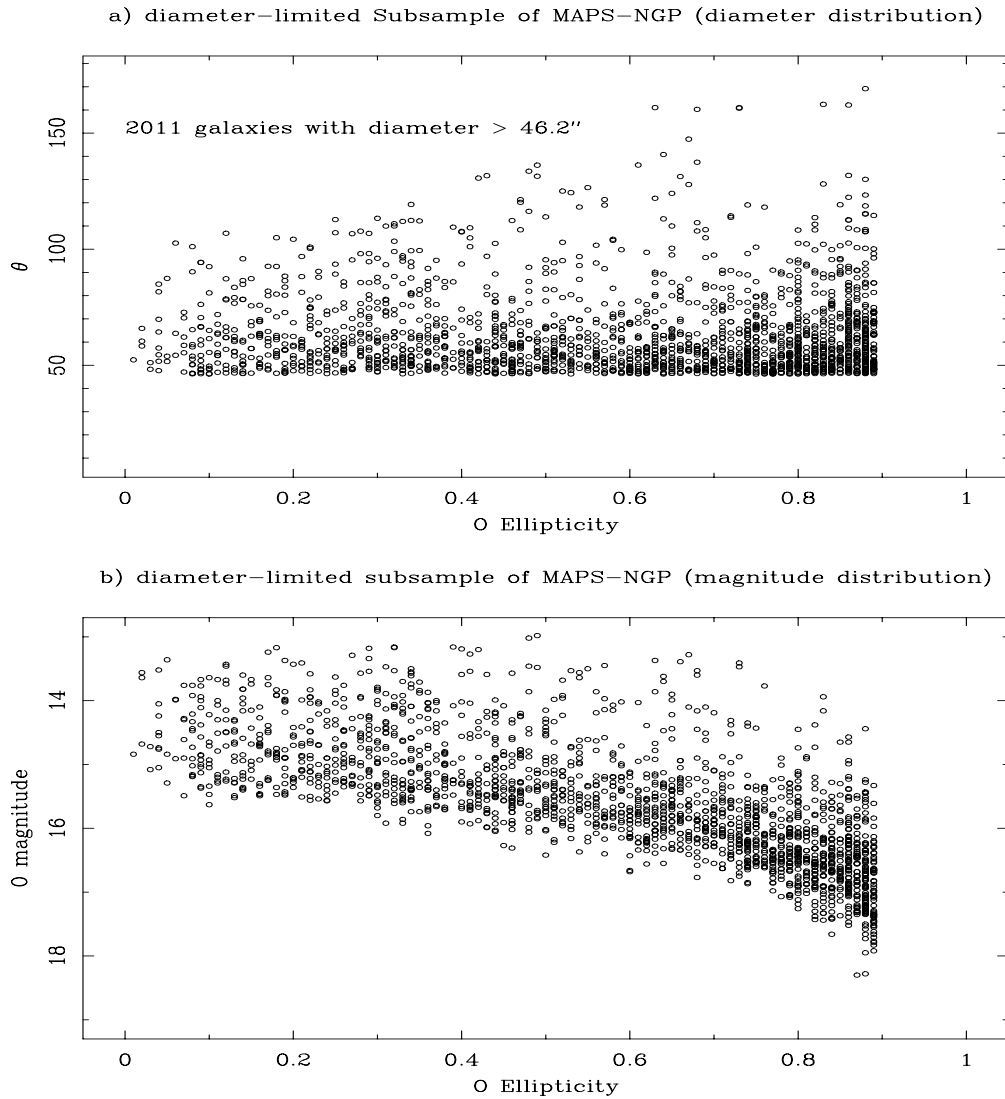


Figure 6.5: Similar to Figure 6.4 but for a diameter-limited subsample of 2011 galaxies in the MAPS-NGP shows that (a) a plot of diameter versus ellipticity in this subsample shows an increase in diameter versus ellipticity whereas (b) a plot of magnitude versus ellipticity shows no strong trend with ellipticity. Therefore, traditional tests would show this sample to be optically thin.

6.4.2 Getting Around Selection Effects with Distance

I noted above that part of the reason for contradicting results seen in previous galaxy survey-based studies of inclination effects is because the typical survey selections are diameter or magnitude limited and don't cut through the dataset in a way to that selects intrinsically similar galaxies. So the question becomes how can one select intrinsically similar galaxies who only vary in inclination? To select an intrinsically similar population of galaxies, we need to consider how such a population would appear to us if scattered isotropically in space. As shown in the brief derivation of equation 6.3, we would expect galaxies at different distances to be scattered along a line of slope -5 in Figure 6.2. Any scatter beyond a simple line of slope -5 would be due to the effects of inclination to the line of sight. Therefore, intrinsically similar galaxies at the same distance will be scattered along the "inclination trajectory" describing how a galaxy changes appearance with inclination. Thus, as Burstein, Haynes, and Faber [1991] pointed out, we can invert the above logic to state that the correct "inclination trajectory" in Figure 6.2 can be determined if the distances to sample galaxies are known. If we know the distances, then galaxies of identical distance, morphological type, and absolute diameter should lie on the correct inclination trajectory in Figure 6.2. Inversely, Burstein, Haynes, and Faber [1991] argue that they could determine the correct inclination trajectory by slicing through the distribution of points in Figure 6.2 at a variety of angles until they find the sample with the least scatter in distance. This test is conceptually similar to the Burstein and Lebofsky [1986] test of plotting the redshift distribution versus diameter. In reality, Burstein, Haynes, and Faber [1991] ignored a serious problem in this method of finding the inclination trajectory. This problem is that there is no way of selecting a sample galaxies with identical absolute diameters. Therefore, simply making slices through the dataset and looking for the least scatter does not assure you of having found the correct inclination trajectory. Instead, in order to find the correct inclination trajectory, I have to consider the statistical behavior of a large number of galaxies.

6.4.3 Statistical Descriptions of Inclination Effects:

Chołoniewski's Estimators

There are three kinds of lies:

lies, damned lies, and statistics

Attributed to British Statesman Benjamin Disraeli (1805-1881) by Mark Twain.

With respect to Mr. Disraeli, statistics are a very useful tool when dealing with describing the behaviors of large numbers of galaxies. In the case of inclination studies, Chołoniewski [1991] introduced a way of empirically describing the effects of inclination on observed luminosity (L), diameter (D), and surface brightness (μ) through some very straightforward statistics. In the process, Chołoniewski showed that distance (redshift) information is necessary in order to disentangle the effects of inclination on diameter and luminosity. I briefly outline his paper here and introduce the Chołoniewski estimators, as it will these estimators provide a very useful way of statistically describing the effect of inclination on a galaxy's appearance. Chołoniewski describes the inclination dependence of L , D , and μ using the dimensionless functions $\alpha(p)$, $\beta(p)$, and $\gamma(p)$ such that:

$$L(p) = \alpha(p)L_0 \tag{6.5}$$

$$D(p) = \beta(p)D_0 \tag{6.6}$$

$$\mu(p) = \gamma(p)\mu_0 \tag{6.7}$$

where p is the axial ratio ($p = 1 - \epsilon$) and the '0' subscript indicates the face-on ($p = 1$) value of the parameter.⁷ Chołoniewski's technique for estimating the form of the $\alpha(p)$, $\beta(p)$, and $\gamma(p)$ functions uses the means of their values in different axial ratio bins based on observed values of diameter, luminosity, surface brightness, and redshift and their predicted relationships. Chołoniewski derives estimators for $\alpha(p)$, $\beta(p)$, and $\gamma(p)$ by making the following assumptions:

- Absolute luminosity and metric diameter can be related to the observed luminosity and angular diameter assuming Euclidean space.

⁷Normalization is such that $\alpha(1)$, $\beta(1)$, and $\gamma(1)$ all equal one.

- Assume the luminosity, diameter, and surface brightness of the galaxies are statistically independent of its spatial position, spatial orientation, or axial ratio.
- Assume galaxies are oriented randomly in space. I note that this is consistent with the results outlined in Chapters 2 and 3 which suggest any preferential galaxy alignments must be very weak.
- Assume galaxies are oblate spheroids, such that we can relate the observed axial ratio (p), intrinsic axial ratio (q), and inclination (i) with a simple relationship.
- An additional unstated assumption is that the diameter or flux limits are “hard” (e.g. - a diameter-limit of $60''$ means *no* galaxies with diameters below $60''$ make it into the sample).

Using these assumptions, Chołoniewski combines a derived distribution-free selection function with the selection functions representing diameter and flux-limited catalogs to obtain conditional distribution functions. Using the conditional distribution functions Chołoniewski derives the functional form of the expectation value functions of $\alpha(p)$, $\beta(p)$, and $\gamma(p)$. Replacing the expectation values with average observed values, Chołoniewski arrives at his estimators for $\alpha(p)$, $\beta(p)$, and $\gamma(p)$, denoted as $\hat{\alpha}(p)$, $\hat{\beta}(p)$, and $\hat{\gamma}(p)$ respectively. Chołoniewski’s technique for computing $\hat{\alpha}(p)$, $\hat{\beta}(p)$, and $\hat{\gamma}(p)$ uses the average values of observables, $\langle x_j \rangle$, computed in $M + 1$ separate axial ratio (p) bins such that

$$\langle X_j \rangle = \frac{1}{N_j} \sum_{k=1}^N X_k(p) \text{ for } p \in [(M - j)\Delta p, (M + 1 - j)\Delta p] \text{ where } j = 0, 1, \dots, M, \quad (6.8)$$

where j is the number of the bin p belongs to, k denotes the galaxies within the j^{th} bin which contains N_j galaxies. The convention used by Chołoniewski is such that $j = 0$ is the face-on bin ($p = 1$). The Chołoniewski estimators are then computed as

$$\left. \begin{aligned} \hat{\alpha}(p) &= \alpha_j \\ \hat{\beta}(p) &= \beta_j \\ \hat{\gamma}(p) &= \gamma_j \end{aligned} \right\} \text{ for } p \in [(M - j)\Delta p, (M + 1 - j)\Delta p], \quad (6.9)$$

where j is the axial ratio index noted in equation 6.8. Where several functional forms for computing α_j , β_j , and γ_j are derived in Chołoniowski [1990]. Some of the equations for α_j , β_j , and γ_j prove to be the same for both flux and diameter-limited samples:

$$\alpha_j = \frac{\langle L_j \rangle}{\langle L_0 \rangle}, \quad (6.10)$$

$$\alpha_j = \text{dex}(\langle \log L_j \rangle - \langle \log L_0 \rangle), \quad (6.11)$$

and

$$\beta_j = \frac{\langle D_j \rangle}{\langle D_0 \rangle}, \quad (6.12)$$

$$\beta_j = \text{dex}(\langle \log D_j \rangle - \langle \log D_0 \rangle), \quad (6.13)$$

and

$$\gamma_j = \frac{\langle \mu_j \rangle}{\langle \mu_0 \rangle}, \quad (6.14)$$

$$\gamma_j = \text{dex}(\langle \log \mu_j \rangle - \langle \log \mu_0 \rangle), \quad (6.15)$$

where L , D , and μ are the absolute luminosities, absolute diameters, and surface brightnesses respectively. In addition to these functions, for the magnitude-limited sample Chołoniowski derived the forms:

$$\alpha_j = \left(\frac{\langle r_j \rangle_f}{\langle r_0 \rangle_f} \right)^2, \quad (6.16)$$

$$\alpha_j = \text{dex}[2(\langle \log r_j \rangle_f - \langle \log r_0 \rangle_f)], \quad (6.17)$$

and

$$\gamma_j = \left(\frac{\langle d_j \rangle_f}{\langle d_0 \rangle_f} \right)^{-2}, \quad (6.18)$$

$$\gamma_j = \text{dex}[-2(\langle \log d_j \rangle_f - \langle \log d_0 \rangle_f)], \quad (6.19)$$

where r and d are the distance and observed diameter respectively. Finally, for a diameter-limited sample Chołoniowski found:

$$\beta_j = \frac{\langle r_j \rangle_d}{\langle r_0 \rangle_d}, \quad (6.20)$$

$$\beta_j = \text{dex}(\langle \log r_j \rangle_d - \langle \log r_0 \rangle_d), \quad (6.21)$$

and

$$\gamma_j = \frac{\langle f_j \rangle_d}{\langle f_0 \rangle_d}, \quad (6.22)$$

$$\gamma_j = \text{dex}(\langle \log f_j \rangle_d - \langle \log f_0 \rangle_d), \quad (6.23)$$

Choloniewski then solves for the covariance matrices and thus standard deviations by noting that equations 6.10 - 6.23 take one of two forms:

$$Y_j^A = \left(\frac{\langle X_j \rangle}{\langle X_0 \rangle} \right)^\eta, \quad (6.24)$$

$$Y_j^B = \text{dex}[\eta(\langle \log X_j \rangle - \langle \log X_0 \rangle)], \quad (6.25)$$

and then deriving the covariance matrices for equations 6.24 and 6.25 to be

$$C_{ji}(Y^{A|B}) = S_{A|B}^2 \left(\frac{\delta_{ji}}{N_i} + \frac{1}{N_0} \right) \quad (6.26)$$

where

$$S_A = \frac{|\eta|}{\ln 10} \sqrt{\frac{\sum_{j=1}^M N_j (\langle X_j^2 \rangle - \langle X_j \rangle^2) / \langle X_j \rangle^2}{\sum_{j=1}^M N_j}} \quad (6.27)$$

and

$$S_B = |\eta| \sqrt{\frac{\sum_{j=1}^M N_j (\langle \log^2 X_j \rangle - \langle \log X_j \rangle^2)}{\sum_{j=1}^M N_j}} \quad (6.28)$$

such that the standard deviation is simply

$$\begin{aligned} \sigma(Y_j^{A|B}) &= \sqrt{C_{jj}(Y)} \\ &= S^{A|B} \sqrt{\frac{1}{N_j} + \frac{1}{N_0}}. \end{aligned} \quad (6.29)$$

Thus, Choloniewski's recipe for estimating the form of $\alpha(p)$, $\beta(p)$, and $\gamma(p)$ is to compute the average values of various forms of those variables (defined by equations 6.10 to 6.23) binned by axial ratio. And in order to simultaneously solve for $\alpha(p)$ and $\beta(p)$, we can see from equations 6.10 to 6.23 that we need distances for all galaxies in a sample. However, as Choloniewski noted, the estimators for $\gamma(p)$ are distance independent, which is somewhat expected, since surface brightness is (in a static Euclidean universe) distance independent.

6.5 Problems with Recent Studies

It is interesting to note that there is a somewhat bimodal distribution to the number of galaxies used in previous studies (see Table 6.1), reflecting the two approaches authors have typically taken toward the problem. Several authors have attacked the problem of internal extinction by looking at single galaxies as examples. This group of authors have almost universally have found spirals to fit the late 1980s paradigm of optically thick inner regions and optically thin outer regions. The other approach is to create a large ensemble of galaxies and test the predicted behavior of galaxies with inclination. Most of the studies which report optically thick behavior from spirals have been the large survey studies. As noted in the previous section, both Burstein, Haynes, and Faber [1991] and Chołoniewski [1991] showed that many of the large survey studies preceding theirs suffered from severe selection effects and thus many of the previous results can be legitimately questioned. However, their result that galaxies behave in an optically thick fashion when selection-effects are taken into account strongly contradicts most single galaxy studies and the large CCD-based studies of Giovanelli *et al.* [1994] and Byun [1992b] which find galaxies are optically thin in their behavior. One could argue that since Giovanelli *et al.* and Byun used *I* band imaging and as the interstellar extinction law of Cardelli, Clayton, & Mathis [1989] indicates that we can expect optical depths in the *B* band to be three times higher than in the *I* band. Therefore, one could argue that Giovanelli *et al.* [1994] and Byun [1992b] only prove transparency in the *I* bandpass and that galaxies could still behave optically thick in the blue *B* bandpass. Davies, Jones, and Trewella [1995] tried to resolve the issue of Burstein, Haynes, and Faber [1991] and Chołoniewski [1991] finding optically thick behavior in galaxies by claiming that Burstein and company had introduced another strongly biasing selection effect by imposing a redshift limit. They claimed that this redshift limit led to an analysis suggesting optically thick behavior. However, there appears to be a much simpler solution to this optically thick behavior in the recent survey work of Burstein, Haynes, and Faber [1991] and Chołoniewski [1991]. Both of these studies UGC visual diameters and assumed they

were isophotal. And as I will demonstrate below, in at least three of the more widely used galaxy catalogs, this is most definitely not true.

6.5.1 Huizinga's Diameter-Inclination Effect

It is unlikely that Nilson's UGC sample would have been biased to find smaller edge-on galaxies than face-on galaxies.

Burstein, Haynes, and Faber [1991]

Huizinga and van Albada [1992] were the first to point out that the visual diameters (such as those in the UGC and ESO catalogs) were not isophotal. Their plot of the ratio of isophotal diameters, D_{25} (measured at the 25 mag/□" isophote), of Sc galaxies from the ESO-LV and the original visual diameters, D_{orig} versus axial ratio shows a very strong trend D_{25}/D_{orig} to increase with increasing inclination. Thus visual diameters do appear to be biased toward finding smaller edge-on galaxies than face-on. Huizinga [1994] called this the *Diameter-Inclination Effect*. A similar plot of the ratio of UGC diameters (which are visually determined) to *I* band isophotal diameters for Sc galaxies in Giovanelli *et al.* [1994] shows the same trend. Courteau [1992] also found a similar trend comparing UGC diameters to his Gunn r bandpass isophotal diameters. Giovanelli *et al.* [1994] and Cabanela and Aldering [1998] point out that this bias will work against anyone attempting to measure the isophotal diameter increase with inclination due to internal extinction. In the appendix of Cabanela and Aldering [1998], we showed that for the ~ 1300 galaxies (of all morphological types) in the MAPS-PP, the ratio of their diameter as mechanically measured by the APS to their published diameters from both the UGC and RC3 shows a substantial increase with increasing inclination. However, at that time one could argue that we did not know which catalog had problem and that it might be a subtle trend of APS diameters to increase with inclination which causes the observed trend of diameter ratio with inclination. As a followup to that previous work, I cross-identified the Courteau [1996] Gunn r band galaxy catalog to the APS catalog. Courteau carefully reduced his repeated observations of over 200 galaxies in order to very accurately determine their surface brightness profiles. His reported

diameters are considered to be isophotal. A plot of the ratio of APS E band diameters versus Courteau's 23 mag/□" Gunn r band isophotal diameters for Sb and Sc galaxies (see Figure 6.6a) shows that the APS diameters are isophotal. The best fit line (shown in the plot) has a slope of only 0.131 ± 0.10 , which is not statistically significant. This plot also illustrates that the mean surface brightness limit of the APS E plates is linear 23 mag/□" since the diameter ratio is very nearly one. I also made a much more expansive cross-identification of over 5500 UGC and RC3 galaxies with the APS O plate catalog (see Figure 6.6b and 6.6c) which shows that there is indeed a very strong trend of D_{APS}/D_{UGC} and D_{APS}/D_{RC3} with ellipticity. There appears to be no significant trend of diameter with ellipticity for $\epsilon < 0.3$ (the best fit lines both have slopes of 0 within errors) but from $\epsilon = 0.3$ to $\epsilon = 0.9$ there is a 45% increase in the D_{APS}/D_{UGC} ratio and a 53% increase in D_{APS}/D_{RC3} ! Because we believe the APS diameters to be isophotal, this indicates that the UGC or RC3 diameters have a bias such that they would hide any isophotal diameter change with inclination, even if it was a 30-50% effect!

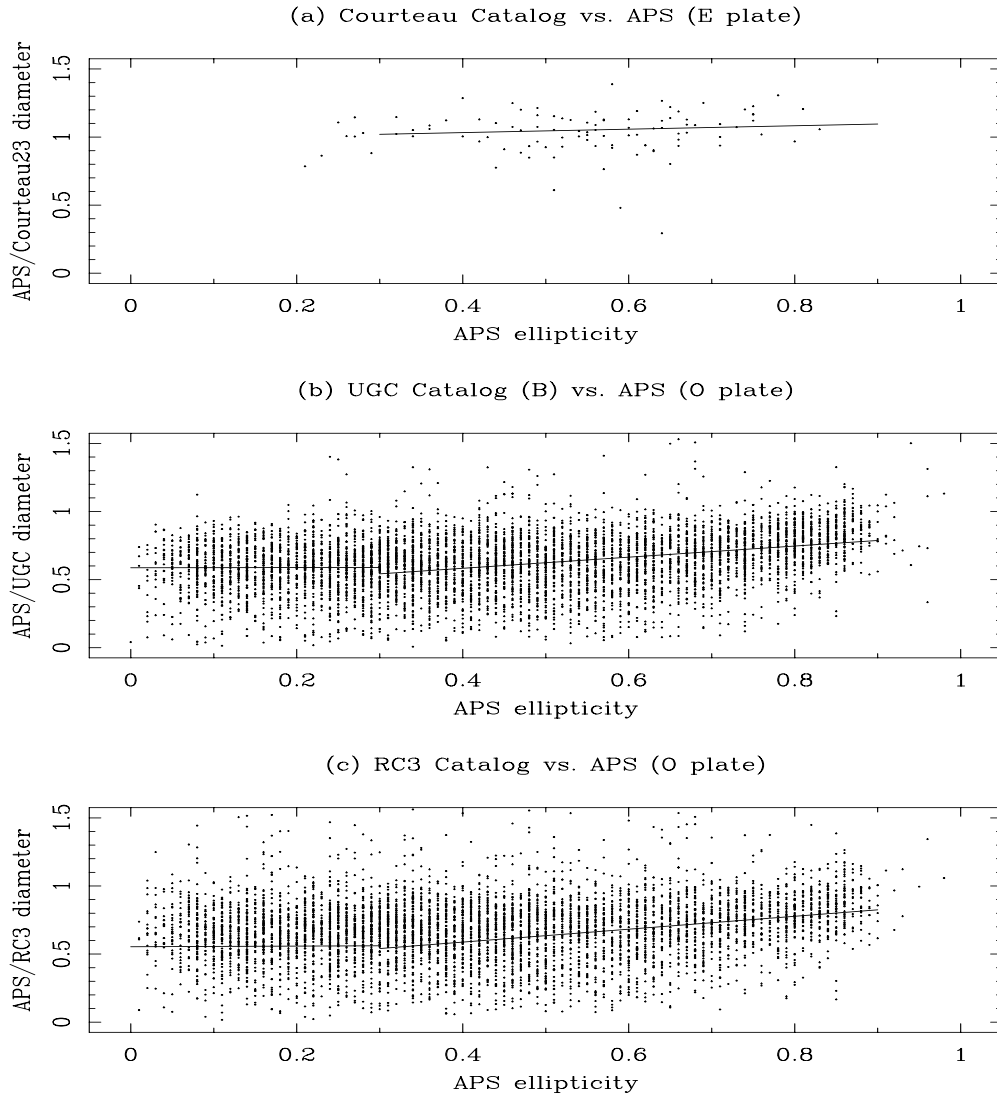


Figure 6.6: These plots show the reality of the Huizinga Diameter-Inclination effect and demonstrate the likelihood that the APS diameters are much closer to isophotal than the visual diameters in other catalogs. (a) This plot of the APS E plate diameters versus the CCD-based isophotal (23 mag/ \square'') Gunn r diameter from Courteau [1996] shows the APS diameters to be roughly isophotal. The best fit line has a slope of one within the uncertainty. (b) and (c) show the ratios of APS O plate diameters versus B band visual diameters. Notice the strong slope in the diameter ratio versus ellipticity for ellipticities greater than 0.3.

This result suggests that studies using visual diameters in the UGC, RC3, or ESO-Uppsala catalogs as isophotal diameters will find galaxies to behave optically thick, since visual diameters do not appear to change with inclination. This can dramatically affect the derived properties of galaxies. For example, Hudson and Lynden-Bell [1991] ignore the effects of inclination on diameters when deriving their diameter function. They cite several previous studies which claim diameters are insensitive to internal extinction, although those studies all used visual diameter estimates. Therefore, their diameter function will likely be smaller than real galaxies (depending on the number of inclined galaxies in their sample), since the visual diameters are smaller than proper isophotal ones. Huizinga in his 1994 PhD thesis outlined what he believed to be the cause of this diameter-inclination effect. He postulates that the “patchy” light distribution of spiral galaxies when viewed face-on combined with the human brain’s pattern recognition capability causes face-on galaxies to have their visual diameters measured to a deeper isophote than edge-on galaxies. Specifically, our physiology is such that we will recognize spiral arms in more face-on spirals and trace them out to a deeper isophote than the same galaxy viewed edge-on (which will appear less “patchy”). In order to test this hypothesis, I divided the UGC and RC3 cross-identified samples used in Figure 6.6 by morphological type. As can be seen in Figure 6.7, for both the UGC and RC3 catalogs, the diameter-inclination effect is almost non-existent in Ellipticals, which have the smoothest appearance. The diameter-inclination effect gets progressively more pronounced as we move toward later morphological types, something that would be expected if Huizinga’s theory for the source of the effect is correct.

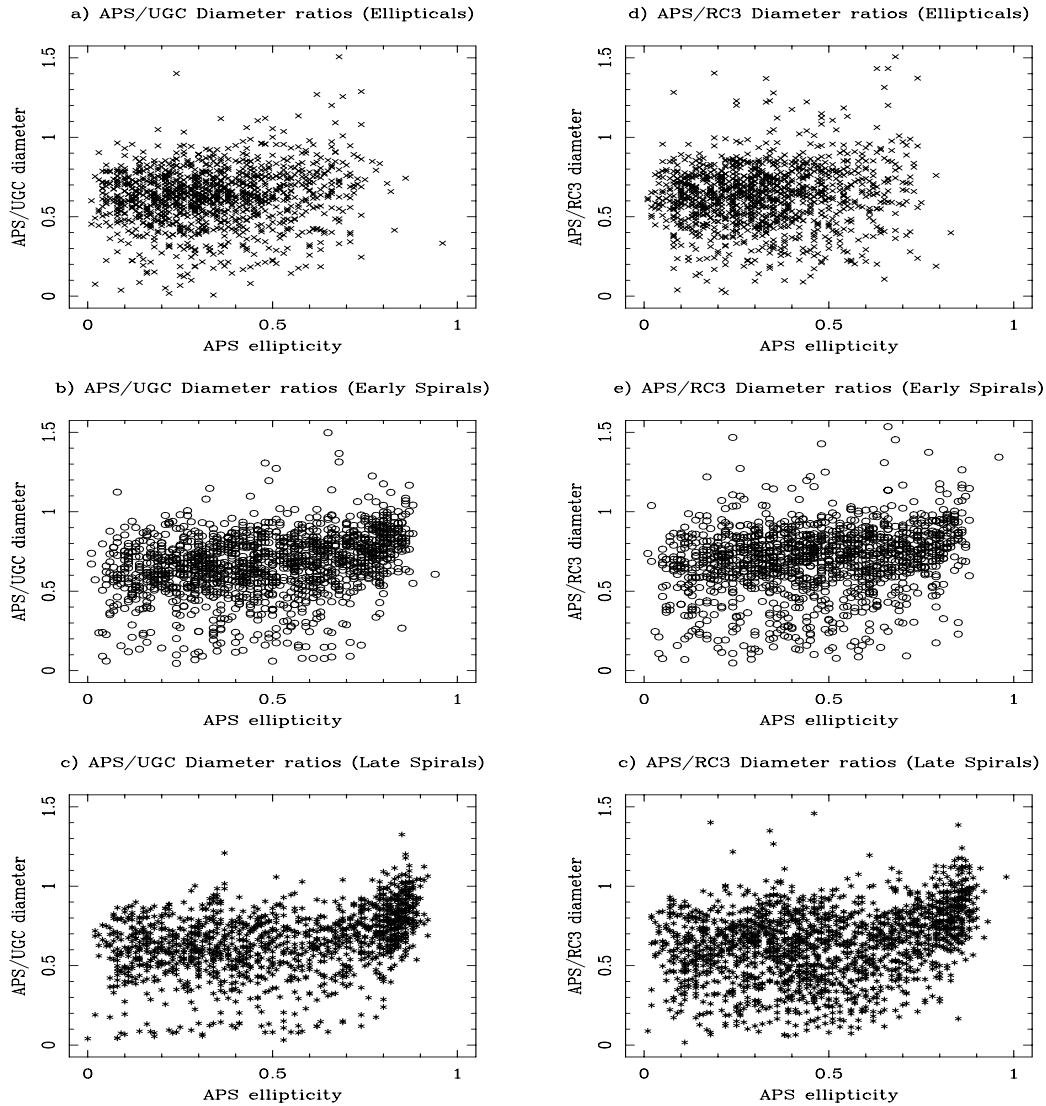


Figure 6.7: These plots show the diameter ratios between the APS and UGC (or RC3) catalogs versus ellipticity like Figure 6.6. In this case however, the datasets are segregated by morphological type: Ellipticals ($-6 \geq T < 0$), Early Spirals ($0 \geq T \geq 4$), and Late Spirals ($T > 4$). Notice that the diameter-inclination effect is much more pronounced in the subset of late spirals than in the ellipticals.

6.6 Requirements For Determining The Proper Inclination Trajectory

Now with an understanding of the previous work in this field, I can now design the proper dataset for an attempt to determine the proper inclination trajectory in both magnitudes and isophotal diameter. As outlined in Section 6.4, it is impossible to uncouple the diameter and magnitude portions of the inclination trajectory without distances. The easiest way to get distances is to use redshifts. In addition to distances, I want to make sure I have sufficient information to select intrinsically similar galaxies once I have obtained distance estimates. Therefore, in addition to redshifts, I also want to collect morphological types. Finally, I want to avoid the use of visual diameters from previous catalogs, since as noted in Section 6.5.1, there is a serious bias in these diameters which directly affects the ability to determine the proper inclination trajectory. While the data reduction techniques will not be changing dramatically from previous studies, the MAPS-NGP catalog offers a dramatically different dataset for study. The machine-measured diameters and magnitudes reported in the MAPS-NGP are will be much more consistent than any previous “human built” galaxy catalogs. The MAPS-NGP catalog also contains image parameters in two bandpasses which will allow some quantification of the variation of inclination trajectory with wavelength. In order to allow proper determination of the inclination trajectory, it will be necessary to cross-identify the MAPS-NGP with another catalog with redshifts and morphological classifications. The resulting cross-identified catalog should be the first mechanically-measured survey used in an investigation of the global properties of internal extinction. As noted by Disney, Davies, and Phillips [1989], large survey studies can not directly resolve the question of whether galaxies actually are optically thick or thin. This is because translating the inclination trajectory into a real dust distribution in the galaxies is highly model dependent. However, while a proper inclination trajectory won’t tell us if the model is correct, it can provide restrictions on it.

Chapter 7

The MAPS-NGPZT: A Dataset for Inclination Effect Studies

A vast field lies open to discoveries and observation alone will give the key.
Immanuel Kant, 1742

7.1 The MAPS-NGPZT Subset of the MAPS-NGP

As noted in Section 6.4.3, we now know that in order to disentangle the effects of galaxy inclination on the observed isophotal diameter and magnitude, we need to know the distances of the galaxies in our sample. The easiest way to do this is to use Hubble's law,

$$v = H_0 d, \text{ where } H_0 = 100h \frac{\text{km/s}}{\text{Mpc}} \quad (7.1)$$

such that redshifts, v , are linearly related to distance, d . Therefore, in order to use the MAPS-NGP to study galaxy inclination effects, I needed to obtain redshifts for as many of its members as possible. In addition to redshifts, astronomers believe that the fractional gas and dust content varies with morphological type. Therefore, it would be advantageous to also secure as many morphological classifications of galaxies as possible.

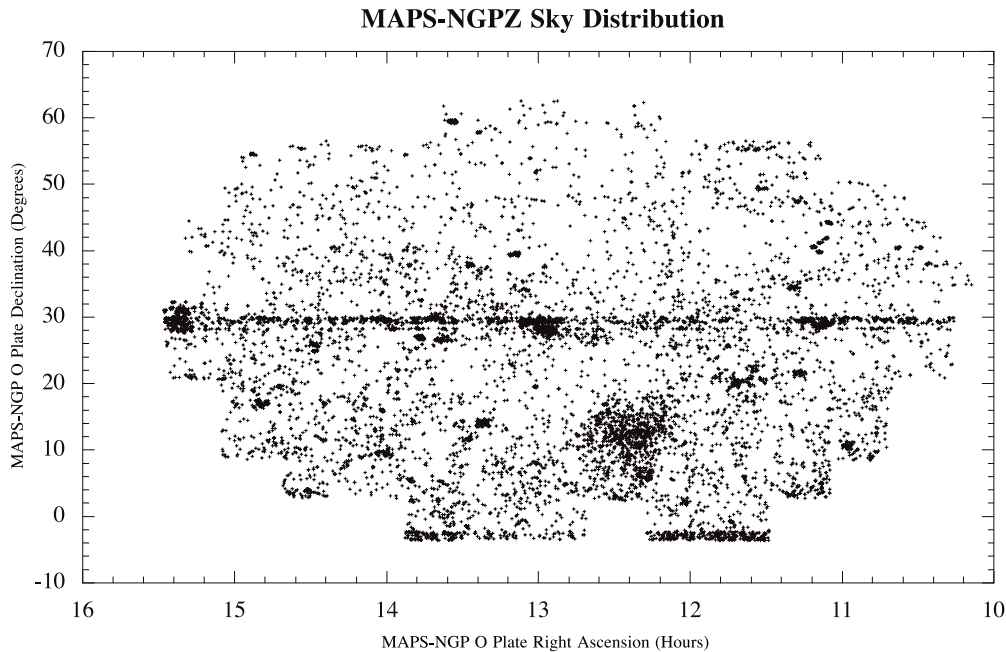


Figure 7.1: This map shows the distribution of the 8913 galaxies in the MAPS-NGPZ. Note the inhomogeneous nature of the distribution. This is partly due to the presence of real clusters in the field (including the Virgo cluster at $\alpha \sim 12^h 24^m, \delta \sim 12^\circ$ and the Coma cluster at $\alpha \sim 12^h 56^m, \delta \sim 28^\circ$). However, the presence of several deep ‘stripe’ surveys (including the Las Campanas Redshift Survey at $\delta \sim -3^\circ$ and Dartmouth Century Surveys at $\delta \sim 29^\circ$) which cover limited ranges in declination to very deep redshifts also affect the distribution.

7.1.1 The MAPS-NGPZ: Cross-identification of MAPS-NGP with ZCAT

Redshift and morphological classifications for galaxies in the MAPS-NGP were obtained by positionally matching the existing CfA Redshift Catalogue maintained by John Huchra (and colloquially known as the ZCAT) with the MAPS-NGP catalog. A copy of the most recent version of the ZCAT (November 23, 1998) was obtained online.¹ This version of the ZCAT contains redshift information for 111906 galaxies with redshifts below 10000 km s^{-1} . I cross-identified MAPS-NGP galaxies with their ZCAT counterparts by searching for overlap between the area on the sky covered by each MAPS-NGP

¹The current version can be downloaded from <ftp://fang.harvard.edu/pub/catalogs/>.

galaxy and the ZCAT reported positions.² Care was taken not to allow matching of one ZCAT object to multiple MAPS-NGP objects. In those cases where one ZCAT galaxy was the closest counterpart to multiple MAPS-NGP galaxies it was matched only to the closest MAPS-NGP galaxy. A total of 8913 MAPS-NGP galaxies were cross-identified with the ZCAT, forming a subset catalog I will refer to as the MAPS-NGPZ (See Figure 7.1). The quality of the matching algorithm can be seen in Figure 7.2, which shows the distribution of positional differences between the ZCAT and MAPS-NGP galaxies. As can be seen, over 90% of the galaxies in MAPS-NGPZ have positional differences of less than 5'' between the two parent catalogs. Given the diameter limit of 10'' imposed on the MAPS-NGP, this implies that the correct ZCAT counterparts to MAPS-NGP galaxies have been determined. While the ZCAT is essentially an all-sky catalog, it is

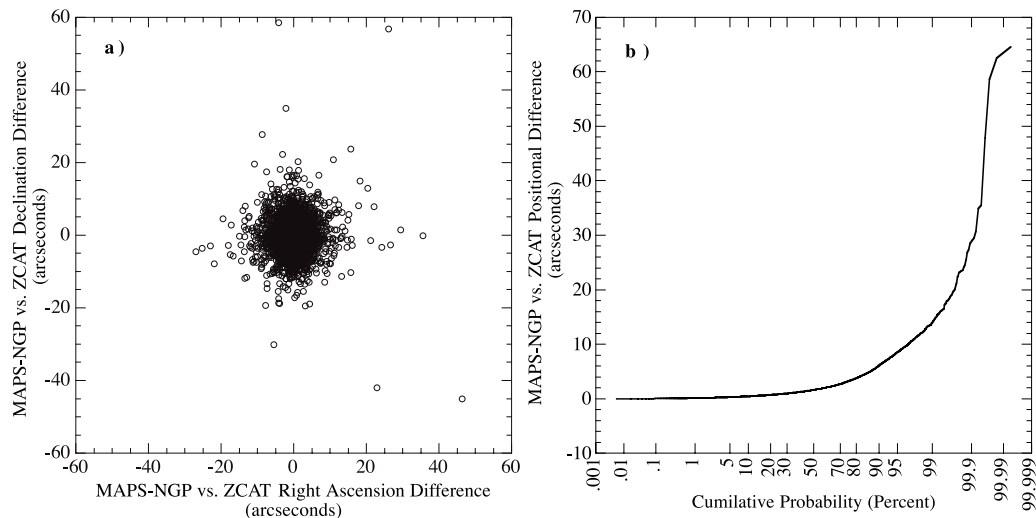


Figure 7.2: Plots of (a) the positional difference between the ZCAT and MAPS-NGP object positions for all objects in the MAPS-NGPZ and (b) the cumulative probability having a positional difference of less than a given value (in arcseconds). The vast majority of galaxies in the MAPS-NGPZ had differences of less than 5'' between the MAPS-NGP and their ZCAT counterparts.

²This requirement of an overlap between the MAPS-NGP galaxy area and reported ZCAT position allowed for easier matching of large galaxies, whose central positions are less accurately known.

not homogenous in either sky or redshift coverage. The first CfA survey [Huchra *et al.* 1983] consisted of 2401 galaxies from the Zwicky’s *Catalogue of Galaxies and Clusters of Galaxies* (CGCG) and Nilson’s Uppsala General Catalogue (UGC) in a restricted portion of the sky. Since then, redshifts for most of the CGCG and UGC have been added, meaning that the ZCAT is fairly complete for $m_{pg} \leq 14.5$. However, in addition to this part of the ZCAT, Huchra now compiles redshifts from many other surveys (the vast majority are magnitude-limited surveys), including much deeper surveys with much more limited sky coverage than the CGCG and the UGC. This means that the current ZCAT is a hodge-podge of surveys of many differing depths and sky coverages. However, for the purposes of this study, since most of the input catalogs are magnitude-limited, I will be treating the ZCAT as a magnitude-limited catalog. This means that the MAPS-NGPZ is (by virtue of being cross-identified with the ZCAT) a magnitude-limited catalog.³ As one might imagine, given the inhomogeneities in the ZCAT, the sky coverage of the MAPS-NGPZ is not homogeneous (see Figure 7.1). Its coverage is concentrated in several clusters (such as the Virgo cluster at $\alpha \sim 12^h 24^m, \delta \sim 12^\circ$ and the Coma cluster at $\alpha \sim 12^h 56^m, \delta \sim 28^\circ$) and in several deep ‘stripe’ surveys which cover limited ranges in declination to very deep redshifts (such as the Las Campanas Redshift Survey at $\delta \sim -3^\circ$ and Dartmouth Century Surveys at $\delta \sim 29^\circ$). These spatial and velocity inhomogeneities should be kept in mind when analyzing research using the MAPS-NGPZ subset. An advantage of cross-identification with the ZCAT is that the MAPS-NGPZ contains galaxy morphological T type classifications for 2687 of its members. Of these objects, 1895 galaxies are identified as spiral galaxies. Using this T type information, we can confirm simple trends of various galaxy parameters versus morphological type seen in previous work. For example, in their work with the nine POSS I fields centered on the NGP, Odewahn and Aldering [1995] noted a relationship between

³The completeness magnitude limit of the ZCAT is considerably shallower than the MAPS-NGP, so it imposes its limits on the MAPS-NGP, not the other way around.

morphological type and several APS image parameters, notably O-E color and C31 concentration index, versus T type. The relationships were expected given previous work in the field of morphological classification, but they were still reassuring. I found similar results for the MAPS-NGPZ O-E color and C31 concentration index versus T type (See Figure 7.3). In 1980, Dressler noted the now famous morphology-density relationship. This relationship can be summarized as follows: elliptical galaxies preferentially reside in high density regions whereas spirals do not. Without making redshift corrections to take into account Virgo infall (outlined in section 7.1.2, I can not make estimates of the absolute surface density (in units of galaxies per Mpc^2) like Dressler did. However, I can compare apparent surface density (in units of galaxies per square degree) versus T type for the MAPS-NGPZ, as in Figure 7.3c. I do indeed find that the distribution of apparent surface density is higher for ellipticals than spirals, just as expected.

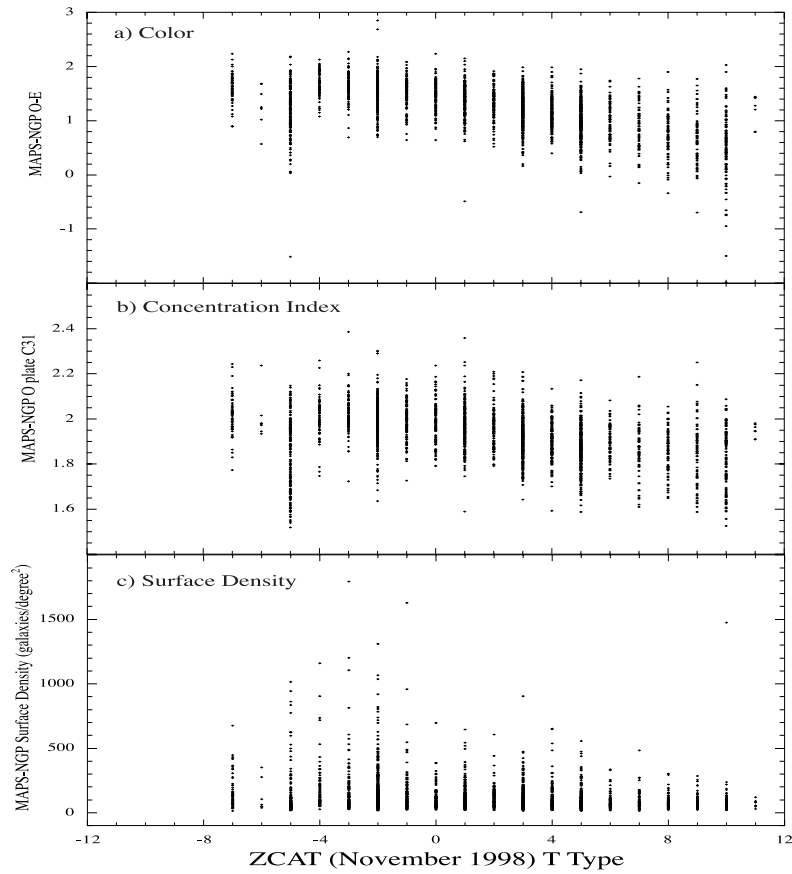


Figure 7.3: (a) The $O - E$ color versus T type for 2472 galaxies in the MAPS-NGPZ showing ellipticals (those with $T < -2$) are redder than spirals ($T > 0$). (b) The O plate C31 concentration index versus ZCAT T type for MAPS-NGPZ shows the trend seen by Odewahn and Aldering [1995]. (c) MAPS-NGPZ surface density versus ZCAT T type, showing the anticipated morphology-density relationship.

7.1.2 Adjusting Redshifts for Virgo Infall

Since I want to estimate actual distances to the galaxies in the MAPS-NGPZ, I assume that galaxies' redshifts are due solely to Hubble flow. However, the universe is not perfectly homogeneous and concentrations of mass (such as galaxy clusters and superclusters) can gravitationally attract galaxies, affecting their motions significantly. These motions not due to the expansion of the universe are called *peculiar velocities*. The largest “source” of peculiar velocities in local space is the Virgo cluster. Infall into the Virgo cluster dramatically affects the local velocity field. Since the Virgo cluster is so close, the peculiar velocities it induces on the galaxies surrounding it are proportionally a larger part of the observed redshifts than for farther clusters. Therefore, if I can model the effect of the Virgo cluster on the observed redshifts, I should remove one of the largest sources of non-Hubble flow redshifts in my sample. In order to model the Virgo infall, I started with a simple linear model for Virgo infall by Schechter [1980]. Schechter noted that Peebles [1976] had developed a solution for the Virgocentric peculiar velocity field under two assumptions:

1. Adopt initial conditions of a close to homogeneous mass distribution, that peculiar velocities are small compared to the scale of peculiar acceleration changes, and that the mass distribution evolves under gravitation alone.
2. That the model is limited to those regions where peculiar velocities can be described by linear perturbation theory.

Making these assumptions, Peebles' found that for a Virgocentric density contrast of $d^{-\gamma}$, where d is the distance from the cluster center, then the Virgocentric peculiar velocity is proportional to $d^{-(\gamma-1)}$. Schechter then takes into account the projection of a galaxy's Virgocentric infall and our own infall onto the line joining the two to find that

$$v_{obs} = v_{Virgo}x - w_{\odot}(\cos \theta - x) \times [1 - (x^2 - 2x \cos \theta + 1)^{-\gamma/2}], \quad (7.2)$$

where x is the distance to the galaxy in question, v_{Virgo} is the observed velocity of the Virgo cluster, w_{\odot} is the Galaxy's Virgocentric infall velocity, θ is the angular separation

on the sky between the galaxy and Virgo cluster center. I used Schechter’s function and the assumption that γ equals 2 (which matches the observed density contrast profiles of Abell clusters and the Virgo cluster) in order to rewrite equation 7.2 as a cubic equation in x

$$0 = (v_{Virgo} + w_{\odot})x^3 + [-v_{obs} - (2v_{Virgo} + 3w_{\odot}) \cos \theta]x^2 + (v_{Virgo} + 2v_{obs} \cos \theta + 2w_{\odot} \cos^2 \theta)x - v_{obs}. \quad (7.3)$$

I can now solve for x given v_{obs} , v_{Virgo} , w_{\odot} , and θ using standard solutions to cubic equations. Since equation 7.3 is a cubic equation, there can be between one and three real solutions for x , which means one must specify which solution is chosen in the triple value region. In this case, I always take the middle value unless it implies an unreasonably high peculiar velocity (greater than 1000 km s^{-1}), in which case a value of x implying lower peculiar velocities is chosen. Within 6° of the Virgo cluster center, the situation gets more complicated. A linear model for Virgo infall probably doesn’t hold. In these cases, some previous authors (e.g. Hudson and Lynden-Bell [1991]) have simply taken all galaxies with $v_{obs} < 2500 \text{ km s}^{-1}$ and $\theta < 6^\circ$ to be at the distance for the Virgo cluster. This ignores the fact that the Virgo cluster has some well established substructure, so assuming a single distance for all the galaxies near Virgo is not ideal. Instead I use the known three-dimensional structure as determined by Gavazzi *et al.* [1999] to assign distances to galaxies near the Virgo cluster center. Gavazzi *et al.* [1999] used H-band Tully-Fisher and Fundamental Plane (more commonly known as $D_n - \sigma$) distance determinations to obtain distances to individual “clouds” of galaxies in the Virgo cluster (whose designations came from observations by de Vaucouleurs). They determined that some of the clouds were indeed at significantly different distances from the rest of the cluster. For this reason, I used their distance modulus estimates to determine the Hubble flow velocity in the Local Group frame, V_{LG} , using their $H_0 = 81.35 \text{ km s}^{-1} \text{ Mpc}^{-1}$. The V_{LG} I assumed for these clouds is shown in Table 7.1. The final solution I choose for MAPS-NGPZ galaxies in the Virgo cluster region was to determine which of cloud

Table 7.1: Distance Information for Virgo Cluster Clouds from Gavazzi *et al.* [1999]

Group	$m - M$	Distance (Mpc)	V_{LG} (km s ⁻¹)	V_{LG} (Observed)	$V_{peculiar}$
A	30.84 ± 0.06	$14.72^{+0.41}_{-0.40}$	1198^{+34}_{-33}	1369	171
N	30.94 ± 0.12	$15.42^{+0.88}_{-0.83}$	1254^{+71}_{-67}	659	-595
S	30.91 ± 0.10	$15.21^{+0.72}_{-0.68}$	1237^{+58}_{-56}	1677	440
E	31.23 ± 0.16	$17.62^{+1.35}_{-1.25}$	1433^{+110}_{-102}	1304	-129
B	31.84 ± 0.10	$23.33^{+1.10}_{-1.05}$	1898^{+89}_{-85}	1282	-616
M	32.77 ± 0.11	$35.81^{+1.86}_{-1.77}$	2913^{+151}_{-144}	2507	-406
W	32.38 ± 0.23	$29.92^{+3.34}_{-3.01}$	2434^{+272}_{-245}	2435	0

the galaxy belongs to (if any) and assign it that cloud’s redshift.⁴ This was done by using a map of the clouds from Gavazzi *et al.* [1999], their Figure 6, as a guide for how to partition the galaxies. I then set the redshift of the MAPS-NGPZ galaxy to the “Hubble flow” velocity corresponding to the distance measured by Gavazzi *et al.* [1999] (See Figure 7.4). If the galaxy was not within the boundaries of a known cloud, it was assumed to reside in the main Virgo cluster cloud (cloud A). If the peculiar velocity for this assumed distance exceeded 1000 km s⁻¹ (which is higher than any observed peculiar velocities associated with the Virgo cluster), I reassigned the galaxy to the background cloud, cloud W. This solution to the inner Virgo cluster galaxy distances attempts to keep the three-dimensional structure of Virgo intact in the MAPS-NGPZ galaxies.

⁴I define the Virgo cluster region of the sky to be the portion of the sky within 6° of the Virgo cluster center and with redshift $v_{obs} < 2500$ km s⁻¹.

Assumed 3D Structure of the Virgo Cluster

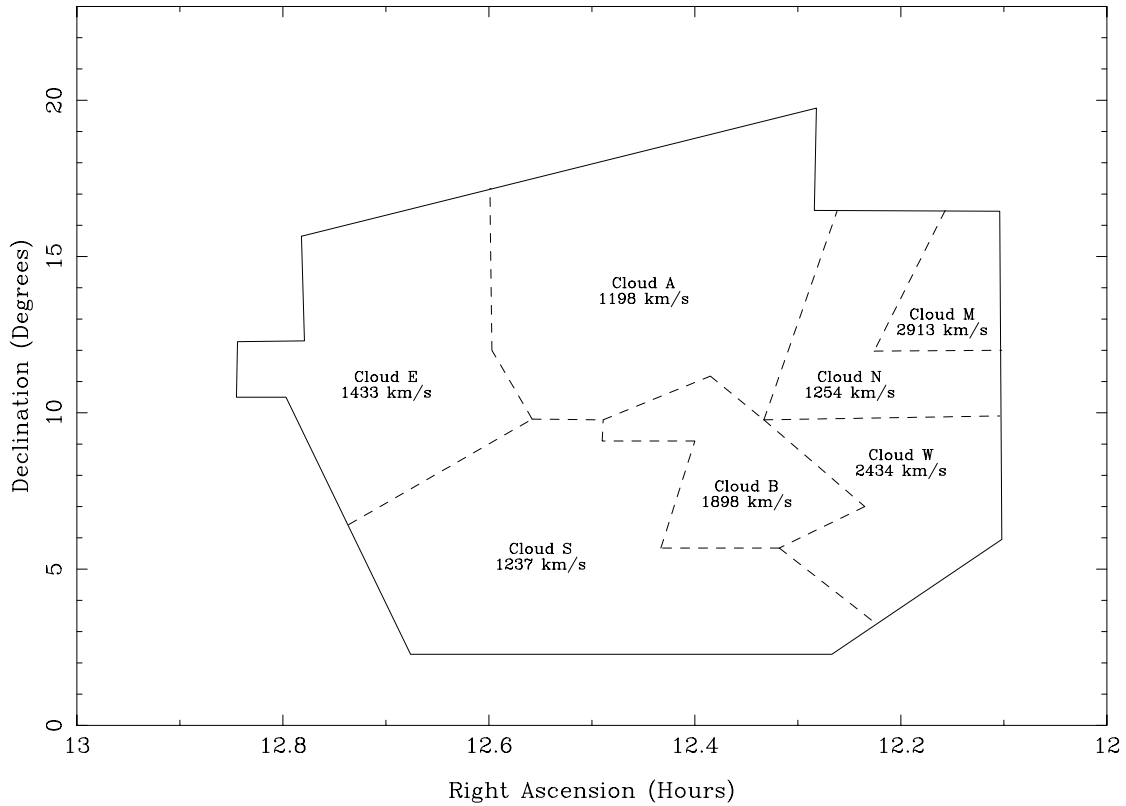


Figure 7.4: This diagram shows how the the Virgo cluster can be partitioned into clouds at differing Hubble flow velocity distances. This diagram is based on the work of Gavazzi *et al.* [1999].

7.1.3 Taking into Account Galactic Extinction

While attempting to determine the effects of internal extinction to the appearance of other galaxies, I have correct for extinction due to dust in our Galaxy. For example, when calculating the distance modulus, $m - M$, of a galaxy, one typically writes

$$m - M = 5 \log r - 5 + A + K \quad (7.4)$$

where r is the distance, K is the K-correction (see next section), and A is the Galactic extinction. Galactic extinction is very wavelength dependent, so I need to obtain separate estimates of A for both the O bandpass, A_O , and the E bandpass, A_E . As noted in

Section 5.9, I have two reddening estimates for each MAPS-NGP galaxy, $E(B - V)_{BH}$ from Burstein & Heiles [1982] and $E(B - V)_S$ from Schlegel, Finkbeiner, and Davis [1998]. Reddening estimates, $E(B - V)$ can be related to extinction, A , using

$$A_V = R_V E(B - V) \quad (7.5)$$

where $R_V = 3.05 \pm 0.15$ [Whittet 1992], for simplicity, I use $R_V = 3$. A_V can be related to A_O and A_E using the extinction law of Cardelli, Clayton, & Mathis [1989]. This extinction law (see Figure 7.5) indicates

$$\begin{aligned} A_O/A_V &= 1.4646 \\ A_E/A_V &= 0.8120 \end{aligned} \quad (7.6)$$

which means

$$\begin{aligned} A_O &= (A_O/A_V) R_V E(B - V) \\ &= 4.3938 E(B - V) \end{aligned} \quad (7.7)$$

$$\begin{aligned} A_E &= (A_E/A_V) R_V E(B - V) \\ &= 2.4360 E(B - V). \end{aligned} \quad (7.8)$$

Equations 7.7 and 7.8 will be used to estimate the Galactic Extinction for each galaxy in the MAPS-NGPZ.

7.1.4 Computing Fractional Light Radii and Intensities

The effective (half-light) radius, r_{eff} and C_{21} concentration index are known for each MAPS-NGP galaxy. Using the relationship between r_{eff} and C_{21} shown in equation 5.11, the radius enclosing 75% of the total flux is found to be

$$r_{75} = C_{21} r_{eff}. \quad (7.9)$$

The mean surface brightness of the galaxy is defined as

$$\begin{aligned} \langle \mu_{mean} \rangle &= -2.5 \log(F) + 2.5 \log(\pi ab) \\ &= -2.5 \log(F) + 2.5 \log(\pi a^2 (b/a)). \end{aligned} \quad (7.10)$$

The Cordelli, Clayton, and Mathis Extinction Law

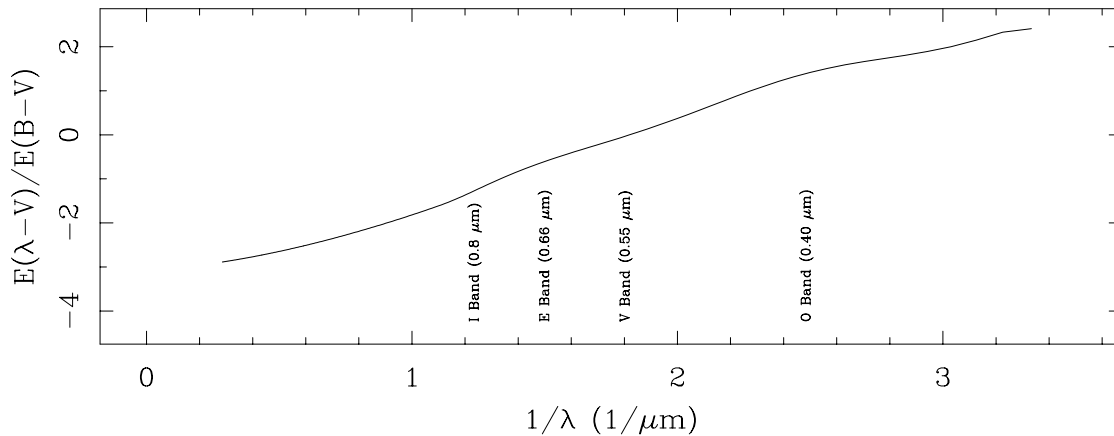


Figure 7.5: The Cardelli, Clayton, & Mathis [1989] NIR to UV extinction law annotated to show the location of the O, E, I, and V bandpasses.

where F is the total flux and $\pi a^2(b/a)$ is the surface area of the galaxy (in units of square arcseconds). So the mean surface brightness within the radii enclosing 50% and 75% of the total flux are defined as

$$\langle \mu_{r_{50}} \rangle = -2.5 \log(F/2) + 2.5 \log(\pi r_{eff}^2(b/a)), \quad (7.11)$$

$$\text{and } \langle \mu_{r_{75}} \rangle = -2.5 \log(3F/4) + 2.5 \log(\pi r_{75}^2(b/a)), \quad (7.12)$$

where there is an assumption that the isophotal ellipticity, $\epsilon = 1 - b/a$, doesn't change. This is not a terribly realistic assumption, but it does allow quick estimates for these fractional light radii and surface brightnesses.

7.1.5 Taking into Account Cosmological Effects

The MAPS-NGPZ mostly contains galaxies with $z < 0.1$. This means that the effects of our residing in an expanding universe are going to be smaller in the MAPS-NGPZ than other deeper (but smaller) galaxy surveys. However, it is going to be important to deal with these effects on the observed diameter, luminosity, and surface brightness of a galaxy, which are critical to this study. There are two major effects:

- The redshift of the galaxy's spectra and its effect on what part of the original

spectra we are observing in our bandpass today.

- The effects of expansion on the angular diameter and luminosity measured for a galaxy with a given metric diameter and luminosity.

Unfortunately, correcting for these cosmological effects and the plate-to-plate variations (detailed in section 7.1.6) will require knowledge of the morphological type of the galaxy, which further restricts the sample size. A total of 2316 galaxies out of the MAPS-NGPZ have morphological type information, forming another subset of the MAPS-NGP which will be referred to as the MAPS-NGPZT.

K-corrections

When a galaxy is observed at cosmological distances in a given bandpass, we do not observe the light emitted at that bandpass, but rather light emitted in another spectral band which has been redshifted into our bandpass. Depending on the spectral profile of a galaxy, this can dramatically change the observed luminosity of a galaxy. Correcting for this is what leads to the so-called K-correction in equation 7.4. Determining the proper K-correction requires a good knowledge of the intrinsic spectral profile of a galaxy and of the bandpass of the observation. I choose to use K corrections based on the work of Frei & Gunn [1994]. Frei & Gunn [1994] used standard spectral profiles from Coleman *et al.* [1980] to determine color-color transformations and K corrections for a large variety of bandpasses as part of the preparation for the Sloan Digitized Sky Survey (SDSS).⁵ Their method involved computationally applying filters (representing each bandpass) to redshifted galaxy spectral profiles. If I assume for this study that $K_O(z) \approx K_B(z)$ and $K_E(z) = K_r(z)$, then I can use their estimates for $K_B(z)$ and $K_r(z)$ to apply K-corrections in the POSS I bandpasses. Using the $k_B(z)$ and $(r - B)(z)$ values for the four morphological types in their study (listed in their Tables 3 through 6), I convert

⁵Coleman *et al.* [1980] obtained spectral profiles ranging from the ultraviolet to the infrared (140 to 1000 nm) for galaxies of four different morphological types (E, Sbc, Scd, Im).

$k_B(z)$, defined as

$$k_B(z) = B(z) - B(z = 0) - 2.5 \log(1 + z) \quad (7.13)$$

into standard K-corrections using

$$\begin{aligned} K_B(z) &= B(z) - B(z = 0) \\ &= k_B(z) + 2.5 \log(1 + z). \end{aligned} \quad (7.14)$$

I then used their $(r - B)(z)$ values to determine $K_r(z)$. And so I have K-correction estimates for both the POSS I O and E plates, for four different morphological types, for redshifts ranging from $z = 0$ to $z = 0.6$ (well beyond the depth of the MAPS-NGPZ). These K-correction estimates are listed in Table 7.2. I have used spline interpolation between the datapoints in Table 7.2 to allow accurate estimation of K_O and K_E for any redshift between $z = 0.0$ and 0.6 . Given that that majority of the MAPS-NGPZ is at $z < 0.1$, the K_O corrections are typically less than one magnitude and K_E corrections less than 0.5 magnitudes.

Table 7.2: K-Corrections Used (based on Frei & Gunn [1994])

Z	K_O -Corrections				K_E -Corrections			
	E	Sbc	Scd	Im	E	Sbc	Scd	Im
0.00	0.00	0.00	0.00	0.00	0.00	0.00	0.00	0.00
0.10	0.59	0.75	0.81	0.73	0.39	0.19	0.20	0.09
0.20	1.19	1.41	1.41	1.19	0.76	0.46	0.43	0.27
0.40	2.13	2.44	2.18	1.70	1.26	0.99	0.79	0.56
0.60	3.23	3.12	2.58	1.82	1.58	1.09	0.78	0.46

Cosmological Dimming and Angular Diameter Changes

To interpret observations of objects at cosmological distances correctly, we must also consider the effects of an expanding universe on our observations. If we assume the observed redshift is due to universal expansion and not due to actual motion in space by galaxies (that is, their co-moving coordinates are unchanged), then redshift is defined as

$$z \equiv \frac{\lambda_{observed} - \lambda_{emitted}}{\lambda_{emitted}}. \quad (7.15)$$

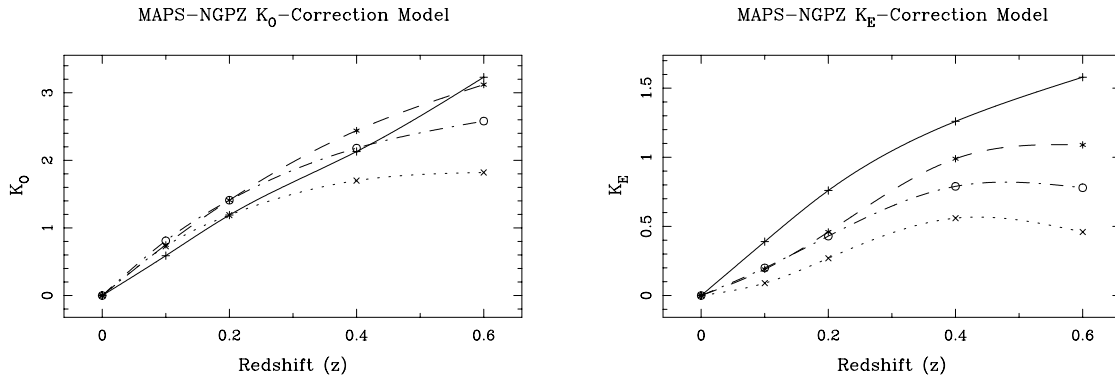


Figure 7.6: These plots illustrate the model I use for K_O and K_E Corrections for E (solid line), Sbc (dashed line), Scd (dash-dot line), and Im (dotted line) galaxies. This model is based on spline interpolation of the K_B and K_r estimates from Frei & Gunn [1994] (See Table 7.2).

By combining this definition of redshift with the standard mathematical description of space-time, Robertson-Walker (R-W) metric, one can fairly easily derive the relationship between the observed values of diameter, luminosity and surface brightness and their intrinsic (local) values at the time of emission.⁶ I start by simply suggesting (without derivation) that $(1+z)$ can be considered a measure of the change in the size scale of the universe between the time of emission and time of observation. Given this, then it can be shown that the observed angular diameter of a galaxy is related to its “intrinsic” value (i.e. - the value which would have been measured if we lived in a static Euclidean universe) by the equation:

$$\theta_{intrinsic} = (z+1)\theta_{observed} \quad (7.16)$$

Therefore, in order to compute the metric diameter of the galaxy, we must multiply the observed angular diameter by a factor of $(1+z)$. Next consider the luminosity of a galaxy. If we assume all the photons initially emitted originally are conserved, then there are two effects which affect the luminosity. The first effect is that of redshift affecting the energy of the photons. Since $E = h\nu$ for photons, then as the frequency ν grows (due to redshift), the observed energy per photon drops by a factor of $(1+z)$. In addition to this

⁶Weinberg [1972], Harwit [1988], and Peacock [1999] all contain the derivations of both the Robertson-Walker metric and the observed versus emitted parameters shown here.

photon energy drop, the redshift also affects the arrival times of the photons, increasing the arrival time between photons by a factor of $(1+z)$. Therefore the observed luminosity of the galaxy is

$$L_{observed} = \frac{L_{emitted}}{(1+z)^2}. \quad (7.17)$$

Note that this correction for cosmological dimming is separate from the K-correction. Finally, we need to consider the observed surface brightness or flux of a galaxy. Again, without derivation, I simply note that the definition of surface brightness as luminosity divided by surface area, then one would expect (and it can be shown) that

$$\mu_{observed} = \frac{\mu_{emitted}}{(1+z)^4}. \quad (7.18)$$

Therefore, in order to correct the observed surface brightness to the value when the galaxy was emitted, we need to multiply the observed surface brightness by a factor of $(1+z)^4$. When constructing the MAPS-NGPZT, I use equations 7.16, 7.17, and 7.18 to convert the observed values of diameter, luminosity, and surface brightness to their values at the source, allowing better determination of the effects of inclination on diameter, luminosity, and surface brightness, independent of redshift.

7.1.6 Obtaining Isophotal Diameter and Magnitude Corrections

The major motivation for this study has been the fact that many studies of the effects of inclination on galaxies have used demonstrably non-isophotal diameters for galaxies, which has dramatically affected their outcome. In this study, we know of several effects that make the effective isophote of the observed diameter and luminosity vary. The first is systematic, the POSS I plates vary in their surface brightness threshold as seen in Figure 5.2. However, we also need to consider the effects of cosmological dimming and Galactic extinction, which cause the limiting isophote of the parameters derived to be brighter than the observational limit. To tackle the effect of Galactic extinction on observed



diameters and magnitudes, Cameron [1990] used plate-based surface photometry of 23 large ellipticals and spirals to model the effects of Galactic extinction on the appearance

of those galaxies. However, Cameron’s study has three limitations which hinder its use in this study:

- Cameron only worked with B band photometry, which depending on the extent of color gradients in galaxies, may not be applicable to other bandpasses.
- Cameron does not take into account the effect of galaxy’s inclination on its appearance.
- Cameron only allows for two morphological types, spirals and ellipticals.

I attempted to improve on Cameron’s methods by including information from multiple bandpasses at a variety of inclinations. I started by gathering 252 B band and 349 Gunn r band CCD-based surface brightness profiles from a variety of sources covering a range in ellipticity and morphological types (See Table 7.3). For each galaxy surface

Table 7.3: Sources of Galaxy Surface Brightness Profiles

Source	N_{galaxy}	Bandpass	Notes
Kent [1985]	80	r	Profiles generated from fit parameters. All morphological types.
Peletier <i>et al.</i> [1990]	39	B	Only Ellipticals.
De Jong & Van Der Kruit [1994]	86	B	UGC Spirals.
Goudfrooij <i>et al.</i> [1994]	54	B	Only Ellipticals.
Courteau [1996]	269	r	Only Sb and Sc galaxies. Photometric profiles provided by S. Courteau.
Héraudeau and Simien [1996]	59	B	Subset of 234 Sa-Sd galaxies.
Cunow [1998]	14	B	Sample of bright Spirals.

brightness profile, I computed the integrated magnitude versus radius (when not available in the original data file). In order to get all the profiles on a consistent system, I converted the galaxy radii (and fractional light radii) into units of their value at a threshold isophote of $25 \text{ mag}/\square''$, and zero-pointed all integrated magnitudes relative to their value at the $25 \text{ mag}/\square''$ isophote. In those cases where the galaxy’s surface brightness profile didn’t extend deep enough, the profile was extrapolated. Once all the surface brightness profiles were placed on a consistent system, I binned the profiles by bandpass, morphological type, and ellipticity and computed the mean surface brightness

profiles in each bin (Sample profiles are shown in Figure 7.7).⁷ The distribution of the profiles in these bins is noted in Table 7.4. These mean profiles were then used

Table 7.4: Morphological and Ellipticity Distribution of Galaxy Profiles

ϵ	T Type Bin Counts (O/E)			
	Ellipticals ($T < 0$)	Early Spirals ($0 \leq T < 4$)	Late Spirals ($4 \leq T < 8$)	Irregulars ($T > 8$)
0.0-0.1	8/0	9/2	9/1	2/0
0.1-0.2	27/2	7/10	21/4	2/0
0.2-0.3	24/1	9/6	16/6	0/0
0.3-0.4	15/1	18/8	17/17	2/0
0.4-0.5	14/2	12/33	5/46	1/0
0.5-0.6	2/0	4/36	7/63	0/0
0.6-0.7	0/1	10/26	4/53	0/0
0.7-0.8	0/4	3/10	4/16	0/0
0.8-0.9	0/0	1/0	0/0	0/0

to compute both $r_{\mu_{25}}/r(\mu_{limit})$, the fractional difference between all radii at different threshold surface brightnesses (μ_{limit}) and their values at a threshold of 25 mag/ \square'' , and $\Delta m_{\mu_{25}}(\mu_{limit})$, the difference between the integrated magnitude at different threshold surface brightnesses and the 25 mag/ \square'' case. I then used Levenberg-Marquardt non-linear least squares techniques (See Press *et al.* [1992]) to fit these mean profiles to the functions

$$r_{\mu_{25}}/r(\mu_{limit}) = 10^{\alpha(25 - \mu_{limit})^\beta} \quad (7.19)$$

and

$$\Delta \mu_{25}(\mu_{limit}) = \phi(25 - \mu_{limit})^\nu \quad (7.20)$$

where α , β , ϕ , and ν are free parameters. Equations 7.19 and 7.20 are forms of functions used by Cameron [1990], although equation 7.19 has a longer history, having been successfully used by Fisher and Tully [1981] and Hauschildt [1987] as models for correcting isophotal diameters for Galactic extinction. Fitting was performed for the profiles of isophotal diameter, fractional (50% and 75%) light radii, and total integrated magnitude. Best fit values for α , β , ϕ , and ν are presented in Tables 7.5 and 7.6. These fits

⁷Technically, it was not the mean profile, as I iteratively eliminated outlier profiles while computing the mean profile.

to equations 7.19 and 7.20 allow me to convert the diameters, radii, and magnitudes to their values at a consistent $23.5 \text{ mag}/\square''$ isophote (roughly the average O plate limiting surface brightness of the POSS I) given the threshold surface brightness limit for a galaxy (which is a combination of plate limits and Galactic extinction). These corrections are illustrated in Figure 7.8. This also allows correction of the concentration indices and mean surface brightnesses to a consistent isophote. Thus all the MAPS-NGPZ galaxies with morphological class information had their isophotal diameters, fractional light diameters, integrated magnitudes, and concentration indices corrected for the combined effects of plate-to-plate surface brightness limit variations and Galactic extinction. Plots of the best fit parameters for equations 7.19 and 7.20 versus ellipticity show that there are significant trends versus ellipticity for each morphological type (see Figures 7.9 and 7.10). This suggests that using Cameron’s fits without taking into account the effect of galaxy’s inclination would have likely introduced a biased set of corrections that would not preserve the trends of diameter and luminosity with inclination. It should also be noted that there may be enough real scatter in the surface brightness profiles of galaxies falling within any bandpass/ellipticity/T-type bin that the best fit mean surface brightness profiles for galaxies in each bin may not be terribly representative. This is to some sense suggested by looking at scatter in the real surface brightness profiles versus the best fit function (indicated by the dark line in Figure 7.7). Thus, any study of the MAPS-NGPZT dataset should be done both with and without these “isophotal corrections.”

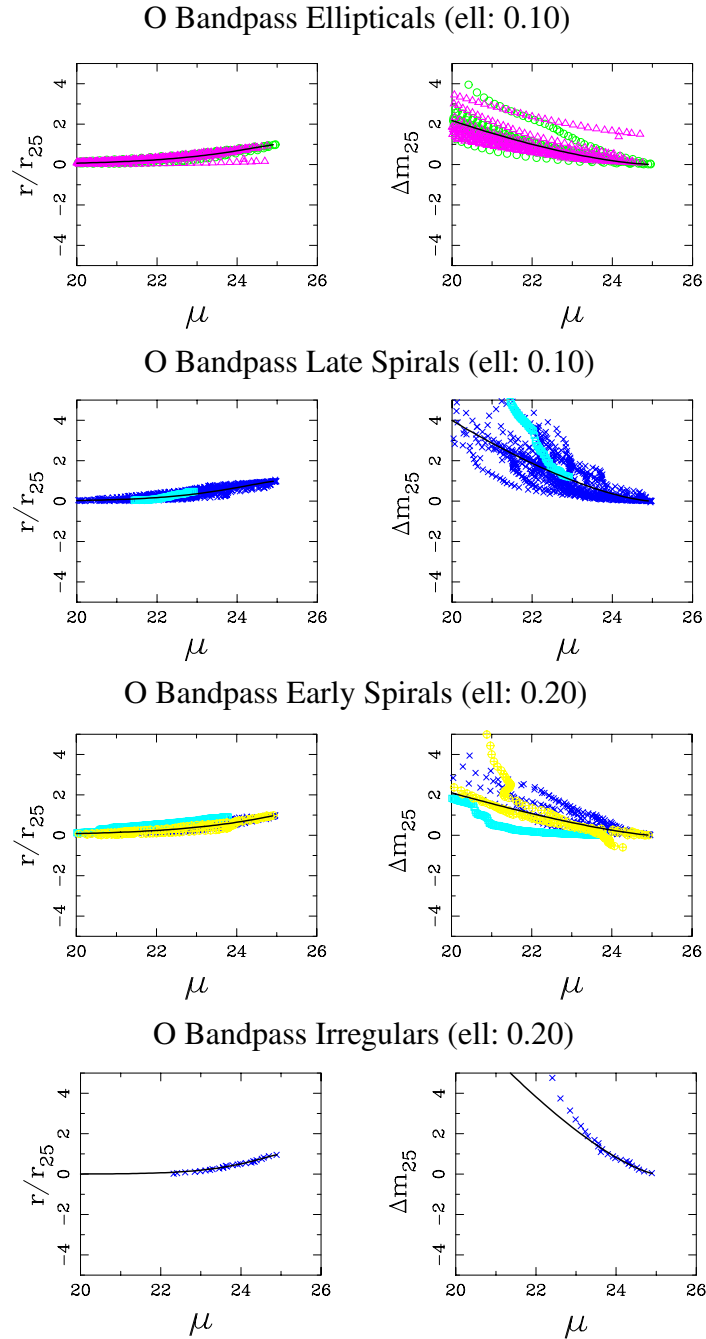


Figure 7.7: Some sample surface brightness profiles used for correcting APS parameters. The different symbols represent different source catalogs. The dark line in each figure is the best fit of equation 7.19 (left) or 7.20 (right).

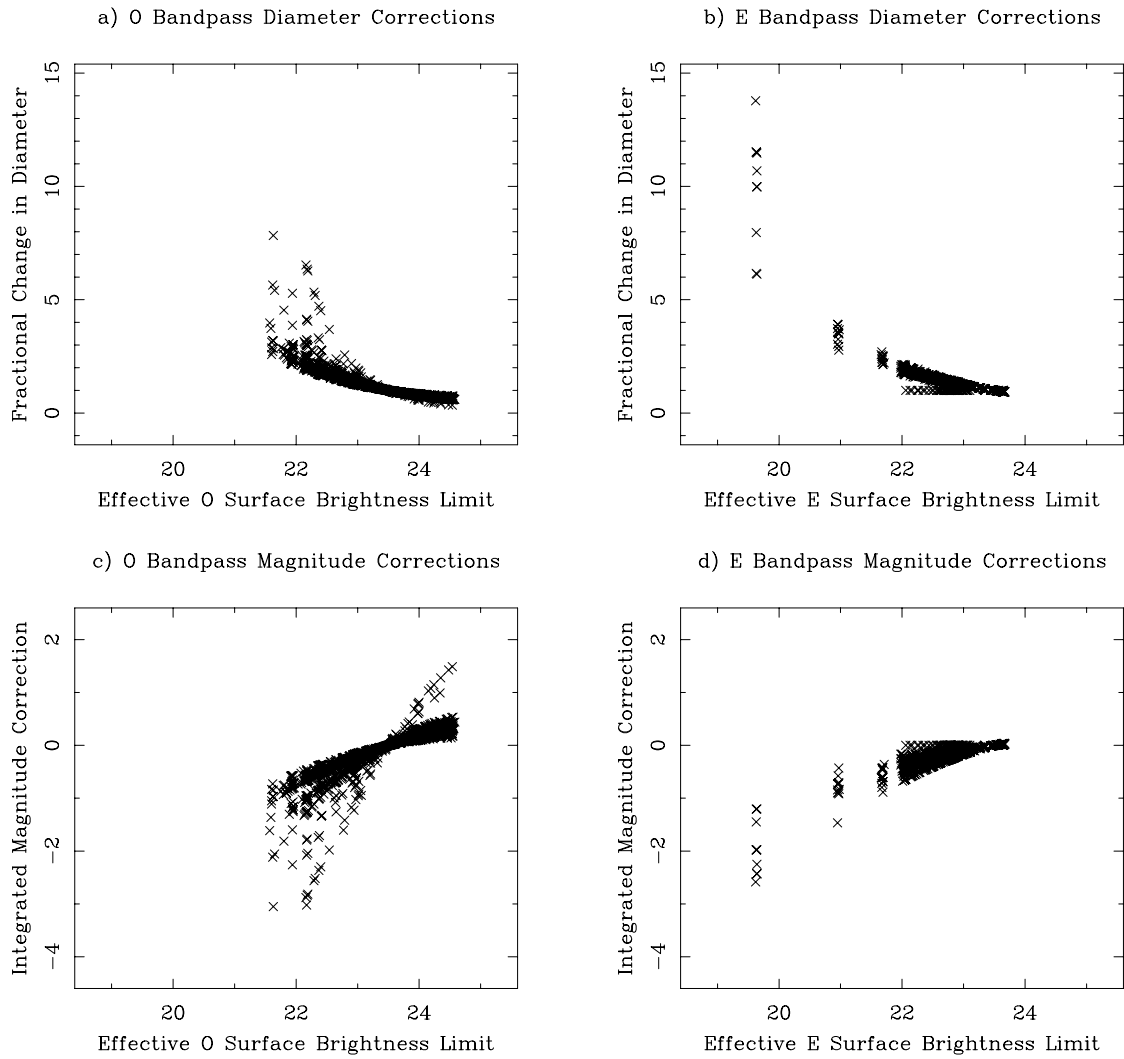


Figure 7.8: These plots show the corrections I applied to the MAPS-NGPZT in order to get diameters [plots (a) and (b)] and magnitudes [plots (c) and (d)] into an isophotal system with a surface brightness limit of 23 mag./ \square'' . Note the extreme values for some of the corrections for surface brightness limits considerably different than 23 mag./ \square'' .

Table 7.5: Best Fit Parameters for Equations 7.19 and 7.20 for the Surface Brightness Profiles of Galaxies

Plate	T	ϵ	α	β	χ^2	ϕ	ν	χ^2
O	-6	0.0	0.156 (0.006)	1.218 (0.023)	0.196	0.176 (0.009)	1.464 (0.044)	0.488
O	-6	0.1	0.168 (0.024)	1.206 (0.070)	0.057	0.186 (0.037)	1.527 (0.097)	0.090
O	-6	0.2	0.183 (0.012)	1.153 (0.033)	0.088	0.243 (0.034)	1.397 (0.083)	0.129
O	-6	0.3	0.182 (0.013)	1.148 (0.037)	0.045	0.353 (0.060)	1.170 (0.092)	0.034
O	-6	0.4	0.204 (0.016)	1.062 (0.042)	0.159	0.351 (0.054)	1.102 (0.079)	0.138
O	-6	0.5	0.106 (0.012)	1.419 (0.081)	0.032	0.118 (0.029)	1.718 (0.196)	0.038
O	2	0.0	0.201 (0.024)	1.225 (0.086)	0.150	0.354 (0.077)	1.407 (0.187)	0.074
O	2	0.1	0.161 (0.019)	1.247 (0.067)	0.564	0.200 (0.036)	1.526 (0.103)	1.164
O	2	0.2	0.190 (0.023)	1.072 (0.085)	0.133	0.256 (0.054)	1.309 (0.135)	0.143
O	2	0.3	0.175 (0.021)	1.220 (0.069)	0.171	0.237 (0.041)	1.485 (0.107)	0.201
O	2	0.4	0.135 (0.014)	1.382 (0.066)	0.305	0.191 (0.031)	1.642 (0.109)	0.339
O	2	0.5	0.072 (0.016)	1.808 (0.148)	0.086	0.056 (0.018)	2.457 (0.232)	0.221
O	2	0.6	0.140 (0.014)	1.387 (0.065)	0.363	0.195 (0.032)	1.625 (0.121)	0.283
O	2	0.7	0.172 (0.010)	1.165 (0.046)	1.035	0.539 (0.025)	0.957 (0.040)	1.192
O	6	0.0	0.169 (0.015)	1.336 (0.068)	0.165	0.282 (0.041)	1.597 (0.124)	0.138
O	6	0.1	0.171 (0.027)	1.342 (0.095)	0.150	0.369 (0.078)	1.480 (0.136)	0.115
O	6	0.2	0.175 (0.021)	1.339 (0.079)	0.100	0.345 (0.056)	1.509 (0.109)	0.128
O	6	0.3	0.152 (0.022)	1.396 (0.099)	0.095	0.245 (0.052)	1.713 (0.150)	0.073
O	6	0.4	0.086 (0.009)	1.638 (0.067)	0.263	0.151 (0.013)	1.798 (0.080)	0.215
O	6	0.5	0.088 (0.004)	1.682 (0.029)	0.486	0.107 (0.015)	2.061 (0.085)	0.323
O	6	0.6	0.070 (0.010)	1.754 (0.098)	0.448	0.071 (0.013)	2.371 (0.125)	0.583
O	6	0.7	0.102 (0.010)	1.849 (0.093)	0.242	0.148 (0.019)	2.316 (0.112)	0.252
O	9	0.0	0.477 (0.016)	0.981 (0.102)	1.075	1.598 (0.073)	1.211 (0.110)	1.380
O	9	0.1	0.210 (0.019)	1.376 (0.148)	0.240	0.524 (0.050)	1.610 (0.157)	0.219
O	9	0.2	0.294 (0.026)	1.275 (0.258)	0.174	0.828 (0.068)	1.393 (0.217)	0.137
O	9	0.3	0.329 (0.014)	1.383 (0.088)	0.152	0.970 (0.051)	1.506 (0.110)	0.132
O	9	0.4	0.078 (0.008)	2.204 (0.112)	0.226	0.166 (0.020)	2.505 (0.121)	0.139
E	-6	0.1	0.156 (0.003)	1.191 (0.013)	0.647	0.115 (0.003)	1.593 (0.018)	2.369
E	-6	0.2	0.144 (0.003)	1.163 (0.014)	0.446	0.076 (0.002)	1.586 (0.019)	1.919
E	-6	0.3	0.143 (0.003)	1.134 (0.016)	0.227	0.067 (0.002)	1.515 (0.021)	1.078
E	-6	0.4	0.138 (0.002)	1.201 (0.012)	1.026	0.076 (0.002)	1.613 (0.024)	1.665
E	-6	0.6	0.153 (0.003)	1.255 (0.011)	1.880	0.120 (0.003)	1.719 (0.015)	5.478
E	-6	0.7	0.146 (0.003)	1.200 (0.016)	0.817	0.096 (0.005)	1.590 (0.039)	0.762
E	2	0.0	0.107 (0.003)	1.401 (0.023)	0.819	0.039 (0.001)	1.649 (0.025)	0.611
E	2	0.1	0.116 (0.006)	1.350 (0.034)	0.294	0.075 (0.008)	1.647 (0.079)	0.275
E	2	0.2	0.154 (0.012)	1.148 (0.047)	0.111	0.109 (0.017)	1.122 (0.101)	0.259
E	2	0.3	0.089 (0.006)	1.485 (0.036)	0.433	0.058 (0.009)	1.949 (0.098)	0.239
E	2	0.4	0.104 (0.009)	1.395 (0.048)	0.187	0.091 (0.014)	1.626 (0.083)	0.227
E	2	0.5	0.080 (0.007)	1.550 (0.052)	0.408	0.049 (0.007)	2.035 (0.098)	0.377
E	2	0.6	0.084 (0.007)	1.493 (0.040)	0.388	0.056 (0.008)	1.909 (0.087)	0.157
E	2	0.7	0.096 (0.008)	1.456 (0.055)	0.489	0.047 (0.007)	2.053 (0.105)	0.486
E	2	0.8	0.097 (0.002)	1.322 (0.013)	4.876	0.041 (0.001)	1.927 (0.018)	10.580
E	6	0.0	0.072 (0.002)	1.490 (0.022)	5.741	0.025 (0.001)	2.645 (0.033)	11.670
E	6	0.1	0.133 (0.009)	1.300 (0.050)	0.250	0.160 (0.032)	1.430 (0.135)	0.196
E	6	0.2	0.104 (0.007)	1.325 (0.046)	0.330	0.064 (0.009)	1.811 (0.098)	0.312
E	6	0.3	0.085 (0.008)	1.574 (0.062)	0.306	0.061 (0.013)	2.189 (0.137)	0.229
E	6	0.4	0.071 (0.006)	1.684 (0.049)	0.492	0.056 (0.009)	2.161 (0.103)	0.358
E	6	0.5	0.084 (0.009)	1.631 (0.070)	0.342	0.071 (0.014)	2.177 (0.134)	0.238
E	6	0.6	0.073 (0.008)	1.635 (0.092)	0.497	0.054 (0.009)	2.300 (0.118)	0.311
E	6	0.7	0.107 (0.007)	1.308 (0.091)	0.374	0.085 (0.014)	2.129 (0.120)	0.338

Table 7.6: 50% and 75% Light Radii Best Fit Parameters for Equation 7.19 for the Surface Brightness Profiles of Galaxies

Plate	T	ϵ	50% Light Radii			75% Light Radii		
			α	β	χ^2	α	β	χ^2
O	-6	0.0	0.105 (0.004)	1.297 (0.027)	0.294	0.127 (0.006)	1.277 (0.032)	0.185
O	-6	0.1	0.133 (0.028)	1.227 (0.103)	0.055	0.158 (0.028)	1.191 (0.088)	0.033
O	-6	0.2	0.139 (0.016)	1.206 (0.067)	0.083	0.157 (0.015)	1.192 (0.055)	0.094
O	-6	0.3	0.158 (0.017)	1.114 (0.056)	0.079	0.175 (0.016)	1.112 (0.047)	0.066
O	-6	0.4	0.157 (0.018)	1.040 (0.062)	0.173	0.191 (0.019)	1.013 (0.052)	0.164
O	-6	0.5	0.071 (0.010)	1.467 (0.100)	0.068	0.088 (0.014)	1.452 (0.105)	0.038
O	2	0.0	0.182 (0.030)	1.175 (0.117)	0.259	0.180 (0.028)	1.249 (0.110)	0.207
O	2	0.1	0.123 (0.021)	1.299 (0.095)	0.389	0.126 (0.018)	1.331 (0.084)	0.436
O	2	0.2	0.135 (0.029)	1.104 (0.143)	0.123	0.142 (0.030)	1.115 (0.145)	0.121
O	2	0.3	0.093 (0.018)	1.456 (0.112)	0.231	0.119 (0.021)	1.371 (0.104)	0.224
O	2	0.4	0.091 (0.016)	1.504 (0.105)	0.365	0.108 (0.023)	1.469 (0.124)	0.315
O	2	0.5	0.025 (0.009)	2.241 (0.238)	0.125	0.044 (0.014)	2.020 (0.220)	0.093
O	2	0.6	0.071 (0.010)	1.624 (0.091)	0.254	0.091 (0.013)	1.576 (0.090)	0.256
O	2	0.7	0.249 (0.011)	0.919 (0.035)	1.009	0.220 (0.011)	0.989 (0.040)	1.118
O	6	0.0	0.115 (0.019)	1.438 (0.113)	0.269	0.129 (0.018)	1.417 (0.100)	0.232
O	6	0.1	0.124 (0.029)	1.450 (0.143)	0.226	0.142 (0.031)	1.397 (0.131)	0.203
O	6	0.2	0.109 (0.018)	1.545 (0.106)	0.154	0.129 (0.021)	1.473 (0.110)	0.142
O	6	0.3	0.091 (0.017)	1.574 (0.125)	0.158	0.106 (0.022)	1.541 (0.137)	0.126
O	6	0.4	0.046 (0.005)	1.891 (0.069)	0.429	0.063 (0.008)	1.740 (0.077)	0.301
O	6	0.5	0.087 (0.006)	1.478 (0.055)	5.724	0.099 (0.006)	1.448 (0.051)	3.538
O	6	0.6	0.027 (0.005)	2.323 (0.134)	0.348	0.029 (0.006)	2.287 (0.150)	0.308
O	6	0.7	0.050 (0.008)	2.280 (0.136)	0.249	0.059 (0.008)	2.188 (0.113)	0.201
O	9	0.0	0.414 (0.023)	0.902 (0.124)	0.938	0.448 (0.018)	0.928 (0.115)	1.042
O	9	0.1	0.148 (0.014)	1.483 (0.161)	0.319	0.178 (0.017)	1.418 (0.158)	0.270
O	9	0.2	0.242 (0.022)	1.351 (0.254)	0.186	0.277 (0.024)	1.230 (0.243)	0.212
O	9	0.3	0.289 (0.013)	1.450 (0.087)	0.184	0.305 (0.014)	1.430 (0.091)	0.170
O	9	0.4	0.036 (0.009)	1.981 (0.320)	16.250	0.041 (0.012)	1.899 (0.353)	13.960
E	-6	0.1	0.072 (0.002)	1.442 (0.016)	1.519	0.100 (0.002)	1.342 (0.015)	1.020
E	-6	0.2	0.053 (0.001)	1.486 (0.018)	1.509	0.076 (0.002)	1.374 (0.016)	0.943
E	-6	0.3	0.050 (0.001)	1.471 (0.021)	1.098	0.071 (0.002)	1.361 (0.019)	0.629
E	-6	0.4	0.048 (0.001)	1.574 (0.017)	2.651	0.073 (0.002)	1.421 (0.017)	1.393
E	-6	0.6	0.076 (0.001)	1.489 (0.014)	2.914	0.104 (0.002)	1.391 (0.013)	2.291
E	-6	0.7	0.059 (0.002)	1.513 (0.030)	1.345	0.085 (0.003)	1.389 (0.026)	0.821
E	2	0.0	0.138 (0.000)	0.193 (0.003)	90.110	0.101 (0.003)	1.428 (0.030)	7.882
E	2	0.1	0.083 (0.013)	1.499 (0.078)	0.313	0.064 (0.006)	1.652 (0.060)	0.193
E	2	0.2	0.191 (0.032)	0.644 (0.119)	0.437	0.124 (0.015)	1.188 (0.066)	0.322
E	2	0.3	0.031 (0.005)	2.020 (0.079)	0.306	0.020 (0.004)	2.235 (0.106)	0.913
E	2	0.4	0.045 (0.009)	1.782 (0.089)	0.171	0.052 (0.009)	1.706 (0.085)	0.150
E	2	0.5	0.027 (0.004)	2.043 (0.078)	0.367	0.032 (0.005)	1.980 (0.082)	0.268
E	2	0.6	0.032 (0.005)	1.959 (0.070)	0.148	0.033 (0.005)	1.918 (0.079)	0.212
E	2	0.7	0.032 (0.006)	1.920 (0.114)	0.363	0.038 (0.006)	1.899 (0.089)	0.400
E	2	0.8	0.027 (0.001)	1.770 (0.018)	8.270	0.041 (0.001)	1.641 (0.017)	6.960
E	6	0.0	0.014 (0.001)	2.197 (0.035)	6.609	0.020 (0.001)	2.083 (0.031)	6.285
E	6	0.1	0.070 (0.009)	1.677 (0.081)	0.340	0.079 (0.012)	1.576 (0.100)	0.306
E	6	0.2	0.062 (0.006)	1.431 (0.081)	6.314	0.040 (0.005)	1.790 (0.071)	0.244
E	6	0.3	0.021 (0.005)	2.301 (0.130)	0.263	0.034 (0.007)	2.024 (0.129)	0.199
E	6	0.4	0.026 (0.006)	1.965 (0.230)	0.651	0.027 (0.004)	2.163 (0.083)	0.353
E	6	0.5	0.028 (0.006)	2.223 (0.119)	0.235	0.036 (0.007)	2.091 (0.115)	0.209
E	6	0.6	0.025 (0.005)	2.113 (0.140)	0.273	0.030 (0.006)	2.054 (0.137)	0.244
E	6	0.7	0.041 (0.005)	1.669 (0.173)	0.323	0.050 (0.006)	1.694 (0.161)	0.313

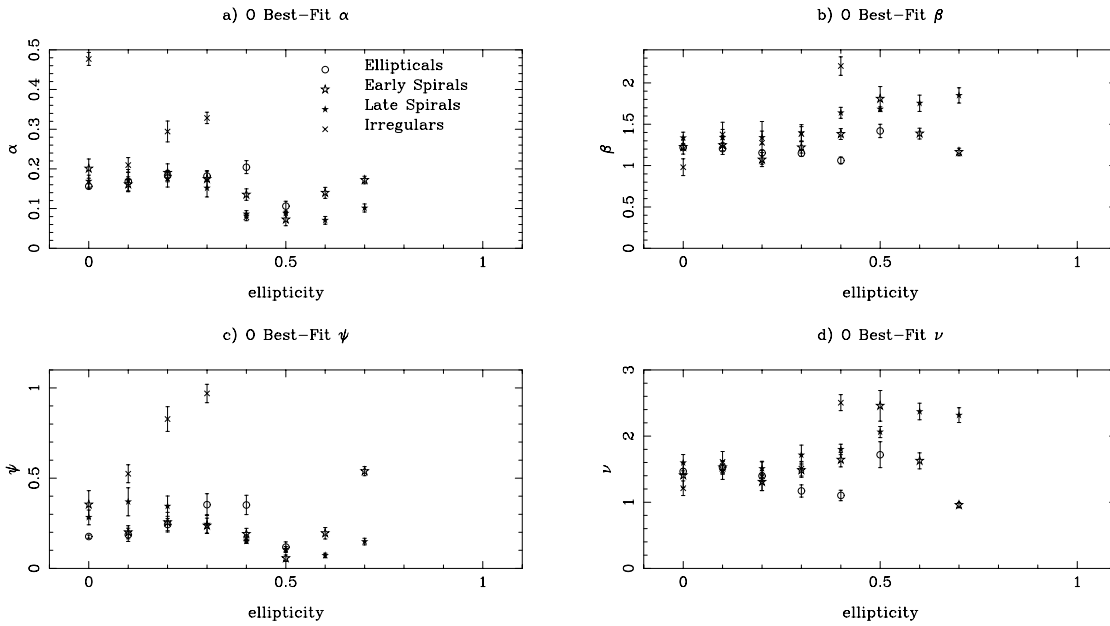


Figure 7.9: These plots show the trends of the best-fit (a) α , (b) β , (c) ϕ , and (d) ν for equations 7.19 and 7.20 versus ellipticity for the O plate data. These plots show that these parameters vary significantly with ellipticity.

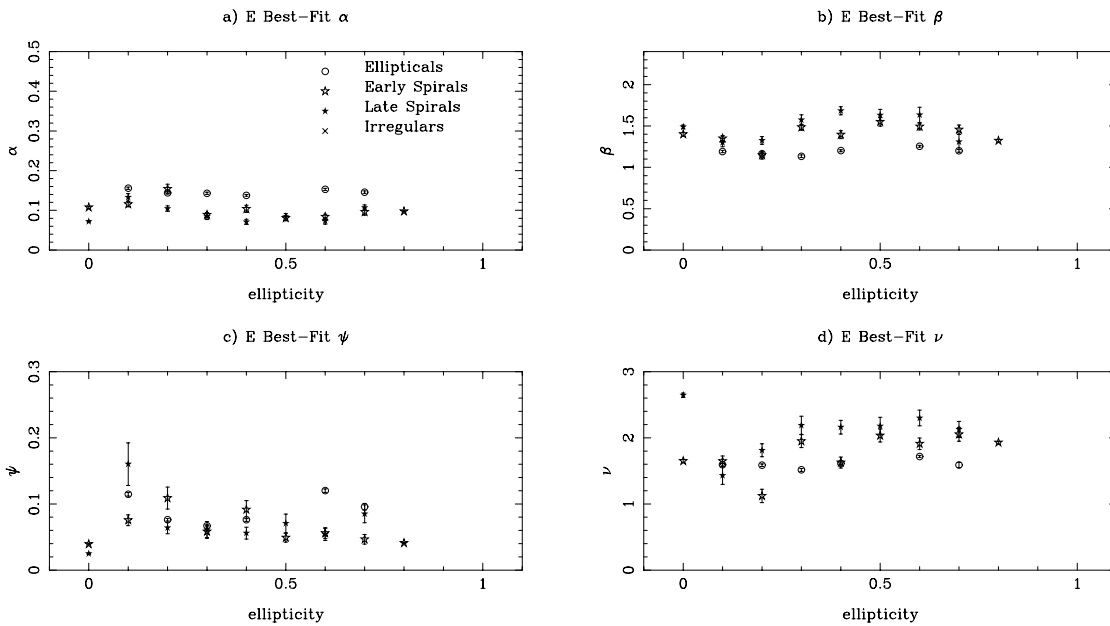


Figure 7.10: Identical to Figure 7.9 except for E plate data. Again, the plots show that these best-fit parameters vary significantly with ellipticity.

7.2 Summary of the MAPS-NGPZT Subset of the MAPS-NGP

A total of 8913 MAPS-NGP galaxies were cross-identified with the ZCAT, forming the MAPS-NGPZ. Because of the necessity of morphological type information in order to perform corrections for both cosmological effects and plate-to-plate variations, a further subsample of 2573 galaxies (1871 classified as spirals) with both redshift and morphological type information, the MAPS-NGPZT, was built. For these MAPS-NGPZT galaxies, corrections for Virgo Infall, cosmological effects, and plate-to-plate variations in the threshold surface brightness have been applied. When determining the completeness limits of the the MAPS-NGPZT, we need to consider that the magnitude and diameter corrections outlined in the last section (and shown in Figure 7.8) tend to drive diameters upward and magnitudes brighter. Given these trends in the varying surface-brightness limits corrections, one expects the diameter and magnitude limits of the MAPS-NGPZT vary with whether or not the corrections have been applied. And in fact, this is seen the $\log(N) - \log(S)$ and $\log(N) - \log(\theta)$ plots (Figure 7.11). The MAPS-NGPZT when not surface brightness profile corrected is fairly complete down to an O (E) magnitude of 15.1 (13.5) and a diameter of $65''$ (either bandpass). With profile corrections, the MAPS-NGPZT is fairly complete down to an O (E) magnitude limit of 13.7 (13.3) and a O (E) diameter limit of $145''$ ($115''$). Note that because of the ZCAT survey methods, the MAPS-NGPZT is a magnitude-limited catalog. This leads to an interesting redshift versus ellipticity effect. Hubble's Law dictates that in general the higher the redshift, the more distant the object. Therefore, there is a linear relationship between the magnitude and redshift (Figure 7.12). And in a magnitude-limited sample, as shown earlier in Figure 6.4, there is a bias toward selecting more face on galaxies than edge on galaxies. This leads to the effect shown in Figure 7.13, in which edge-on galaxies tend to be at lower redshifts than face-on galaxies. The effect is much less pronounced in the MAPS-NGPZT than the MAPS-NGPZ, likely because morphological typing requires detailed

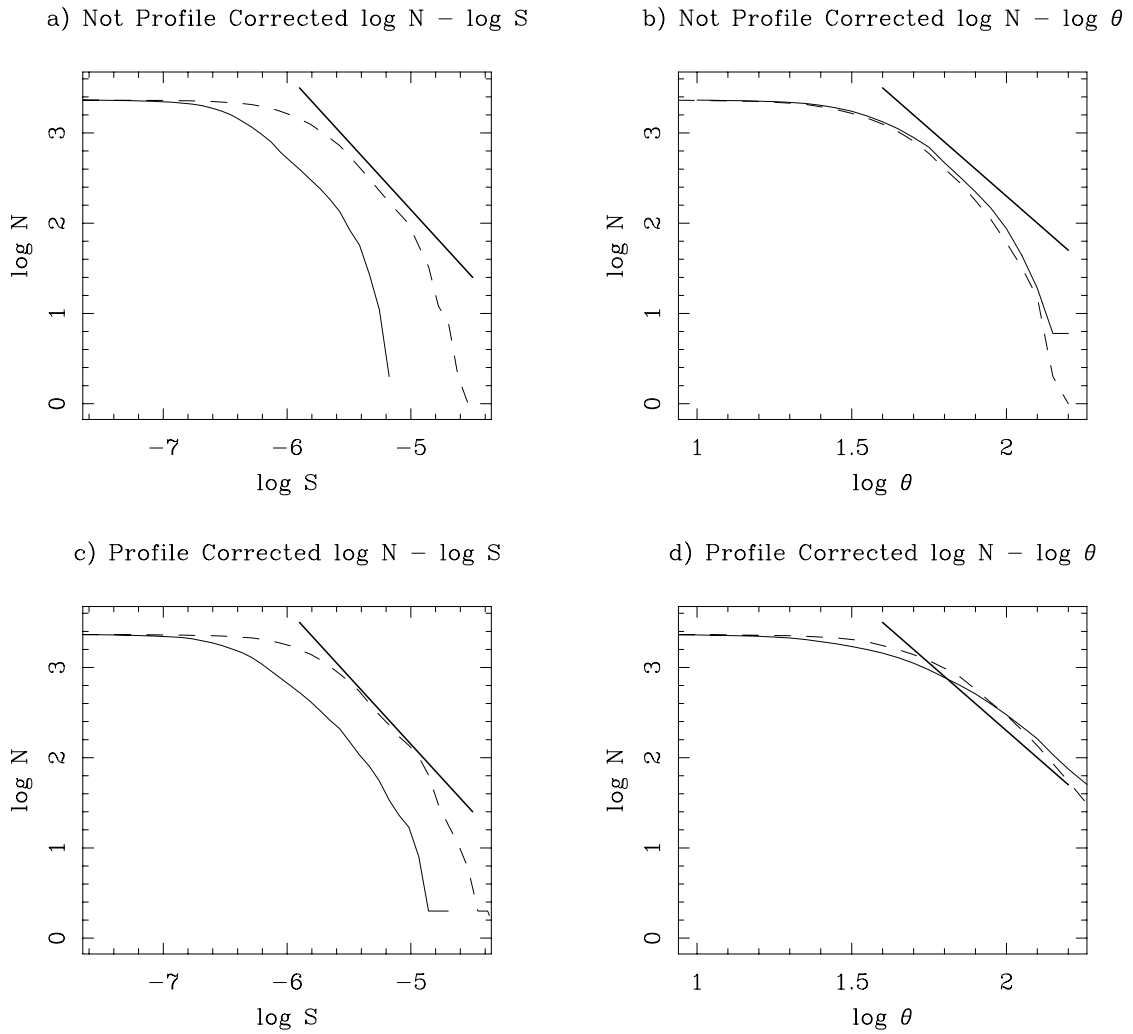


Figure 7.11: $\log(N) - \log(S)$ and $\log(N) - \log(\theta)$ diagrams for the MAPS-NGPZT both with and without the surface brightness profile corrections outlined in Section 7.1.6.

images, and thus is biased toward nearby galaxies.

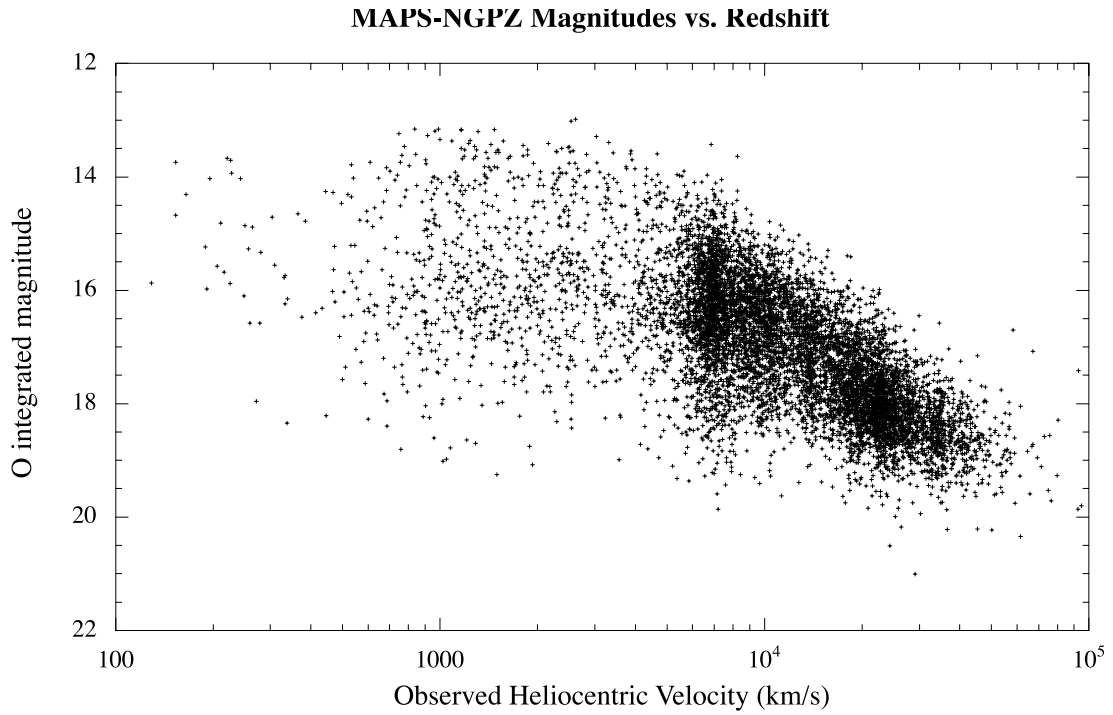


Figure 7.12: MAPS-NGPZ magnitudes (from APS O plate) versus ZCAT redshift. Note that the high redshift objects are the faintest, as expected.

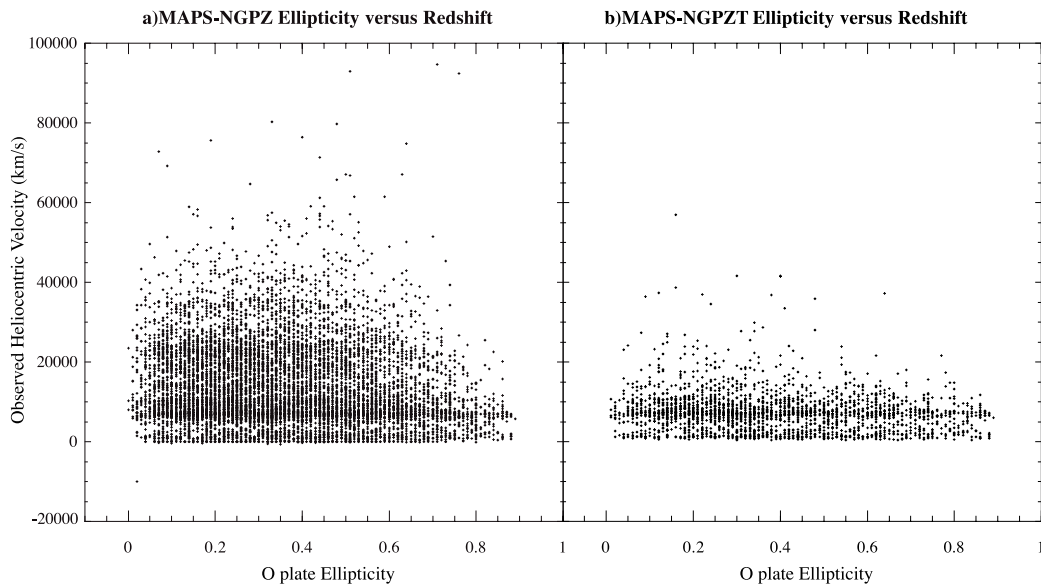


Figure 7.13: (a) MAPS-NGPZ and (b) MAPS-NGPZT ellipticities (from APS O plate) versus ZCAT redshift. Note that the highly inclined galaxies tend to have lower redshifts than face-on galaxies.

Chapter 8

The Effect of Inclination on a Galaxy's Appearance

Now that we have constructed the MAPS-NGPZT using machine-measured image parameters combined with previously published redshifts and morphological classifications, we have a useful catalog for investigating the effect of inclination on a galaxy's appearance.

8.1 Initial Examination of Data: Considering Selection Effects

I start by performing some simple tests of the ellipticity distribution for different subsets of the MAPS-NGP (See Figure 8.1). In the diameter-limited subset, we see a preponderance of high-ellipticity galaxies. As noted earlier in Section 6.3, this has been interpreted in the past as an indication that galaxies are optically thin by Jones, Davies, and Trewhealla [1996] and Cabanela and Aldering [1998]. However, when we look at a magnitude-limited subset of the same galaxy catalog, we see, if anything, a dearth of high ellipticity objects. This suggests that high ellipticity galaxies are typically fainter than face-on galaxies, which is traditionally interpreted as evidence that galaxies are optically

thick. Thus we arrive at conflicting evidence using the same test on different subsets of the same original catalog. I then conducted the test originally proposed by Burstein and Lebofsky [1986], in which one plots the diameter versus redshift for separate low and high ellipticity subsets of the MAPS-NGPZT (See Figure 8.2). Burstein and Lebofsky predicted that if there was an increase in isophotal diameter with inclination, then one would expect to see a broader redshift distribution with increasing inclination, because highly inclined galaxies, appearing larger, should be seen to a deeper redshift. This effect is seen in the diameter-limited complete subset of the MAPS-NGPZT (See Figure 8.2a).¹ This sample therefore supports the idea that diameters increase with increasing inclination. However, a magnitude-limited complete subset of the same MAPS-NGPZT shows no such effect (see Figure 8.2b). We do see the distribution shift to higher diameters with increasing inclination, but there is no evidence of a broader redshift distribution with increasing inclination. This may again support the idea that diameters increase with increasing inclination, but the failure to see these inclined galaxies at higher redshifts conflicts with this interpretation. These conflicting results using subsets of the same datasets with different selection criteria illustrates the strength of selection effects on the final observed inclination effects, a problem discussed in Section 6.4.1. This is precisely why Chołoniewski's estimators are so important [Chołoniewski 1991]. Chołoniewski [1991] took into account selection effects when determining the predicted behavior of a sample of galaxies with inclination. Therefore, application of Chołoniewski's estimators should allow the unambiguous determination of how magnitude and diameter change with inclination.

¹The diameter limit of 65'' is designed to generate a complete subsample.

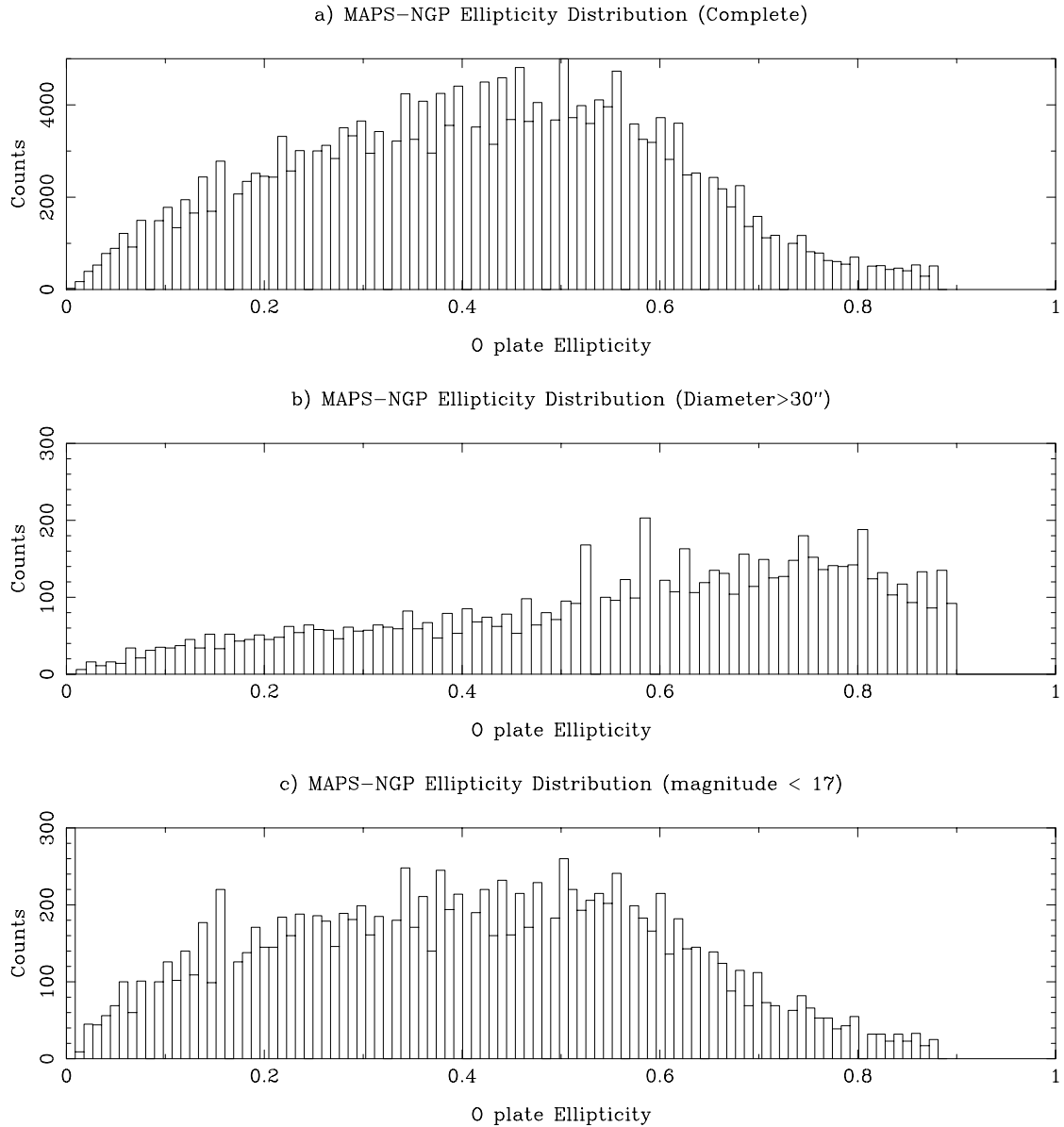


Figure 8.1: Plot (a) shows the ellipticity distribution for the entire MAPS-NGP. Note that seeing has significantly affected the appearance of small galaxies (e.g. small, intrinsically edge-on galaxies will look much rounder), causing a shift in the peak ellipticity to lower ellipticities. A plot of the ellipticity distribution of the MAPS-NGP for both (b) diameter-limited and (c) magnitude-limited subsets using very large/bright limits show significantly different trends, presumably because they are less affected by seeing.

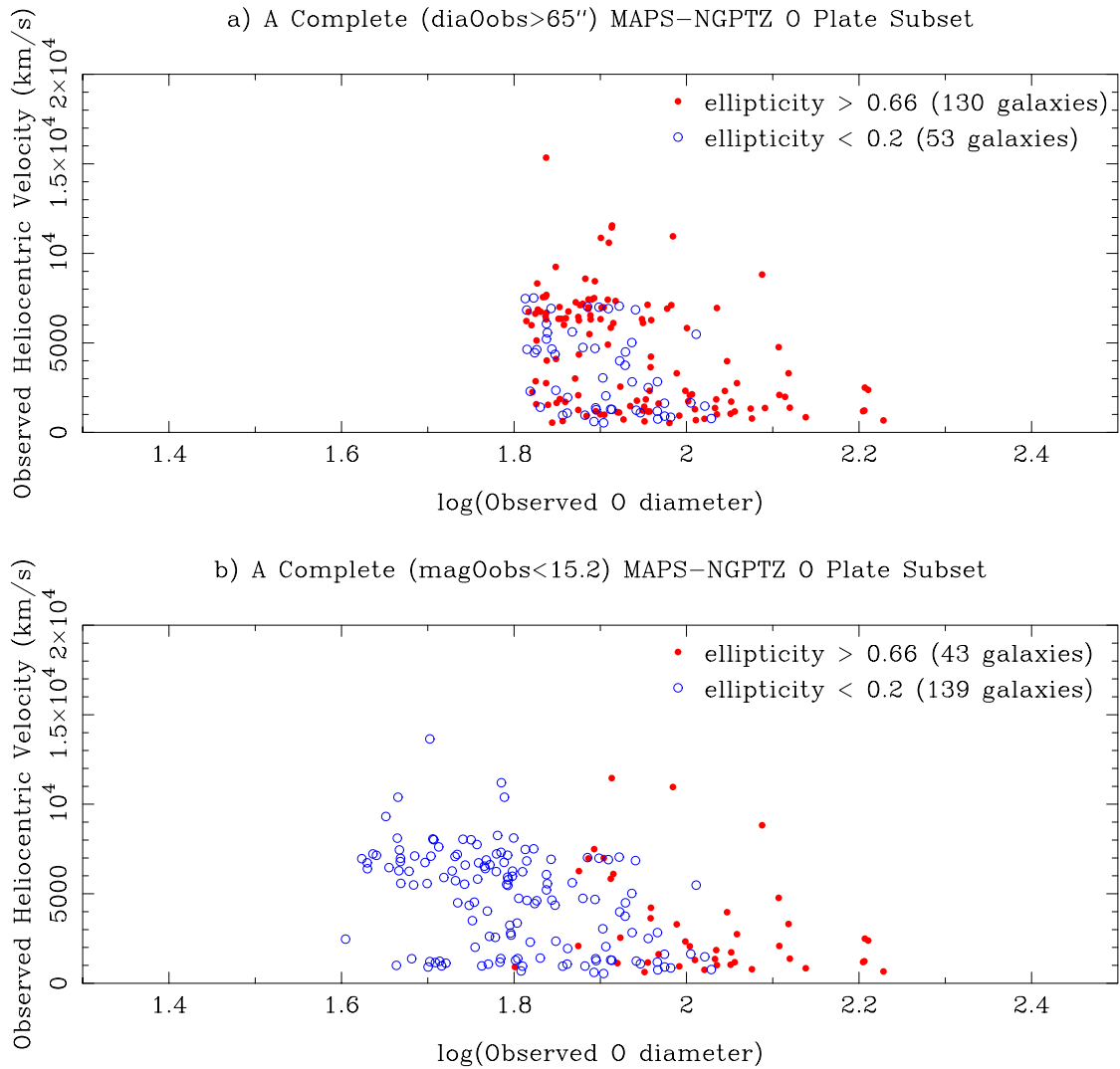


Figure 8.2: Plots of the diameter versus redshift for a (a) diameter-limited and (b) magnitude limited subsets of the MAPS-ZT. The low ellipticity ($\epsilon < 0.20$) galaxies are indicated by empty circles, which high ellipticity ($\epsilon > 0.66$) galaxies are filled circles.

8.2 Application of Chołoniewski's Estimators

Using the method outlined by Chołoniewski [1991] (See Section 6.4.3), I examined the MAPS-NGPZT subset, attempting to determine the behavior of the observed luminosity, diameter, and surface brightness for varying inclination by using the estimators for $\alpha(p)$, $\beta(p)$, and $\gamma(p)$ he derived. After some experimentation, I found that a good balance between resolving how $\alpha(p)$, $\beta(p)$, and $\gamma(p)$ vary with morphological type and the need for enough objects in each axial ratio bin to fit those functions, can be found by binning the data into 10 morphological types (shown in Table 8.1) and 5 axial ratio bins (each 0.2 wide). I then computed the estimators for both the O and E bandpasses. I computed

Table 8.1: Morphological Binning Used With MAPS-NGP And Chołoniewski's Estimators

bin	T	Name
1	$-6 \leq T \leq -4$	Ellipticals
2	$-4 \leq T \leq -1$	S0
3	0	S0a
4	1	Sa
5	2	Sab
6	3	Sb
7	4	Sbc
8	5	Sc
9	6	Scd
10	$7 \leq T \leq 11$	Irregulars

Chołoniewski's estimators using the complete MAPS-NGPZT as well as diameter-limited and magnitude-limited subsets of the MAPS-NGPZT for those tests appropriate to such subsets. The diameter and magnitude limits were the completeness limits outlined in Section 7.2. This allowed for four estimates of $\alpha(p)$ and $\beta(p)$, and six estimates of $\gamma(p)$ for the MAPS-NGPZT. An additional set of estimates was made for the MAPS-NGPZT constructed *without* the magnitude, diameter, and surface brightness corrections for variations in limiting surface brightness, μ_{limit} , as outlined in Section 7.1.6. Given the untested nature of these μ_{limit} corrections, it was important to compare the results both with and without them. The results are shown in Figures 8.3 - 8.5. Figures 8.6 -

8.8 shows their counterparts for the MAPS-NGPZT without varying μ_{limit} corrections.

There are several features of interest to note in these plots of the estimators:

- It appears that the various estimates for $\alpha(p)$, $\beta(p)$, and $\gamma(p)$ are more consistent with one another in the MAPS-NGP sample without the corrections for varying μ_{limit} . However, there does not appear to be a strong dependence on the form of $\alpha(p)$, $\beta(p)$, and $\gamma(p)$ with whether the μ_{limit} corrections have been applied or not. This gives us some confidence that the results derived here are *not* dependent on the application of μ_{limit} corrections.
- From the $\alpha(p)$ function estimates (Figures 8.3 and 8.6), we see that luminosity generally drops with increasing inclination (and lower axial ratio, p). The drop in luminosity seems more pronounced for the later spiral types than the early ones. It is notable that for some spiral types, such as Sb, there seems to be an initial *increase* in the observed integrated diameter before a final drop. This sort of luminosity increase with inclination is not predicted by any previously published models.
- The $\beta(p)$ function estimates (Figures 8.4 and 8.7) show that isophotal diameters do increase with increasing inclination. The increase tends to be larger for earlier spiral types than later ones. There are some cases where $\beta(p)$ seems to indicate a decrease in isophotal diameter with increasing inclination, although the trend is weak. This might be expected with very strong internal extinction, but is generally not expected.
- There appears to be a weak trend for the mean surface brightnesses to drop with increasing inclination, but only for the late spiral types. This is indicated by the generally “flat” $\gamma(p)$ functions seen for early spiral types in Figures 8.5 and 8.8.
- Surprisingly, there is not a big difference in the behavior of $\alpha(p)$, $\beta(p)$, and $\gamma(p)$ between the blue (O) and red (E) bandpasses, even though extinction between

these two bandpasses varies by almost a factor of two according to the extinction law of Cardelli, Clayton, & Mathis [1989].

These results are generally consistent with the idea that early spirals are more optically thin than late spirals, which contradicts the results of Chołoniewski [1991]. It should be noted that Chołoniewski [1991] fit his $\alpha(p)$, $\beta(p)$, and $\gamma(p)$ functions with simple power laws of the form

$$x(p) = p^{D_x}. \quad (8.1)$$

While I did fit my $\alpha(p)$, $\beta(p)$, and $\gamma(p)$ estimated functions with power laws (using non-linear least squares fitting), I found the power laws were not very good fits, in part because my functions did not always monotonically increase or decrease, as required by a power law. The power law fits also tended to lock on to the behavior of the high axial ratio (low inclination) points, not being profoundly influenced by low axial ratio datapoints. I also computed the $\alpha(p)$, $\beta(p)$, and $\gamma(p)$ for the fractional light radii. And while we expect $\alpha(p)$ for the fractional light radii to be identical to $\alpha(p)$ for diameters (since their luminosity is related to the total integrated luminosity by a constant), I also found that $\beta(p)$ and $\gamma(p)$ for the fractional light radii are not significantly different from the full diameter values. It should be noted that the fractional light radii are *not* isophotal, so it is not clear what relationship one would expect.

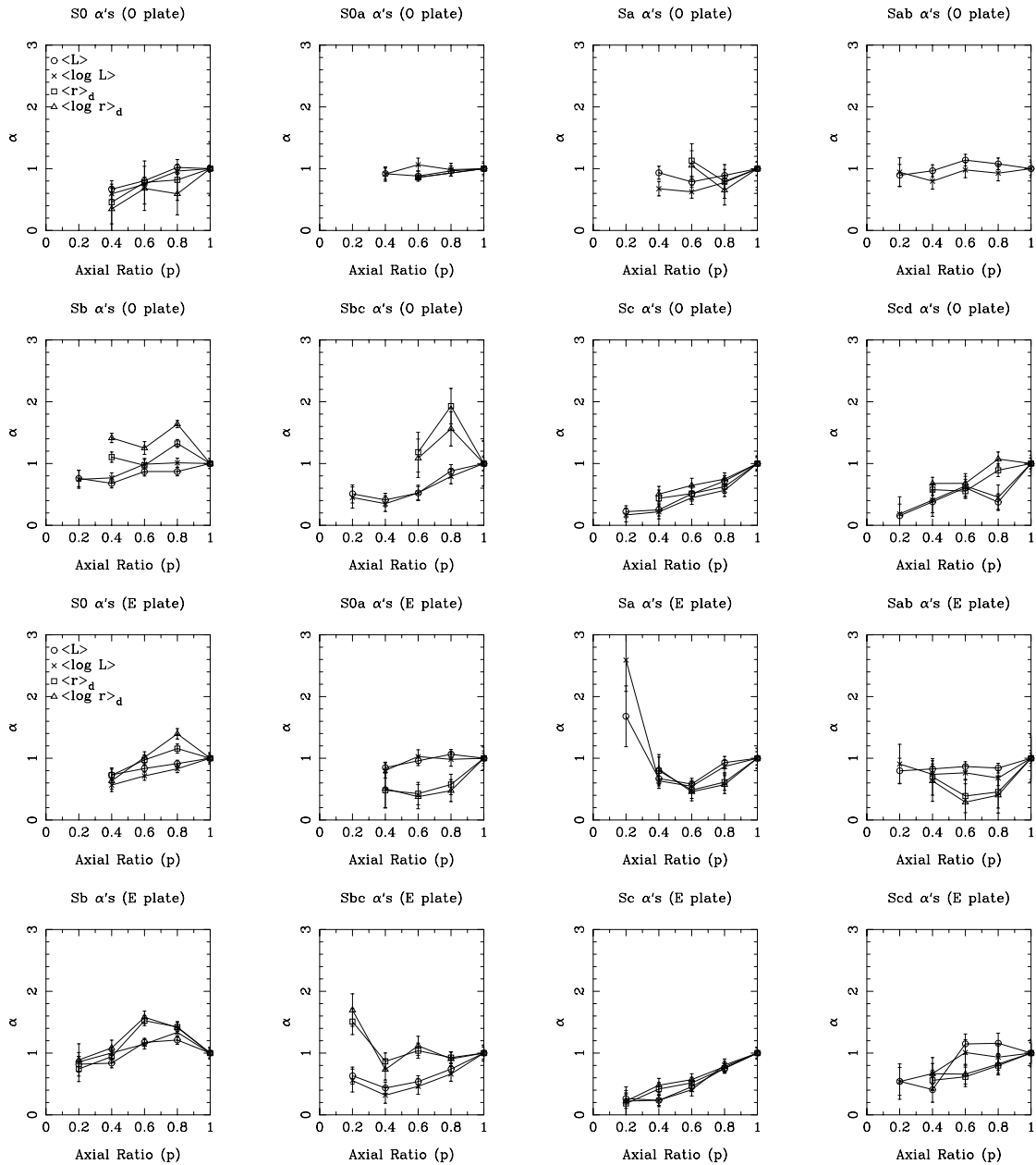


Figure 8.3: Plots of the estimators for the $\alpha(p)$ functions of eight spiral type subsets of the MAPS-NGPZT in both O and E as determined using Choloniewski's estimators. $\alpha(p)$ is the ratio of the observed luminosity at a given axial ratio to its face-on value (when $p = 1$). The full luminosity, diameter, and surface brightness corrections for changes in observed limiting surface brightness, μ_{limit} , (as outlined in Section 7.1.6) are included here.

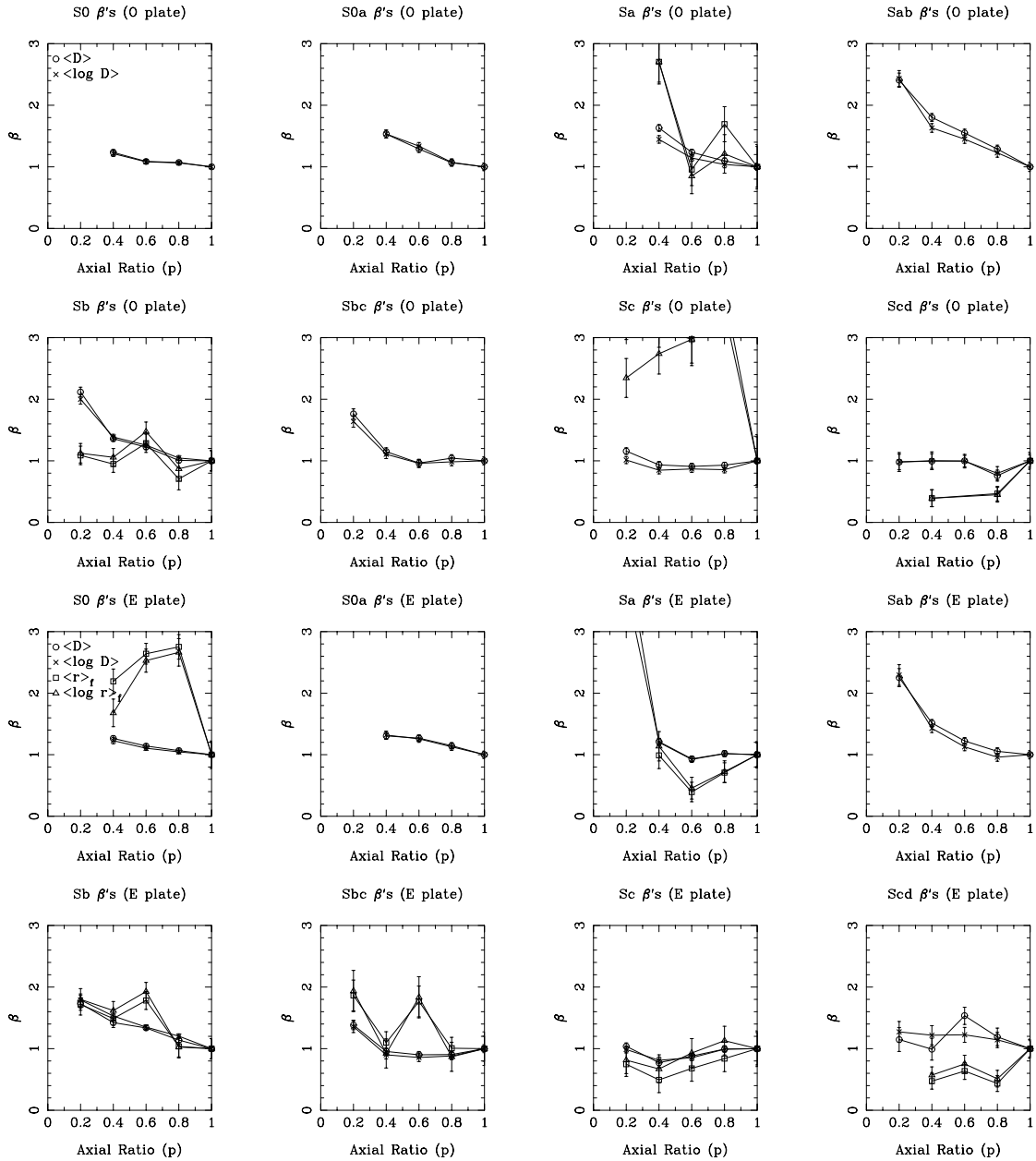


Figure 8.4: Like Figure 8.3, except that these are the derived $\beta(p)$ functions. $\beta(p)$ is the ratio of the observed diameter at a given axial ratio to its face-on value (when $p = 1$). As in Figure 8.3, all corrections for varying μ_{limit} have been included.

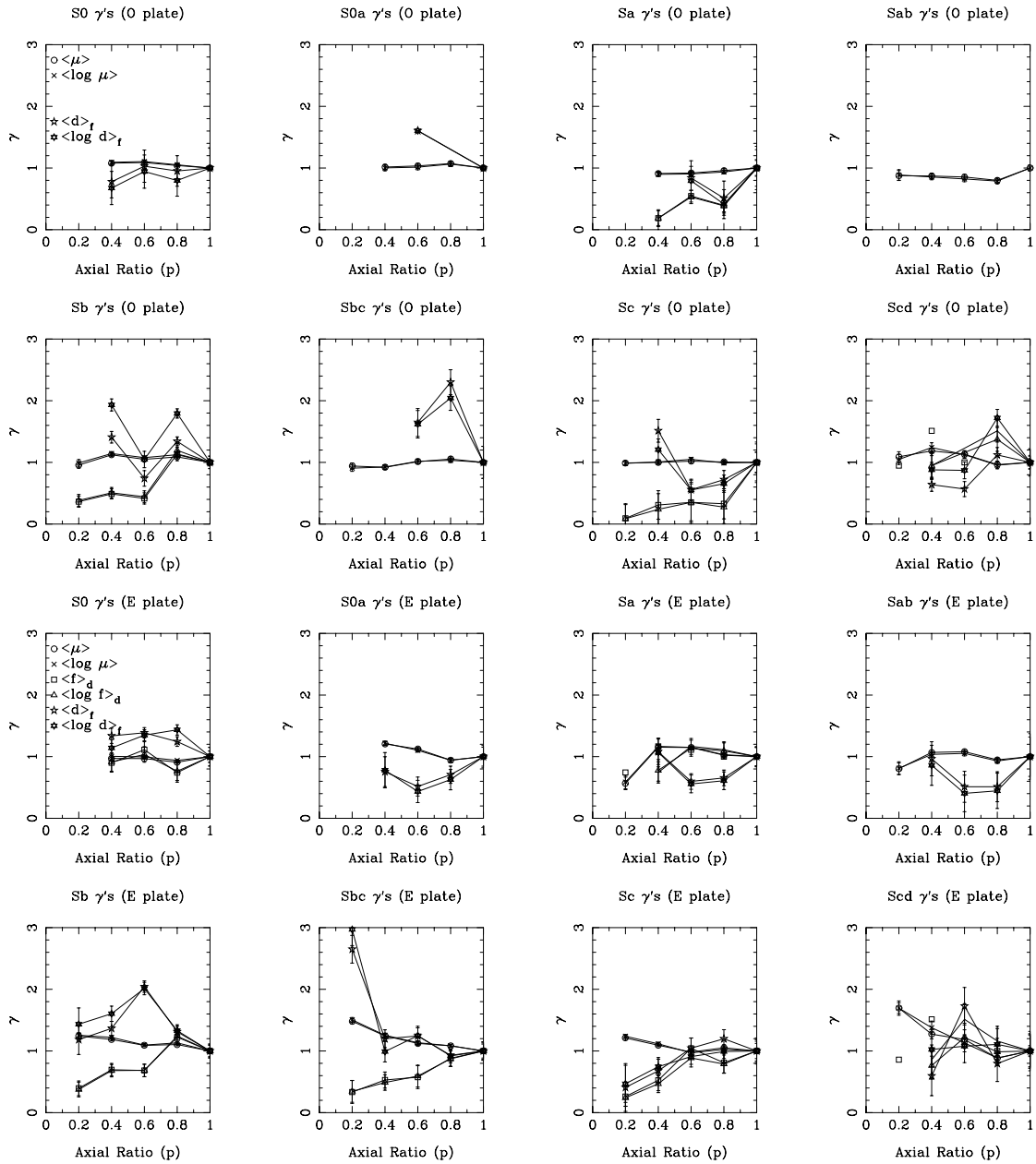


Figure 8.5: Like Figure 8.3, except that these are the derived $\beta(p)$ functions. $\gamma(p)$ is the ratio of the observed surface brightness at a given axial ratio to its face-on value (when $p = 1$). As in Figure 8.3, all corrections for varying μ_{limit} have been included.

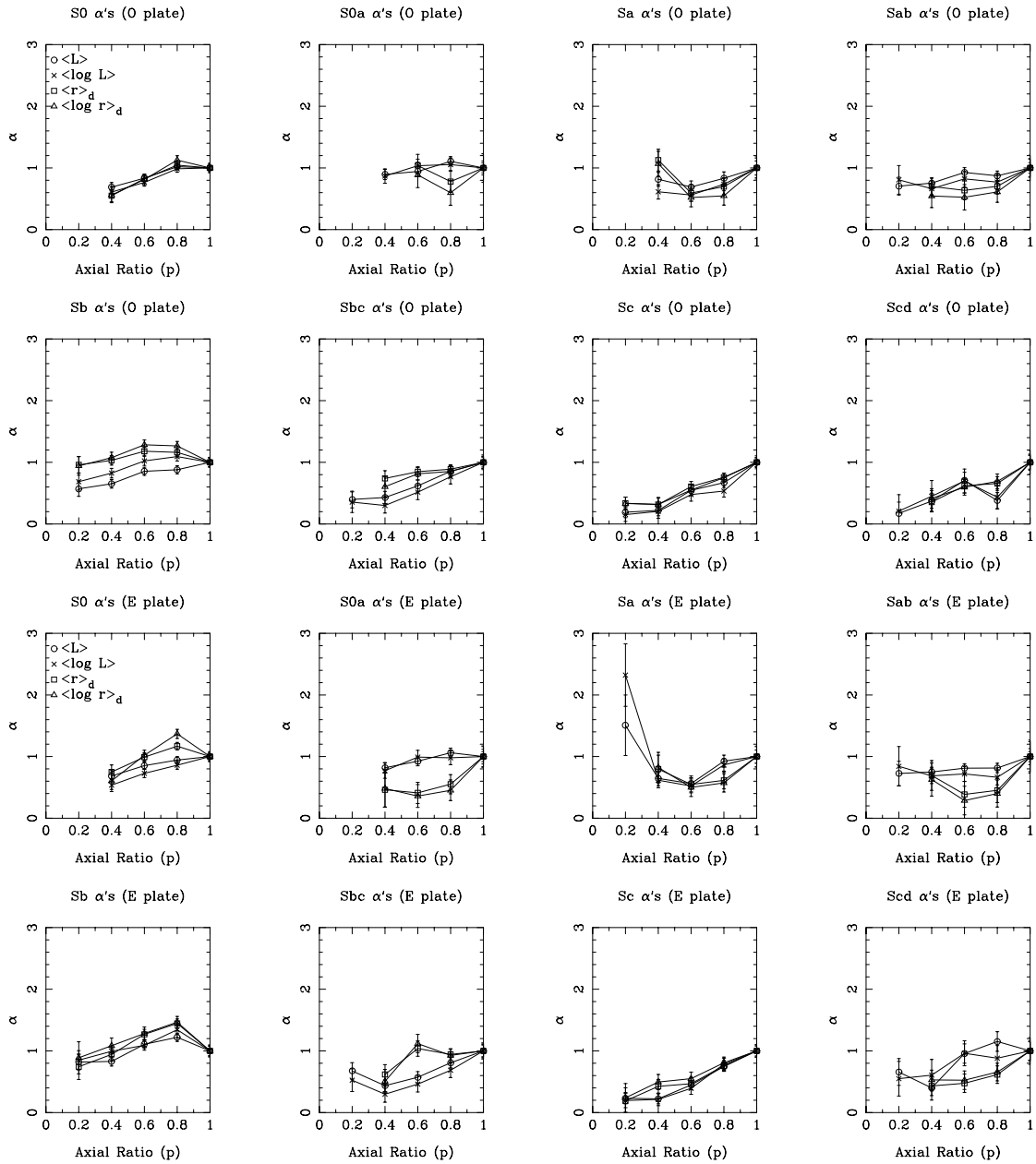


Figure 8.6: A plot of $\alpha(p)$ for the MAPS-NGPZT, like Figure 8.3, except that no corrections for varying μ_{limit} have been applied to the data.

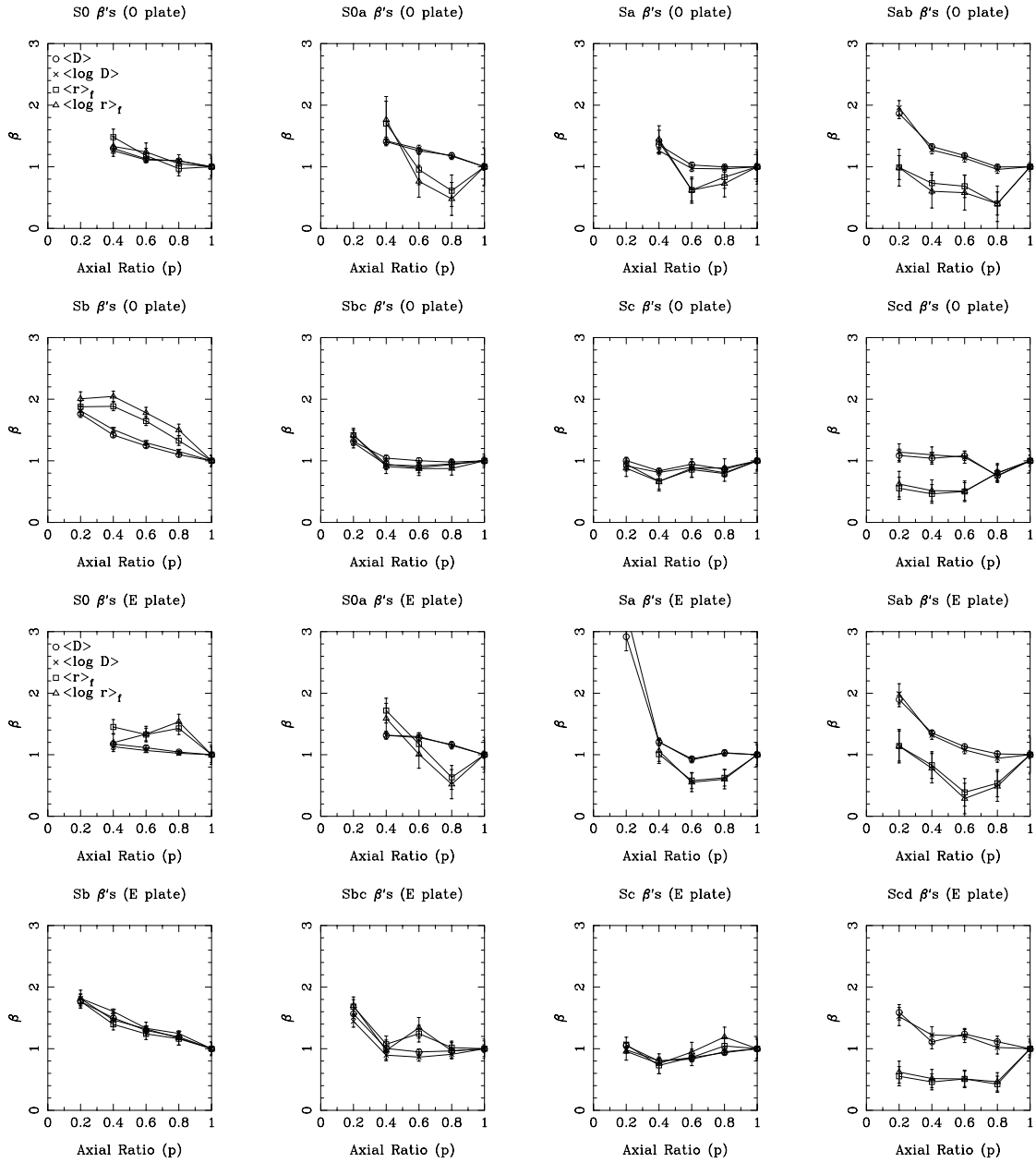


Figure 8.7: A plot of $\beta(p)$ for the MAPS-NGPZT, like Figure 8.4, except that no corrections for varying μ_{limit} have been applied to the data.

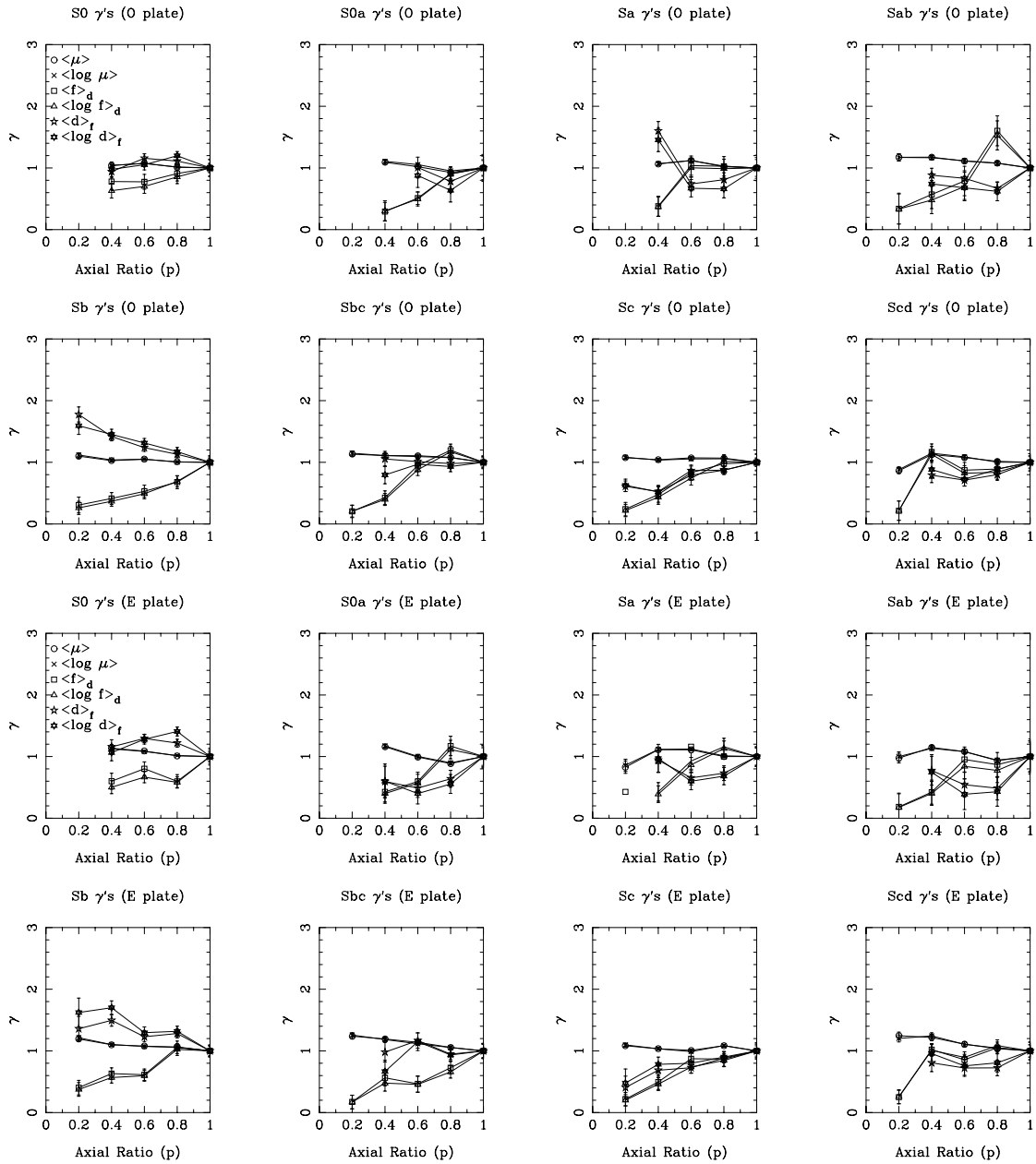


Figure 8.8: A plot of $\gamma(p)$ for the MAPS-NGPZT, like Figure 8.5, except that no corrections for varying μ_{limit} have been applied to the data.

8.2.1 Determining Inclination Trajectories

Once we have determined $\alpha(p)$ and $\beta(p)$, we know how luminosity and diameter vary with inclination. This information can be combined to determine the inclination trajectory of a galaxy in a plot of diameter versus magnitude (like Figure 6.2). This also allows an easy way to visualize the simultaneous effects of inclination on observed diameter and luminosity and to categorize their combined behavior as optically thin or thick (as indicated by the arrows in Figure 6.2). Examination of the inclination trajectories for the MAPS-NGPZT (see Figures 8.9 and 8.10) supports and extends the conclusions made earlier.² Examination of these plots shows:

- Comparing Figures 8.9 and 8.10 shows some significant differences in the exact path and length of the inclination trajectory, but the general trends in the inclination trajectory noted below were seen in both sets of inclination trajectories.
- For S0 and S0a spiral types, the inclination trajectories are unclear, as all the points remain clustered near the face-on “origin” position in the diagram. If one considers just the sample with μ_{limit} corrections, we do see what appears to be an significant increase in isophotal diameter with inclination in S0a galaxies.
- For Sa-Sab galaxies, we have inclination trajectories that are only a little more extended, with increasing inclination leading to about a 0.2 (0.5 in the uncorrected data) magnitude drop in luminosity and a 25% to 200% increase in the isophotal diameter for edge-on galaxies relative to face-on. This behavior fits the traditional paradigm of an optically thin galaxy. This optically thin behavior reaches its maximum in the Sb galaxies, in which the isophotal diameters increase by $\sim 80\%$ between face-on and edge-on orientations, with a drop in luminosity of less than 0.5 magnitudes.
- There appears to be a rather sudden shift to optically thick behavior in the Sbc-Sc

²Not a surprise since these inclination trajectories are essentially replots of $\alpha(p)$ and $\beta(p)$ on one plot.

galaxies, in which the luminosity drops by 1-2 magnitudes but the diameter doesn't dramatically increase (except in the μ_{limit} corrected data), and in fact, in the case of the Sc galaxies, it actually appears the diameters tend to *decrease*!

- Scd galaxies have a very confused inclination trajectory, although given how these galaxies are essentially irregular galaxies with spiral structure, it may be difficult to associate axial ratio with inclination.
- Finally, there appears to be little difference in the O and E bandpass inclination trajectories, reflecting the lack of differences seen in the plots of $\alpha(p)$, $\beta(p)$, and $\gamma(p)$.

The most confusing aspect of interpreting these inclination trajectories is the sharp change in behavior between Sb galaxies which behave optically thin and Sc galaxies, which appear optically thick.

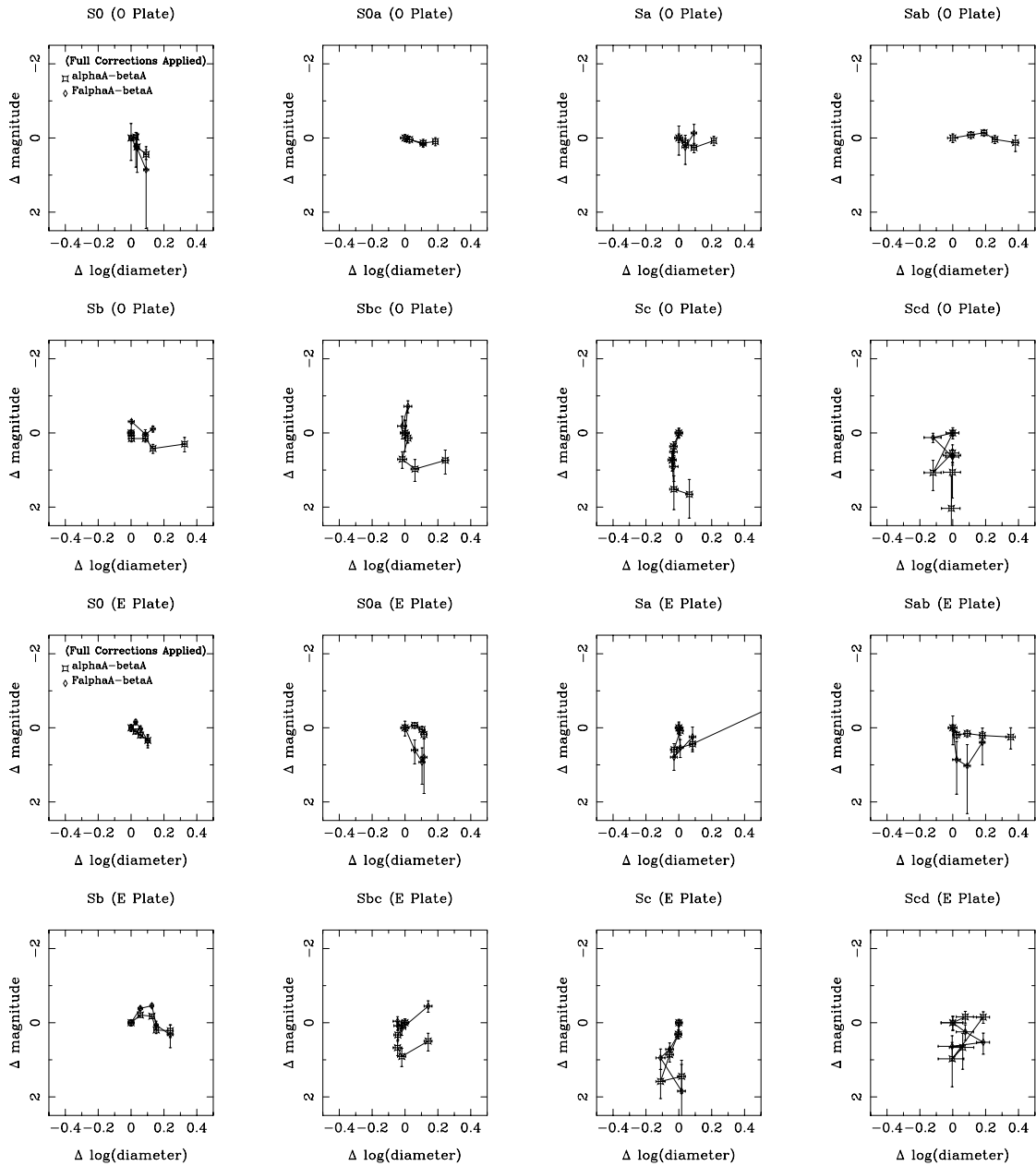


Figure 8.9: A plot of the inclination trajectories of spiral galaxies in the MAPS-NGPZT based on the derived $\alpha(p)$ and $\beta(p)$ functions. All trajectories are relative to the face-on ($p = 1$) appearance of the galaxies, each point representing a change of $\Delta p = 0.2$.

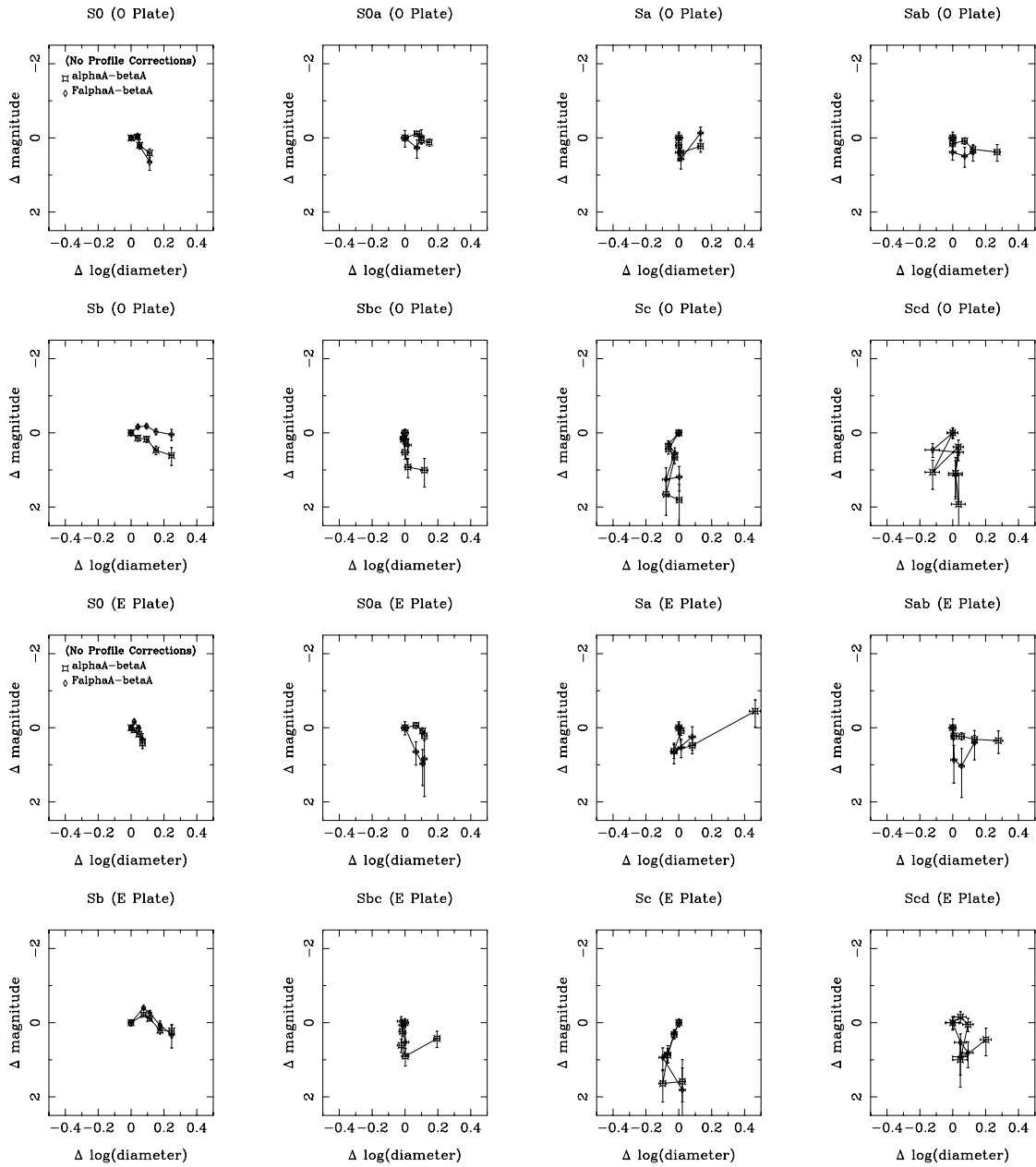


Figure 8.10: Same as Figure 8.9 but with no μ_{limit} corrections applied.

8.2.2 Testing Effects of Morphological Classification Method

The sudden shift in observed inclination trajectories between Sb and Sc galaxies was unexpected, so I investigated possible sources of uncertainty. One possibility is the heterogeneity of sources of the morphological type used in the ZCAT. It is well known that morphological classification is a somewhat subjective activity and that even among very experienced classifiers there is a scatter of one to two T types in their classifications. To test if the morphological classifications in the ZCAT may be biased in their distribution, I matched the RC3 to the MAPS-MGPZT and revised the T types in the MAPS-NGPZT to the RC3 morphological classifications (which are presumably more homogenous than the ZCAT, since they all come from one source). Of the 2009 objects cross-identified between the MAPS-NGPZ and RC3, 1529 had their T types revised, although in vast majority of cases by only one or two T types (see Figure 8.11). The difference made by “revising” T types in the MAPS-NGPZ to RC3 values when available can be seen in Figure 8.12. It shows that, at least for spiral galaxies, the distribution is a bit smoother when RC3 classifications supplant ZCAT classifications in the MAPS-NGPZT. The revised MAPS-NGPZ has 2709 T types (instead of 2687 in the original MAPS-NGPZ) of which 1889 are spirals (up from 1871 in the MAPS-NGPZ).

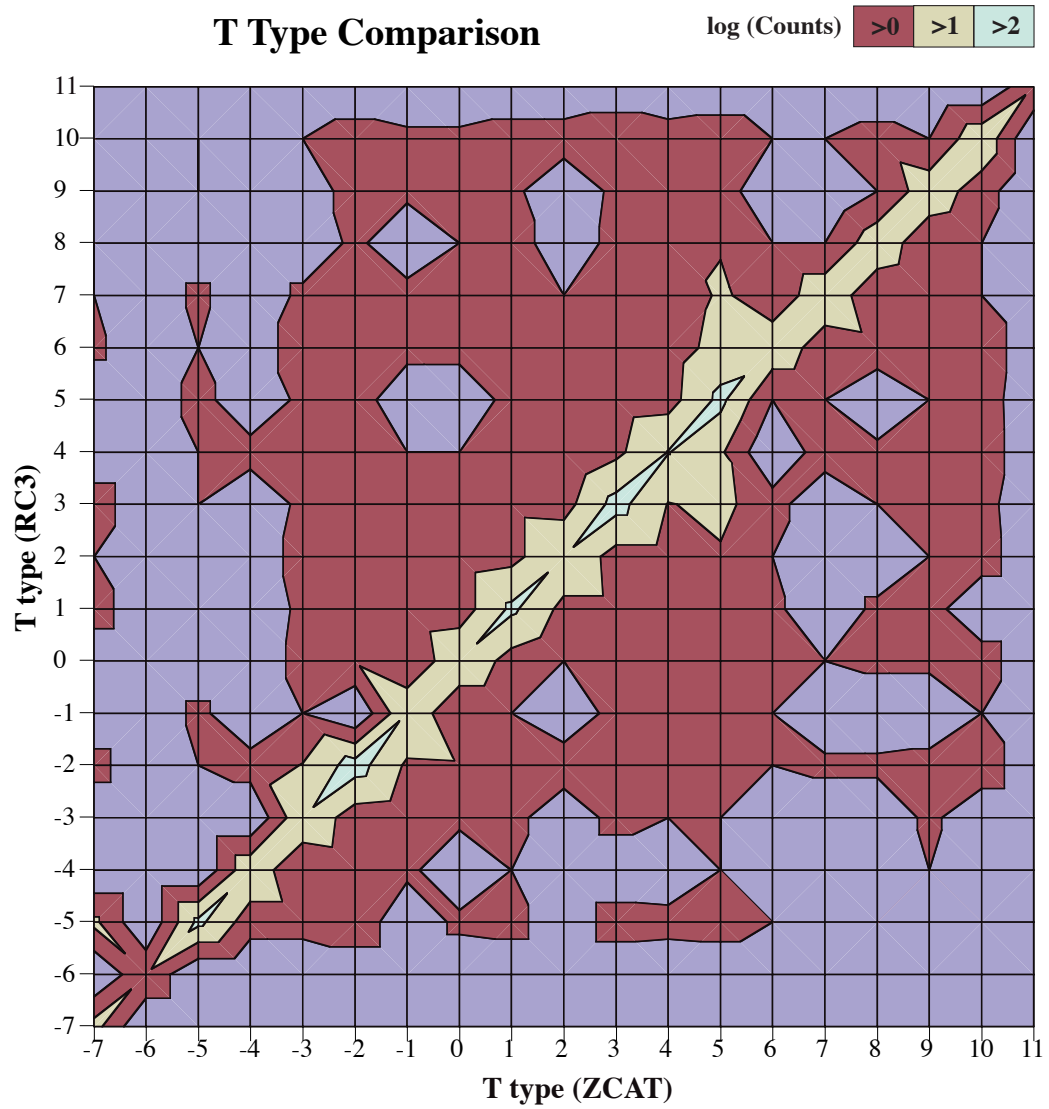


Figure 8.11: A comparison of 2009 ZCAT and RC3 galaxy morphological classifications. Notice that the morphological classifications are fairly consistent with only a few T types of scatter.

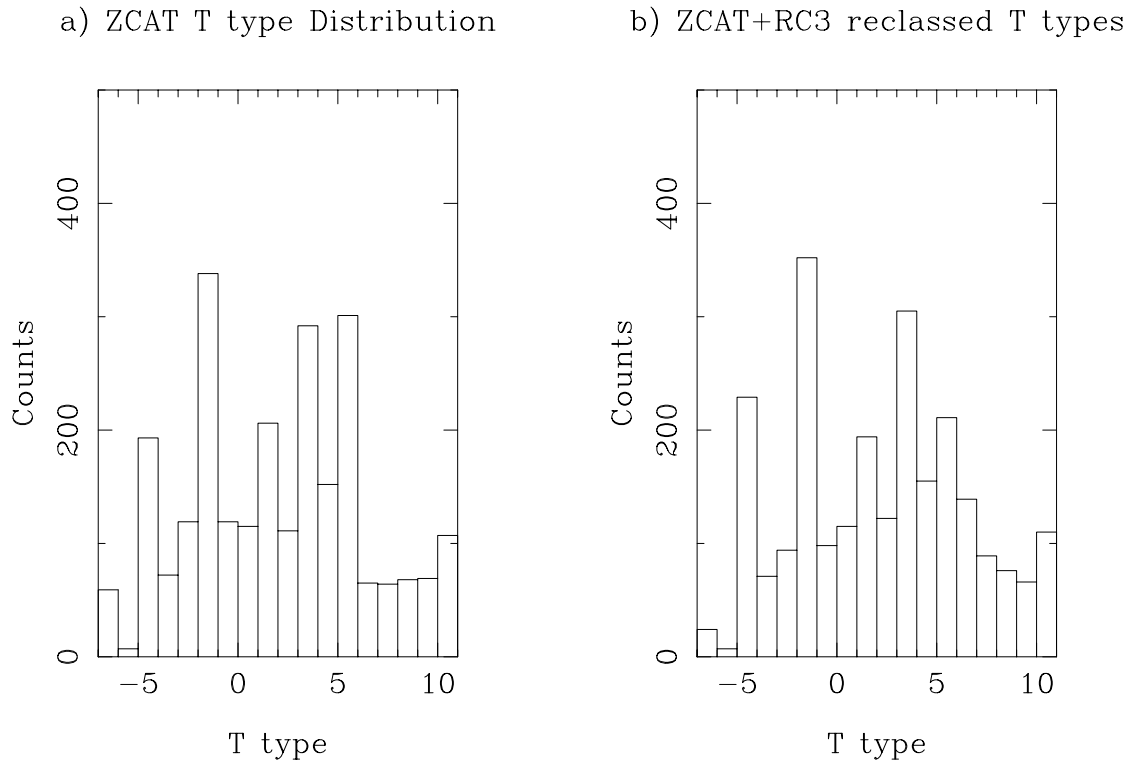


Figure 8.12: Morphological T type distributions for the MAPS-NGP with (a) only ZCAT (November 1998) T types or with (b) RC3 revisions to those T types.

When the inclination trajectories are recomputed using the RC3 morphological classifications available (see Figures 8.13 and 8.14), we see that the transition from optically thin to optically thick behavior as we progress to later spiral types is still present, it is a bit smoother. The fact that the trend continues to be present indicates that while there remains some uncertainty in the precise form of the transition from optically thin to optically thick behavior, later spiral types do indeed tend to behave as if they are more optically thick than early spiral types.

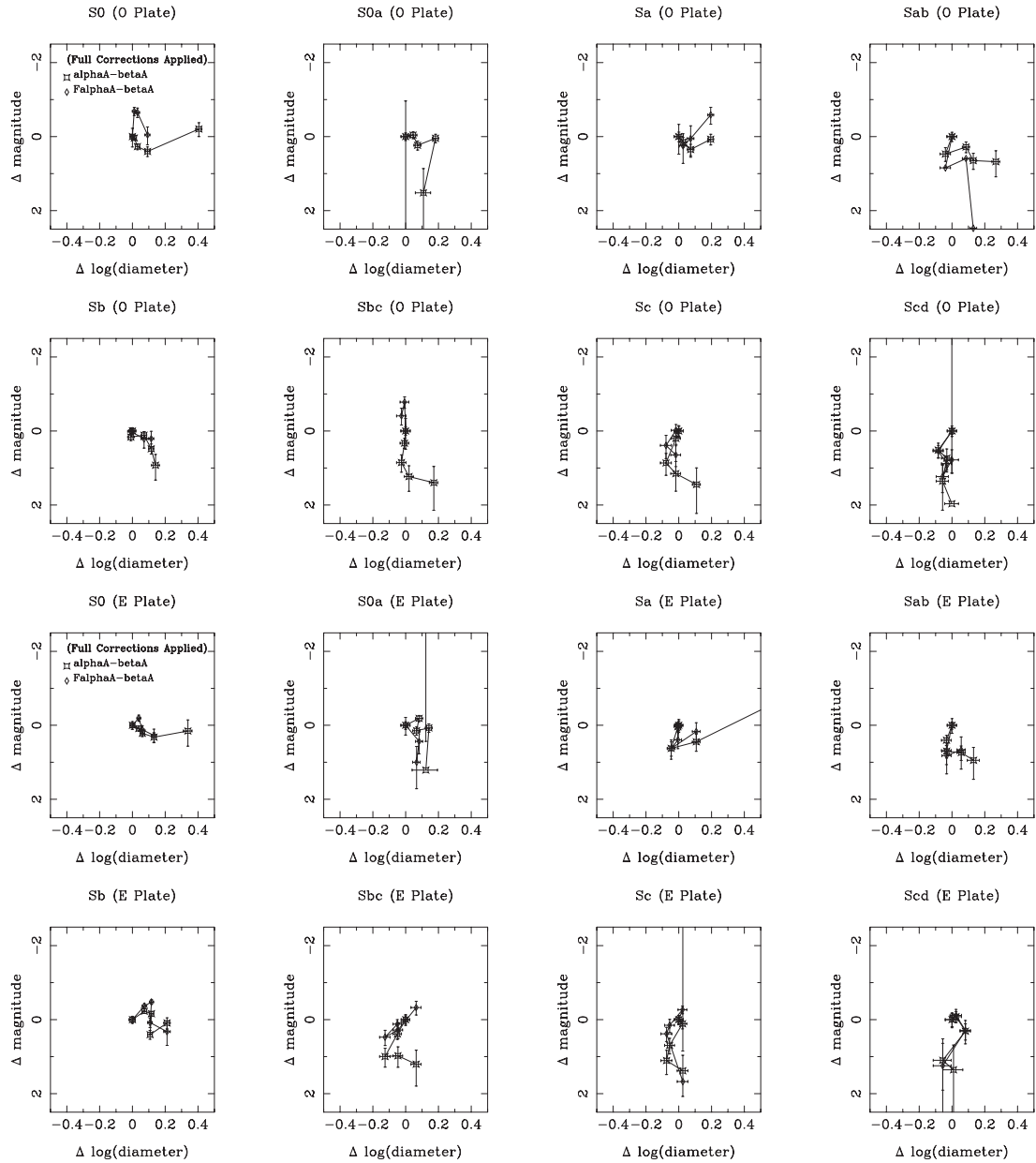


Figure 8.13: A plot of the inclination trajectories of spiral galaxies in the MAPS-NGPZT where RC3 morphological classifications have supplanted ZCAT classifications. Corrections for μ_{limit} variations have been made. These plots should be compared to those in Figure 8.9 in order to understand the changes caused by the addition of RC3 morphological classifications.

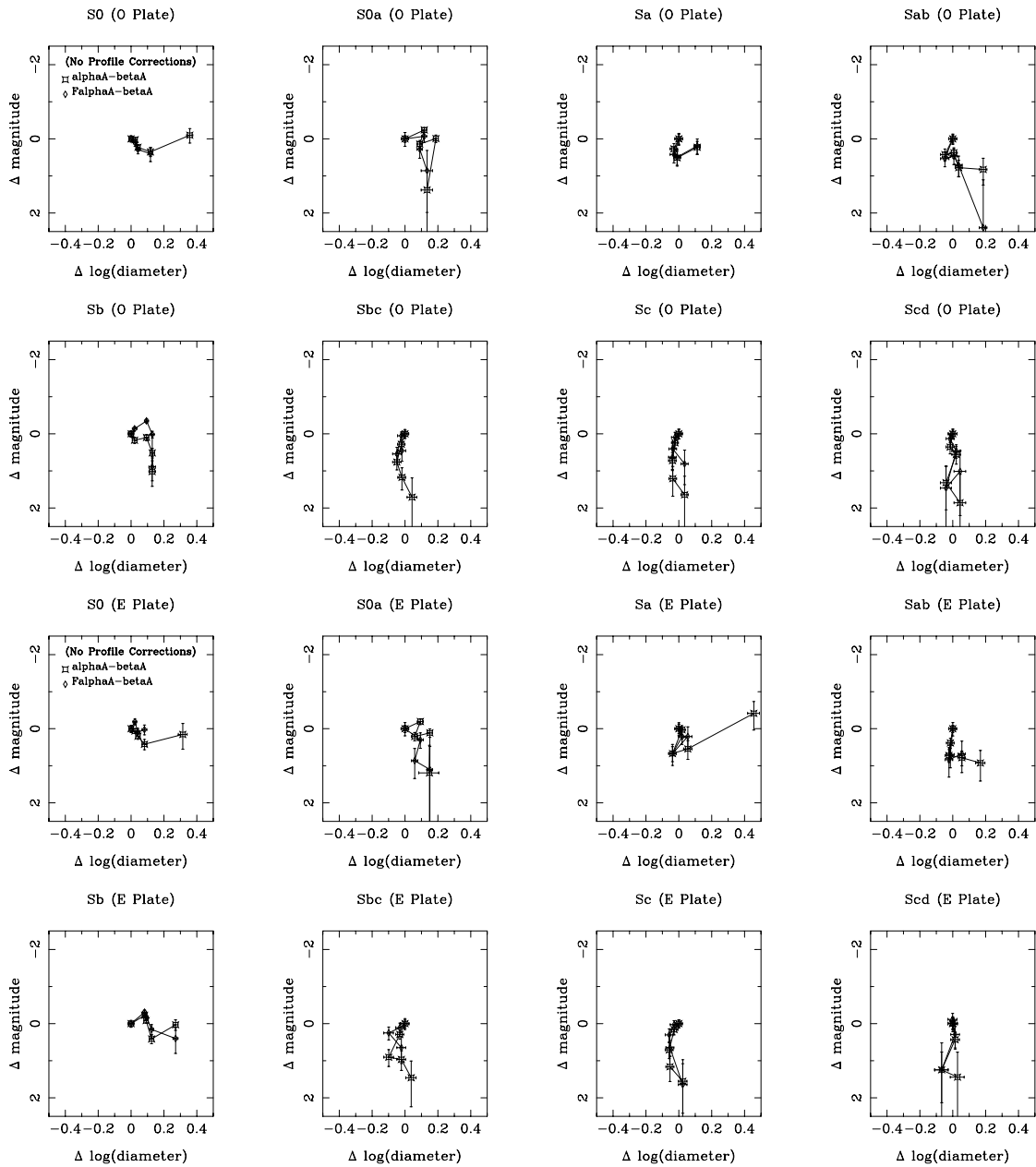


Figure 8.14: Same as Figure 8.13 but with no μ_{limit} corrections applied. The plots here should be compared to those in Figure 8.10.

8.2.3 Inclination Trajectories versus Galaxy Color

Part of the difficulty in interpreting the behavior of the inclination trajectories of galaxies versus morphological type is the relatively small number of galaxies with morphological classifications relative to the number with redshifts. In the MAPS-NGPZ, there are a total of 8727 galaxies with redshifts versus ~ 2700 with morphological classifications. If I could use all of them, it might reduce the uncertainty in the behavior of galaxies with inclination. Since I have $O - E$ color for each MAPS-NGPZ galaxy, it should be possible to use all 8727 MAPS-NGPZ with redshifts to find the relationship between inclination trajectory and color. As we know from Figure 7.3, $O - E$ color does have a definite linear relationship with morphological type. Therefore, the relationship between inclination trajectory and color can provide additional evidence to the behavior of inclination trajectory versus morphological type. In determining the behavior of inclination trajectories versus color in the MAPS-NGPZ, I had to drop some of the corrections applied to the MAPS-NGPZT. Since both the K correction (detailed in Section 7.1.5) and the corrections for varying μ_{limit} (outlined in Section 7.1.6) require information on morphological type, I am not applying them for this test. For binning, constant-width $O - E$ bins would not be useful since the $O - E$ distribution is very peaked around $O - E \approx 1.44$. Instead I sorted the galaxies by color and plotted successive decimal portions of the MAPS-NGPZ as shown in Figure 8.15. Finally, since this sample is larger (and likely deeper, since morphological typing requires sufficient image resolution and thus is biased toward brighter and therefore closer galaxies), I recomputed the diameter and magnitude completeness limits for the MAPS-NGPZ. For the purposes of computing the inclination trajectories, I used a diameter limit of $56''$ in both bandpasses and a magnitudes limit of 15.55 and 14.40 in O and E respectively. Figure 8.15 shows that there is a trend for the inclination trajectory to shift from optically thick behavior in the bluest galaxies to optically thin behavior for redder galaxies. This behavior breaks down somewhat for the reddest galaxies, those with $O - E > 1.75$. However, the group of galaxies this red are dominated by ellipticals, for which axial ratio is not clearly related

to inclination, thus the inclination trajectories for these color bins are really not terribly related to the inclinations for these galaxies. If we disregard the most extremely red bins, this trend of inclination trajectory with color is consistent with the idea that the bluer, later spiral galaxies behave more optically thick than the redder, earlier spirals.

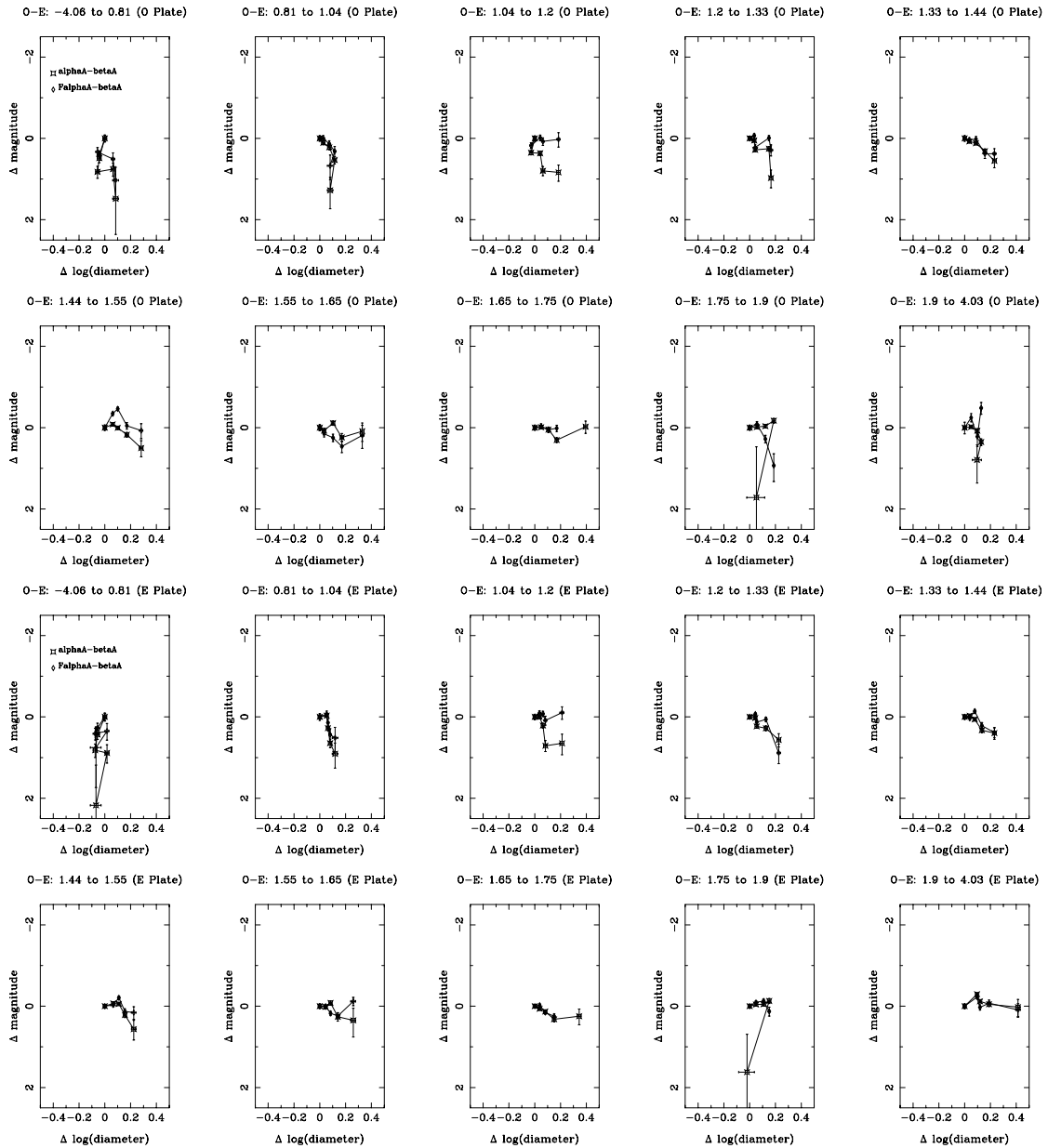


Figure 8.15: This plot of the inclination trajectories for different $O - E$ bins of the MAPS-NGPZ indicates that there is indeed a trend for more optically thick behavior in blue galaxies versus red galaxies. This trend is quite dramatic and is seen on both the O and E plates.

8.3 Analysis

Our results differ markedly from those of Burstein, Haynes, and Faber [1991] and Chołoniewski [1991], despite using somewhat similar techniques. Both of these previous studies had found that all spirals behaved optically thick, with “vertical” inclination trajectories. Those studies used diameters measured to presumably deeper isophotes than our 23.5 magnitude isophote but yet found optically thick behavior in the early-type spirals in which I see optically thin behavior. I believe that this difference can be attributed for the most part to the diameter-inclination effect. Both Burstein, Haynes, and Faber [1991] and Chołoniewski [1991] used the UGC as their source of galaxy image parameters. As demonstrated in Section 6.5.1, the UGC suffers from a very strong bias such that face-on diameters will be measured to a deeper isophote than edge-on diameters. If a galaxy’s true isophotal diameter increases with inclination, then the diameter-inclination effect would cancel it out. Therefore, the diameter-inclination effect will force an optically thick behavior from any diameter versus inclination tests performed with the UGC. Similarly, since the UGC is a visual diameter-limited catalog, it will be very different sample than an isophotal diameter-limited galaxy catalog. The UGC will contain face-on galaxies seen to a deeper isophote than edge-on galaxies, which implies the face-on portion of the UGC should be deeper than the edge-on portion. This will act to counteract the expected trend for an optically thin sample of galaxies, for which we expect the sample will be deeper for edge-on galaxies than for face-on galaxies (since the edge-on isophotal diameters will be larger than their face-on counterparts). In essence, the existence of the diameter-inclination effect in the UGC means the optically thick results of Burstein, Haynes, and Faber [1991] and Chołoniewski [1991] are questionable. This study has shown the expected trend for spiral galaxies to appear more optically thick as we progress to later morphological types. This trend is expected because it is known that later spiral types have higher gas content than earlier types and thus likely have higher dust content. This thesis supports the results of previous studies which have looked at small numbers of galaxies in great detail (e.g. - Byun [1992a], Bosma *et al.* [1992],

Andredakis and van der Kruit [1992], White and Keel [1992], Peletier *et al.* [1995], and Xilouris *et al.* [1997]). In fact, I note that Bosma *et al.* [1992] found that while galaxies are optically thin at the 25 magnitude/ \square'' , they found galaxies behave optically thick at at shallower isophotes (possibly accounting for the optically thick behavior we see in later spiral types. Furthermore, direct observations of extinction in overlapping galaxies by White and Keel [1992] found that while galaxies are generally optically thin, spiral arms have higher optical depth than interarm regions. This suggests that the Sc galaxies, in which the disk is much more prominent than the bulge and the spiral arms are more prominent, the spiral pattern would dominate what we see. Thus we would be examining regions of higher extinction, leading to optically thick behavior in later spiral types.

8.4 Future Directions and Considerations

The most critical new aspect of this study has been to apply a large galaxy catalog with *machine-measured* image parameters to the problem of inclination effects in galaxies. I have derived inclination trajectories for galaxies which take into account (and in fact exploit) the magnitude and diameter limits of the source catalog. This study has resolved the previously noted conflict in recent inclination studies of the statistical behavior of large samples of spiral galaxies (which have repeatedly reported optically thick behavior) versus those which concentrate on a small number of spiral galaxies (which repeatedly report optically thin behavior). This has been accomplished by avoiding the diameter-inclination effect in galaxy catalogs with visually measured diameters and by using reduction techniques (developed by Chołoniewski [1991]) which take into account diameter and magnitude limitations of the catalog. The fact that early-type galaxies appear optically thin does not mean they are optically thin. As noted by Disney, Davies, and Phillips [1989], the interpretation of an inclination trajectory is very highly model dependent. For example, if galaxies had a very thin, but optically thick, layer of dust, we would always see just the half of the galaxy above the dust layer, but this upper layer would be unaffected by dust, and therefore the galaxy would behave optically thin, while

actually being optically thick. It is only observations of individual galaxies which actually measure the extinction directly which can determine if galaxies actually are optically thin or thick. This thesis simply gives a measure of the observed behavior. A future direction for this study will be the comparison of galaxy behavior versus the behavior expected from galaxy models, such as the “Triplex” galaxy model of Disney, Davies, and Phillips [1989], which models a galaxy as a double-exponential (both radial and vertical relative to the galaxy midplane) distribution of stars and a double-exponential dust distribution with equal radial scale length to the stellar distribution but different vertical scale height. So while the observed inclination trajectory can not definitively determine the opacity of galaxies, this observed behavior can provide very useful constraints on any models of the dust distribution in galaxies. And while not actually determining the dust distribution in galaxies, this thesis has shown that if we use galaxies of varying inclinations to derive (or exploit) their diameters or luminosity, we must correct for the effects of inclination on the appearance of the galaxies. Studies of the luminosity functions or diameter functions of galaxies must correct for inclination, *but very few studies have*. In fact, a byproduct of this study is a sample of metric diameters, which in addition to the inclination corrections outlined above, could be used to compute a proper diameter function for spiral galaxies. One use of an accurately determined diameter function would be to allow estimation of the depth of galaxy clusters identified in the MAPS-NGP without requiring redshifts. Even more interesting, if late-type spirals are optically thick, then it may be necessary for us to model the dust evolution in addition to models of stellar evolution in galaxies, in order to properly interpret observations of galaxies at cosmological distances (see Calzetti and Heckman [1999] for a more thorough discussion of this issue). Finally, there are several problems which still have to be dealt with to determine the intrinsic properties of galaxies. One potential stumbling block is the problem of atmospheric seeing. As shown in Figure 8.1, seeing can dramatically affect the appearance of small galaxies. Furthermore, depending on how flattened the outer portions of the radial surface brightness profiles of galaxies are, it is possible that

seeing could dramatically affect the observed diameter of a galaxy. This problem can be countered in one of two ways:

- Attack atmospheric seeing at the observational end, by either performing space-based observations or through adaptive-optics techniques of restoring the seeing-free optical wavefront. Or...
- Attack seeing by computationally reconstructing the non-seeing affected image (if possible).

As large all-sky surveys probe deeper, the only way they will add galaxies to existing catalogs will be to add fainter, smaller galaxies previously unobserved. These galaxies will typically be more affected by seeing than the large galaxies on the sky, so understanding the effects of seeing on these images will be very important to the proper derivation of diameter functions which include these fainter galaxies. Another major issue is the lack of morphological classifications for galaxies in the MAPS-NGP. Less than 2% of the MAPS-NGP galaxies have morphological classifications available. And while I was able to use color to study a larger sample of galaxies than currently morphologically typed, it would be very useful if there were some automated morphological classification possible for the MAPS-NGP galaxies such that trends versus morphological type could more directly determined without use of an external galaxy catalog with less well understood selection effects. In fact, there is currently an effort underway for such morphological classification of APS images which should allow such an extension to the current study.

References

- Abell, G. O. 1958, ApJS, **3**, 211.
- Aldering, G. 1993, BAAS, **183**, 73.02.
- Andredakis, Y. C. and van der Kruit, P. C. 1992, A&A, **265**, 396.
- Barnes, J. and Efstathiou, G. 1987, ApJ, **319**, 575.
- Binggeli, B. 1982, A&A, **107**, 338.
- Barsony, M. 1988, Ph.D. thesis, California Institute of Technology.
- Boselli, A. and Gavazzi, G. 1994, A&A, **283**, 12.
- Bosma, A., Byun, Y-I., Freeman, K. C., and Athanassoula, E. 1992, ApJ, **400**, 21.
- Bunclark, P. J. and Irwin, M. J. 1983, *Proc. Statistical Methods in Astronomy Symposium*, ESA SP-201.
- Burstein, D. 1982, ApJ, **253**, 539.
- Burstein, D. and Lebofsky, M.J. 1986, ApJ, **300**, 683.
- Burstein, D. and Heiles, C. 1982, AJ, **87**, 1165.
- Burstein, D., Haynes, M., and Faber, S.M. 1991, *Nature*, **353**, 515.
- Byun, Y-I. 1992a, PASP, **105**, 993.
- Byun, Y-I. 1992b, Ph.D. thesis, Australian National University.
- Byun, Y-I., Freeman, K. C., and Kylafis, N. D. 1994, ApJ, **432**, 114.
- Byun, Y-I. and Freeman, K. C. 1995, ApJ, **448**, 563.
- Cabanela, J. E. and Aldering, G. L. 1998, AJ, **106**, 1094.
- Cabanela, J. E. and Dickey, J. M. 1999, AJ, **118**, 46.

- Calzetti, D. and Heckman, T. M. 1999, *ApJ*, **519**, 27.
- Coleman, G. D., Wu, C.-C., & Weedman, D. W. 1980, *ApJS*, **43**, 393.
- Cardelli, J. A., Clayton, G. C, and Mathis, J. S. 1989, *ApJ*, **345**, 245.
- Chołoniewski, J. 1991, *MNRAS*, **250**, 486.
- Ciotti, L. and Dutta, S. N. 1994, *MNRAS*, **270**, 390.
- Ciotti, L. and Giampieri, G. 1998, *Preprint*, astro-ph/9801261.
- Colberg, J. M., White, S. D. M., Jenkins, A., and Pearce, F. R. 1998, *Preprint*, astro-ph/9711040.
- Cornell, M. E., Aaronson, M., Bothun, G., and Mould, J. 1987, *ApJ*, **64**, 507.
- Courteau, S. 1996, *ApJS*, **103**, 363.
- Coutts, A. 1996, *MNRAS*, **278**, 87.
- Cunow, B. 1998, *A&AS*, **119**, 593.
- Curtis, H. D. 1918, *Bull. Lick Obs.*, 13.
- 45 Davies, J. I., Jones, H., and Trewhella, M. 1995, *MNRAS*, **273**, 699.
- De Jong, R. S. and Van Der Kruit, P. C. 1994, *A&AS*, **106**, 451.
- de Vaucouleurs, G. and de Vaucouleurs, A. 1964, *Reference Catalogue of Bright Galaxies* (Austin: University of Texas Press).
- de Vaucouleurs, G., de Vaucouleurs, A., and Corwin, H. G. Jr. 1976, *Second Reference Catalogue of Bright Galaxies* (Austin: University of Texas Press).
- de Vaucouleurs, G., de Vaucouleurs, A., Corwin, H. G. Jr., Buta, R. J., Paturel, and G., Fouqué, P. 1991, *Third Reference Catalogue of Bright Galaxies* (New York: Springer-Verlag).
- de Vaucouleurs, G. 1959, *ApJ*, **64**, 397.
- Dekel, A. 1985, *ApJ*, **298**, 461.
- Disney, M., Davies, J., and Phillips, S. 1989, *MNRAS*, **239**, 939.
- Doroshkevich, A. and Shandarin, S. 1978, *MNRAS*, **184**, 643.
- Djorgovski, S. 1983, *ApJ*, **274**, L7.

- Djorgovski, S. 1987, in *Nearly Normal Galaxies*, ed. Faber, S.M. (New York: Springer-Verlag), p.227.
- Dressler, A. 1980, ApJ, **236**, 351.
- Fisher, J. R. and Tully, R. B. 1981, ApJS, **47**, 139.
- Flin, P. 1988, MNRAS, **235**, 857.
- Flin, P. and Godłowski, W. 1986, MNRAS, **222**, 525.
- Frei, Z. and Gunn, J. 1994, AJ, **108**, 1476.
- Gavazzi, G., Boselli, A., Scodreggio, M., Pierini, D., and Belsole, E. 1999, MNRAS, **304**, 595.
- Giovanelli, R. and Haynes, M.P. 1988, in *Large-Scale Structures of the Universe*, ed. Audouze, J., Pelletan, M., & Szalay, A. (Dordrecht: Kluwer Academic Publishers), p.113.
- Giovanelli, R. and Haynes, M.P. 1993, AJ, **105**, 1271.
- Giovanelli, R. Haynes, M.P., Salzer, J.J., Wegner, G., Da Costa, L.N., and Freudling, W. 1994, AJ, **107**, 2036.
- Godłowski, W. 1994, MNRAS, **271**, 19.
- Goudfrooij, P., Hansen, L., Jørgensen, H. E., Nørgaard-Nielsen, H.U., De Jong, T., Van Den Hoek, L. B. 1994, A&AS, **104**, 179.
- Gregory, S., Thompson, L., and Tifft, W. 1981, ApJ, **243**, 411.
- Han, C., Gould, A., and Sackett, P.D. 1995, ApJ, **445**, 46.
- Harrington, R. G. 1952, PASP, **64**, 275.
- Harwit, M. 1988, *Astrophysical Concepts, 2nd Edition* (New York: Springer-Verlag).
- Hauschildt, M. 1987, A&A, **184**, 45.
- Hawley, D. L. and Peebles, P. J. E. 1975, AJ, **80**, 477.
- Helou, G. and Salpeter, E. 1982, ApJ, **252**, 75.
- Helou, G. 1984, ApJ, **284**, 471.
- Héraudeau, Ph. and Simien, F. 1996, A&AS, **118**, 111.

- Heidmann, J., Heidmann, H., and de Vaucouleurs, G. 1972, MNRAS, **75**, 85.
- Heidmann, J., Heidmann, H., and de Vaucouleurs, G. 1972, MNRAS, **76**, 105.
- Heidmann, J., Heidmann, H., and de Vaucouleurs, G. 1972, MNRAS, **76**, 121.
- Hoffman, G. L., Lewis, B. M., Helou, G., Salpeter, E. E., & Williams, H. L. 1989, ApJS, **69**, 95.
- Holmberg, E. 1958, *Medd. Lund Ser. II*, No. 136.
- Holmberg, E. 1975, in *Stars and Stellar Systems, vol. IX*, ed. Sandage, A., Sandage, M., & Kristian, J. (Chicago: U of Chicago), p.123.
- Huchra, J. and Geller, M. 1982, ApJ, **257**, 423.
- Huchra, J., Geller, M., Clemens, C., Tokarz, S and Michel, A. 1992, *Bull. C.D.S*, **41**, 31.
- Huchra, J., Davis, M., Tonry, J., & Latham, D. 1983, ApJS, **52**, 89.
- Hudson, M. and Lynden-Bell, D. 1991, MNRAS, **252**, 219.
- Huizinga, J. E. and van Albada, T. S. 1992, MNRAS, **254**, 677.
- Huizinga, J. E. 1994, Ph.D. thesis, Groningen.
- Infante, L. and Pritchett, C. J. 1995, ApJ, **439**, 565.
- Jaaniste, J. and Saar, E. 1978, in *The Large Scale Structure of the Universe*, ed. Longair, M.S. and Einasto, J. (Dordrecht: Reidel), p.448.
- Jones, H., Davies, J. I., and Trewhella, M. 1996, MNRAS, **283**, 316.
- Kapteyn, J. C. 1909, ApJ, **30**, 163.
- Kapteyn, J. C. and van Rhijn, P. 1920, ApJ, **52**, 23.
- Kashikawa, N. and Okamura, S. 1992, PASJ, **44**, 493.
- Kent, S. M. 1985, ApJS, **59**, 115.
- Kodaira, K., Okamura, S., and Ichikawa, S. 1990, *Photometric Atlas of Northern Bright Galaxies* (Tokyo: U of Tokyo Press).
- Kodaira, K., Doi, M., and Shimasaku, K. 1992, AJ, **104**, 569.
- Lambas, D. G., Groth, E. J., and Peebles, P. J. E. 1988a, AJ, **95**, 975.

- Lambas, D. G., Groth, E. J., and Peebles, P. J. E. 1988b, *AJ*, **95**, 996.
- Larsen, J. A. 1996, Ph.D. thesis, University of Minnesota.
- Laubscher, B. E. 1994, Ph.D. thesis, University of New Mexico.
- Lauberts, A. 1982, *The ESO/Uppsala Survey of the ESO (B) Atlas* (Garching: European Southern Observatory).
- Lauberts, A. and Valentijn, E. A. 1989, *The Surface Photometry Catalogue of the EDO-Uppsala Galaxies* (Munich: European Southern Observatory).
- Lavezzi, T. E. and Dickey, J. M. 1997, *AJ*, **114**, 2437.
- Lequeux, J., Dantel-Fort, M., and Fort, B. 1995, *A&A*, **296**, L13.
- Lund, J. M. and Dixon, R. S. 1973, *PASP*, **85**, 230.
- Maddox, S.J., Efstathiou, G., Sutherland, W.J., Loveday, J. 1990, *MNRAS*, **243**, 692.
- Marzke, R. O., Huchra, J. P., and Geller, M. J. 1994, *ApJ*, **428**, 43.
- McArthur, B., Jeffreys, W., and McCartney, J. 1994, *BAAS*, **184**, 28.04.
- Mihalas, D. and Binney, J. 1981, *Galactic Astronomy, Second Edition* (New York: W. H. Freeman and Company).
- Minkowski R.L. and Abell, G. O. 1963, in *Stars and Stellar Systems, vol. III*, ed. Strand, K. A. (Chicago: U of Chicago), p.481.
- Monet, D. 1993, private communication.
- Monella, R. 1985, *Coelum LIII*, 287.
- Muriel, H. and Lambas, D. G. 1992, *AJ*, **103**, 393.
- Nilson, P. 1973, *Uppsala Astron. Obs. Annals*, No. 6.
- Nousek, J. and Shue, D. 1989, *ApJ*, **342**, 1207.
- Odehahn, S. C., Humphreys, R. M., Aldering, G., and Thurmes, P. 1993, *PASP*, **105**, 1354.
- Odehahn, S. C., Stockwell, E. B., Pennington, R. L., Humphreys, R. M., and Zumach, W. A. 1992, *AJ*, **103**, 318.
- Odehahn, S. C. and Aldering, G. L. 1995, *AJ*, **110**, 2009.

- Peacock, J. A. 1999, *Cosmological Physics* (Cambridge: Cambridge University Press).
- Peebles, P. J. E. 1969, ApJ, **155**, 393.
- Peebles, P. J. E. 1976, ApJ, **205**, 318.
- Peletier, R. F., Davies, R. L., Illinworth, G. D., Davis, L. E., and Cawson, M. 1990, AJ, **100**, 1091.
- Peletier, R. F., Valentijn, E. A., Moorwood, A. F. M., Freudlin, W., Knapen, J. H., and Beckman, J. E. 1995, A&A, **300**, L1.
- Pennington, R. L., Humphreys, R. M., Odewahn, S. C., Zumach, W., Thurmes, P. M. 1993, PASP, **105**, 521.
- Press, W. H., Teukolsky, S. A., Vetterlin, W. T., and Flannery, B. P. 1992, *Numerical Recipes in C (Second Edition)* (New York: Cambridge University Press).
- Quinn, T. and Binney, J. 1992, MNRAS, **255**, 729.
- Sakai, S., Giovanelli, R., and Wegner, G. 1993, AJ, **108**, 33.
- Sandage, A. and Tammann G. A. 1981, *Revised Shapley-Ames Catalog of Bright Galaxies* (Washington: Carnegie Institution of Washington Publication).
- Schombert, J. M., Wallin, J. F., and Struck-Marcell, C. 1990, AJ, **99**, 497.
- Shane, C. D., and Wirtanen, C. A. 1967, *Publ. Lick. Obs. 22*, part 1.
- Schechter, P. L. 1976, ApJ, **203**, 297.
- Schechter, P. L. 1980, AJ, **85**, 801.
- Schlegel, D., Finkbeiner, D.P., and Davis, M. 1998, AJ, **500**, 525.
- Schmidt, M. 1968, ApJ, **151**, 393.
- Shapley, H. 1918, ApJ, **48**, 154.
- Shapley, H. and Ames, A. 1932, *A Survey of the External Galaxies Brighter than the Thirteenth Magnitude* (Cambridge: Harvard Observatory).
- Smithsonian Institution 1966, *Smithsonian Astrophysical Star Catalog* (Washington: US Government Printing Office).
- Sofue, Y. 1992, PASJ, **44**, L1.

- Stavely-Smith, L. and Ravies, R.D. 1987, MNRAS, **224**, 953.
- Strom, S. and Strom, K. 1978, AJ, **83**, 732.
- Sugai, H. and Iye, M. 1995, MNRAS, **276**, 327.
- Trasarti-Battistoni, R., Invernizzi, G., & Bonometto, S. A. 1997, ApJ, **475**, 1.
- Trimble, V. 1995, PASP, **107**, 1133.
- Trumpler, R. J. 1930, *Lick Obs. Bull.*, **14**, 154.
- Trewhella, M., Davies, J. I., Disney, M. J., and Jones, H. G. W. 1997, MNRAS, **288**, 397.
- Tully, R. B. and Fouqué, P. 1985, ApJS, **58**, 67.
- Valentijn, E. A. 1990, *Nature*, **346**, 153.
- Verner, D. A. and Chernin, A. D. 1987, AZh, **64**, 244.
- Weinberg, S. 1972, *Gravitation and Cosmology: Principles and Applications of the General Theory of Relativity* (New York: Wiley).
- West, M. J. 1994, MNRAS, **268**, 79.
- White, R. E. and keel, W. C. 1992, *Nature*, **359**, 129.
- White, S. D. M. 1984, ApJ, **286**, 38.
- Whittet, D. C. B. 1992, *Dust in the Galactic Environment* (Bristol: Institute of Physics Publishing).
- Willick, J. A. 1990, ApJ, **351**, L5.
- Willick, J. A., Courteau, S., Faber, S.M., Burstein, D., Dekel, A., and Strauss, M.A. 1997, ApJS, **109**, 333.
- Xilouris, E. M., Kylafis, N. D., Papamastorakis, J., Paleologou, E. V., and Haerendel, G. 1997, A&A, **325**, 135.
- Xu, C. and Buat, V. 1995, A&A, **293**, L65.
- Zaritsky, D. 1994, AJ, **108**, 1619.
- Zel'dovich, Y. B. 1970, A&A, **5**, 84.

Zwicky, F., Herzog, E., Wild, P., Karpowicz, M., and Kowal, C. T. 1961–68, *Catalogue of Galaxies and Clusters of Galaxies* (Pasadena: California Institute of Technology Press).